UNIVERSITÉ DE STRASBOURG

UNIVERSITÉ DE STRASBOURG

ÉCOLE DOCTORALE de Physique et Chimie-Physique (ED182)
Observatoire Astronomique de Strasbourg (UMR 7550)

THÈSE présentée par :

Pierre-Antoine ORIA

soutenue le : **22 septembre 2022**

pour obtenir le grade de : **Docteur de l'université de Strasbourg**

Discipline/ Spécialité : Astrophysique

Exploration des théories de matière noire et de gravitation modifiée dans l'Univers Local et la Voie Lactée

THÈSE dirigée par :
  M. IBATA Rodrigo   Directeur de recherches, Observatoire de Strasbourg, CNRS
  M. FAMAEY Benoit   Directeur de recherches, Observatoire de Strasbourg, CNRS

RAPPORTEURS :
  Mme COMBES Françoise   Professeure, Collège de France
  Mme DI MATTEO Paola   Astronome, Observatoire de Paris, GEPI

AUTRES MEMBRES DU JURY :
  M. OCVIRK Pierre   Astronome adjoint, Observatoire de Strasbourg
  M. ZHAO Hongsheng   Reader, Université de St Andrews

Liste des publications

Ci-dessous une liste des travaux publiés dans ou soumis à des journaux scientifiques avec évaluation par des pairs produits durant cette thèse.

En tant que premier auteur

2022   *Antaeus: a retrograde group of tidal debris in the Milky Way's disk plane*
Oria, P.-A.; Tenachi, W.; Ibata, R.; Famaey, B.; Yuan, Z.; Arentsen, A.; Martin, N.; Viswanathan, A.
The Astrophysical Journal Letters, Volume 936, Issue 1, id.L3, 6 pp.

2022   *Revisiting a disky origin for the faint branch of the Sagittarius stellar stream*
Oria, P.-A.; Ibata, R.; Ramos, P.; Famaey, B.; Errani, R.
The Astrophysical Journal Letters, Volume 932, Issue 2, id.L14, 7 pp.

2021   *The phantom dark matter halos of the Local Volume in the context of modified Newtonian dynamics*
Oria, P.-A.; Famaey, B.; Thomas, G. F.; Ibata, R.; Freundlich, J.; Posti, L.; Korsaga, M.; Monari, G.; Müller, O.; Libeskind, N. I.; Pawlowski, M. S.;
The Astrophysical Journal, Volume 923, Issue 1, id.68, 20 pp

En tant que co-auteur

2022   *Typhon: a polar stream from the outer halo raining through the Solar neighborhood*
Tenachi, W.; **Oria, P.-A.**; Ibata, R.; Famaey, B.; Yuan, Z.; Arentsen, A.; Martin, N.; Viswanathan, A.
The Astrophysical Journal Letters, Volume 935, Issue 2, id.L22, 6 pp.

2021   *The Sagittarius stream in Gaia eDR3 and the origin of the bifurcations*
P. Ramos; T. Antoja; Z. Yuan; A. Arentsen; **P.-A. Oria**; B. Famaey; R. Ibata; C. Mateu; J.A. Carballo-Bello
Accepté pour publication dans A&A; arXiv:2112.02105

2021   *On the Effect of the Large Magellanic Cloud on the Orbital Poles of Milky Way Satellite Galaxies*
Pawlowski, M. S.; **Oria, P.-A.**; Taibi, S.; Famaey, B.; Ibata, R.
The Astrophysical Journal, Volume 932, Issue 1, id.70, 10 pp.

2021   *Probing the radial acceleration relation and the strong equivalence principle with the Coma cluster ultra-diffuse galaxies*
Freundlich, J.; Famaey, B.; **Oria, P.-A.**; Bílek, M.; Müller, O.; Ibata, R.
Astronomy & Astrophysics, Volume 658, id.A26, 29 pp

À mes parents, et à Paul.

Remerciements

Je ne pourrai jamais assez remercier mes directeurs Benoit et Rodrigo pour avoir cru en moi et m'avoir donné la chance d'effectuer cette thèse en astrophysique. Non contents de cette confiance précieuse que vous avez placée en moi, vous avez de plus toujours été bienveillants, disponibles, et des mentors humains et scientifiques hors du commun. Grâce à vous, j'ai vécu trois ans durant lesquels travailler était un plaisir. J'emporte avec moi, ainsi que bien d'autres choses, ce goût pour de nombreux domaines variés de la recherche que vous m'avez inculqué. Merci infiniment.

J'adresse un grand merci à Françoise Combes, Paola Di Matteo, Pierre Ocvirk, et Hong-sheng Zhao qui me font l'honneur de constituer le jury de cette thèse. Je vous en suis extrêmement reconnaissant. Je remercie de plus Françoise et Pierre, membres du comité de suivi, pour leurs retours et encouragements lors de la présentation de mi-thèse.

L'observatoire de Strasbourg est un cadre de travail accueillant et formidable que je quitte avec une grande peine ; j'en remercie tous les membres pour la bonté et la bonne ambiance qui y règnent. Mes pensées se tournent plus particulièrement vers l'équipe du lundi que je connais le mieux : Anke, Clément, Giacomo, Jonathan, Lorenzo, Marie, Nicolas, Paolo, Pau, Rapha, Simon, et Zhen. Un grand merci pour votre bonne humeur, votre soutien, et les discussions scientifiques où j'ai tant appris. J'arrive maintenant à mes collègues doctorant(e)s, des personnes extraordinaires qui ont donné de la magie à mon séjour à l'observatoire : Amandine, Élisabeth, Émilie, Hussein, Ivan, Jakub, Julien, Rashi, Thibaut, Thomas et Wassim. Merci pour les midis, les pauses thé, le ping-pong, les jeux ; merci à mon FdO pour les showdowns ; merci à mes PAWT pour la semaine de folie à Besac (maintenant immortalisée de la façon que vous savez) ; merci pour avoir fait de ma vie une sitcom durant quelques mois. Chaque moment passé avec vous fut un véritable plaisir, et je déplore grandement que nos relations aient été écourtées par la pandémie. PS : on pourra toujours se voir à votre fast food favori ;)

Enfin, je tiens de façon générale à remercier chaque personne dont l'existence seule est ou fut une joie pour moi, chaque personne qui a eu une influence considérable - parfois sans se rendre compte à quel point, ou sans en avoir même la moindre idée - sur la mienne. C'est en grande partie grâce à vous que mes choix se sont portés vers ce parcours, et que j'ai eu la force et l'envie de le mener à terme. Je pense aux personnes déjà mentionnées précédemment. Je pense à ma famille, et en particulier à mes frères et soeurs, à Kathy, et à Brigitte. Je pense à la bande du Cambrésis : Adrien, Bertrand, Florian, Julien, Kévin, Maxime, Samuel ; à la bande de Lille : Antoine, Gauthier, Hana, Ibrahima, Loïc ; aux Strasbourgeois(es) : Bianca, Jérôme, Karim, Stéphane, et enfin Laure, qui occupera toujours une place spéciale en moi. Je pense aussi, par exemple, à des enseignants (M. Gentilhomme, M. El Kacimi), à des auteurs, musiciens, réalisateurs, et créateurs de toute sorte. Je pense, enfin, à tous les animaux qui ont partagé ma vie, et qui ont été autant d'amis et de compagnons.

Contents

Chapter 1 Gravitation, dark matter, and galactic archeology

One of the longest-standing and most pressing challenges in present day astrophysics is explaining the mass discrepancy problem. The issue can be summarized as follows: mass and energy inferred from observations of various structures of many different scales in the universe do not agree with the predictions of General Relativity (GR), the currently widely accepted theory of gravitation brilliantly introduced by Einstein (Einstein, 1916). This is often addressed by involving two components of unknown origin: dark matter (DM) and dark energy.

Historically, claims of a mass discrepancy started in the beginning of the 20th century. In 1932, Jan Oort studied the stellar motions of stars in the vicinity of the sun and concluded that additional mass was needed to reproduce his observations (Oort, 1932). In 1933, Zwicky inferred from high velocity dispersions in galaxy clusters a required mass more than a hundred times the observed baryonic mass for the objects to remain gravitationally bound (Zwicky, 1933). This is of course a very high discrepancy, which we can now impute both to bad estimations of distances leading to bad stellar masses, and to the fact that most of the baryonic mass of galaxy clusters, lying in the intracluster medium gas, was not detected then, since it emits X-rays and requires observations from space. To this day however, Zwicky was right in the sense that there remains a mass discrepancy in galaxy clusters, albeit a much smaller one.

On the smaller scale of galaxies, early N-body simulations of cold galactic disks showed that they were prone to major instabilities. In order for disks to survive and reconcile the theory with the observation of numerous spiral galaxies, it was suggested in (Ostriker & Peebles, 1973) that galactic disks should be immersed in a more or less spherical potential, of a component they called "halo", although without mentioning dark matter at this point. Stabilizing disks in this fashion will later be one of the uses of the dark matter halo, although at the time the halo-to-disk mass ratios suggested (2.5 : 1) were much lower than the ones inferred now.

In the same decade, the rotation curves of spiral galaxies, representing the circular velocity of stars at a given radius r from the center, were found to be asymptotically flat, whereas Newton's law of gravity predicts a decline proportional to $r^{-1/2}$. This started to be observed in the late 1970s, with an historical report of this phenomenon being Rubin et al. (1980), in which the rotation curves of 21 galaxies were obtained from spectral observations, and where this stunning conclusion can be read:

"*This form for the rotation curves implies that the mass is not centrally con-*

densed, but that significant mass is located at large r. The integral mass is increasing at least as fast as r. The mass is not converging to a limiting mass at the edge of the optical image. The conclusion is inescapable that non-luminous matter exists beyond the optical galaxy."

With hindsight, we could now think it might have been more cautious to state that from these observations, it follows that either there is some mass the observations did not detect, or our comprehension of gravitation is imperfect (or both). In fact, Vera Rubin herself will later say in an interview:

"If I could have my pick, I would like to learn that Newton's laws must be modified in order to correctly describe gravitational interactions at large distances. That's more appealing than a universe filled with a new kind of sub-nuclear particle."

Those discrepancies, mostly dynamical and at galactic scales, are not the only reason to invoke dark matter. On larger, cosmological scales also the presence of unseen mass seems hard to avoid.

Indeed, in the first few minutes of the universe, as the universe is hot and dense enough in the radiation-dominated era, a process called Big-Bang nucleosynthesis (the idea of which originated in the famous $\alpha\beta\gamma$ paper (Alpher et al., 1948); see also Copi et al. (1995) and references therein) creates the light elements (deuterium, helium, lithium) by nuclear reactions. The abundance of these elements and thus the baryonic mass density Ω_b of the universe has since been constrained by observations (*e.g.* of the Cosmic Microwave Background (CMB) by Planck, of highly ionized gas in metal-poor dwarf galaxies, and of quasars with absorption lines (Cyburt et al., 2016)). However, the total mass density of matter Ω_m inferred from *e.g.* the large scale peculiar velocities of galaxies and the gravitational pull needed to reproduce the evolution of large scale structures from the CMB to present time inevitably lead to $\Omega_m > \Omega_b$. The angular power spectrum of the CMB also strongly hints at the presence of non-baryonic matter as we will see in Section 1.4.1. It follows that, in the context of General Relativity, we need additional matter, and that this matter should be non-baryonic.

In order to solve the missing mass problem, we are left with two obvious options, or a combination of them: dark matter theories, in which the presence of undetected "dark" particles that only interact via gravity is assumed to make up for the mass needed to make GR and cosmological observations concordant; and modified gravity theories, in which the equations describing gravitation differ from the Newtonian and GR equations, in the low-acceleration regime of galaxies in particular.

After many years now of fruitless direct or indirect detection experiments, constraints have become tighter but the nature of the dark matter particles remains elusive. At the same time, extraordinary regularity is observed at galactic scales (see Section 1.4), suggesting that baryons could play a bigger role than anticipated. In light of this, it is of utmost importance to consider all possibilities, from modified gravity to more exotic DM particles (or DM "fluid") than the most popular candidates. The aim of this thesis was to explore our Galaxy the Milky Way (MW) and the Local Universe surrounding us in order to probe and place constraints on different dark matter and gravitation models. The MW, with its complex history, many satellite galaxies and stellar streams, and exquisite observational data brought in particular by *Gaia* (Gaia Collaboration et al., 2016) constitutes an ideal laboratory for such a project.

Streams extending to large radii can for instance provide invaluable information on the shape of the gravitational potential in the outskirts of the Galaxy. An example is the Sagittarius stream which is, in principle, a superb probe to test gravitational theories and various DM models. However, as we will see, it still poses serious modelling challenges, which hinders our ability to use it effectively as a prospective probe of the MW gravitational potential at large distances. These challenges can in part be due to the modelling of the inner dynamics of the progenitor itself (see Chapters 5 and 6). This means that, while the MW with its exquisite *Gaia* data represents the ideal laboratory to test our cosmological models on local scales, this has to go hand in hand with a detailed modelling of the stellar dynamics, which involves many subtleties. This thesis will both explore predictions of alternatives to our standard cosmological model, which we will now describe below, and explore the subtleties that can affect the kinematics and morphology of tracers of the MW potential such as the Sagittarius stream.

In the following subsections, we review some famous models for gravitation and cosmology, and see how they fare when confronted to observations of the universe at various scales.

1.1 ΛCDM

The Λ Cold Dark Matter (ΛCDM) model, introduced in Ostriker & Steinhardt (1995) as the concordance model of cosmology, is now widely regarded as the standard model of cosmology. In this context, the Λ component is the cosmological constant of the field equations of General Relativity - the underlying theory of gravitation - and represents dark energy, a negative pressure fluid that is necessary to explain the acceleration of the expansion of the universe. Cold dark matter constitutes $\sim 5/6$ of the matter content of the universe, with the last sixth being baryonic matter. "Cold" here is meant dynamically, meaning that the dark matter particle is rather massive (if it is a fermion, but note that very light bosons such as axions can also act as cold DM), and in the early universe (roughly at the time of recombination, see Section 1.4.1), it was far from reaching relativistic speeds, allowing structure formation on many scales (warmer, lighter particles would suppress the formation of small halos).

The ΛCDM theory relies on the assumption of the cosmological principle, which states that the universe is homogeneous and isotropic, roughly meaning that it is more or less the same in every location and every direction. This is heavily dependent on the scales considered of course, since locally, huge differences are observed (*e.g.* galaxies and clusters on one hand, voids on the other hand). Realistically, this principle means that if one looks at different regions of the same size scale (which should be large enough), they should be rather similar. It also means that we should not expect too many significant overdensities or underdensities (large structures, voids) bigger than this size scale. In Yadav et al. (2010), it is estimated that this principle should be verified over scales of $260h^{-1}\,\mathrm{Mpc}$[1].

The model led to very impressive predictions at cosmological scales including the acceleration of the expansion of the universe, the scale of the baryon acoustic oscillations in galaxy surveys over a wide range of redshifts (Reid et al., 2016), and probably the most notable one:

---

[1]$h = H_0/100$ (where H_0 is the Hubble constant introduced just below) is the expansion rate of the universe, allowing to talk in terms of comoving distances.

the fit to the power spectrum of the CMB (Section 1.4.1).

1.1.1 The model

General Relativity describes gravitation by connecting matter and energy in the universe to its geometry via the beautiful Einstein Field Equations:

$$R_{\mu\nu} - (\frac{1}{2}R - \Lambda)g_{\mu\nu} = \frac{8\pi G}{c^4}T_{\mu\nu}. \tag{1.1}$$

In the right-hand side of Equation (1.1), matter and energy are represented by the stress-energy tensor $T_{\mu\nu}$. The left-hand side of the equation describes the geometry via the metric tensor $g_{\mu\nu}$, the Ricci curvature tensor $R_{\mu\nu}$ involving second derivatives of the metric tensor, and the scalar curvature R (an invariant obtained from the two previous tensors).

ΛCDM relies on GR and the Friedmann-Lemaître-Robertson-Walker metric, describing a homogeneous and isotropic universe (Cosmological principle) and providing a framework for the expansion of the universe discovered by Hubble, with a Hubble constant $H_0 = 67.81 \pm 0.92 \, \mathrm{km \, s^{-1} \, Mpc^{-1}}$ as estimated by Planck Collaboration et al. (2016) (although this has since been in conflict with subsequent measurements for H_0 at higher values, leading to the "Hubble tension"; see e.g. Riess et al. (2021) using supernovae and Cepheids).

Also from observations of the CMB by Planck Collaboration et al. (2016), the total matter density parameter has been found to be $\Omega_m = 0.308 \pm 0.012$ while the baryonic matter density is $\Omega_b = 0.048$, and the ratio of dark energy density over critical density is $\Omega_\Lambda = 0.692 \pm 0.012$, leading to a flat geometry ($\Omega_m + \Omega_\Lambda = 1$). The mission also provides values for the following important parameters: the amplitude of primordial fluctuations is $\sigma_8 = 0.8149 \pm 0.0093$ (this corresponds to the dispersion in mass when sampling the Universe at random places within spherical volumes of $8h^{-1} \, \mathrm{Mpc}$, a scale that is still in the linear regime of cosmological perturbations); the reionization optical depth parameter, linked to the formation of the first stars, is $\tau = 0.066 \pm 0.016$; and the spectral index, describing how the primordial density fluctuations vary with scale, namely as a nearly scale-invariant power-law $\propto k^{n_s-1}$ where k is the wavenumber (in $h \, \mathrm{Mpc}^{-1}$), is $n_s = 0.9677 \pm 0.0060$.

1.1.2 Dark matter halo profiles

At smaller scales, ΛCDM assumes that every galaxy is embedded in a cold dark matter halo which brings mass needed for the stability of the baryonic structures they host, such as galactic disks, and to reproduce the observed kinematics. Indeed, CDM is able to form structures before recombination, while the baryons are still coupled to the photons; this creates deep potential wells that will attract baryonic matter after its decoupling from photons, which will then form the first stars and galaxies. ΛCDM predicts a bottom-up scenario for galaxy formation, in which the first galaxies that form are small, and later merge together to form the bigger galaxies observed at present time such as our MW.

From simulations of hierarchical clustering, Navarro et al. (1997) found that at equilibrium, the dark matter density of halos is well fit to first order by the following Navarro-Frenk-White (NFW) profile:

$$\rho_{\mathrm{NFW}}(r) = \frac{\rho_0}{\frac{r}{r_s}\left(1 + \frac{r}{r_s}\right)^2} \tag{1.2}$$

where r is the distance from the center of the galaxy, r_s is a scale radius, and ρ_0 a characteristic density. The characteristic density ρ_0 is proportional to the critical density of the universe ρ_{crit} at the time of the halo's formation. We usually assume that a halo extends up to its virial radius r_{vir}, defined by

$$r_{\mathrm{vir}} = \left(\frac{M_{\mathrm{vir}}}{(4/3)\pi 200\rho_{\mathrm{crit}}} \right)^{1/3}, \tag{1.3}$$

where M_{vir} is the virial mass (enclosed in the virial radius) and obtain the relation $r_s = r_{\mathrm{vir}}/c$ where c is called halo concentration.

This makes the NFW halos a two-parameters family, depending on total halo mass M_{vir} and concentration. However, the halo mass-concentration relation (Dutton & Macciò, 2014) constrains the concentration and thus size of the halo as a function of its mass, effectively narrowing the range of realistic NFW profiles, and virtually making it a one-parameter family. One feature of note is that this implies that all DM halos should look the same internally (they are "self-similar" across all scales), no matter the characteristics and physical parameters of the underlying galaxy.

The NFW profile is cuspy, meaning that in the inner parts of the halo, the density profile diverges when approaching the very center of the galaxy. This is sometimes in conflict with observations, which seem to favour a "cored" profile with constant slope for dark matter in the inner regions of the halo for several galaxies. Other analytical DM density profiles are also popular: the Einasto (Einasto, 1965) profile in particular which does not have this central divergence, cored alternatives such as the Burkert (Burkert, 1995) profile, or more flexible profiles from the Dekel-Zhao family (Dekel et al., 2017; Freundlich et al., 2020) with free parameters for the inner slope.

It is argued that initially cuspy distributions of dark matter could flatten via feedback mechanisms leading to core formation. For example, supernovae and active galactic nuclei could alter the distribution of baryons such that the effect on the gravitational potential would push out some dark matter from the inner parts of galaxies (see *e.g.* Pontzen & Governato (2012); Li et al. (2022)). In cosmological simulations of galaxy formation, the efficiency of cusp-core transformation is however wildly disagreeing from one simulation to the other and very dependent on the feedback recipes, often leading to too many cusps or too many cores, known as the diversity problem (see Section 1.4.7).

1.1.3 Structure formation

Structure formation in ΛCDM is based on the primordial fluctuations, gravitation, and the expansion of the universe. In a hierarchical growth scenario, dark matter halos form first and attract baryonic matter to host small galaxies which will then become bigger and bigger by successive mergers. The most massive DM halos are expected to host many less massive subhalos, which in turn can themselves host galaxies. For example, satellite galaxies in our MW are expected to have been born in and to still be surrounded by a dark matter halo, with some of them being direct subhalos of the MW born *in situ*, while others have been accreted.

This scenario has several consequences that can be confronted to observations, for example: few giant galaxies and clusters should be observed at very high redshift, large galaxies at

the present time should have a rich history of accretions, pure disk galaxies should be scarce as consecutive mergers will often lead to the creation of a bulge.

After recombination, baryonic matter in the universe is mostly made of neutral hydrogen atoms, in what is a rather opaque "Dark Ages" period. Then as structures condense and start to form stars, the neutral hydrogen environment will get reionized, and the universe will shift to an ionized plasma state. This is the Epoch of Reionization (EoR), lasting up to $\sim 1\,\mathrm{Gyr}$ after the Big Bang.

The EoR is thus intricately linked to the formation of the first stars and galaxies in the universe and it is crucial to understand it thoroughly. Reionization also has consequences on galaxy formation, since stellar feedback can suppress star formation in the smallest galaxies. As such this will have a direct impact on the number of satellites expected around a MW-like galaxy for example. Ocvirk et al. (2016, 2020) investigate this using Cosmic Dawn (CoDa), a suite of large scale cosmological hydrodynamical simulations, showing the impact of the EoR on structure formation compared to the expected CDM power spectrum.

1.2 MOND

Almost forty years ago now, Milgrom proposed (Milgrom, 1983) that gravity might behave differently in the weak acceleration field limit. This suggestion is summarized as the following force law:

$$\mu(\frac{g}{a_0})g = g_N. \tag{1.4}$$

Here g is the MONDian gravitational acceleration of the considered system, g_N is its Newtonian equivalent, a_0 is a critical acceleration constant occurring naturally in several observational relations and of the order of 10^{-10} ms^{-2}, and μ is a function assuring a smooth transition between the Newtonian and Milgromian regimes. In particular, this μ function should verify

$$\mu(x) \to 1 \ (x \gg 1) \tag{1.5}$$

in order to agree with Newtonian dynamics (if the acceleration is much greater than a_0, then Equation (1.4) tells us that the potential agrees with the Newtonian one), and

$$\mu(x) \to x \ (x \ll 1) \tag{1.6}$$

giving the Milgromian regime for low accelerations:

$$g = \sqrt{a_0 g_N} := \nu(\frac{g_N}{a_0})g_N. \tag{1.7}$$

The right-hand side term of Equation (1.7) is just inverting Milgrom's law Equation (1.4). It will sometimes be more convenient, as in Section 1.2.1, to use this formulation instead, in which ν is an interpolation function linked to μ and the behaviour of which is limited by Equations (1.5) and (1.6):

$$\nu(x) \to 1 \ (x \gg 1) \text{ and } \nu(x) \to x^{-1/2} \ (x \ll 1). \tag{1.8}$$

The simple prescription of Equation (1.4) directly yields the asymptotic flatness of rotation curves (which it was built for). Indeed, in the Newtonian case, equilibrium between centripetal and gravitational acceleration at radius r in a system with point mass M is

$$g_N = \frac{GM}{r^2} = \frac{V_c^2(r)}{r}, \tag{1.9}$$

where V_c is the circular velocity. In the low acceleration regime, replacing g_N by the MONDian g of Equation (1.7) we get

$$\sqrt{a_0 g_N} = \sqrt{\frac{GMa_0}{r^2}} = \frac{V_c^2(r)}{r}, \tag{1.10}$$

and thus finally

$$V_c^4(r) = GMa_0, \tag{1.11}$$

yielding that the circular velocity only depends on the mass of the system, which for a point mass here is a constant, removing the dependency on radius. In more realistic systems in which $M = M(r)$, this still yields that at large-enough radii, the circular velocity becomes asymptotically flat: $V_{\text{flat}} := V_f = (GMa_0)^{1/4}$, with M being the total mass of the system. In Section 1.2.2, a mechanism to counteract this asymptotic flatness (which could in theory extend forever in an isolated system) depending on the environment will be introduced.

When proposed in 1983, this law's aim was to get this asymptotic flatness, as well as to reproduce the slope of the Tully-Fisher relation (the original one based on luminosity, not the baryonic version as seen in Section 1.4.4). However as time went on, it yielded many agreements with empirical relations and observations that have been discovered much later than its inception, such as *e.g.* the diversity of rotation curves, Renzo's rule, and the Radial Acceleration Relation, as we will see in Section 1.4.

Milgrom's formula (1.4) should however only be an approximation usable in specific conditions, and cannot represent an universal force law. Indeed, in the case of a two-body system, the implied force is not symmetric, and there is no conservation of momentum. Equation (1.4) in this form is only a scaling relation between the true gravitational acceleration (the one generated by DM plus baryons in DM theories) and that generated by baryons. It should be a specific case of a more general framework, resulting from Lagrangian mechanics, in order to obey conservation laws. Several full-fledged theories unified under the Modified Newtonian Dynamics (MOND) paradigm are exactly that. We take a closer look at one of those theories in the next subsection. For a detailed review of MOND, its different formulations, and comparisons to ΛCDM, see for example Famaey & McGaugh (2012).

1.2.1 QUMOND

We will be interested in the Quasi-linear formulation of MOND (QUMOND), introduced in Milgrom (2010), and thus named because only one non-linear step is required in computations. Let us start by deriving the modified QUMOND Poisson's equation using field theory.

Field theory allows us to describe the behaviour and the symmetries of a system via the introduction of an appropriate real-valued function of configuration space (and associated velocities) and time coordinates, the Lagrangian, with units of energy. An action S is a

functional, a real-valued function of functions, returning the integral over time along a given path of a given Lagrangian. The principle of stationary action states that the equations governing a system, such as the equation of motion of particles, are obtained by seeking where the rate of change of the action S is zero (the path followed by the system is the one corresponding to the extremum of the action).

In the example of Newtonian gravity, the Lagrangian density seen as a function of the gravitational potential Φ is given by

$$\mathcal{L}(\Phi, \nabla\Phi) = -\rho\Phi - \frac{(\nabla\Phi)^2}{8\pi G} \tag{1.12}$$

where ρ is the matter density and is, like Φ, a real-valued function of space and time. The action S in this case is thus given by

$$S(\Phi) = \int \mathcal{L}(\Phi, \nabla\Phi)d^3x dt. \tag{1.13}$$

Varying this action spatially with respect to Φ to the first order using a small perturbing real function h (*i.e.* such that $\forall\, x \in \mathbb{R}^3$, $|h(x)| << 1$) which vanishes at the boundaries gives us

$$\begin{aligned}
\delta S = S(\Phi + h) - S(\Phi) &= \int \Big(\mathcal{L}(\Phi + h, \nabla\Phi + \nabla h) - \mathcal{L}(\Phi, \nabla\Phi)\Big)d^3x dt \\
&= \int \Big(\mathcal{L}(\Phi, \nabla\Phi) + h\frac{\partial\mathcal{L}}{\partial\Phi} + \nabla h\frac{\partial\mathcal{L}}{\partial\nabla\Phi} - \mathcal{L}(\Phi, \nabla\Phi)\Big)d^3x dt. \\
&= \int \Big(-h\rho - \frac{\nabla h\nabla\Phi}{4\pi G}\Big)d^3x dt \\
&= \int \Big(-h\rho + \frac{h\Delta\Phi}{4\pi G}\Big)d^3x dt - \int \Big(\underbrace{\int_M \frac{h\nabla\Phi}{4\pi G}dM}_{=0}\Big)dt
\end{aligned}$$

where the divergence theorem was used for the last equation, and the integral on the boundary surface M vanishes along with h. Requiring that $\delta S = 0$ leads to a famous result linking the density to the gravitational potential, Poisson's equation:

$$\Delta\Phi = 4\pi G\rho. \tag{1.14}$$

In QUMOND, the gravitational Lagrangian is altered in order to introduce the a_0 constant and an auxiliary acceleration field which is a function of the Newtonian field, giving

$$\mathcal{L}(\Phi, \Phi_N) = \rho(v^2/2 - \Phi) - \frac{1}{8\pi G}(2\nabla\Phi \cdot \nabla\Phi_N - a_0^2 Q(|\nabla\Phi_N|^2/a_0^2)) \tag{1.15}$$

where Φ_N represents the Newtonian gravitational potential while Φ represents the QUMOND gravitational potential, and Q is, for the moment, an arbitrary real function. A spatial variation of the action as before for this new Lagrangian with respect to the total potential Φ leads to Poisson's equation for the Newtonian potential:

$$\Delta\Phi_N = 4\pi G\rho. \tag{1.16}$$

With respect to the Newtonian potential Φ_N, it leads to a generalized Poisson's equation Milgrom (2010, Section 2.2):

$$\Delta\Phi = \nabla \cdot \left[\nu\left(\frac{|\nabla\Phi_N|}{a_0}\right)\nabla\Phi_N\right] \tag{1.17}$$

where $\nu : y \mapsto Q'(y^2)$. The form of Q will be imposed by Milgrom's law and the conditions on the interpolation function ν from Equations (1.4) and (1.8).

The QUMOND formulation involves a theoretical component called "Phantom Dark Matter" (PDM) which corresponds to the matter that one would need in the context of Newtonian gravity to obtain the modification of gravity of QUMOND. This is very useful from a theoretical viewpoint since it allows direct comparisons to dark matter theories and gives a better understanding of the MOND effects, but what is more, it is also an invaluable tool for practical purposes since it offers a way to obtain the QUMOND gravitational potential. Indeed, Equation (1.17) can be recast as an analog of the standard Poisson's equation:

$$\Delta\Phi = 4\pi G(\rho_{\text{PDM}} + \rho_b) \tag{1.18}$$

where ρ_{PDM} is the PDM density. By combining Equation (1.17) and Equation (1.18), one gets an analytical expression for the PDM density

$$\rho_{\text{PDM}} = \frac{1}{4\pi G}\,\nabla \cdot \left[(\nu\left(\frac{|\nabla\Phi_N|}{a_0}\right) - 1)\nabla\Phi_N\right]. \tag{1.19}$$

This last expression shows us that the only ingredient that is required to compute the PDM density is the (baryonic) Newtonian potential. This makes QUMOND very interesting and practical from a computational point of view: in practice, one solves Poisson's equation twice. The first time is the standard Poisson's equation (1.14) to get the Newtonian potential Φ_N from the baryonic density ρ_b, which then yields the PDM density ρ_{PDM} via Equation (1.19), and the second time is the QUMOND generalized Poisson's equation (1.18) to get the QUMOND potential Φ. In Section 2, we will detail ways to compute those quantities numerically.

1.2.2 The external field effect

In Newtonian gravity, a constant external acceleration field through a studied system has no effect (meaning that in this case the system can be treated as isolated), and a varying external field causes tidal effects (*e.g.* a satellite galaxy orbiting its host undergoes tidal disruption).

In MOND however, when studying a system, the total acceleration has to be taken into account, including the external one. This is a very specific feature called the External Field Effect (EFE). It breaks the Strong Equivalence Principle (SEP) of GR, which establishes that the internal dynamics of a system are not affected by a constant external gravitational field that the system might be embedded in.

In practice then, if we consider g the internal gravitational acceleration of a studied system, and g_e the external acceleration field, we only have MOND effects in what is called

the "deep-MOND" regime, *i.e.* when

$$g_e < g < a_0. \tag{1.20}$$

However when g_e is stronger:

$$g < g_e < a_0, \tag{1.21}$$

then the dynamics get closer to the Newtonian case, but with a renormalized gravitational constant depending on the external field.

A constant external acceleration field will then have effects on the internal dynamics of a system, as opposed to the Newtonian case, and no system can be treated as isolated in MOND. A varying external field will also cause tidal effects, in addition to the EFE. As such, tidal disruption of a satellite galaxy orbiting its host will be exacerbated in MOND, making the satellite even more fragile at pericenter compared to the Newtonian case.

In Famaey & McGaugh (2012), a formula induced from the one-dimensional approximation is proposed for the QUMONDian gravitational acceleration g of a system with Newtonian gravitational acceleration g_N under a constant (Newtonian) external field g_{N_e}:

$$g = g_N \nu \left(\frac{g_N + g_{N_e}}{a_0} \right) + g_{N_e} \left(\nu \left(\frac{g_N + g_{N_e}}{a_0} \right) - \nu \left(\frac{g_{N_e}}{a_0} \right) \right). \tag{1.22}$$

In the context of our work, this formula has been confronted to the QUMONDian g obtained from a numerical computation of the gravitational potential. Our conclusion is that Equation (1.22) tends to systematically overestimate the importance of the EFE. This is expected since Equation (1.22) is obtained from a one-dimensional case where the internal and external field are aligned, while in reality the direction of the EFE and the shape of the system (*e.g.* orientation of a galactic disk) will have a considerable influence. In Section 4, we will propose a new formula which we introduce in Freundlich et al. (2022), based on approximations of g over spherical shells, with results in much better agreement with numerical computations, as also seen in Oria et al. (2021) and Chae & Milgrom (2022).

Recently, in the context of QUMOND, Chae et al. (2020, 2021) looked at the EFE induced from large scale structures, and especially at its impact on rotation curves of disky galaxies by using the SPARC (Lelli et al., 2016a) survey data. They obtain a statistically significant detection on the EFE, with a stark contrast depending on the environment: nearly isolated galaxies have data consistent with a very low external field, while galaxies in dense environments have data consistent with a strong external field, as expected by MOND.

The EFE can also be quantified thanks to the PDM density. Indeed, in transition regions where $g \simeq g_e$, negative PDM density zones are expected, with orientation and intensity depending on the dominating external acceleration source. This can make the gravitational potential asymmetric, but also weaker, since the overall PDM mass of the system gets lowered. This will all be studied in detail in Section 3, in which we take a deeper look at the EFE and its consequences by mapping the Local Universe in QUMOND.

1.2.3 Cosmological extensions of MOND

A relativistic extension of MOND has to be in agreement with several observations and phenomena, in particular the power spectrum of the CMB (Section 1.4.1), gravitational

lensing, dynamics in the solar system (precession of Mercury's pericenter). MOND as a modification of gravity cannot address those observations "out of the box", but it is interesting to look for an extension model that reduces to Milgrom's law on the scale of galaxies. One of the most famous relativistic MOND theory is the Tensor-Vector-Scalar (TeVeS) model of Bekenstein (2004), in which gravitation is mediated by a metric, a scalar field and a vector field. This model was recently ruled out by the confirmation that gravitational waves travel at the speed of light, while TeVeS predicted a small departure from c. However see Skordis & Złośnik (2019) who have shown how to modify the original TeVeS theory in a large class of modified gravity models where light and gravitational waves travel at exactly the same speed. In any case the model constituted a big step forward, especially for reproducing gravitational lensing without the need for dark matter. We briefly introduce below two possibilities of relativistic extensions for MOND.

Sterile neutrinos (νHDM).[2] Introduced in Angus (2009), this model makes no assumption on the relativistic extension of MOND (apart from assuming that dynamics and lensing are concordant and, more recently, that there is no gravitational wave speed problem), and assumes that sterile neutrinos (sterile meaning that they only interact through gravity) of mass ~ 11 eV replace CDM in the same proportions, but act as hot dark matter in the sense that they do not cluster on galactic scales. Note that the assumption that this HDM component is made of sterile neutrinos is not necessary, other light non-baryonic hot dark matter particles could do the job. Angus (2009) shows that the same expansion history as in ΛCDM can be recovered this way, along with a good fit to the angular power spectrum of the CMB. In addition, these neutrinos play the role of dark matter in galaxy clusters (see Section 1.4.2 and Section 1.4.3), allowing to reconcile MOND with observations in this context. More recently, this model has been shown to also be in agreement with producing large underdensities such as the KBC void in Haslbauer et al. (2020).

Obviously, this has the downside of yet requiring a DM-like component that has so far not been detected, losing some of the simplicity of MOND, and more importantly raising the question of gaining too much flexibility as in ΛCDM.

Scalar field acting as effective dark matter. Very recently, Skordis & Złośnik (2021) introduced a new relativistic theory reducing to MOND in the non-relativistic regime, featuring the notable achievement of fitting the power spectrum of the CMB extremely well. In this framework, the scalar field leading to MONDian behaviour also plays the role of an effective DM component in the cosmological regime, allowing for the CMB power spectrum fit. It will be highly interesting to see how this model further develops, especially in the context of galaxy clusters where MOND still faces a mass discrepancy, which perhaps this effective DM could solve (see *e.g.* discussions in Freundlich et al. (2022)).

1.3 A glimpse of other theories

Many different dark matter models have been introduced, each having pros and cons compared to ΛCDM when compared to observations (as we will see in Section 1.4). These

---

[2]This model was coined νHDM, with ν alluding both to the neutrino component and the interpolation function of MOND.

can vary for example in particle mass (lighter particles will lead to Warm or Hot Dark Matter), allowing or suppressing structure formation at different scales, but can also in some cases generate new forces via self-interaction or interaction with other particles (*e.g.* Self-Interacting Dark Matter). While our work will focus on ΛCDM and MOND (or will sometimes be model-agnostic), we introduce succinctly here a model that will be relevant to some of our studies.

Superfluid Dark Matter (SFDM) is a hybrid theory resulting in MOND phenomenology at galactic scales and ΛCDM phenomenology at cosmological scales (Berezhiani & Khoury, 2015; Berezhiani et al., 2018) via DM particles able to condense into a superfluid state. In this context, each galaxy has a superfluid core within which the collective excitation of DM condensates mediates a new force between baryons to reproduce the MONDian law of gravitation, and outside of which DM particles in their normal state form a halo akin to those expected in ΛCDM. This is a particularly enticing perspective in the context of galaxy clusters where this superfluid core could introduce a screening mechanism for the EFE, as discussed in Freundlich et al. (2022).

## 1.4 What do observations tell us?

How well do these models fare when confronted to what is observed in the universe? Several observational relations or phenomena on different scales are problematic for the theories introduced before. Without being exhaustive, we list here some of the most notable ones and discuss possible options and constraints for models. For recent detailed reviews of these topics, see also *e.g.* Famaey & McGaugh (2012), Bullock & Boylan-Kolchin (2017), Banik & Zhao (2021).

1.4.1 Cosmic Microwave Background

The Cosmic Microwave Background (CMB) is the oldest information on the universe that we can observe, coming to us from approximately 380 000 years after the Big Bang, or equivalently at a redshift $z \approx 1100$. Before this point, photons had a very short mean free path due to encountering electrons that ran rampant in the very hot early universe, and could not possibly reach us. As the universe cooled down however, electrons started to combine with protons to form hydrogen atoms (a process called "recombination"), leaving more and more room for photons to travel freely. The CMB is thus a map of the universe provided by the photons at the time of the combination of electrons and protons into hydrogen atoms.

Its precise observation has been the goal of several surveys over the last decades: the Cosmic Background Explorer (COBE), the Wilkinson Microwave Anisotropy Probe (WMAP), and more recently Planck. A wealth of information has come from those missions. In particular, small fluctuations of temperature of the order of 10^{-5} K of the mean temperature can be observed. Those fluctuations are the premises of the first baryonic structures to form in the universe.

For observers such as us, the CMB appears as a sphere seen from the inside, and a decomposition in spherical harmonics seems the natural way to study it. A Fourier analysis of those temperature fluctuations yields the power spectrum of the CMB which gives information on different angular scales. In Figure 1.1, such an analysis has been done with the data from
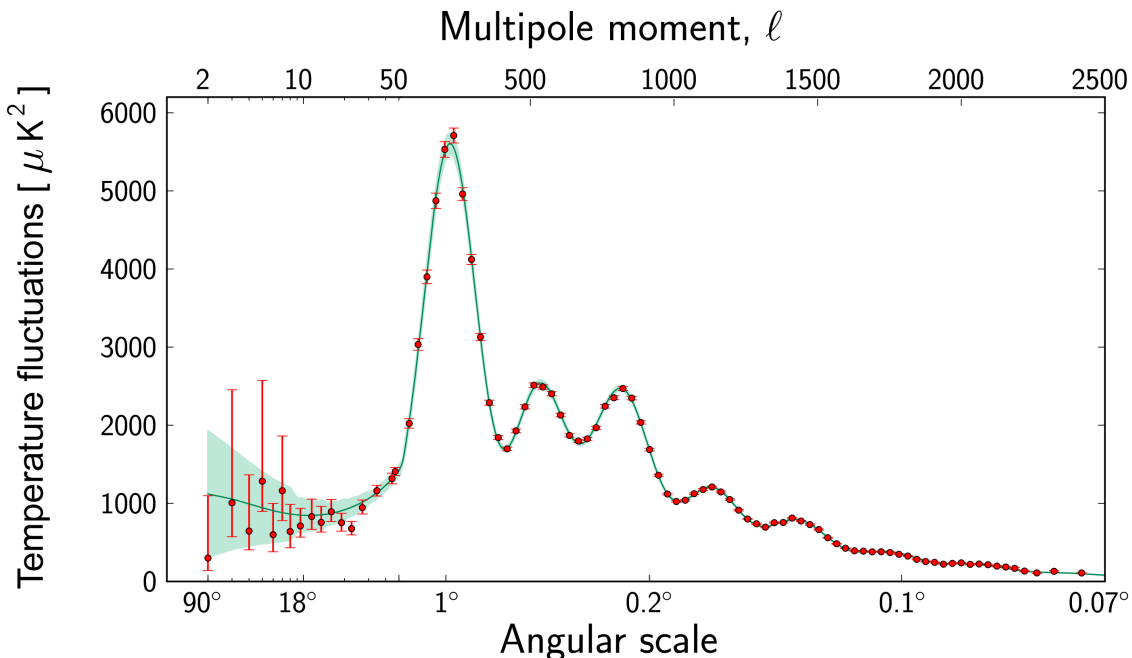
Figure 1.1: The CMB power spectrum as measured by the Plank mission collaboration (Planck Collaboration et al., 2016). Data points are in red, while the green curve is the ΛCDM model expectation, providing a spectacular match.

the Planck mission. Error bars are bigger for large scales, since we have fewer of them to study (we only have one CMB, of which we can extract a lot of small scale structures, but only a few very large scale ones). Peaks on this plot correspond to local maxima and minima of temperature fluctuations, and thus of matter density fluctuations.

What we see on Figure 1.1 is a series of peaks and valleys; those are the result of the baryonic acoustic oscillations. Gravitation tends to make matter accumulate in potential wells, but on the other hand, radiation pressure emanating from photons counteracts gravitation by dilatation. As a result, matter oscillates between contracted (denser, hotter peaks) and dilated phases. As we go towards smaller scales, we expect the peaks to go down in size due to Silk damping (diffusion of photons).

The height of the different peaks in this power spectrum yield invaluable information on the matter content of the universe: the odd peaks are compression peaks, while the even ones are rarefaction peaks. Odd peaks are boosted with respect to even ones if the baryon density of the universe goes up, through a mechanism known as "baryon loading". The ratio of the height of the first to second peak hence gives a constraint on Ω_b, which turns out to be compatible with BBN. On the other hand, the second peak would be boosted by a phenomenon known as "potential decay" if it corresponded to a perturbation which entered the horizon in the radiation era, and would be higher than the third peak. However the second and third peaks appear on the plot to be of equal height. In order to damp the second

peak without being affected by baryon loading, an additional non-baryonic component fully decoupled from the baryon-photon plasma can be added, to bring the height of the second peak at the right level. This hints strongly at the presence of a non-baryonic matter that would interact only gravitationally and would not be subject to radiation pressure, thus acting as an external potential bringing the second peak in line with the third one. A simple gravitational boost of the baryons would not give the same effect: the new degree of freedom must be decoupled from the baryon-photon plasma to yield the desired effect. This is perhaps the most convincing argument for a need for dark matter.

The green curve on Figure 1.1 is the prediction of the ΛCDM model, which provides an extraordinary agreement to the data and constitutes a major success. In the context of modified gravity, one can for instance turn to relativistic extensions of MOND like those introduced in Section 1.2.3, providing options to reproduce the power spectrum of the CMB either via a massive particle such as a sterile neutrino, or via a scalar field, although in an unsatisfying *ad hoc* way. Vanilla MOND can not hope to reproduce the CMB power spectrum however, as a pure baryonic model will have a lower third peak than observed.

1.4.2 Galaxy clusters

Galaxy clusters, like individual galaxies, also harbour a discrepancy between observed and dynamically-inferred masses, thought to be around a factor of 6 to 10. This is not an issue in DM theories and in the ΛCDM context in particular where dark matter is expected to cover this discrepancy. In the MOND context however, we would expect the modification of gravitation to be enough to match the observations. Sanders (2003) has shown that this is not the case, and that a mass discrepancy of a factor of 2 to 3 subsists. A possible solution to this problem would be missing mass, which could very well be of baryonic origin, just like hot gas in clusters was not detected until X-ray probing was possible. This is proposed in Milgrom (2008) under the form of Cluster Baryonic Dark Matter, which would be needed in approximately the same quantity as hot gas. Another way is to add sterile neutrinos as in the νHDM paradigm introduced in Section 1.2.3. This has been shown in Angus et al. (2010) to lead to a good agreement with the dynamics at equilibrium of their sample of 30 galaxy clusters and groups. One could also consider that a_0 is not a constant but rather varies with parameters such as the depth of the potential well, as proposed by Zhao & Famaey (2012). If the MONDian critical acceleration is higher in the deep potential well of galaxy clusters, then gravity is further boosted and the mass discrepancy could disappear. This has been explored further in Hodson & Zhao (2017) with partial success regarding fitting the dynamics of clusters, and issues with very strong potentials such as the vicinity of black holes.

Recently, we have shown in Freundlich et al. (2022) that Ultra-Diffuse Galaxies, usually found in a cluster environment (those we worked on being located in the Coma cluster), have dynamics that seem to agree very well with isolated MOND predictions while we expect a strong EFE from the gravitational environment. Perhaps this breakdown of the EFE in this context, where MOND already has a mass discrepancy issue, highlights a fundamental difference in the way MOND works in deep potential wells such as galaxy clusters. See Section 4 for more on this topic.

1.4.3 Bullet cluster event

The Bullet cluster event refers to the collision of two galaxy clusters (the Bullet cluster being the smallest one of the two) and is often regarded as one of the main reasons to invoke dark matter. Indeed, after both clusters collided, the gravitational lensing analysis shows that most of the mass is offset from the observable X-ray emitting gas, hinting at a collisionless dark matter that could continue its course freely while the gas from both galaxies stayed clumped in the middle. This scenario is in perfect agreement with ΛCDM.

From the point of view of MOND, this event is very difficult to explain, especially without adding unseen matter. First of all, it requires a relativistic extension to reproduce the lensing. Then, it is known that while MOND diminishes the mass discrepancy in galaxy clusters down to a factor of 2 to 3, it does not eliminate it completely. As such, the lenses from the bullet cluster event would need this missing matter in galaxy clusters to be in collisionless form, be it baryons (of which a large fraction in the universe is still undetected) necessarily in the form of dim stars or compact clouds of cold molecular gas (but not in a diffuse component!), or even maybe sterile neutrinos or the massive scalar field of Skordis & Złośnik (2021) that must still act as collisionless dark matter on such scales. But it could also be linked to the failure that MOND has to reproduce galaxy clusters dynamics in another way.

Another important point is the collisional velocity of the event, estimated at the very high value of ~ 4700 km s^{-1}. Angus & McGaugh (2008) show that while such an event in MOND can reach velocities of this order, it was initially thought complicated for ΛCDM to reach values above ~ 3800 km s^{-1}. Later works however have shown that the morphology of the Bullet cluster event could be reproduced without reaching extreme velocities in the ΛCDM context (Lage & Farrar, 2014).

The Bullet cluster event, with all its intricacies, is a very interesting observation putting constraints on many models.

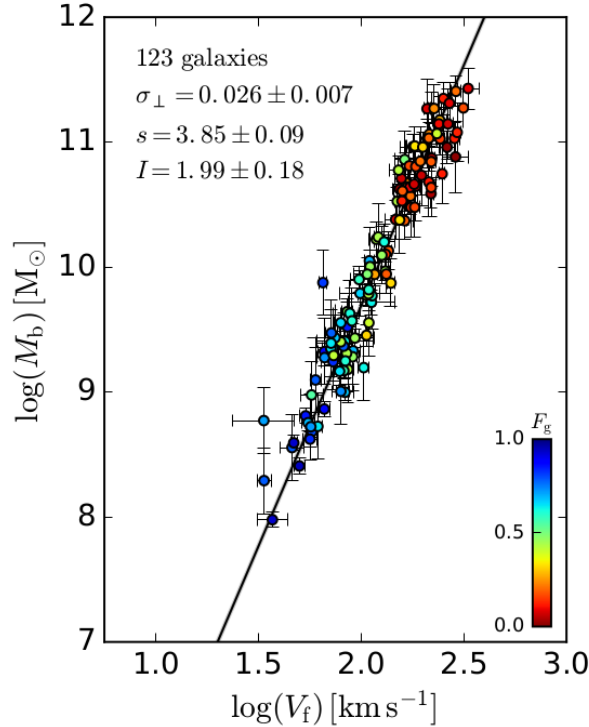### 1.4.4 The Baryonic Tully-Fisher relation

Several scaling relations have been established from observations of galaxies, and they all tend to the conclusion that galactic dynamics are dictated by the distribution of baryons. This could imply a strong coupling between baryonic and dark matter distributions which is not a natural expectation in the ΛCDM context. One of the most famous examples is the Baryonic Tully-Fisher Relation (BTFR) (McGaugh et al., 2000), linking the baryonic mass of galaxies to their rotation velocity (Figure 1.2). This relation is a direct, more impressive successor to the classical Tully-Fisher relation (Tully & Fisher, 1977), which only considers stellar mass (based on luminosity) and does not extend to gas-dominated low stellar mass galaxies.

The best fit to this relation is a power law:

$$M_b = V_f^\alpha / Ga, \tag{1.23}$$

where M_b is the total baryonic mass, V_f is the asymptotic circular velocity, and a is an acceleration constant of order 10^{-10}m s^{-2}. Taking $\alpha = 4$ and $a = a_0$, one gets the MOND result of $V_f = (GMa_0)^{1/4}$ (Equation (1.11)), which was built for the classical Tully-Fisher relation and still fits the BTFR.

Figure 1.2: The Baryonic Tully-Fisher Relation. This particular version plots the baryonic mass M_b of galaxies as a function of their asymptotic circular velocity V_f, with the color bar representing the gas fraction F_g. Plot taken from Lelli et al. (2019).

In the ΛCDM context, let us assume that each halo hosts the same fraction of baryons, which we could expect to be the same as the global ratio of baryonic matter over total matter, namely $f_b := \Omega_b/\Omega_m \approx 1/6$. Based on Steinmetz & Navarro (1999), the expected fit relation is then $V_f = (10 G M_b f_V^3 H_0)^{1/3}$ where H_0 is the Hubble constant and f_V is a constant introduced to link the observed V_f to the one expected at virial radius by the theory. This relation (with a slope $\alpha = 3$) clearly fails to fit the data, and one can understand this since galaxies actually do not usually have a baryonic mass that is the baryonic fraction times their total mass, *i.e.* $M_b = f_b M$. In fact, the fraction of baryons varies wildly between galaxies, with dwarf galaxies being heavily dark matter dominated while MW-like spirals are not as much. But we also face a missing baryons issue: observations fail to match the expected quantity of baryons given by Ω_b, a good chunk of which could be in galaxies in some yet undetected form, helping to reconcile the discrepancy with the data for ΛCDM, i.e. the difference between the observed baryons and the total amount of baryons expected by the model in a galaxy.

A possibility is offered by abundance matching, which is the process of assigning a certain halo mass to a galaxy depending on its luminosity, based on an empirical relation between those quantities (the stellar-to-halo mass relation, see for example Moster et al. (2013)). Surprisingly, Di Cintio & Lelli (2016) have shown that abundance matching does lead to having galaxies matched to halos that give velocities in agreement with the slope and normalization of the BTFR.

The real problem hence does not lie so much in the slope, but in the scatter. The extremely low scatter of the relation is in agreement with MOND (which predicts none), while in ΛCDM, it would mean that every galaxy would "show" a different amount of baryons depending on its asymptotic velocity V_f, which sounds very unlikely at best. In the context of abundance matching as described previously, Desmond (2017a) have shown that the disagreement in scatter is $\approx 3\sigma$.

It would be extremely interesting to see if the BTFR can be extended to additional mass and velocity ranges, or if outliers are found. In this vein, Di Teodoro et al. (2022) show that extremely massive spirals in the Local Universe with stellar mass $M_\star \geq 10^{11}\,\mathrm{M}_\odot$ do lie on the BTFR. These spectacular galaxies are expected to have enjoyed rather isolated evolution with continous star formation, without being perturbed much by mergers, tidal effects, or feedback. The authors also reinforce the case for a branching in Stellar-to-Halo Mass relations based on type and environment, with isolated spirals such as these having a lower DM halo mass compared to their elliptical counterparts in cluster environments, for a given stellar mass.

At the other end of the relation, Mancera Piña et al. (2019) observe 6 low surface brightness "Ultra-Diffuse Galaxies" (UDGs) and infer their circular velocity profiles. They find that those 6 galaxies lie above the BTFR, with circular velocity too low for their baryonic masses, and a baryonic fraction close to the cosmological value, which they attribute to inefficient feedback. However UDGs are mysterious objects which are not well understood yet, and tiny changes in the morphology of these nearly face-on galaxies can produce large changes in the measured inclination which is the most crucial quantity to derive the correct amplitude of the rotation curve. For example, one of the galaxies among the 6 has later been re-observed and found to be consistent with having no DM whatsoever (see Section 1.4.6). See also our work involving UDGs in Section 4. Further observations of such structures will likely prove to be decisive in settling those matters.
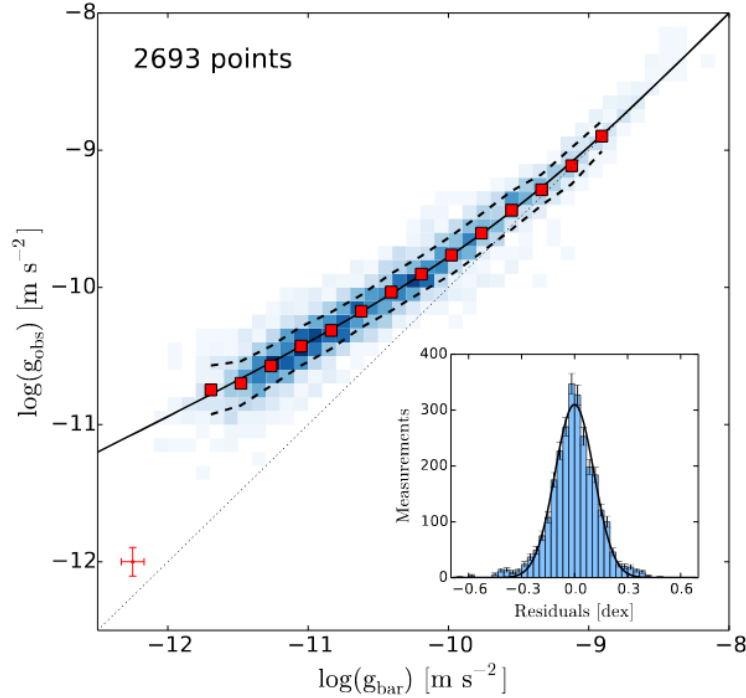
1.4.5 Radial Acceleration Relation

The Radial Acceleration Relation (RAR) (McGaugh et al., 2016; Lelli et al., 2017) is a galactic dynamics relation highlighting the tight correlation between the observed gravitational acceleration g_{obs} (inferred from rotation curves and velocity fields from 21cm observations tracing the atomic gas) and the baryonic-induced gravitational acceleration g_{bar} (computed from Poisson's equation (Equation (1.14)) using the observed stellar density profile in near-infrared). The relation is shown in Figure 1.3.

Much like for the BTFR (Section 1.4.4), the RAR suggests that baryons dictate dynamics inside galaxies. It also highlights that the need for additional mass in Newtonian gravity happens at a characteristic acceleration around the value of $a_0 = 1.2 \times 10^{-10}\mathrm{ms}^{-2}$.

The best fit to the data is a function of the form

$$g_{\mathrm{obs}} = \frac{g_{\mathrm{bar}}}{1 - e^{-\sqrt{g_{\mathrm{bar}}/g_\dagger}}} \tag{1.24}$$

where $g_\dagger = 1.2 \pm 0.26 \times 10^{-10}\mathrm{ms}^{-2}$ is an acceleration scale extremely close to a_0. Note that while this is not stated in McGaugh (2016) in order to remain as model-agnostic as possible, this virtually reproduces isolated MOND phenomenology for a certain choice of interpolation function.

Figure 1.3: The Radial Acceleration Relation shows the observed gravitational acceleration g_{obs} as a function of baryonic-induced gravitational acceleration g_{bar}. The black curve is the best fit to the data, corresponding to Equation (1.24). Plot taken from McGaugh et al. (2016) using data from SPARC (Lelli et al., 2016a).

MOND thus naturally predicts the RAR with the prescription of Equation (1.4), more than thirty years before the relation was even noticed. However the relation is tricky to explain for most dark matter theories. In ΛCDM in particular, there is no reason why the mass discrepancy should be linked to a physical scale, and that there should be a transition region for it at all.

However, see Navarro et al. (2017) in which the authors argue that this is the result of the self-similar nature of NFW halos (Section 1.1.2). Dark matter halos in ΛCDM, if described by the NFW profile, are scale free: the NFW family is virtually a one parameter family (this parameter being the virial mass M_{vir}), meaning that halos surrounding galaxies of different *e.g.* baryonic mass, brightness, shape, size, will have the same internal structure. As a result this would mean that accelerations greater than a_0 can only be reached in regions dominated by baryons, where $g_{\mathrm{obs}} \approx g_{\mathrm{bar}}$ is expected. At the other end, the minimum acceleration for which we have observations coincides with the minimum halo mass needed for hosting a galaxy. The low scatter would follow from scaling relations such as the stellar-to-halo mass relation and abundance matching (e.g. Moster et al. (2013)). However, the real question is not why acceleration larger than a_0 can only appear at $g_{\mathrm{obs}} \approx g_{\mathrm{bar}}$, but rather why galaxies that have inner parts dominated by DM, hence with $g_{\mathrm{obs}} > g_{\mathrm{bar}}$ in those regions, have these inner parts still lying on the RAR. This actually leads to the diversity problem (see, e.g., detailed discussions in Ghari et al. (2019)).

In Freundlich et al. (2022), we show that a sample of UDGs from the Coma cluster do lie

on the RAR (Section 4.2), probing lower acceleration regimes. But the RAR has recently also been extended to even lower accelerations using weak-lensing measurements in Brouwer et al. (2021). The authors find a good agreement with modified gravity theories such as MOND and Emergent Gravity (Verlinde, 2017) and compare with various cosmological simulations for ΛCDM with mixed results, which could help understand which feedback models or stellar-to-halo mass relations are better suited to the data. For MOND, a crucial component to take into account at these very low accelerations is the EFE. The authors do consider it and conclude that the EFE-induced decrease is not steep enough to match the data with hot gas estimations, although it would be very interesting to do the same exercise with recent more accurate analytical formulations for a constant EFE as in Freundlich et al. (2022); Chae & Milgrom (2022).

1.4.6 Galaxies without dark matter

Recently, a team of astronomers have resolved the kinematics of faraway (distance $d \approx 76$ Mpc) disk galaxy AGC114905 (Mancera Piña et al., 2021), concluding that it does not need dark matter. In their work, the observed baryonic matter is sufficient to explain the rotation curve, leading to bad results if additional dynamical mass is considered (either with DM or a modification of gravity).

In the context of ΛCDM, galaxies could in theory form without dark matter in the tidal tails of galaxy-galaxy mergers or interactions (Tidal Dwarf Galaxies), but this explanation seems unlikely in this case since according to Mancera Piña et al. (2021) AGC114905 is fairly isolated. Note that while it might not apply in this particular instance, following this discovery, Moreno et al. (2022) successfully produced galaxies without (or with very little) DM in cosmological simulations. Such galaxies could be the result of very strong interactions in their history.

Another reaction article from Sellwood & Sanders (2022) suggests that a galaxy with a very structured velocity map like AGC114905 couldn't possibly exist in this state without a DM halo. Their argument is based on the fact that DM haloes are known to stabilize stellar disks (Ostriker & Peebles, 1973); their simulations of similar galaxies feature disks that fall apart whenever they are not included in a DM halo.

In the context of MOND, the only mechanism to get from the deep MOND regime to a "DM-less" galaxy obeying Newtonian mechanics is the EFE. However, Mancera Piña et al. (2021) rule out this option, again due to the isolation of the galaxy. Should the result stand, it would thus deal a very serious blow to MOND. Although see the recent rebuttal article by Banik et al. (2022a) invoking the difficulties linked to the inclination of AGC114905 (nearly face-on) and the fitting of isophotes, especially in the context of MOND where non-axisymmetric features are common in disks.

Some other objects are invoked as well when discussing this topic. In the NGC1052 group of galaxies, van Dokkum et al. (2022) propose that the DF2 and DF4 dwarf galaxies could be dark matter free, as tidal dwarves born in the tails made by the collision of two gas rich galaxies (which they coin a "bullet dwarf" event, in a nod to the Bullet cluster event described in Section 1.4.3). In the context of MOND, those galaxies are less problematic than isolated ones thanks to the EFE (see Famaey et al. (2018) for an analysis on DF2).

Note that every galaxy mentioned in this Section is an Ultra-Diffuse Galaxy. It will be

very interesting in the future to obtain more and better data on this type of object which clearly we do not fully understand yet.

1.4.7 Diversity of rotation curves
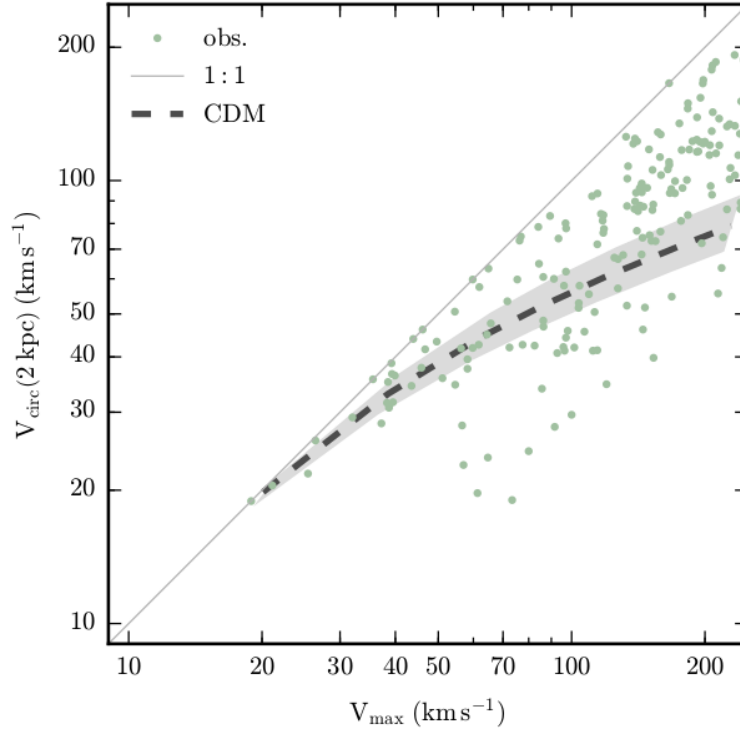
Figure 1.4: Diversity of rotation curves. Circular velocity at 2 kpc as a function of maximum circular velocity. The shaded grey area represents the ΛCDM expectation from simulations, while the green dots come from observational data. Plot taken from Creasey et al. (2017), adapted from Oman et al. (2015).

In the ΛCDM context, the shape of rotation curves in the DM-dominated regions should show little to no variation at fixed V_{max}, since NFW halos (see Section 1.1.2) are self-similar and the mass-concentration relation offers very little wiggle room in size scaling for a given halo mass. Oman et al. (2015) highlight this fact by compiling the data from different ΛCDM simulation suites, but more importantly they have shown that this is in disagreement with observed galaxies, and in particular with dwarf galaxies which are heavily DM-dominated. Figure 1.4 shows the huge scatter on circular velocity at 2 kpc $V_{\mathrm{circ}}(2\,\mathrm{kpc})$ as a function of V_{max} for observed galaxies. This is compared to the ΛCDM expectation from simulations (shaded grey area). For a given V_{max}, $V_{\mathrm{circ}}(2\,\mathrm{kpc})$ is observed to vary wildly, highlighting the difference between slowly and steeply rising circular velocities and thus the diversity of rotation curves.

This issue is often linked to (and can be regarded as the newest version of) the "core vs. cusp" problem, with core and cusp in this context referring to the shape of the inner DM density profile. The usual NFW profile for dark matter density features a cusp near the

center of galaxies, while cores correspond to a much flatter distribution. It is argued that core formation in CDM halos could take place due to feedback mechanisms. However Oman et al. (2015) conclude that core formation is not a satisfactory answer to the complexity and irregularities of observed rotation curves. Indeed, while core formation can be pretty effective, galaxies similar in baryonic properties should produce cores of very different sizes, which is very difficult to achieve.

The core vs. cusp issue is in any case only a relic of this new diversity challenge. Some dwarfs are observed to be cored, while others are cuspy, and some even more cuspy than NFW. This observation is very difficult to solve for ΛCDM. See Sales et al. (2022) for a recent review of this and other tensions in dwarf galaxies.

MOND does not have this issue since dynamics directly depend on the distribution of baryons. For a given asymptotic velocity, high surface brightness galaxies with steep baryonic density profiles will naturally have a quickly rising rotation curve, while low surface brightness galaxies will have a slowly rising rotation curve, leading to different values of $V_{\mathrm{circ}}(2\,\mathrm{kpc})$.

1.4.8 Gravitational lensing

Gravitational lensing is caused by light rays from far away sources getting deviated by the gravitational influence or a massive source closer to the observer in the line of sight. In the context of GR, light follows the geodesics of the curved spacetime around the lens; it is a clear prediction that has been observed countless times (the Bullet cluster being a famous example, but see also the deep field view of galaxy cluster SMACS0723-73, especially the latest one from JWST). Furthermore, the mass discrepancy is apparent in a lensing event, since the distortion caused by the baryonic mass of the lens alone is not enough to reproduce observations.

Strong lensing happens when the lens is massive enough and the object of interest stands behind the lens at almost the same projected position in the sky. This kind of lensing leads to the production of (often several) images of the lensed object. Some examples of observed signatures are Einstein rings (the lensed object appearing circular around the lens), or an Einstein crosses (the lensed object appearing four times in a cross pattern around the lens).

Weak lensing happens when the lens is not as massive, or the alignment with the lensed object is not as good, often resulting in no clear image being produced by the distortion. It is very informative however in the context of analysing deep fields with hundreds of galaxies. For instance, Brouwer et al. (2021) used weak lensing to extend the RAR (Section 1.4.5) to low stellar mass galaxies with data from the Kilo-Degree Survey. Upcoming surveys from the Euclid mission will allow even more accurate work in this direction.

Any cosmological model must thus reproduce lensing. ΛCDM relies on GR and as such is in very good agreement with the observed lensing, once DM is added to the systems acting as lenses to address the mass discrepancy. This is however another thing that MOND cannot hope to address without a relativistic extension with for example a change in metric and the addition of a vector field as in TeVeS or Skordis & Złośnik (2019).

1.4.9 Too big to fail

ΛCDM simulations of Milky Way-like galaxies produce massive subhalos that have no observed counterpart (Boylan-Kolchin et al., 2011). One would naturally expect that the most massive subhalos in the Milky Way host its most massive satellite galaxies. However, it has been shown that while the number of subhalos in simulations is in agreement with the number of observed dwarf galaxies, the most massive subhalos in simulations are too centrally dense compared to the halos hosting the most massive Milky Way satellites. From an observational point of view, it is very dubious at this point that we would have failed to detect those massive satellites. The question is then: if those massive subhalos exist, why have they failed to form stars, when less massive subhalos have succeeded? They are expected to be too big to fail to host galaxies.

A simple, immediate way to alleviate the issue would be that the DM halo of the MW is actually less massive than believed (and especially less than it is in cosmological simulations), leading to the presence of less massive DM subhalos. However the dynamical mass of the MW, while not accurately measured, is lower-bounded by *e.g.* the presence of the massive Large Magellanic Cloud, or proper motions of distant satellites such as Leo I (Boylan-Kolchin et al., 2013); a mass low enough to significantly ease the Too big to fail issue would be in tension with those observations.

Another possible way to reconcile simulations with observations is considering stellar feedback. Many feedback mechanisms (*e.g.* stellar winds, active galactic nuclei, supernovae) often absent from simulations can significantly alter the central baryonic distribution of galaxies, and act on the gravitational potential in such a way that the DM profile becomes cored, lowering the central density. Thus, including stellar feedback to simulations and/or taking into account that we might observe cored galaxies that were previously cuspy alleviates the issue. However feedback is a tricky mechanism to accurately quantify and include in simulations. In addition, dwarf galaxies with low stellar mass ($M_* \leq 10^7$ M$_\odot$) are also observed with central density cores; in this mass regime where gas is largely dominant over stars, it is difficult to attribute this low central density to stellar feedback.

Note that while the MW could be a statistical anomaly, subsequent studies highlighted the same issue for the M31 system (Tollerud et al., 2014), making the problem even bigger. In this context, M31 surveys such as the Pan-Andromeda Archaeological Survey (PAndAS, Martin et al. (2013)) are crucial to constrain the global properties of Andromedas system of satellite dwarf galaxies, as studied in *e.g.* Doliva-Dolinsky et al. (2022).
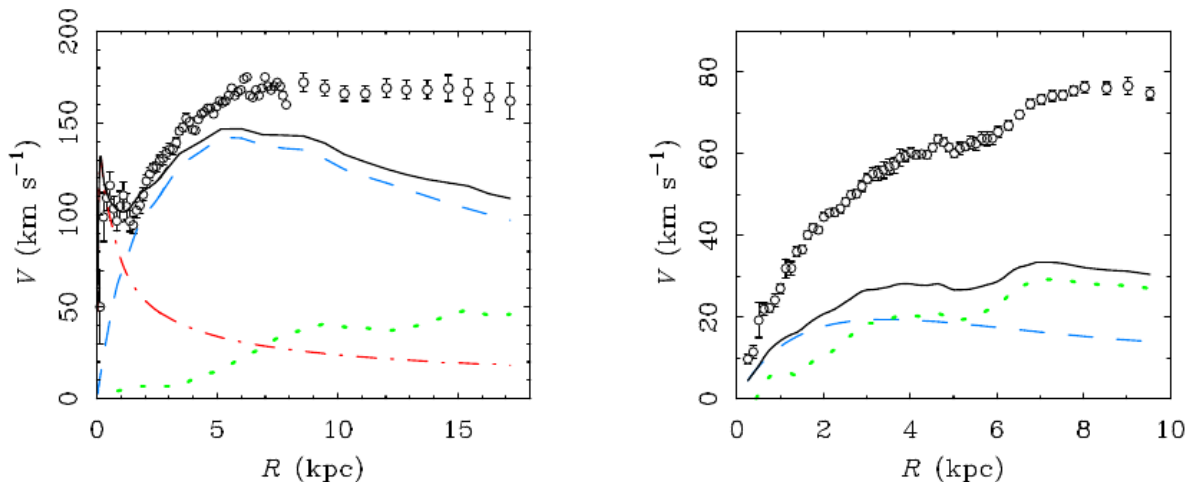
1.4.10 Renzo's rule

Stated in the abstract of his work on the apparent coupling between observable matter and dark matter (Sancisi, 2004), Renzo Sancisi's rule is as follows:

> "*For any feature in the luminosity profile there is a corresponding feature in the rotation curve and vice versa.*"

Sancisi (2004)'s work starts with an interrogation brought by the maximum disk hypothesis (van Albada & Sancisi, 1986). For an adequate mass to light ratio, the inner parts of the rotation curve of a High Surface Brightness (HSB) spiral galaxy can be well reproduced

by considering only its stellar disk, naturally providing an explanation for Renzo's rule (at least, again, for the inner parts). This phenomenon is understandable in the context of HSB galaxies since baryons dominate over dark matter there up to rather large radii. But what would happen if one were to do the same exercise for Low Surface Brightness (LSB) galaxies? Very surprisingly, the maximum disk hypothesis gives good rotation curve fits for the inner parts of LSB galaxies too (albeit with unrealistic mass to light ratios, since LSB galaxies are very much *not* maximum disks)! There should be no reason for baryonic matter to dictate the dynamics in regions when they are expected to be a very minor component.

Figure 1.5: Renzo's rule. Rotation curves for HSB spiral NGC 6946 (left) and LSB galaxy NGC 1560 (right). The data are circles with error bars, the black curve is the rotation curve from all baryonic components, the blue curve is from the disk, the red curve is from the bulge, and the green curve is from the gas. In both cases, the ressemblance in shape between the baryonic-inferred rotation curve and the observed one is clear. Plot taken from Famaey & McGaugh (2012).

More importantly, they find a strong correlation between the shapes of the luminous profile, or visible matter-inferred rotation curves, and of the observed rotation curves. Figure 1.5 gives an example of this for both a HSB and a LSB galaxy. This is an obvious illustration of Renzo's rule: in the LSB galaxy in particular, the features of the gas-inferred component of the rotation curve can be directly seen in the data (*e.g.* the kink around 5 kpc and the rise around 6 kpc). In a galaxy in which dark matter dominates so clearly (as seen here by the gap in values from the baryonic-inferred curve and the data), how to explain that the baryons dictate the dynamics?

This rule is hard to reconcile with dark matter as we understand it in galaxies, since no strong coupling between the DM and baryonic matter is expected. A possibility for ΛCDM to reconcile itself with this observation would be that non-axisymmetric motions, once averaged, could mimic Renzo's rule even in DM dominated disks, but this has never been shown. Obviously this is not a problem at all for MOND; on the contrary, since baryons are expected to dictate dynamics, this is a prediction.

1.4.11 Planes of satellites

It has been observed that the phase space distribution of satellite galaxies around their host is not isotropic. Indeed, many satellite galaxies around the Milky Way lie on a thin planar structure (Vast Polar Structure, VPOS), as has first been put forward by Lynden-Bell (1976), and in addition most of them are co-orbiting. This observation is in conflict with the expected chaotic distribution of subhalos in ΛCDM structure formation induced by frequent mergers. Kroupa et al. (2005), comparing the observed plane to cosmological simulation results, reject the possibility in the context of ΛCDM with more than 99.5% confidence. Even more problematic, such planar distributions of satellite galaxies have also been subsequently observed for M31 (Ibata et al., 2013) and Centaurus A (Müller et al., 2018), making it seem a lot less likely that those phase space correlations are simply statistical outliers.
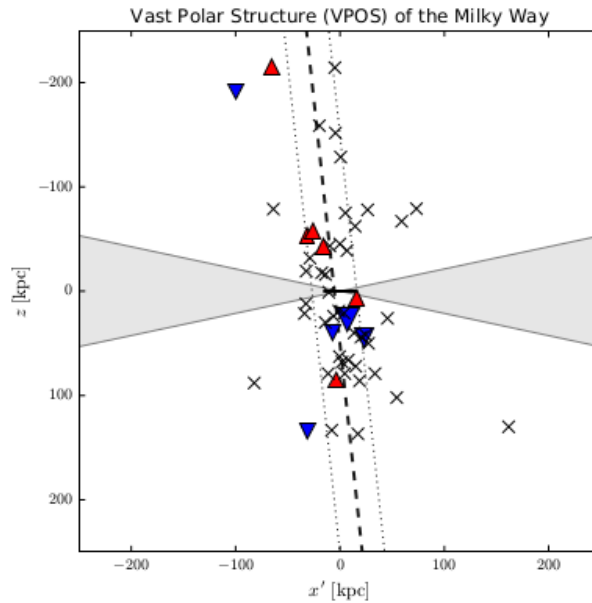
Figure 1.6: Edge-on view of the plane of satellites of the Milky Way (VPOS). Individual galaxies are plotted as blue triangles if they are approaching, red triangles if they are receding, and crosses if no data is available. Plot taken from Pawlowski (2018).

Some proposed solutions in the context of ΛCDM have been accretion through cosmic filaments, or accretion of dwarf galaxy groups, but they have been found to be unsatisfactory and should in any case already be included in cosmological simulations, which do not yield the observed phase space distribution.

Perhaps a more interesting possiblity would be that of Tidal Dwarf Galaxies (TDGs), formed during an interaction or a merger between two galaxies. Their formation in tidal tails would provide ideal conditions for the strong correlation in phase space that we observe. However, this requires that the host galaxy has been the subject of a major merger or interaction during its evolution; this requirement seems to hold for the MW and M31, but would put this idea into trouble if planes of satellites were detected around isolated galaxies. Moreover, TDGs are expected to be devoid of dark matter due to their peculiar formation environment, while dwarf galaxies are observed to be heavily dark matter dominated. Dwarf

galaxies can also not all be TDGs, since many satellites are expected to be born *in situ* in dark matter subhalos.

The possibility of TDGs is more appealing in the context of MOND where high dynamical mass in dwarf galaxies is achieved without dark matter, where a previous interaction between the MW and M31 is expected, and where furthermore, formation of TDGs happens more frequently than in ΛCDM (Bílek et al., 2021). See Banik et al. (2022b) for a recent hydrodynamical simulation of the Local Group in MOND leading to good agreements with observed orbital poles for the respective tidal debris of the MW and M31, although lacking in resolution to properly form TDGs. One should also take into consideration that dwarf galaxies might not be systems in equilibrium, which would make any conclusion on their dynamics difficult.

See Pawlowski (2018) for an exhaustive review of this issue, Pawlowski (2021) for a brief summary, and Section 9 for a work related to this topic, in which we investigate the possible role of the recent infall of the LMC.

1.4.12 Galactic bars

Galactic bars are a local bar-shaped overdensity of stars observed in the inner parts of many disk galaxies. In the ΛCDM context, dynamical friction with dark matter particles is expected to slow the rotation of those bars. When comparing the rotation speed of observed bars to those obtained in hydrodynamical simulations, Roshan et al. (2021) notice a large discrepancy. These authors also highlight a discrepancy with the fraction of bars, with the trends from simulations and observations being very different (while the trends from simulations are rather consistent between them), especially for galaxies with stellar mass $M_\star \leq 10^{10.5}$. Reddish et al. (2022) show that this "missing bars" issue is present in all cosmological simulations.

In the context of MOND, no dark matter is present to slow the bars through dynamical friction, and their speed stays approximately constant, resulting in much better agreement with observed ones (Tiret & Combes, 2007; Combes, 2016).

1.4.13 Bulgeless big galaxies

In the context of ΛCDM and its hierarchical clustering model, classical bulges[3], either merger-built or born from the early life of galaxies when gas clumps are drawn towards the center via dynamical friction with dark matter, are expected in most big galaxies, and as a consequence pure-disk galaxies should be infrequent. This is indeed the behaviour obtained from various cosmological simulations, as shown for example in Haslbauer et al. (2022). However, most of the observed galaxies in the Local Volume are bulgeless (*e.g.* Kormendy et al. (2010) with $\sim 2/3$ of their Local Volume "giant" galaxy sample without a classical bulge).

The picture is slightly better in the MOND framework since both galaxy mergers and clump-induced bulges are expected to be less frequent without the dynamical friction from dark matter halos (Combes, 2014, 2016).

---

[3]We are talking here about classical bulges, and not pseudo-bulges that are the results of the secular evolution of galactic disks.

Hotter dark matter particles such as in the WDM model could also do better with this issue, since less small scale structures and thus less mergers would be expected, leading to the formation of less bulges. However WDM is not without issues itself (see *e.g.* conflicts with observations from the Lyman-α forest (Iršič et al., 2017)).

1.5 Galactic archeology

In order to understand the issues faced by our models, it is primordial to have access to quality data and to understand them thoroughly. This is where galactic archeology comes in. Galactic archeology is the exciting study of observational data of a galaxy in order to understand its history, evolution, gravitational potential and more. This observational data can for example be astrometry (the measurement of positions and velocities of stars), or can be focused on the luminosity and chemical composition of stars via photometry or spectroscopy, or gas abundance. With the exquisite data brought by *Gaia* for our Milky Way, galactic archeology has gained a lot of traction, and possibilities have greatly increased. In this thesis, we mostly focus on the dynamical side of galactic archeology, but this vast domain is much more than this, encompassing studies of galaxy formation and stellar populations.

1.5.1 Tidal disruption

Satellites of a massive galaxy, such as globular clusters and smaller galaxies, undergo tidal disruption during their orbits in the potential well of their host. This disruption is caused by the difference of gravitational potential applied by the host to the satellite: the region of the satellite closest to the host will suffer a stronger gravitational pull than the region furthest. This process strips stars from the progenitor, and those stars will escape at two of the Lagrange points of the system, namely L1 (among the two, closest to the host) and L2 (furthest from the host).

In an orbital 2-body system, Lagrange points are the locations in space where the gravitational fields from both bodies balance the centripetal force, and thus where a particle can stay fixed with regard to the 2 bodies along their orbital evolution. There are 5 Lagrange points in such a system, which correspond to critical points of the effective potential Φ_{eff} (which encapsulates the gravitational potential and angular momentum information). In the Sun-Earth system for example (Figure 1.7, left panel), Lagrange point L2 is where many observational satellites are sent.

One can compute the distance at which those L1 and L2 points are located with respect to the disrupted satellite: the Jacobi (or Roche, or Hill) radius is the distance from the center of a disrupting satellite at which stars are not bound to it anymore. Using the fact that the effective potential has saddle points at L1 and L2 leads to an equation that can be solved numerically, but which to a reasonable approximation gives Binney & Tremaine (2008):

$$r_J = r \left(\frac{M_{\text{sat}}}{3 M_{\text{host}}(r)} \right)^{\frac{1}{3}} \tag{1.25}$$

where r is the distance between the satellite and the host, and M_{sat} and M_{host} are their respective masses. A few caveats are to note regarding this quantity. The main ones being
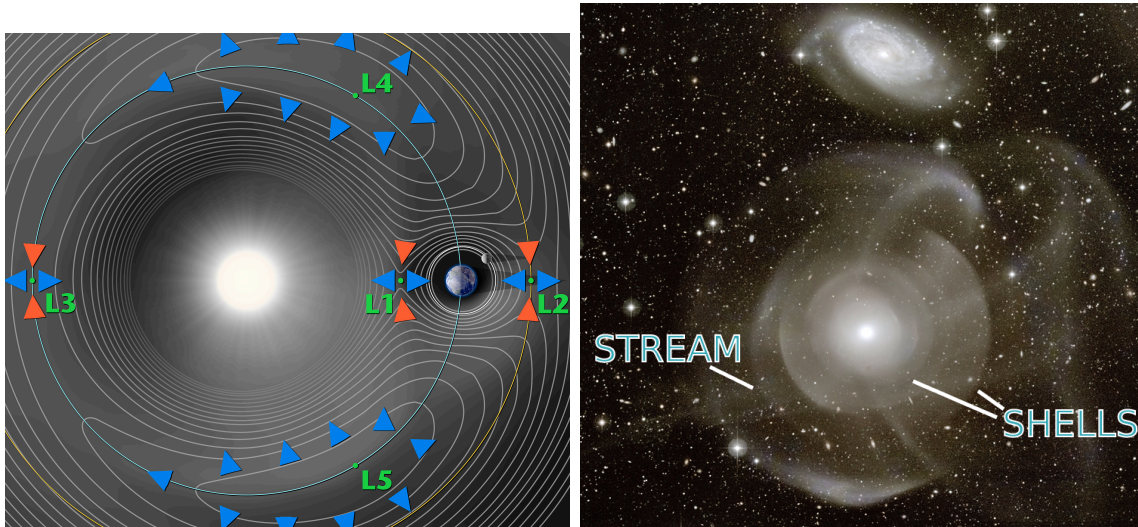
Figure 1.7: *Left panel:* illustration of Lagrange points in the case of the Sun-Earth system. Lines are isocontours of the effective potential Φ_{eff}. Image from NASA. *Right panel:* lenticular galaxy NGC 474 and its tidal shells and streams. Original image from the MATLAS survey (Duc et al., 2015).

(i) that the zero-velocity surface around the satellite is not perfectly spherical, so a radius is unfit to describe it accurately, and (ii) that this computation should in principle only hold for satellites on a circular orbit. For a comprehensive list of issues, see Binney & Tremaine (2008, Section 8.3.1).

Of course this r_J radius is actually a function of time, as the masses enclosed will change during the disruption process (timescale of a few Gyr), but also on the position of the progenitor on its orbit (for eccentric orbits, there can be a huge difference in the enclosed mass $M_{\text{host}}(r)$ between pericenter and apocenter). Overall though, stars will be stripped closer and closer to the progenitor as time goes, as its mass decreases from previous stripping.

As a result a stellar stream has two distinct components: the leading arm, preceding the progenitor, formed by stars stripped at the L1 point, and the trailing arm, lagging behind it, formed by stars stripped at the L2 point. They show a glimpse of what the orbit of the progenitor was and will be, since over time stars will be stripped and launched into different orbits with different energies, leading to the spectacular structures that we can observe now.

Note that stellar streams are not the only outcome of tidal disruption: the result varies based on the ratio between the masses of host and progenitor, and orbital parameters. Streams are the outcome of minor mergers, i.e. with ratio $M_{\text{sat}}/M_{\text{host}} \leq 1/10$, with a progenitor on a circular to mildly eccentric orbit.

For intermediate mergers (reaching up to $M_{\text{sat}}/M_{\text{host}} \leq 1/5$) with a satellite on a very eccentric, almost radial orbit, the most likely outcome are tidal shells, concentric arc-like features that are the result of the dynamical heating produced at successive pericentric passages (Ebrova, 2013; Bílek et al., 2022). See Figure 1.7 (right panel) for a spectacular example in NGC 474.

Finally, tidal tails are elongated stellar structures which differ from the previous two options by the fact that its constituent stars belong to the host galaxy. Tails are most likely

the result of a major merger ($M_{\mathrm{sat}}/M_{\mathrm{host}} \geq 1/5$) or a close fly-by with another galaxy of comparable mass.

For recent work on classifying and making an inventory of tidal features, with the future aim of constraining the number of mergers and their types, and thus galaxy formation and evolution models, see e.g. Duc et al. (2015); Sola et al. (2022).

1.5.2 The stellar halo

The stellar halo component of our Galaxy, extending up to distances greater than 100 kpc and surrounding the disk, is host to many stars that were previously members of accreted structures, dwarf galaxies and their globular clusters that fell into the potential well of the Milky Way and got disrupted by tides. Some of these structures still have a discernable progenitor while others are completely destroyed. The accreted stars now take the form of tidal shells or streams, or sometimes are phase-mixed, *i.e.* have lost their kinematic signature and are perfectly assimilated dynamically in the MW.

But the stellar halo is also host to many *in situ* stars that were born there. It has been known for a while that metallicity and orbital parameters are a good way to separate *in situ* and accreted stars. Carollo et al. (2007) have indeed shown that the outer halo is mostly made of metal-poor retrograde accreted stars, while the inner halo has a mostly mild prograde rotation and is more metal-rich. More recently, Di Matteo et al. (2019) estimated that approximately 40% of the metal-poor stars (mean metallicity [Fe/H] ≤ -1) of the halo come from the heated Galactic disk, while the rest of those metal-poor stars are accreted.

Digging into the stellar halo is thus effectively uncovering the past of the MW. Each kinematically and chemically coherent substructure identified constitutes a piece of the merger history puzzle of our Galaxy. Furthermore, debris with coherent peculiar motion such as stellar streams also provide invaluable information on the ambient acceleration field and thus on the dynamical mass.

An effective way to detect substructures in the stellar halo is to look at quantities that are conserved along orbits in a given potential, i.e. integrals of motion, such as energy and angular momentum. If the actual gravitational potential changes only slightly and slowly over time, we expect those quantities to be well conserved; this should be a reasonable assumption to make over timescales of a few Gyr in the MW for example, since from our understanding (see paragraphs below), the last major accretion event - the infall of the Sagittarius dwarf (Ibata et al., 1994), now almost entirely destroyed - started $5 \sim 6$ Gyr ago, and the only large perturber in recent times is the Large Magellanic Cloud, currently on its first infall.

Searching for clumps in E (total energy) vs. L_z (z-axis component of the total angular momentum L) space has thus become the standard method for detecting substructures, and has been showcased as such in Helmi & de Zeeuw (2000), who predicted that this technique would work with *Gaia* data 16 years before its first data release.

However, Jean-Baptiste et al. (2017) warn against using kinematics and especially clumping in integrals of motion spaces, since in their live-only (thus including accurate dynamical friction and tidal heating) N-body simulations of the Milky Way and mergers, they find that it is hard to determine which overdensities are caused by which satellite, with many overlaps, even with *in situ* stars.

Adding the information of age and metallicity completes the puzzle and makes structures

stand out quite well: groups are identified by both their kinematics and stellar populations. Spectroscopic surveys are used to provide this information as well as radial velocities. This has been done in *e.g.* Conroy et al. (2019) with the H3 survey.

The past few years (mostly since *Gaia* DR2 in 2018) have been ripe in works applying this technique to discover many accretion events and substructures in the halo. The biggest accretion event, dubbed the Gaia-Enceladus-Sausage (Belokurov et al., 2018; Helmi et al., 2018), has been unveiled as a radial major merger which happened $\sim 10\,\mathrm{Gyr}$ ago and still constitutes an important chunk of the inner halo to this day. Then retrograde populations in the halo were linked to another major merger event dubbed Sequoia (Myeong et al., 2018, 2019). Following studies (e.g. Yuan et al. (2020); Naidu et al. (2020); Ruiz-Lara et al. (2022)) provided even more information, discovering other large groups (Arjuna, I'itoi, LMS-1/Wukong) and many smaller substructures.

Finally, in a fantastic effort of centralization, Malhan et al. (2022b) recently provided a global atlas of mergers and structures in the Milky Way, detecting new ones and linking groups together; the result, representing our current sum of knowledge on the MW's history, can be seen in Figure 1.8.
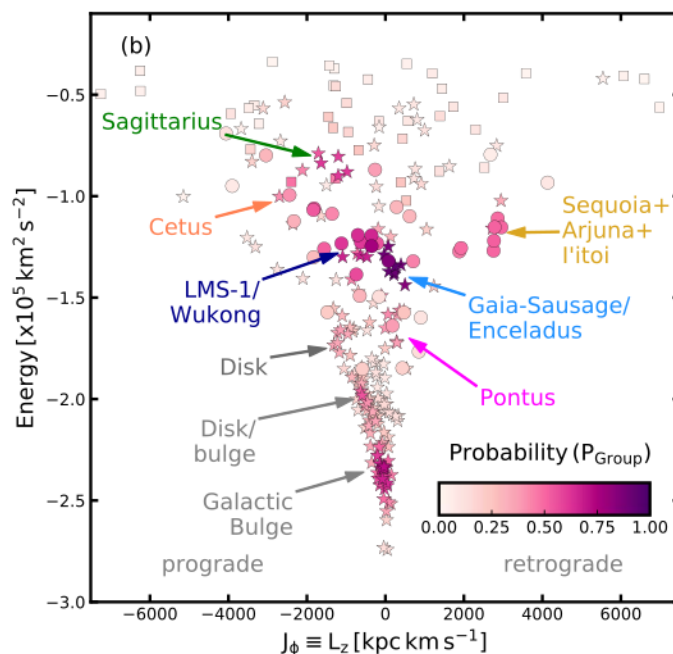
Figure 1.8: The global atlas of structures known so far in the stellar halo of the Milky Way, colored by probability of belonging to the same group. Plot taken from Malhan et al. (2022b).

1.5.3 Stellar streams: tracers of the gravitational potential

As we have seen, stellar streams are produced by the tidal disruption of a globular cluster or dwarf galaxy. In fact, it is in general possible to deduce which of the two is the progenitor. Globular clusters are very compact objects supposedly born from a single molecular cloud, leading to a single stellar population. As such, we expect them to produce thin streams

made of stars with very close metallicity values. On the other hand, streams made from dwarf galaxies can be as thick as a few kpc and have a significant spread in metallicity, coming from the different stellar populations of the progenitor (either through accretions or distinct star formation events). Although in some extreme cases, the identification remains difficult, such as with the uniquely metal poor (mean $[Fe/H] = -3.38 \pm 0.06$) C-19 stream (Martin et al., 2022; Errani et al., 2022; Yuan et al., 2022).

Looking at stellar streams is akin to looking at the history of the progenitor and thus gives us a way to probe the gravitational environment and merger history of its host. In the context of the Milky Way for example, any gravitational potential should reproduce the orbits of the observed stellar streams, which is a very tight constraint. Additional difficulty lies in the fact that realistically, no static potential could reproduce the history of the Milky Way. It has notably recently been shown in Vasiliev et al. (2021a) that the infall of the Large Magellanic Cloud (LMC) and its influence on the potential are of crucial importance when trying to reproduce the stream induced by the Sagittarius (Sgr) dwarf galaxy (see Section 5). In the same vein, Woudenberg et al. (2022) show the importance of taking into account the Sgr when trying to model the Jhelum stellar stream.

In addition to this, stellar streams can tell us a lot about the cosmological context we live in, namely when talking about how gravity acts or the nature of dark matter particles. Indeed, some objects such as the GD-1 stream feature a gap, a spur, and overdensities, which could possibly have been caused by the crossing of a cold dark matter subhalo, as proposed by Bonaca et al. (2019). First of all, depending on the dark matter particle (mass, cross-section), those gaps and features would be of very different nature. Secondly, one could estimate the number of dark matter subhalos expected to be hosted by the Milky Way for various dark matter theories, and then statistically estimate the likelihood that a stream crosses one or several during its orbit, and compare it to the number of streams in which gaps are observed. Indeed, depending on the mass of the dark matter particle, the number of expected subhalos vary, with lighter particles (as in warm and hot dark matter theories) having a higher velocity dispersion and forming less small clumps than heavier particles (as in ΛCDM) do. In addition, Malhan et al. (2021, 2022a) show that one can recover information on the DM density profile of a dwarf satellite galaxy by looking at accreted GC streams, *i.e.* streams produced by the tidal disruption of a GC inside a galaxy that later on fell in the gravitational well of a bigger galaxy. They find that such accreted streams are wider, fluffier and hotter when they were originally disrupted inside a cuspy DM halo, compared to those that formed within a cored DM halo.

However one should not forget baryonic causes when discussing such topics. Gaps could very well be caused by globular clusters instead of dark matter subhalos. This is exactly what Doke & Hattori (2022) investigate, and they come to the conclusion that all gaps in the GD-1 stream being caused by GCs is very unlikely. Globular clusters, of course, have the advantage of being readily observable, and their orbits computable, making such studies more accurate than DM based ones. Furthermore, Qian et al. (2022) show that gaps and spurs could be the result of accreted streams. In general, it is very difficult to assert whether those features are of baryonic or dark matter origin.

In the context of MOND, tidal disruption of dwarf galaxies and globular clusters have been studied in Thomas et al. (2017, 2018) with the examples of the Sgr dwarf and Palomar 5 in particular. Tidal disruption is expected to be slightly more efficient in MOND because

of the EFE making the satellites even more vulnerable at pericentric passages. Moreover, the absence of dynamical friction with dark matter will also induce differences with the ΛCDM case. The MONDian N-body simulations of the tidal disruption of Sgr in Thomas et al. (2017) show a good agreement with the observed stellar stream, a remarkable feat for a MOND model with very little wiggle room, since the distribution of baryons alone dictates the gravitational potential, while the stream extends to distances up to $\sim 80\,\mathrm{kpc}$, *i.e.* regions of the halo that are well into the missing mass regime. The main issue with those simulations was the discrepancy in radial velocities for some leading arm stars, which was until then a problem for every model, and was only recently solved by the addition of the infall of the LMC by Vasiliev et al. (2021a). Incorporating the influence of the LMC to a MONDian model for the Sgr stream is a task that remains to be done. There was also the issue of reproducing the bifurcation, which understandably does not emerge naturally from a spherical progenitor in MOND just as it does not in Newtonian gravity, and which we address in detail in Chapters 5 and 6.

Stellar streams are thus among the most interesting and useful laboratories for practicing galactic archeology from a dynamical point of view. In the era of Gaia, stream detecting algorithms such as the STREAMFINDER (Malhan & Ibata, 2018) are detecting many new structures in the Milky Way, and more are being developed at the time of writing of this thesis. They provide a wealth of model-agnostic information, charting the acceleration field and thus dynamical mass in the MW.

1.6   This thesis

1.6.1   EN version

Through this introductory chapter, we have confronted different models of gravitation and dark matter to observations and empirical laws, exposed modern problems of astrophysics (at the scale of galaxies in particular), and explored - in our modern era with its high quality observational data - different ways to solve them. During this thesis, I have taken a closer look at several of these problems in the laboratory constituted by the Local Universe and the Milky Way in particular, in order to bring answers and constraints on different models.

I first looked at the external field effect in the Local Universe for the QUMOND theory. I wanted to quantify the EFE applied to galaxies in this volume, including the one caused by large distant structures such as galaxy clusters, and to understand its precise effects. It was also an opportunity to provide a global picture of the Local Universe in QUMOND, which can be compared with the ΛCDM view through the theoretical quantity of Phantom Dark Matter. This work is detailed in Chapters 2 and 3.

Then, in Chapter 4, we studied in a work led by Jonathan Freundlich the validity of the strong equivalence principle by examining, in the Coma galaxy cluster, the EFE applied to a sample of galaxies with very low surface brightness. Indeed, the strong gravitational field of a cluster like Coma makes it an ideal laboratory for a test of the EFE: the structures with weak internal gravitational acceleration should be strongly affected by it and their internal dynamics should then become quasi-Newtonian according to QUMOND. This work was also the occasion to check whether these galaxies agree with the Radial Acceleration Relation, and to introduce a new analytical formula for the computation of the MOND gravitational

acceleration under a constant EFE.

In Chapters 5 and 6 I present the spectacular Sagittarius stellar stream before focusing on its "bifurcation": each arm of the stream is itself composed of two distinct arms, one brighter and thicker than the other. I revisit a model based on a rotating disk to create the faint branch of the bifurcation.

Then I used the opportunity brought by DR3 of the *Gaia* satellite to explore the solar neighborhood, and detected new tidal debris, one in the disk with retrograde motion and an unusually low amount of vertical displacement, and the other following a polar orbit extending to more than 100 kpc. In Chapters 7 and 8, I detail the characteristics of these structures and discuss their possible origin.

Chapter 9 presents the results of a study carried out with and led by Marcel Pawlowski concerning the impact of the fall of the Large Magellanic Cloud on the plane of satellites of the Milky Way: this massive satellite being itself part of the structure, might its recent arrival be the cause of its formation?

Finally, Chapter 10 presents my general conclusions and Chapter 11 details some possible ways to continue the work of this thesis.

1.6.2 FR version

Au travers de ce chapitre d'introduction, nous avons pu confronter différents modèles de gravitation et de matière noire aux observations et lois empiriques, exposer les problèmes modernes de l'astrophysique (à l'échelle des galaxies en particulier), et explorer - à l'ère actuelle avec ses données observationnelles de qualité - différentes pistes pour les résoudre. Durant cette thèse, je me suis intéressé à plusieurs de ces problèmes dans le laboratoire constitué par l'Univers Local et la Voie Lactée en particulier, afin d'apporter des réponses et des contraintes sur différents modèles.

Je me suis d'abord penché sur l'effet de champ externe dans l'Univers Local pour la théorie QUMOND. Nous souhaitions quantifier l'EFE appliqué aux galaxies dans ce volume, y compris celui causé par les grandes structures lointaines comme les amas de galaxies, et comprendre ses effets précis. Ce fut aussi l'occasion d'offrir un portrait global de l'Univers Local en QUMOND, à comparer avec la vision ΛCDM grâce à la quantité théorique de la matière noire fantôme (PDM). Ces travaux sont détaillés dans les Chapitres 2 et 3.

Ensuite, dans le Chapitre 4, nous avons étudié dans un travail mené par Jonathan Freundlich la validité du principe d'équivalence fort en examinant, dans l'amas de galaxies Coma, l'EFE appliqué à un échantillon de galaxies à très faible brillance de surface. En effet, le champ gravitationnel fort d'un amas comme Coma en fait un laboratoire idéal pour un test de l'EFE : les structures à faible accélération gravitationnelle interne devraient le subir fortement et leur dynamique interne devrait alors devenir quasi-Newtonienne selon QUMOND. Ce travail fut aussi l'occasion de vérifier que ces galaxies vérifient bien la Relation de Accélération Radiale, et d'introduire une nouvelle formule analytique pour le calcul de l'accélération gravitationnelle MOND sous un EFE constant.

Dans les Chapitres 5 et 6 je présente le spectaculaire courant stellaire du Sagittaire avant de m'intéresser plus particulièrement à sa "bifurcation" : chacun des bras du courant est lui-même composé de deux bras distincts, l'un plus brillant et plus épais que l'autre. Je revisite un modèle basé sur un disque en rotation afin de créer la branche peu lumineuse de

la bifurcation.

Puis j'ai profité de la DR3 du satellite *Gaia* afin d'explorer le voisinage solaire. Cela a mené à la détection de nouveaux débris de marée, l'un dans le disque en mouvement rétrograde avec une quantité de déplacement vertical exceptionnellement basse, et l'autre suivant une orbite polaire s'étendant à plus de 100 kpc. Dans les Chapitres 7 et 8, je détaille les caractéristiques de ces structures et discute de leur possible origine.

Le Chapitre 9 présente les résultats d'une étude menée avec et sous la direction de Marcel Pawlowski concernant l'impact de la chute du Grand Nuage de Magellan sur le plan de satellites de la Voie Lactée : ce satellite massif faisant lui-même parti de la structure, son arrivée récente pourrait-elle en être la cause?

Enfin, le Chapitre 10 présente mes conclusions générales et le Chapitre 11 détaille quelques pistes possibles afin de continuer les travaux de cette thèse.

Chapter 2 Computing the phantom density and gravitational potential in QUMOND

In QUMOND, as seen in Section 1.2.1, the modification of gravity can be represented as dynamical mass via a fictitious quantity dubbed Phantom Dark Matter (PDM) which allows easy comparisons to dark matter models and provides a way to quantify the EFE. In this context, galaxies can be seen as surrounded by PDM halos dictating the dynamics in their outskirts and keeping rotation curves flat, and also possess a "dark disk" component, relevant for dynamics close to the disk plane (Milgrom, 2001).

In this Chapter, we detail our computation of both the PDM density and the gravitational potential in the context of QUMOND, using numerical tools. Those codes will be used in Chapter 3 to study the Local Universe.

2.1 Computing the PDM density

Computing the PDM density can be done from Equation (1.19) which we rewrite here for convenience:

$$\rho_{\mathrm{PDM}} = \frac{1}{4\pi G} \, \nabla \cdot \left[(\nu \left(\frac{|\nabla \Phi_N|}{a_0} \right) - 1) \nabla \Phi_N \right]. \tag{1.19}$$

2.1.1 Analytical case

With an analytical expression for the baryonic Newtonian potential Φ_N, one can theoretically differentiate by hand and find an analytical formula for the PDM density. Practically, this is doable if the potential is simple enough, and models two or three bodies at most. Let us do this here for the case of a MW-type galaxy of mass $7.5 \times 10^{10} \, \mathrm{M_\odot}$ modeled by a Miyamoto-Nagai (Miyamoto & Nagai, 1975) bulge and disk and let us add as well a point mass which could represent a distant galaxy cluster such as Virgo, at a distance of $D = 17 \, \mathrm{Mpc}$ on the x-axis with a mass of $M = 2 \times 10^{14} \, \mathrm{M_\odot}$. This particular case is interesting theoretically because it allows us to see the influence, in terms of EFE, of a distant massive galaxy cluster on an otherwise isolated galaxy.

The Newtonian potential at a point (x, y, z) in Galactic Cartesian coordinates is thus the

following:

$$\Phi_N(x, y, z) = -G \left(\Phi_d(x, y, z) + \Phi_b(x, y, z) + \frac{M}{\sqrt{(x + D)^2 + y^2 + z^2}} \right) \tag{2.1}$$

where G is the gravitational constant and Φ_d and Φ_b represent the Miyamoto-Nagai disk and bulge components of the potential respectively. In the end, we obtain the following formula for the PDM density:

$$\rho_{\text{PDM}} = \frac{1}{4\pi G} \left[\frac{1}{2} \left(\frac{\partial^2 \Phi_N}{\partial x^2} + \frac{\partial^2 \Phi_N}{\partial y^2} + \frac{\partial^2 \Phi_N}{\partial z^2} \right) (-1 + \alpha) \right.$$
$$\left. - \frac{a_0}{\alpha |\nabla \Phi_N|^2} \left(\frac{\partial \Phi_N}{\partial x} \frac{\partial |\nabla \Phi_N|}{\partial x} + \frac{\partial \Phi_N}{\partial y} \frac{\partial |\nabla \Phi_N|}{\partial y} + \frac{\partial \Phi_N}{\partial z} \frac{\partial |\nabla \Phi_N|}{\partial z} \right) \right] \tag{2.2}$$

where $\alpha = \sqrt{1 + 4a_0/|\nabla \Phi_N|}$.

Computing the values of the partial derivatives and plugging the formula in a code for a cube of size $1000 \times 1000 \times 1000 \, \text{kpc}^3$ centred on the MW yields us Figure 2.1. In these plane cuts of the PDM density around the MW-like galaxy, the most interesting feature is the lens-shaped area on the right panel appearing between our galaxy and the point mass we artificially put 17 Mpc from it. This white area represents negative PDM density, and is the direct result of the EFE of the Virgo-like point mass.
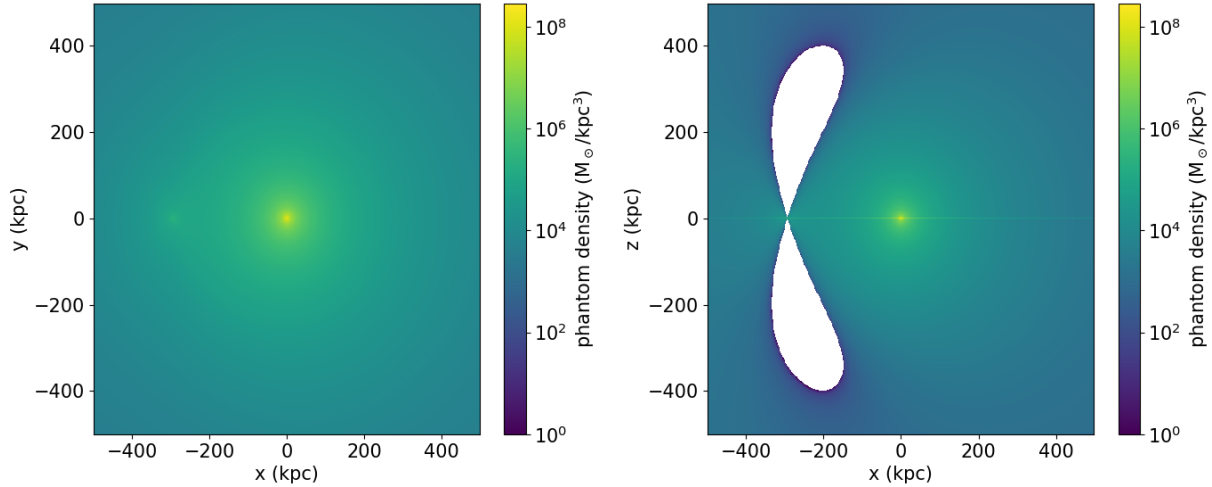
Figure 2.1: PDM density map centred on the MW at the position $(x, y, z) = (0, 0, 0) \, \text{kpc}$. Plane cuts. *Left panel:* MW galactic plane $z = 0$. *Right panel:* MW edge-on view $y = 0$. The white area represents negative PDM. The Virgo-like point mass is located at $(x, y, z) = (-17000, 0, 0) \, \text{kpc}$.

Plotting this situation in three dimensions as in Figure 2.2 gives us a lot more information on the shapes of those PDM structures. In this view, we see that the PDM distribution around the MW-like galaxy takes the expected halo shape, while the negative PDM lens shape seen in the plane cuts of Figure 2.1 turns out to be a frisbee- or shield-like structure oriented towards the point mass causing the EFE. We also expect to see a dark disk, *i.e.* a

distribution of PDM closely following that of the baryonic disk, which is exacerbated here by the slightly unrealistically extending disk of the Miyamoto-Nagai profile.
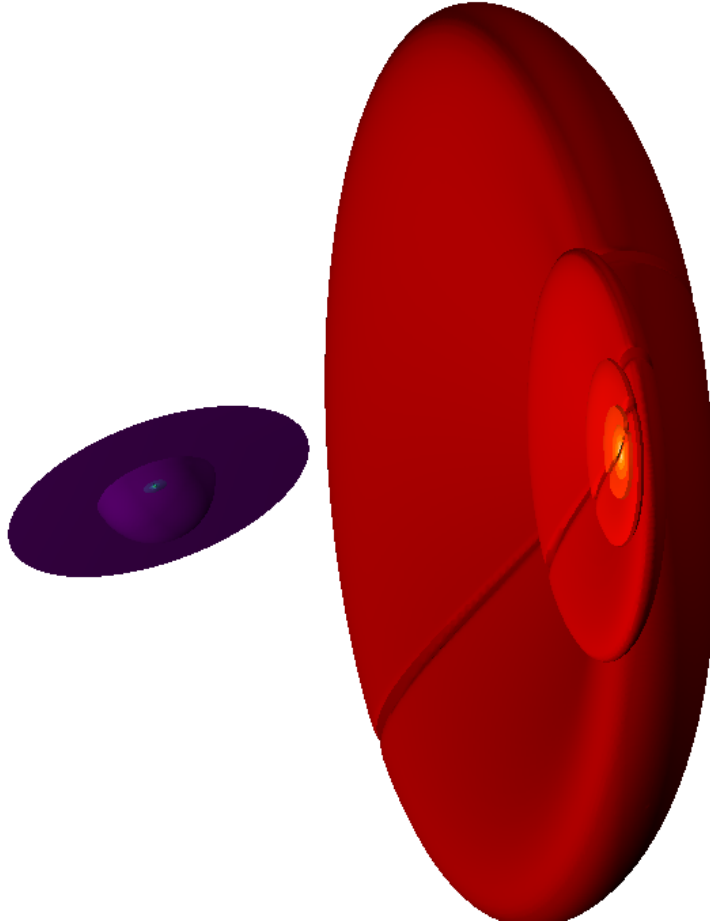
Figure 2.2: The same situation as Figure 2.1 but seen in three dimensions. The purple halo-like shape represents the PDM around the Milky Way-type galaxy. The red shield- or frisbee-like shape is negative PDM density and corresponds to the white area in the right panel of Figure 2.1.

2.1.2 Numerical implementation

If one wants to compute the PDM density from a potential involving (many) more bodies however, which we aim to do, this previous approach is not viable as one can imagine by taking a look at the case for two bodies of Equation (2.2), and one must thus turn to a numerical computation. In this context, Equation (1.19) can be discretized so as to compute the PDM density on a grid pattern using finite differences as done for example in Lüghausen et al. (2015) for the N-body code Phantom of Ramses. For this thesis, a version of this method was implemented in FORTRAN to compute the PDM density in a three-dimensional

grid, in which the value at the (i, j, k) vertex of a cube of the grid is given by

$$
\begin{aligned}
\rho_{\text{PDM}}(i, j, k) = \alpha[&\tilde{\nu}\left(\frac{|\nabla\Phi_N(i+1, j, k)|}{a_0}\right)\frac{\partial\Phi_N}{\partial x}(i+1, j, k) \\
&- \tilde{\nu}\left(\frac{|\nabla\Phi_N(i-1, j, k)|}{a_0}\right)\frac{\partial\Phi_N}{\partial x}(i-1, j, k) \\
&+ \tilde{\nu}\left(\frac{|\nabla\Phi_N(i, j+1, k)|}{a_0}\right)\frac{\partial\Phi_N}{\partial y}(i, j+1, k) \\
&- \tilde{\nu}\left(\frac{|\nabla\Phi_N(i, j-1, k)|}{a_0}\right)\frac{\partial\Phi_N}{\partial y}(i, j-1, k) \\
&+ \tilde{\nu}\left(\frac{|\nabla\Phi_N(i, j, k+1)|}{a_0}\right)\frac{\partial\Phi_N}{\partial z}(i, j, k+1) \\
&- \tilde{\nu}\left(\frac{|\nabla\Phi_N(i, j, k-1)|}{a_0}\right)\frac{\partial\Phi_N}{\partial z}(i, j, k-1)],
\end{aligned}
\tag{2.3}
$$

with $\alpha = 1/(8\pi G h)$ where G is the gravitational constant, h is the width of a cubic cell, and $\tilde{\nu} = \nu - 1$. Schematically, the situation in two dimensions can be represented as the stencil shown in Figure 2.3.
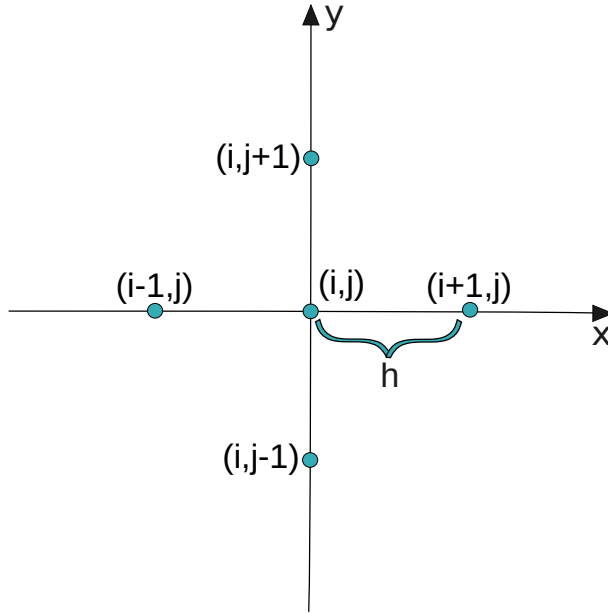
Figure 2.3: A 2D version of the stencil used for the discretization of Equation (2.3).

Note that in Equation (2.3), the partial derivatives of Φ_N also are computed using finite differences. Here is the equation for the x direction, with the y and z directions being treated in a similar fashion:

$$
\frac{\partial\Phi_N}{\partial x}(i, j, k) = \frac{1}{12h}[\Phi_N(i-2, j, k) - 8\Phi_N((i-1, j, k) + 8\Phi_N(i+1, j, k) - \Phi_N(i+2, j, k)]. \tag{2.4}
$$

(a) analytical case

(b) numerical case
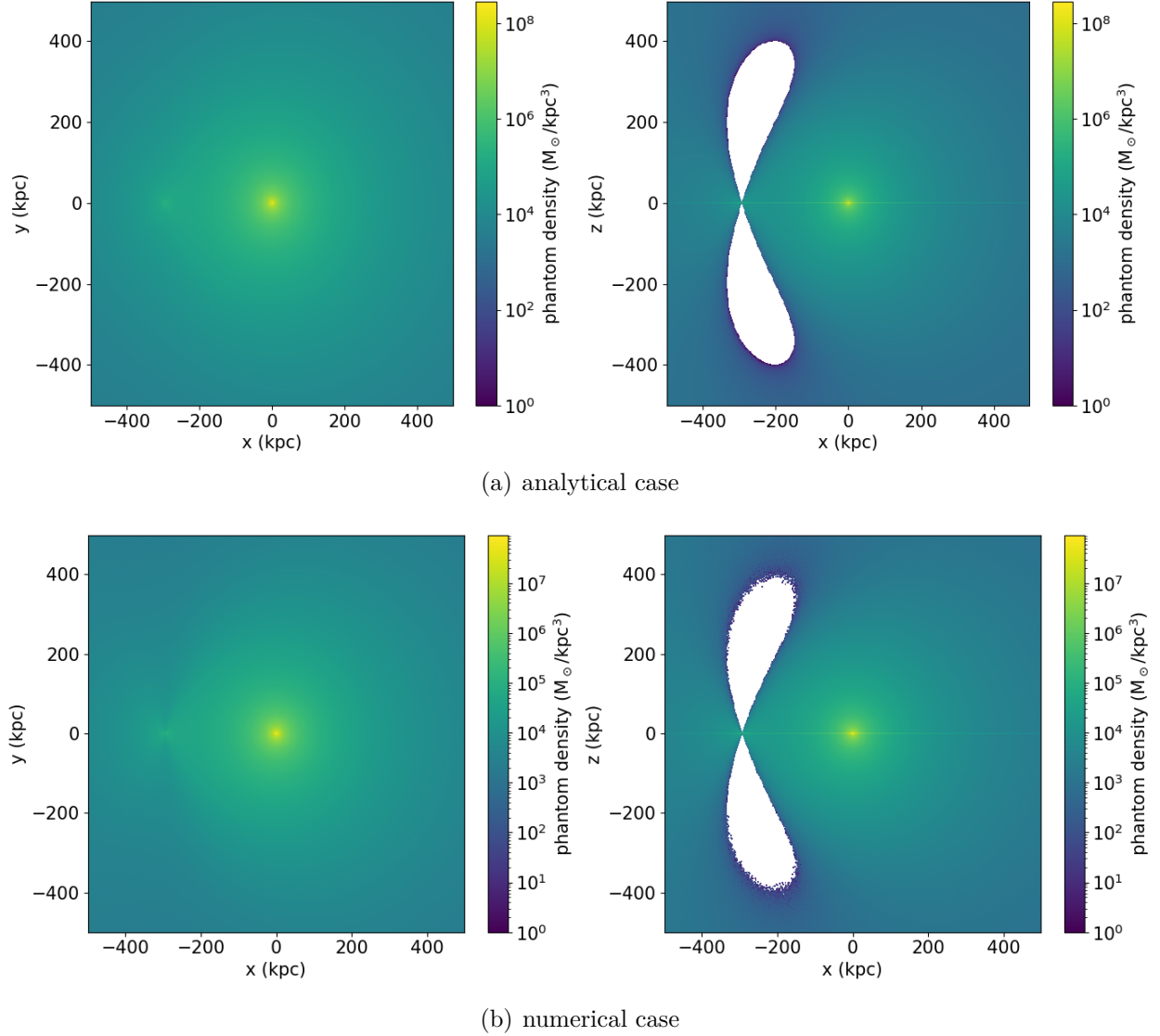
Figure 2.4: Comparison of PDM density profiles obtained from different methods. The MW is at the position $(x, y, z) = (0, 0, 0)$ kpc. Plane cuts with the xy plane being the MW disk plane. *Top panel:* (a) analytical case of Section 2.1.1. *Bottom panel:* (b) finite differences computation as in Section 2.1.2.

2.1.3 Accuracy and performance

In this section we investigate the accuracy of our finite differences solver by comparing its output with analytical values. Let us place ourselves again in the case of a MW-like galaxy and a Virgo point mass as in Section 2.1.1. In Figure 2.4, we compare the PDM density obtained by the analytical formula of Equation 2.2 (top panel) to the one obtained from the numerical scheme of Equation 2.3. The resolution is 500 cubes per direction for a volume of $1000 \times 1000 \times 1000$ kpc^3 centred on the MW. The difference in enclosed masses in the computation volume is very small, around 1%, with 3.29×10^{12} M$_\odot$ for the analytical case and 3.25×10^{12} M$_\odot$ for the numerical case. The features are very similar, with the only notable

43

difference being rough edges for the negative PDM zones in the numerical case. Those are due to the finite differences approximation combined with resolution (width of a cell), but have very little effect on the final outcome.

Now if we take the same computation but zoom on the inner 50 kpc cube, we get Figure 2.5. This time the difference in enclosed mass is slightly bigger, around 5%, with 4.66×10^{11} $M_\odot$ for the analytical case and 4.42×10^{11} $M_\odot$ for the numerical case. But obviously the resolution is not suitable here since the underlying computation volume was much bigger.

(a) analytical case

(b) numerical case
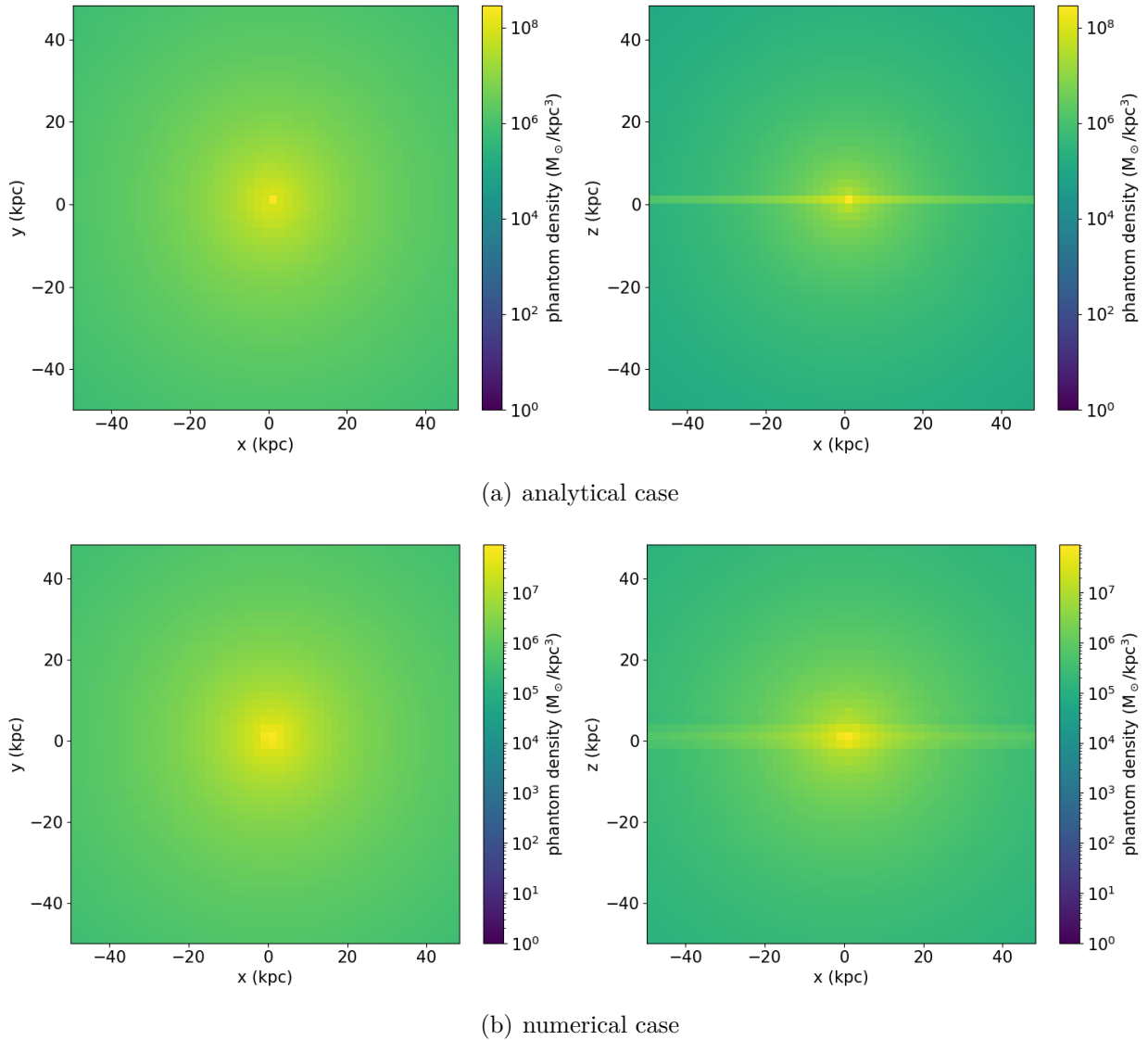
Figure 2.5: Comparison of PDM density profiles obtained from different methods. The MW is at the position $(x, y, z) = (0, 0, 0)$ kpc. Plane cuts with the xy plane being the MW disk plane. Zoom in the inner regions of the MW-like galaxy, from the computation of Figure 2.4. *Top panel:* (a) analytical case of Section 2.1.1. *Bottom panel:* (b) finite differences computation as in Section 2.1.2.

If however we do the direct computation for this smaller volume with much better resolution (500 cells per direction, Figure 2.6), we get a much better agreement with virtually no difference in enclosed mass.

After an extensive usage of the code, we find that the resolution corresponding to a cell length of 1 kpc yields good results when looking at the PDM in a single galaxy (with virial length ~ 250 kpc, this makes ~ 500 cells per direction). However when trying to map bigger volumes as we will do in Section 3 for the Local Universe, the number of cells per direction has to be increased, making for much longer computation times.

The running time mostly depends on the number of external sources included in the computation. For a single isolated galaxy with the optimal resolution discussed in the last paragraph, the code runs in a couple of minutes at most (on a single core on a standard modern CPU with ~ 3GHz clock speed). However for the same galaxy under the external influence of ~ 200 (point mass) sources, as in our work of Section 3, the PDM computation can take up to thirty to sixty minutes (on the same hardware as before). For the map of the Local Universe ($20 \times 20 \times 20 \, \mathrm{Mpc}^3$), the number of cells per direction had to be increased, leading to a computation of several hours.

2.2 Solving Poisson's equation

We now want to solve Equation (1.18) which we rewrite here for convenience

$$\Delta \Phi = 4\pi G (\rho_{\mathrm{PDM}} + \rho_b) \tag{1.18}$$

where ρ_{PDM} has been computed by the previous step of Section 2.1. This MONDian Poisson's equation is really practical since it has the same form as the standard Newtonian Poisson's equation (Equation (1.14)) and can thus be treated by standard solvers.

For the purpose of this work, I coded my own Poisson's equation solver in FORTRAN, relying on finite differences computation and the Gauss-Seidel iterative process. Just like we did for the computation of the PDM density, we solve Equation (1.18) on a three-dimensional grid.

2.2.1 Boundary conditions

Equation (1.18) is a differential equation, and as such requires initial, or rather here boundary conditions, to get a solution. Their value depends on our purposes. For a standard Newtonian system, it is reasonable to take zero as boundary conditions for a large enough box since the gravitational potential will eventually go down to zero at large distances. However in MOND, for an isolated system, the gravitational potential actually diverges logarithmically. In addition, for our purposes, the EFE has to be taken into account.

One method that we often used is to start with a bigger box than the one we are actually interested in. Say we want to solve the equation for a galaxy in a box of size $200 \times 200 \times 200 \, \mathrm{kpc}^3$. Then we could start with a box of size $1000 \times 1000 \times 1000 \, \mathrm{kpc}^3$ or bigger, and find appropriate boundary conditions for this big box. In the case of a constant external field, there exists an analytical expression for the potential in the external field dominated regions that can be used: Famaey & McGaugh (2012, Eqs (63) and (64)).

(a) analytical case

(b) numerical case
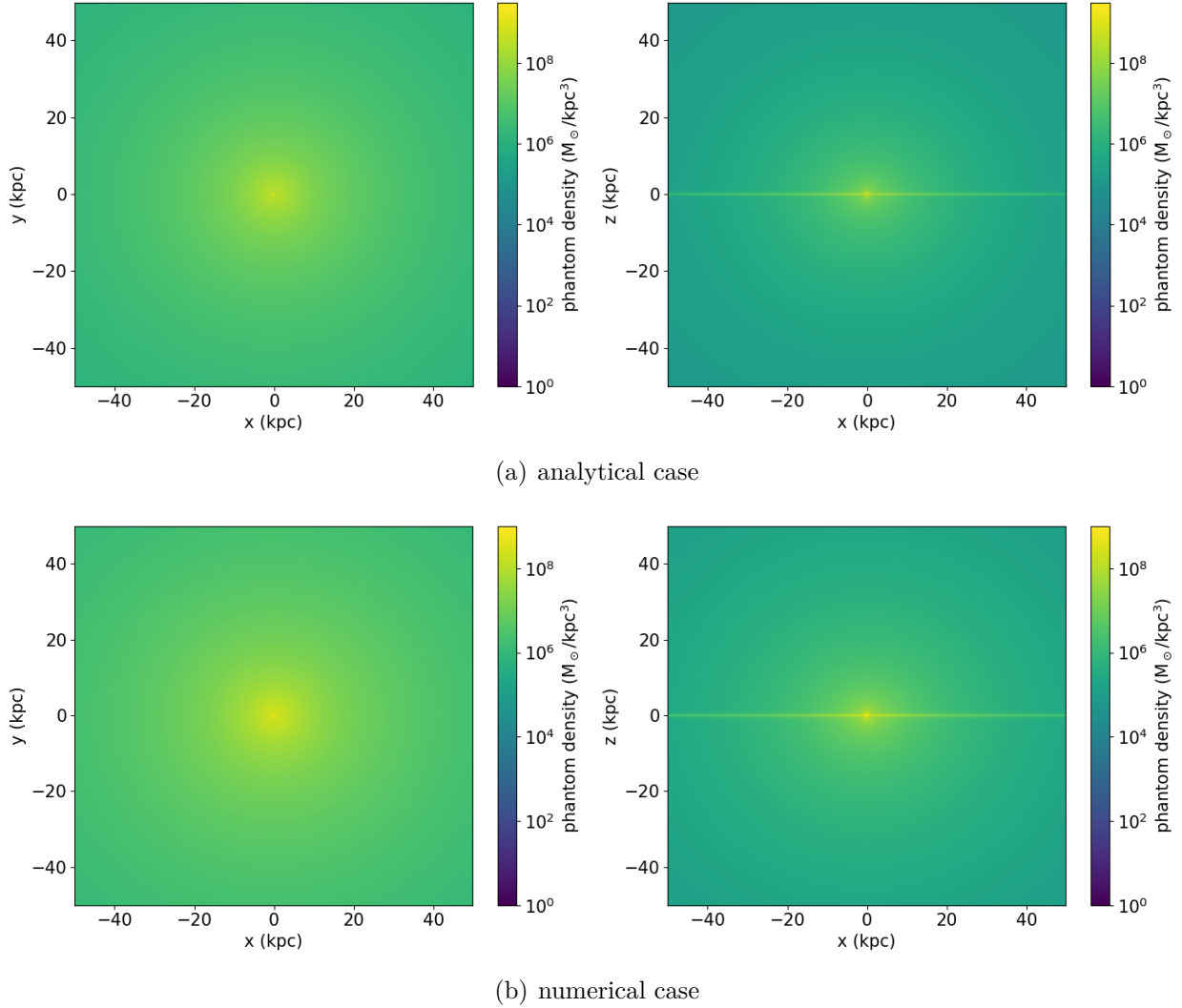
Figure 2.6: Comparison of PDM density profiles obtained from different methods for the inner regions of a MW-like galaxy. The MW is at the position $(x, y, z) = (0, 0, 0)$ kpc. Plane cuts with the xy plane being the MW disk plane. *Top panel:* (a) analytical case of Section 2.1.1. *Bottom panel:* (b) finite differences computation as in Section 2.1.2.

Most of our studies involved a non-constant external field however. In this case, we usually computed the PDM density in the big box first, based on the Newtonian potential of every object located both inside or outside the box. Then an adequate boundary condition for the big box is to take the spherical approximation $-G(M_b(r) + M_{\text{PDM}}(r))/r$ where r is the distance to the center of the box, and $M_b(r)$ and $M_{\text{PDM}}(r)$ are the enclosed baryonic and phantom masses respectively in a ball of radius r.

After solving Equation (1.18) for the big box with this boundary condition, we can go back to the smaller refined box around the galaxy of interest for another integration of the MONDian Poisson's equation. In this case, we can now take as boundary conditions the potential obtained from the integration of the big box, with the values corresponding to the boundaries of our smaller box. We have found that this permitted to reproduce the external

field-induced structures of the bigger box accurately at the boundaries of the small box, thanks to the previously computed phantom density source term.

2.2.2 Numerical implementation

The idea here again is to discretize Equation (1.18). Doing it for the x direction as an example, we get from a Taylor expansion the value at the (i, j, k) vertex of a cube from our three-dimensional grid:

$$\frac{\partial^2 \Phi(i, j, k)}{\partial x^2} = \frac{\Phi(i - 1, j, k) + \Phi(i + 1, j, k) - 2\Phi(i, j, k)}{h^2} \tag{2.5}$$

where h is the length of the side of the cube. The y and z partial derivatives are obtained in an analog fashion. Summing for every direction, we get

$$
\begin{aligned}
S(i, j, k) :&= 4\pi G h^2 \rho(i, j, k) \\
&= \Phi(i - 1, j, k) + \Phi(i + 1, j, k) + \Phi(i, j + 1, k) \\
&+ \Phi(i, j - 1, k) + \Phi(i, j, k + 1) + \Phi(i, j, k - 1) - 6\Phi(i, j, k)
\end{aligned} \tag{2.6}
$$

where $\rho := \rho_b + \rho_{\mathrm{PDM}}$ and we have defined for simplicity the source function S as the density term multiplied by the appropriate constants.

Isolating $\Phi(i, j, k)$ we thus have, for each of our vertices, a linear equation to solve to obtain the gravitational potential at the corresponding location in space:

$$
\begin{aligned}
\Phi(i, j, k) = \frac{1}{6}[&\Phi(i - 1, j, k) + \Phi(i + 1, j, k) + \Phi(i, j + 1, k) \\
&+ \Phi(i, j - 1, k) + \Phi(i, j, k + 1) + \Phi(i, j, k - 1) - S(i, j, k)].
\end{aligned} \tag{2.7}
$$

Obviously, one notices that the adjacent values of the potential are however required. The idea of the Gauss-Seidel method is to get more and more accurate values by iterating on the lines of our three-dimensional Φ matrix, and using the boundary conditions and the source term as anchor points. The novelty is that values are immediately replaced in the same matrix rather than creating a new one for each iteration, thus using the newly obtained values immediately in the computation of the next value. The convergence of the process can be evaluated and used as a stopping condition by computing the norm of the Φ matrix (by *e.g.* summing every term squared and comparing with the norm of the previous iteration).

The convergence of the Gauss-Seidel method is sadly a rather slow process. Thankfully, there exists a technique called acceleration by over-relaxation to greatly enhance the convergence speed. The trick is to introduce a new parameter $1 < \epsilon < 2$ in such a way that you will adopt at each iteration a value which is not the current iteration result, but that goes further in the direction that the Gauss-Seidel process gives you. The value of the gravitational potential at the n-th iteration Φ_n becomes thus:

$$\Phi_n(i, j, k) = (1 - \epsilon)\Phi_{n-1}(i, j, k) + \epsilon\Phi_{n,\mathrm{GS}}(i, j, k) \tag{2.8}$$

where Φ_{GS} denotes the value one would have obtained in the normal Gauss-Seidel process, based on Equation (2.7).

2.2.3 Accuracy and performance

In order to test the accuracy of our code, we compare the results of Poisson's equation solved using the machinery described in Section 2.2.2 to an analytical gravitational potential. An ideal profile to use for such a comparison is the spherically symmetric Plummer profile, for which we have an analytical formula for both the density and the gravitational potential, with the latter being:

$$\Phi(r) = -\frac{GM}{\sqrt{r^2 + a^2}} \tag{2.9}$$

where r is the radius, M is the total mass of the system, and a is a scale radius inherent to the system.

We do this comparison in the baryonic Newtonian case for an object with baryonic mass comparable to that of the MW ($M = 7.5 \times 10^{10} \, \mathrm{M_\odot}$). We first get the baryonic density profile from the analytical formula, then use it as the ρ in the S term of Equation (2.7). Then we get the boundary conditions from the analytical formula of Equation (2.9). For this test, we probe a volume of $200 \times 200 \times 200 \, \mathrm{kpc}^3$ with 200 cells per direction, so that each cube of the grid has volume $1 \, \mathrm{kpc}^3$.

The result of the numerical integration of Poisson's equation, yielding the gravitational potential, can be seen on the right panel of Figure 2.7, next to the analytically derived left panel. There is visually no difference, looking at those plots, between the numerical and analytical cases. We confirm numerically that the agreement is very good, with differences between the mean potentials at each radius being $\leq 1\%$ in this test case.

Using this solver with density data stored in a cube of $500 \times 500 \times 500$ cells - corresponding to our ideal resolution for a single galaxy as discussed in Section 2.1.3 - takes around ten hours on a single core on a modern CPU.

(a) analytical case

(b) numerical case
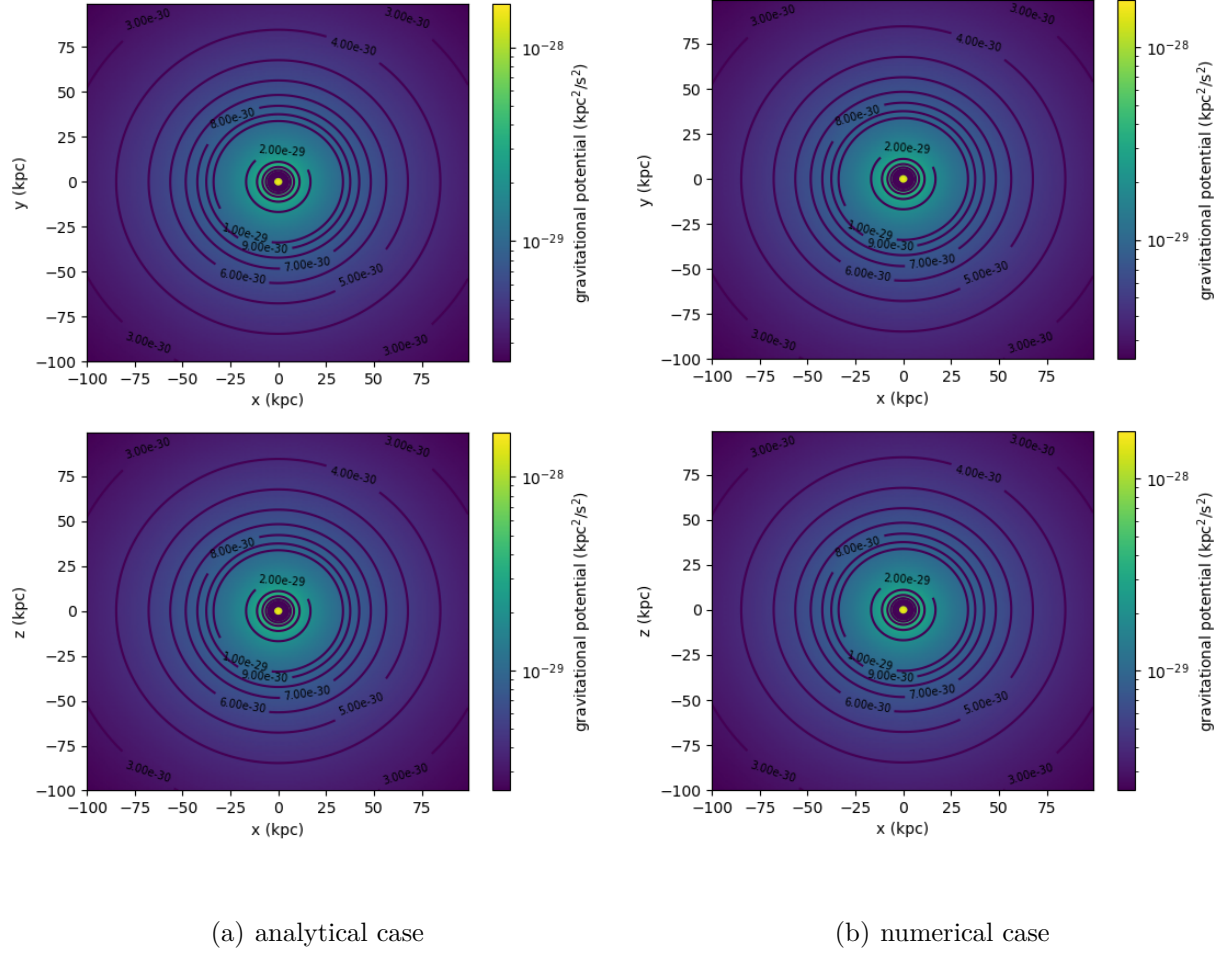
Figure 2.7: Comparison of gravitational potentials for a Plummer sphere obtained from different methods. We show two different projections to confirm that the profile is spherically symmetric as expected. *Left panel:* (a) analytical formula of Equation (2.9). *Right panel:* (b) using the Poisson solver of Section 2.2.

Chapter 3 The phantom dark matter halos of the Local Volume in the context of MOND

Equipped with the numerical tools presented in Chapter 2, we are now able to take a look at the Local Universe in the QUMOND framework.

Foreword

This is a slight modification, to fit this manuscript, of the work of Oria, P.-A.; Famaey, B.; Thomas, G.; Ibata, R.; Freundlich, J.; Posti, L.; Korsaga, M.; Monari, G.; Müller, O.; Libeskind, N.; Pawlowski, M. which was published in The Astrophysical Journal, Volume 923, Issue 1, id.68, 20 pp. (Oria et al., 2021).

Abstract

We explore the predictions of Milgromian gravity (MOND) in the Local Universe by considering the distribution of the 'phantom' dark matter (PDM) that would source the MOND gravitational field in Newtonian gravity, allowing an easy comparison with the dark matter framework. For this, we specifically deal with the quasi-linear version of MOND (QUMOND). We compute the 'stellar-to-(phantom)halo-mass relation' (SHMR), a monotonically increasing power-law resembling the SHMR observationally deduced from spiral galaxy rotation curves in the Newtonian context. We show that the gas-to-(phantom)halo-mass relation is flat. We generate a map of the Local Volume in QUMOND, highlighting the important influence of distant galaxy clusters, in particular Virgo. This allows us to explore the scatter of the SHMR and the average density of PDM around galaxies in the Local Volume, $\Omega_{\rm pdm} \approx 0.1$, below the average cold dark matter density in a ΛCDM Universe. We provide a model of the Milky Way in its external field in the MOND context, which we compare to an observational estimate of the escape velocity curve. Finally, we highlight the peculiar features related to the external field effect in the form of negative PDM density zones in the outskirts of each galaxy, and test a new analytic formula for computing galaxy rotation curves in the presence of an external field in QUMOND. While we show that the negative PDM density zones would be difficult to detect dynamically, we quantify the weak lensing signal they could produce for lenses at $z \sim 0.3$.

3.1 Introduction

The missing mass problem is one of the most pressing questions in present day (astro)physics. The current dominant Λ Cold Dark Matter (ΛCDM) paradigm – while reproducing with impressive accuracy a large number of observations on all scales – still has some pending issues, both at cosmological scales (e.g., Riess et al., 2019; Bowman et al., 2018) and on small scales (e.g., Bullock & Boylan-Kolchin, 2017). This includes challenges in explaining the diversity of galaxy rotation curve shapes (e.g. Oman et al., 2015), the suprisingly low scatter of the Baryonic Tully-Fisher Relation (BTFR, McGaugh et al., 2000; Lelli et al., 2016b; Desmond, 2017a; Lelli et al., 2019), the high baryon fraction in massive discs (e.g. Posti et al., 2019a; Marasco et al., 2020), the planes of satellite galaxies problem (Pawlowski, 2018), or the prevalence of cold stellar kinematics and the absence of bulges (or massive stellar halos) in most disc galaxies (e.g., Peebles, 2020). This justifies exploring alternative frameworks, which can range from modifications of the dark matter properties to radical modifications of gravity.

In galaxies – especially rotationally-supported ones – the observed dynamics can be predicted surprisingly well based on the distribution of baryons alone, through Milgrom's law (Milgrom, 1983) which is at the heart of the Modified Newtonian Dynamics (MOND) paradigm (Milgrom, 1983; Famaey & McGaugh, 2012). Milgrom's law posits that gravitational accelerations below $a_0 \simeq 10^{-10} \mathrm{m\,s^{-2}}$ approach $(g_N a_0)^{1/2}$, where g_N is the Newtonian gravitational attraction generated by the baryons. In the case where $g \gg a_0$, the dynamics is Newtonian (hence no dark matter-like effect is present), and a smooth transition can be prescribed between the two regimes.

This very simple law directly predicts the observed slope and an effectively zero intrinsic scatter for the BTFR, as well as the universal relation which is observed between the baryonic and dynamical central surface densities of disc galaxies (Lelli et al., 2016c; Milgrom, 2016), and therefore also the diversity of rotation curve shapes, driven by the different surface density of the baryons in different galaxies (e.g., Ghari et al., 2019). The universal relation predicted by MOND is one between the Newtonian gravitational acceleration generated by the baryons and the total one, a relation that is now known as the Radial Acceleration Relation (RAR, McGaugh et al., 2016; Lelli et al., 2017), which in the ΛCDM context suggests a strong coupling between DM and baryonic mass that has yet to find a fully satisfying explanation. There have been multiple investigations of the relation in the ΛCDM context, but while the general shape of the relation can be accounted for indeed (Di Cintio & Lelli, 2016; Keller & Wadsley, 2017; Navarro et al., 2017; Ludlow et al., 2017), its normalization and small scatter (Desmond, 2017b), the latter being actually accounted for solely by observational errors on the inclination and distance of galaxies (Li et al., 2018), remain puzzling.

With a suitable extension of gravity – either classical (Bekenstein & Milgrom, 1984; Milgrom, 2010) or relativistic (e.g., Skordis & Zlosnik, 2020) – giving rise to Milgrom's law in the weak-field limit[1], no dark matter would then actually be needed in galaxies. Moreover, such a framework could avoid the over-formation of bulges in disc galaxies compared to observations (Combes, 2014, 2016). In galaxy clusters, the situation is however different (see, e.g., Angus et al., 2008; Bílek et al., 2019).

---

[1]exactly so in highly symmetric configurations, and approximately in more complex ones

This is one of the most radical existing alternatives to the whole *Imago Mundi* carried by the ΛCDM model: it is actually so different that it is sometimes difficult to even phrase the description of stellar systems in the same way. However, despite fundamental differences in the nature of its ingredients, it is useful to ask oneself whether a MONDian Universe really would look so different from our current standard picture. It has for instance been recently demonstrated by Skordis & Zlosnik (2020) that matter power spectra on linear cosmological scales could be very similar within the particular relativistic MOND theory considered by the authors. A lot of work remains to be done in this context, to connect these linear scales to the non-linear regime, and especially to understand whether the MOND "missing mass" in galaxy clusters could be addressed naturally in such a framework, without resorting to an additional dark matter component (beyond the *k*-essence scalar field playing the role of dark matter on linear scales in that theory). Here, rather than taking a top-down cosmological approach, we will explore how our Local Volume (within ~ 11 Mpc) of the Universe looks in the context of MOND. For this endeavour, we resort to the concept of "Phantom Dark Matter" (PDM) introduced in, e.g., Milgrom (1986) in the context of the Bekenstein & Milgrom (1984) version of MOND. The PDM distribution is the distribution of additional dark matter that *would* give rise to the MOND gravitational field in Newtonian gravity. This concept allows one to look at a MONDian Universe with Newtonian eyes, which can ease the comparisons with the standard picture. For instance, relations between the stellar and (phantom) halo mass, as well as between the gas and (phantom) halo mass can then be explored in detail. While the PDM distribution can be computed as $\rho_{\mathrm{PDM}} = \Delta\Phi/(4\pi G) - \rho_b$ (where ρ_b is the baryonic density) in any MONDian framework, it takes a central role within the quasi-linear version of MOND (QUMOND Milgrom, 2010) as it is there typically computed *before* the MONDian potential itself, as we will detail in Sect. 2. All the investigations of the present paper will be carried out in the QUMOND context, which should qualitatively be generic but could quantitatively deviate from other formulations such as the Bekenstein & Milgrom (1984) version of MOND.

One fundamental aspect in the context of MOND is that the strong equivalence principle must be broken, meaning that the physics in a free-falling frame depends on its gravitational environment. As shown early by, e.g., Milgrom (1986), the PDM distribution in the outskirts of a galaxy is therefore heavily influenced by the gravitational environment in which the galaxy resides, and can even be negative in places. This is known as the external field effect (EFE) of MOND: in Newtonian dynamics, the internal dynamics of a system embedded in a constant external field g_e does not depend on that field, but in the MOND paradigm it does, since the total gravitational acceleration (including the external one) is considered. In MOND, Milgrom's law thus only applies when the internal gravitational field is larger than the external one, $g \gg g_e$. If the situation is any different, the EFE has to be taken into account. This is why ultra-diffuse galaxies embedded in an external field can lack a dark matter-like effect in MOND (e.g., Famaey et al., 2018). This effect has also been used to predict the velocity dispersions in pairs of photometrically indistinguishable dwarf satellites of Andromeda (McGaugh & Milgrom, 2013a,b, where the velocity dispersions of the dwarfs And XIX, And XXI, and And XXV were predicted and verified (Collins et al., 2014)). More generally, the gravity from surrounding structures should cause the rotation curves of any galaxy to decline at large radii (e.g., Hees et al., 2016; Chae et al., 2020, 2021), and this decline should depend on the environment. Whether this applies inside galaxy clusters,

where the origin of the "MOND missing mass" remains unclear, is still to be investigated. But in the field, the EFE is an inevitable consequence of the MOND framework. Other possible signatures of the EFE include effects on the secular evolution of discs, including the evolution of bar instabilities (Banik et al., 2020), warp formation (Brada & Milgrom, 2000), or asymmetries in tidal tails from disrupting satellites (Thomas et al., 2018).

Maps of Newtonian potential and acceleration up to a distance of 200 Mpc have been established by Desmond et al. (2018), in which zones of exceptionally strong external accelerations are highlighted as good testing grounds to probe the EFE. However, high external accelerations can also occur locally. With this in mind, we aim herafter at computing the detailed PDM density distribution around galaxies in our Local Volume, by rigorously taking into account the full non-linearity of MOND. This exercise should both ease the comparison with the standard picture, and help quantify and locate the consequences of the EFE in MOND: zones of negative PDM should actually arise perpendicular to the external field direction (see e.g. Famaey & McGaugh, 2012), and around the point where g and g_e are equivalent. When the escape speed curve of a galaxy can be measured (which is essentially the case only in the Milky Way today), its confrontation with MOND must also take into account the EFE (Famaey et al., 2007; Wu et al., 2008; Banik & Zhao, 2018a), as without it no escape would be possible at all due to a logarithmically divergent potential.

For such an endeavour, we need, in principle, to numerically solve the generalized Poisson equation of MOND (Bekenstein & Milgrom, 1984; Milgrom, 2010). Numerical solvers have been developed in the past, especially in the context of the development of MOND N-body codes (Brada & Milgrom, 1999; Tiret & Combes, 2007; Llinares et al., 2008; Londrillo & Nipoti, 2009; Angus et al., 2012; Candlish et al., 2015; Lüghausen et al., 2015). Hereafter, for the aforementioned purpose of computing the PDM density distribution around galaxies in the Local Volume, we shall use our own solver, following the approach of, e.g., Angus et al. (2012) and Lüghausen et al. (2015), using the quasi-linear formulation of MOND (Milgrom, 2010) to directly compute it. In this formulation, the non-linearity of MOND is entirely contained within the computation of the PDM density, and the Newtonian Poisson equation can then be solved to compute the associated gravitational field.

We will first introduce in Section 3.2 some aspects of MOND and its quasi-linear formulation, and start by exploring some simple scaling relations between the stellar, gas, and phantom halo masses in the case where no EFE is present. In Section 3.3, we then make a full and rigorous calculation of the PDM density in the Local Volume, and present a map of the PDM density in the Local Volume, allowing to explore the consequences of the EFE on the scaling relations between the stellar and halo masses. In Section 3.4, we take advantage of this model of the Local Universe to present an up-to-date fiducial MOND model of the Milky Way (MW) in its environment. Finally, Section 3.5 illustrates the action of the EFE on galaxies in a strong external field, where we show that the negative PDM density zones could be detected via gravitational lensing.

3.2 MOND and phantom halos

3.2.1 Quasi-linear MOND

The concept of the theoretical matter that would source the MOND force field in Newtonian gravity, denoted as PDM, is particularly useful for comparisons with various dark matter-based models, and also permits to conceptually visualize some peculiar aspects of MOND such as the external field effect (EFE). In the quasi-linear formulation of MOND (QUMOND Milgrom, 2010), the whole non-linearity of the framework is contained within the computation of the PDM density, from which one obtains the gravitational potential by solving the Newtonian Poisson equation[2].

Indeed, in QUMOND, the generalized Poisson equation takes the form (Milgrom, 2010):

$$\Delta\Phi = \nabla \cdot \left[\nu\left(\frac{|\nabla\Phi_N|}{a_0}\right) \nabla\Phi_N \right] \tag{3.1}$$

where Φ is the MOND potential, Φ_N is the Newtonian potential, a_0 is the critical acceleration constant mentioned in Section 3.1, the value of which we fix hereafter at 1.2×10^{10} m s^{-2} (e.g., Gentile et al., 2011), and ν is the function allowing for a smooth transition between the Newtonian and MOND regimes. In particular, this ν function should verify

$$\nu(x) \to 1 \ (x \gg 1) \tag{3.2}$$

in order to agree with Newtonian dynamics (if the acceleration is much greater than a_0, then Equation (3.1) tells us that the MOND potential agrees with the Newtonian one), and

$$\nu(x) \to 1/\sqrt{x} \ (x \ll 1) \tag{3.3}$$

giving the MOND regime for low accelerations. In this paper we adopt the following ν function (Famaey & Binney, 2005; Gentile et al., 2011; Famaey & McGaugh, 2012; Banik & Zhao, 2018b):

$$\nu : x \mapsto \left(\frac{1}{4} + \frac{1}{x}\right)^{1/2} + \frac{1}{2}. \tag{3.4}$$

This is very close to the interpolating function adopted by McGaugh et al. (2016); Lelli et al. (2017); Li et al. (2018) to describe empirically the relation between $\nabla\Phi_N$ and $\nabla\Phi$ in galaxies (see Famaey & McGaugh, 2012). Note however that a modification is needed at the high mass end to pass Solar System constraints (Hees et al., 2016), but this has no consequence for the study conducted hereafter.

The above Poisson equation can also be recast as

$$\Delta\Phi = 4\pi G(\rho_{\mathrm{PDM}} + \rho_b) \tag{3.5}$$

where G is the gravitational constant, ρ_{PDM} is the PDM density, and ρ_b is the baryonic density. Combining Equation (3.1) and Equation (3.5), we readily get a formula for the PDM density:

$$\rho_{\mathrm{PDM}} = \frac{1}{4\pi G} \ \nabla \cdot \left[(\nu\left(\frac{|\nabla\Phi_N|}{a_0}\right) - 1)\nabla\Phi_N \right]. \tag{3.6}$$

---

[2]This version of MOND gravity differs slightly from other formulations outside of spherical symmetry (Zhao & Famaey, 2010), which means that the EFE can also have a different quantitative effect.

Numerically, this formula can be discretized and the PDM density can be computed on a grid pattern using finite differences following, e.g., the method used in Lüghausen et al. (2015). For the present work, we wrote our own version of this method to compute the phantom density. The value at the (i, j, k) vertex is given by:

$$
\begin{aligned}
\rho_{\text{PDM}}(i, j, k) = \alpha[&\tilde{\nu}\left(\frac{|\nabla\Phi_N(i+1, j, k)|}{a_0}\right)\frac{\partial\Phi_N}{\partial x}(i+1, j, k) \\
&- \tilde{\nu}\left(\frac{|\nabla\Phi_N(i-1, j, k)|}{a_0}\right)\frac{\partial\Phi_N}{\partial x}(i-1, j, k) \\
&+ \tilde{\nu}\left(\frac{|\nabla\Phi_N(i, j+1, k)|}{a_0}\right)\frac{\partial\Phi_N}{\partial y}(i, j+1, k) \\
&- \tilde{\nu}\left(\frac{|\nabla\Phi_N(i, j-1, k)|}{a_0}\right)\frac{\partial\Phi_N}{\partial y}(i, j-1, k) \\
&+ \tilde{\nu}\left(\frac{|\nabla\Phi_N(i, j, k+1)|}{a_0}\right)\frac{\partial\Phi_N}{\partial z}(i, j, k+1) \\
&- \tilde{\nu}\left(\frac{|\nabla\Phi_N(i, j, k-1)|}{a_0}\right)\frac{\partial\Phi_N}{\partial z}(i, j, k-1)]
\end{aligned}
\tag{3.7}
$$

with $\alpha = 1/(8\pi Gh)$ where h is the width of a cell, and $\tilde{\nu} = \nu - 1$. Notice that when $\nu = 1$, i.e. when in the Newtonian regime, $\tilde{\nu} = 0$ and thus there is no PDM. Here the partial derivatives of Φ_N are also computed with finite differences. The formula for the x direction reads

$$
\begin{aligned}
\frac{\partial\Phi_N}{\partial x}(i, j, k) = \frac{1}{12h}[&\Phi_N(i-2, j, k) - 8\Phi_N((i-1, j, k) \\
&+ 8\Phi_N(i+1, j, k) - \Phi_N(i+2, j, k)],
\end{aligned}
\tag{3.8}
$$

with the other directions being treated similarly. From Equation (3.7), one can see that the only information needed to compute ρ_{PDM} is thus the Newtonian potential Φ_N. However, it is also clear that the PDM density will depend on the gravitational environment of an object, meaning that a rigorous exploration of the structure of phantom halos around galaxies needs to fully take into account its environment. This is what we will explore in Section 3.3 for the Local Volume. However, before delving into these detailed calculations which mostly affect the outskirts of the PDM halos around galaxies, it is useful to consider the expected relations between the baryonic contents of a galaxy and its PDM halo in the isolated case.

3.2.2 The SHMR and gas-to-halo mass relations in isolated MOND

While the distribution of baryons alone (albeit with an influence from baryons located far away) dictates the gravitational field around galaxies in the MOND context, this is not the case in the ΛCDM context where dark matter is playing the key role. In the latter context, the connection between galaxy and halo properties is of utmost importance, and the most explored bit of this connection is the relation between galaxy stellar mass and halo mass, the so-called stellar-to-halo-mass relation (SHMR). One key feature of ΛCDM is that the halo mass function and the galaxy stellar mass functions have very different shapes: matching the halo mass function to the observed stellar mass function, known as the "abundance

matching" ansatz, then yields a characteristic SHMR (Vale & Ostriker, 2004; Kravtsov et al., 2004; Behroozi et al., 2013; Moster et al., 2013). This SHMR is non-linear in a log-log plot, and displays a break at around L_* galaxies. While this break is observed when considering early-type galaxies (mostly residing in groups and clusters), this is not the case for spirals in the field, which tend to display a monotonically increasing power-law (e.g. Posti et al., 2019a,b; Posti & Fall, 2021).

It is therefore useful to ask what the SHMR would look like in a MOND context (see also Wu & Kroupa, 2015). While a detailed modelling of a large volume around each galaxy is needed to assess in details the effect of the external gravitational field, we can start by considering the consequence of the isolated MOND predictions on the SHMR. In MOND, the fundamental relation is between the total amount of baryons and the gravitational field, hence we first need to consider the observed scaling between the gas and stellar mass in spiral galaxies. For this, we can consider the scaling relation found by Papastergis et al. (2012) between the HI and stellar mass, with a typical scatter of 0.2 dex

$$\log\left(\frac{M_H}{M_\star}\right) = -0.43\log(\mathrm{M_\star}) + 3.75. \tag{3.9}$$

This, in turn, can be used to compute the total gas mass for each galaxy using a multiplicative factor to account for helium: $M_{\mathrm{gas}} = 1.4 M_H$. This however neglects the molecular gas component which should be small in spiral galaxies.

In the standard context, a pure NFW (Navarro et al., 1997) profile extending to infinity would have an infinite mass, but the virial mass is usually defined at a radius r_{200} where the mean density is 200 times the critical density of the Universe. Hence in MOND we can do the same and integrate the PDM density profile up to a radius r_{200}. To do this we choose in agreement with Karachentsev et al. (2013) the value $\rho_{\mathrm{crit}} = 1.46 \times 10^2$ $\mathrm{M_\odot kpc^{-3}}$ for said critical density. In a spherical case (e.g. point mass approximation), the enclosed PDM mass $M_{\mathrm{PDM}}(r)$ at a radius r can be computed as

$$M_{\mathrm{PDM}}(r) = M_b \times \left(\nu\left(\frac{GM_b}{r^2 a_0}\right) - 1\right) \tag{3.10}$$

where M_b is the baryonic mass obtained from the stellar mass via Eq (3.9), and ν is the interpolating function of Eq (3.4). For a given stellar mass, applying this at r_{200} yields the isolated MOND M_{200} in terms of PDM.

We display the result on Figure 3.1, where it appears clearly that the SHMR is monotonically increasing in the isolated MOND case. The SHMR from Behroozi et al. (2013) (for a redshift $z \sim 0.1$) is plotted to highlight the differences with the MOND case. While the values are in good agreement for the range of halo mass considered, the MOND curve shows a very linear behaviour and no break is predicted at high halo masses. Interestingly, if we consider the gas-to-halo mass relation, we find an almost flat relation, meaning that the MOND effect is quite precisely counterbalanced by the observational scaling relation between the stellar and gas mass of galaxies, so as to yield an almost constant $M_{\mathrm{gas}}/M_{\mathrm{PDM}}$ ratio in the isolated MOND case. We will now explore hereafter how a full treatment of the EFE alters these results.
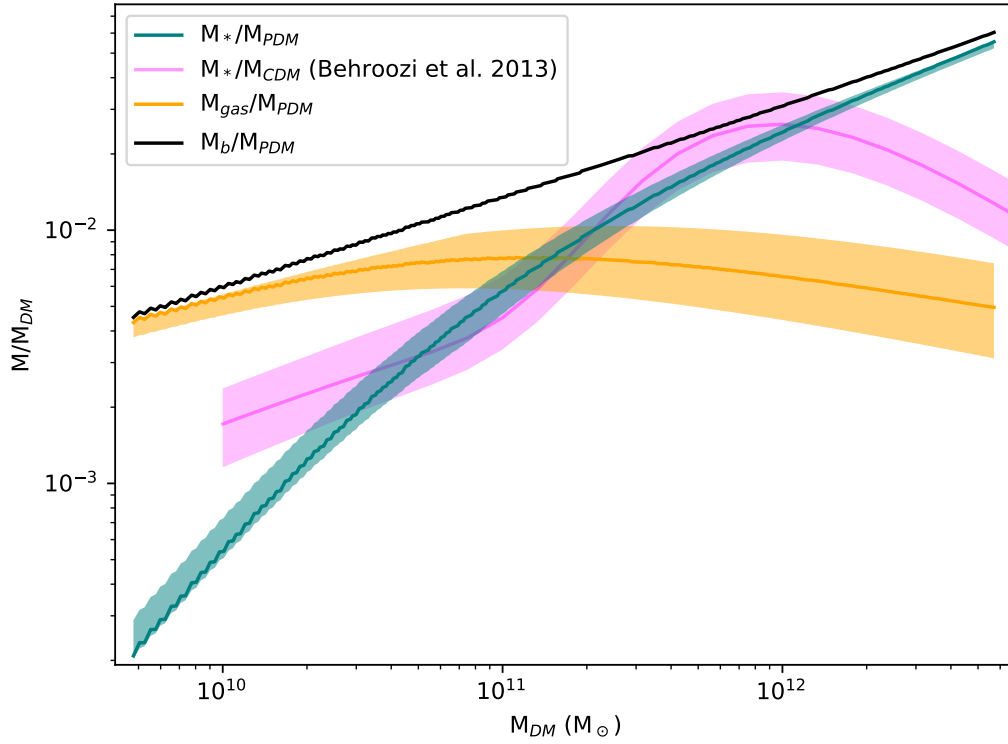
Figure 3.1: Stellar, gas, and baryonic masses (respectively M_*, M_{gas} and M_b) over PDM mass M_{PDM} at a computed r_{200} as a function of M_{PDM} in the isolated MOND case. The coloured areas represent the scatter of 0.2 dex in the HI to stellar mass relation of Eq (3.9). As a means of comparison, the SHMR for ΛCDM of Behroozi et al. (2013) (for a redshift $z \sim 0.1$) is also plotted.

3.3 Mapping the phantom dark matter in the Local Volume

3.3.1 The Updated Nearby Galaxy Catalog (UNGC)

To explore numerically the structure of PDM halos in MOND, galaxies cannot be treated in isolation, due to the non-linearity of MOND and the EFE. We will therefore now model the whole Local Volume, and even take into account the effect of large structures outside of it.

Throughout this article, we use a Galactic cartesian coordinate system with the centre of the MW at $(x = 0, y = 0, z = 0)$, with xy being the MW galactic plane. The Local Volume is modeled in our code as a cube of 20 Mpc side length centred on the MW, comprising 800 identical cells in each dimension, giving a resolution of 25 kpc. In order to obtain a map of the PDM distribution for this volume, we require the baryonic gravitational potential.

We use the UNGC catalog from Karachentsev et al. (2013) to get the position and mass (from the K_s band) of 869 galaxies either at a distance less than 11 Mpc from the MW or having a radial velocity with respect to the Local Group inferior to 600 $\mathrm{km\,s^{-1}}$.
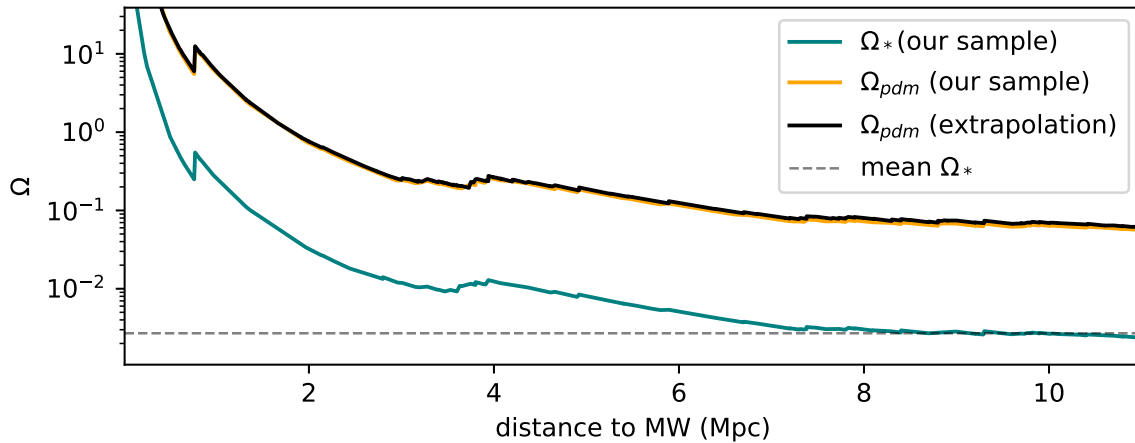
Figure 3.2: Mean density of matter Ω as a function of distance to the MW. The dashed line is the mean stellar density of the observable universe computed by Fukugita & Peebles (2004). The teal curve corresponds to the mean stellar density Ω_* of our sample. The orange curve correspond to the mean PDM density Ω_{pdm} of our sample. The black curve corresponds to the same value obtained by extrapolating our SHMR of Subsection 3.3.3 to the whole UNGC. The difference between the orange and black curves is very small, which shows that the galaxies that did not make our cut do not contribute much to the mass of the Local Universe. We notice a particularly good agreement with Karachentsev & Telikova (2018, Figure 2).

More than 50% of the stellar mass in the Local Volume is contained in the 21 highest luminosity galaxies. Here, for computational purposes, we first choose to only keep galaxies with absolute magnitude M_{K_s} in the K_s band less than or equal to -19. Since we will be interested in computing the 'stellar to (phantom) halo mass relation' in the MOND context and in assessing the gravitational environment of the Milky Way in order to produce a fiducial

mass model of our Galaxy in MOND, we also include galaxies with apparent magnitude in the K_s band less than or equal to 10 (in order to retain the smaller galaxies in the nearby environment). This gave us a sample of 206 objects, which are listed in the Appendix (Table 11.1). The stellar mass $m_\star$ in solar masses of a given galaxy was obtained from the following formula:

$$M_\star = 0.7 \times 10^{(3.27-M_{K_s})/2.5} \tag{3.11}$$

where 3.27 is the magnitude of the sun in the K_s band (Willmer, 2018), and we assume a 0.7 the mass-to-light ratio for the K_s band. Our 206 galaxies comprise more than 95% of the stellar mass of the whole UNGC. We show on Figure 3.2, as in Karachentsev & Telikova (2018), the mean stellar density Ω_* (where the value of the critical density of the Universe is again $\rho_{\rm crit} = 1.46 \times 10^2$ $M_\odot {\rm kpc}^{-3}$) of our sample of galaxies as a function of distance to the MW.

To compute the MONDian PDM, the whole baryonic mass of galaxies needs to be estimated. We again follow Papastergis et al. (2012) as in Eq (3.9) to estimate the hydrogen mass m_H for each system as a function of their stellar mass, and the gas mass via a multiplicative factor to account for helium: $M_{\rm gas} = 1.4 M_H$. Note that here we ignore the scatter of this relation, meaning that our results involving stellar and gas masses of individual galaxies will typically underestimate the scatter.

For computational reasons, each of the selected galaxies is added to the Newtonian potential as a point mass with total mass $M_* + M_{\rm gas}$, with the exception of the MW and M31 (and later on, NGC5055). M31 is modeled as an exponential disk based on Equation (2.154) of Binney & Tremaine (2008) with scale radius 5.9 kpc, and a Miyamoto-Nagai bulge (Miyamoto & Nagai, 1975), with density parameters adjusted for a total baryonic mass of 1.03×10^{11} $M_\odot$.

As a first step, the MW is modeled with a Miyamoto-Nagai bulge and disk with parameters from Table 3 of Irrgang et al. (2013) adjusted for a baryonic mass of 7.5×10^{10} $M_\odot$ of which 6.8×10^{10} $M_\odot$ is in the disk and 7×10^9 $M_\odot$ is in the bulge. We choose to adopt the above MW set-up for this first computation as it gives an analytical expression for the baryonic gravitational potential. However, we will then upgrade the model to a more realistic configuration in Section 3.4.

3.3.2 Phantom dark matter maps

Equipped with the theoretical tools and catalogue described in the previous sections, we can now use Equation (3.7) to compute the PDM density. The result of this first computation is showcased in Figure 3.3 for plane cuts of the MW disk plane (z=0) and the edge-on view (y=0). Interestingly, zones of negative PDM density are immediately apparent, mostly perpendicular, for each galaxy, to the direction of the Local Group, which is the dominant EFE source for most of the galaxies sampled. In addition to the plane cuts shown in Figure 3.3, we show in Figure 3.4 a capture of a 3D contour plot for the PDM density obtained by using the Mayavi Python package (Ramachandran & Varoquaux, 2011). The 3D visualization allows us to see the actual shape of the negative PDM zones due to the EFE without projection effects. Furthermore, it allows us to depict many more interactions than would appear on the 2D plane cuts.
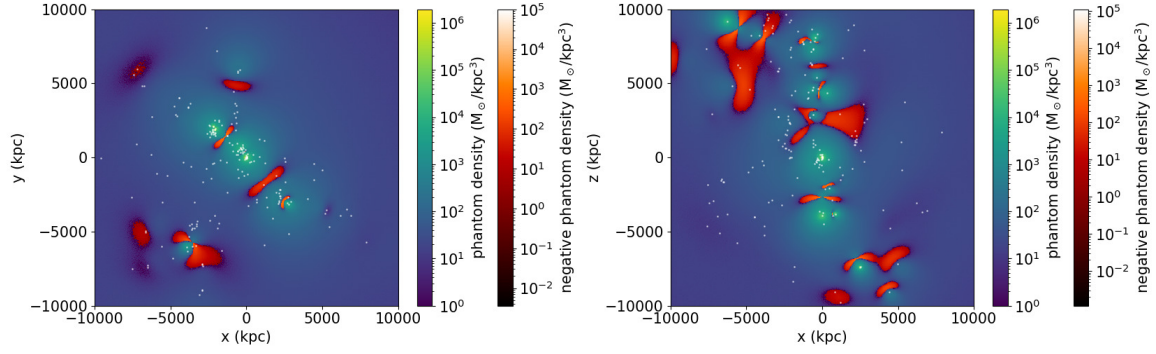
Figure 3.3: PDM density map of the Local Volume centred on the MW at the position $(x, y, z) = (0, 0, 0)$ kpc. Plane cuts. *Left panel:* MW galactic plane z=0. *Right panel:* MW edge-on view y=0. White dots are the projections on the respective planes of all the galaxies considered. M31 is at the position $(x, y, z) = (-383, 619, 286)$ kpc.

This first result however ignores the influence of larger scales on the Local Volume, which we will now add to highlight this peculiarity of MOND that larger scales can never be ignored when modelling small ones.

Adding galaxy clusters. The dominant EFE inside the Local Volume is indeed from the influence of sources located outside it, such as galaxy clusters and superclusters. To estimate their influence, we select the most important sources from Cosmicflows-3 (Tully et al., 2016) in terms of Newtonian gravitational field at the MW. Those sources located outside the Local Volume are included as point masses to the computation. The chosen sample can be found in Table 3.1. It has long been known that in the MOND context, the dynamics of galaxy clusters cannot be solely explained by their baryonic content, and an extra source of mass is required (e.g., Sanders, 1999; Angus et al., 2008). Various hypotheses have been proposed for this residual missing mass, including hot dark matter (Angus et al., 2010; Haslbauer et al., 2020), baryonic dark matter in the form of cold dense molecular clouds (Milgrom, 2008), and massive gravitating fields that give rise to MOND on small-scales but could behave as DM both on the scale of the CMB and on cluster scales (Skordis & Zlosnik, 2020). Here we thus estimate a MOND dynamical mass M_{MOND} for these clusters by assuming that at the virial radius, the ΛCDM and MOND acceleration should coincide. In our point mass approximation, this leads to

$$M_{\mathrm{MOND}} = \frac{GM_{\mathrm{CDM}}^2}{r_{200}^2 a_0} \tag{3.12}$$

where G is the gravitational constant and r_{200} is used as a substitute to the virial radius, and computed via[3]

$$r_{200} = \left(\frac{GM_{\mathrm{CDM}}}{100H_0^2} \right)^{1/3} \tag{3.13}$$

where H_0 is the Hubble constant. Table 3.1 then gives the Newtonian acceleration g_N generated by M_{MOND} of each cluster at their estimated r_{200}. Note however that this radius in principle does not play any specific role in the MOND context. Therefore, we checked that

---

[3]This is obtained by equalling $200\rho_{\mathrm{crit}} = 200 \times 3H_0^2/(8\pi G)$ to $\rho_{200} = 3M_{200}/(4\pi r_{200}^3)$.
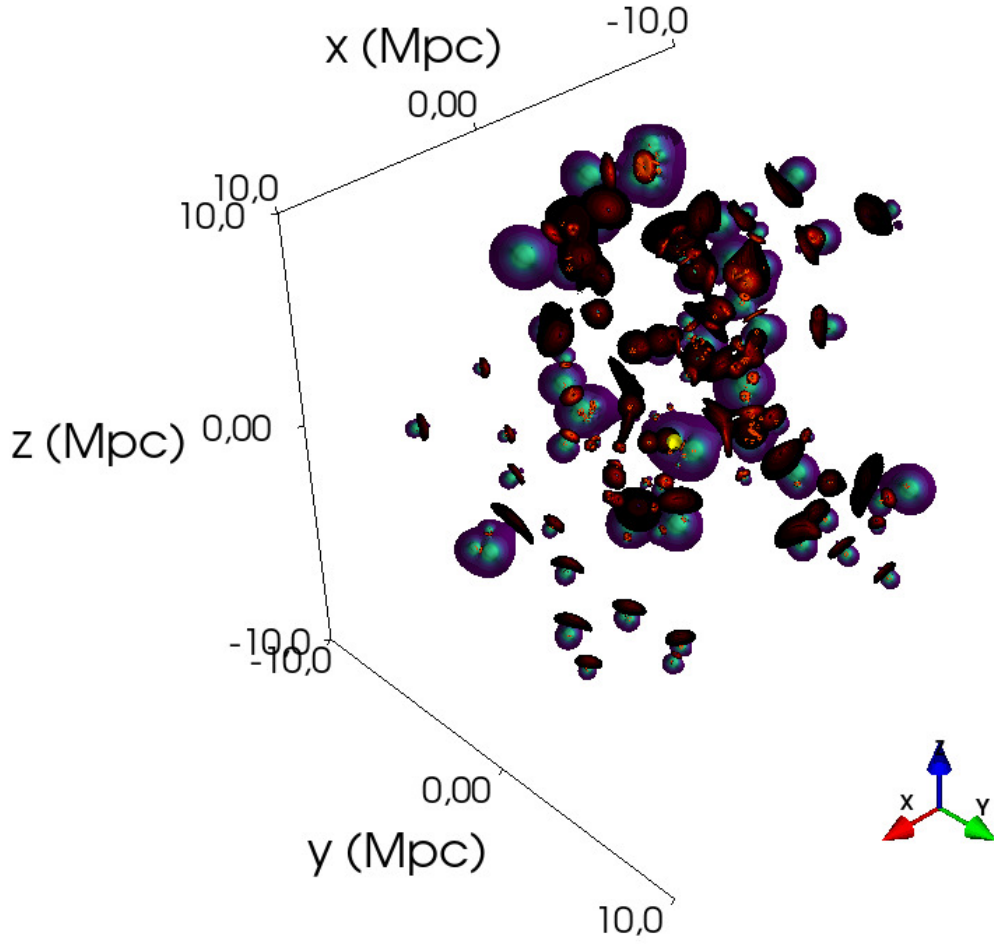
Figure 3.4: Capture of a 3D contour plot of the PDM density of the Local Volume using only the Local Universe sources of Table 11.1. The MW is the yellow ball at the center. The xy plane at $z = 0$ is the MW disk plane. Color bars are the same as in Figure 3.3.

our procedure yields a reasonable lower bound on M_{MOND} by converting full NFW enclosed mass profiles to $M_{\mathrm{MOND}}(r)$ profiles for the range of virial masses corresponding to the clusters considered here. These $M_{\mathrm{MOND}}(r)$ profiles typically reach a maximum value of M_{MOND}, which we find to be systematically only $5\%-15\%$ higher than our estimate of M_{MOND} at r_{200}. Our values of M_{MOND} estimated at r_{200} are therefore a reasonable (lower bound) estimate, and the high values we obtain show that it is very reasonable to assume that their enclosed mass should not be significantly altered itself by an EFE from large-scale structure. We also give in Table 3.1 the Newtonian acceleration g_N generated by each of these sources at the position of the MW. One can see that some clusters generate a Newtonian acceleration of several times $10^{-4}a_0$, whilst it had been estimated in Famaey et al. (2007) that the external field caused by the Great Attractor on the MW is of the order of $0.01a_0$, i.e. that the Newtonian gravitational field g_N of the Great Attractor at the position of the MW is of the order of $10^{-4}a_0$. Furthermore, we computed the Newtonian acceleration at the MW for all the sources in the MCXC (Piffaretti et al., 2011) catalog: while we cannot include the whole catalog for computational reasons, we found that all the top contributors (the Virgo, Perseus, Centaurus and Coma clusters) are already in our sample picked from Cosmicflows-3, and that the first source absent from our sample has a Newtonian gravitational field one order of magnitude below that of Virgo.

With those new contributions, the PDM landscape changes drastically as can be seen on the plane cuts on Figure 3.5, or the 3D visualization in Figure 3.6. In this configuration, the Virgo supercluster, of which we place the centre at the position (375,2260,17600) kpc, is the dominant EFE source and thus all negative zones of PDM are perpendicular to its direction. Furthermore, this influence brings much less diversity as a lot of galaxy-galaxy interactions between sources in the Local Volume observed on Figure 3.3 and Figure 3.4 are smoothed away. Due to a stronger EFE, PDM halos do not extend as far as in the previous case and are less massive, a point we inspect further in the next subsection.

Let us note here that modeling things this way leads us to having galaxy clusters as the only sources of gravity outside the Local Volume. This could certainly be an issue at the scale of the most distant clusters, in terms of average density in particular, because underdensities are *de facto* neglected: these could lower the EFE strength and change its direction. However, with Virgo being by far the dominating source of EFE for the Local Volume, and with it being so close (17.8 Mpc), our assumptions should cause no issue at the scale of the Local Volume.

Finally, as an interesting alternative possibility (if we imagine for instance that the residual missing mass in MONDian clusters does not contribute to the EFE), we show the same computation when only the baryonic mass from clusters is taken into account in the Appendix (Figure 3.16). The EFE from distant sources still dominates in this case, albeit less overwhelmingly.

3.3.3 SHMR

When a galaxy is embedded in an external field, its total PDM mass is finite. If the external field is constant over the size of the galaxy, the total mass is given by equation (57) of Milgrom (2010). However, this does not compare well to the virial mass of DM halos, usually defined at r_{200}. Wu & Kroupa (2015) have computed a SHMR for MOND, both
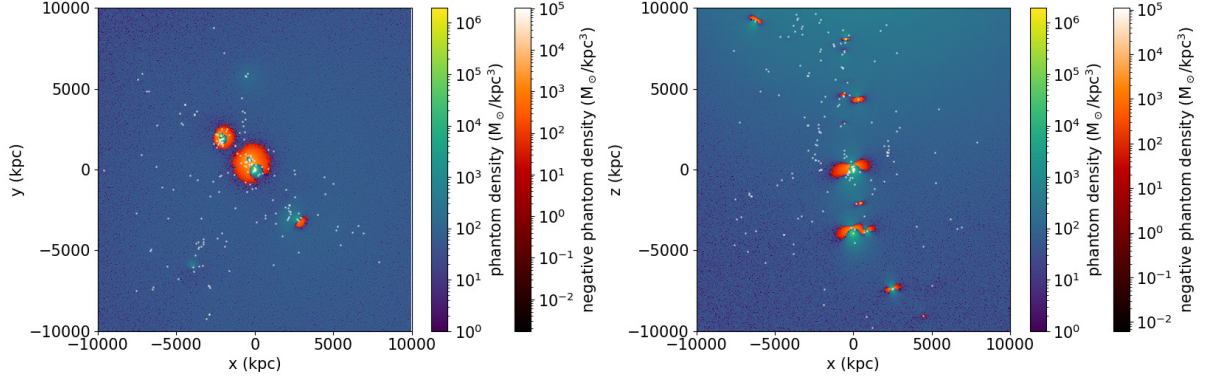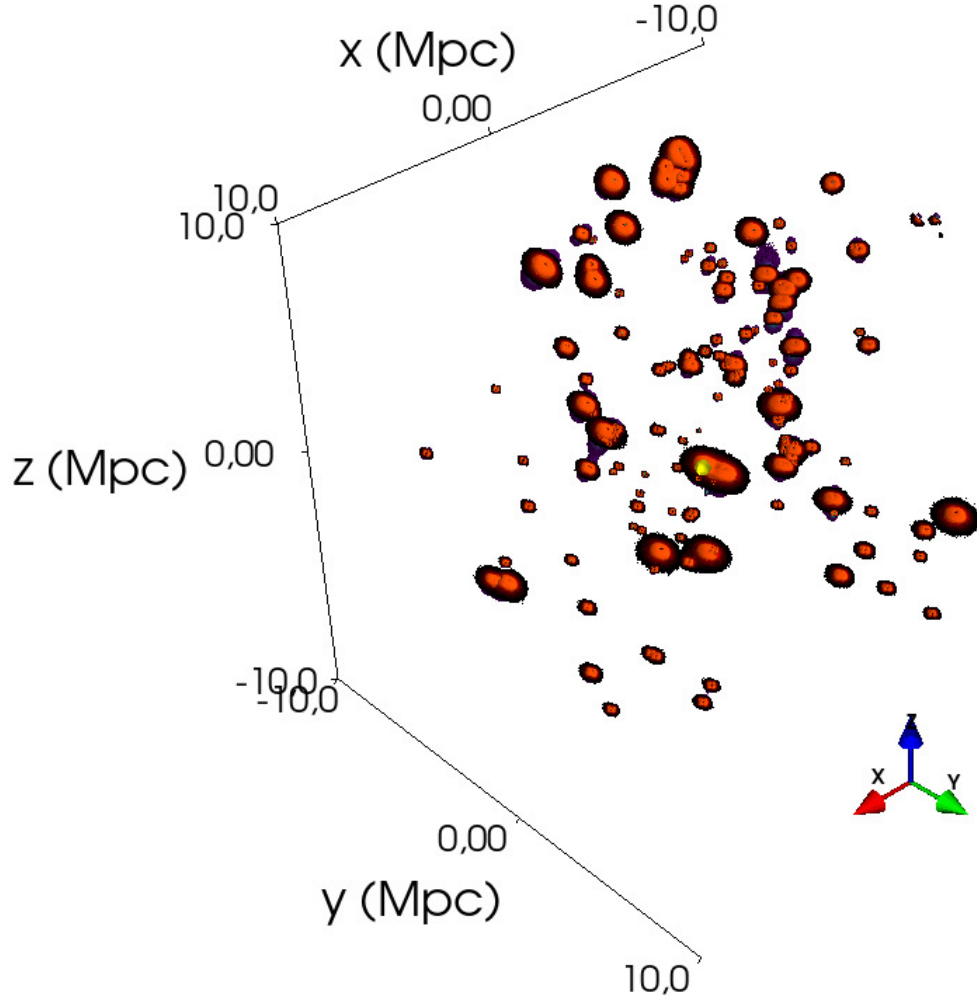
Figure 3.5: PDM density map of the Local Volume centred on the MW at the position $(x, y, z) = (0, 0, 0)$ kpc when massive distant sources are added. Plane cuts. *Left panel:* MW galactic plane z=0. *Right panel:* MW edge-on view y=0. White dots are the projections on the respective planes of all the galaxies considered. M31 is at the position $(x, y, z) = (-383, 619, 286)$ kpc. The Virgo supercluster, source of the dominating EFE in the Local Universe, is at the position $(x, y, z) = (0.38, 2.26, 17.60)$ Mpc.

isolated and with EFE, using analytical formulas, and predict truncation radii in PDM halos due to the EFE, leading to less enclosed mass. We will also derive a SHMR based on our sample, but our computation herafter will be purely numerical.

In order to compute the individual PDM mass within r_{200} for galaxies in our sample, we make a zoomed computation of the PDM density around each galaxy with resolution 1 kpc by growing a sphere around it until a mean density of $200\rho_{\rm crit}$ is reached. The result can be found in the Appendix (Table 11.1). Some galaxies too embedded into the halo of another neighbouring galaxy for it to make sense to compute their PDM mass were excluded from the computation. This includes mostly small satellite galaxies of massive hosts, but also some close systems such as M81 and M82. For this computation, the EFE from the distant sources of Table 3.1 is correctly taken into account.

Figure 3.7 now shows the MOND "stellar-to-PDM" relation where each galaxy of our catalogue is represented by a dot coloured according to the Newtonian external gravitational acceleration g_{Ne} at their location, and a lower limit can be found as the red curve representing the isolated MOND situation as in Subsection 3.2.2. The broad range of external gravitational accelerations for different galaxies has two effects compared to the isolated MOND case: (i) it induces a PDM mass loss in galaxies, with the effect being more pronounced in the less massive ones, and (ii) it creates some scatter for a given stellar mass, as can be seen by the vertical gradient in colour representing g_{Ne}. Globally, the shape of the SHMR is well represented by a single power-law (hence a straight line in log-log) with scatter 0.14 dex. Note that, since we neglected in this case the scatter on the stellar-to-gas mass relation, the true scatter should be larger. The single power-law behaviour is similar to the behaviour of the SHMR that has been found for disk galaxies in the ΛCDM context, in disagreement with abundance matching expectations (e.g. Posti et al., 2019a,b), and has been attributed to a morphologically-dependent SHMR by Posti & Fall (2021). However, in the MOND context, morphology should (in principle) play no role in the shape of the SHMR, so the

Figure 3.6: Capture of a 3D contour plot of the PDM density of the Local Volume when distant clusters from Table 3.1 are taken into account. The MW is the yellow ball at the center. The xy plane at $z = 0$ is the MW disk plane. Color bars are the same as in Figure 3.5. Because of projection effects, and because halos have less PDM at a given radius compared to the previous case due to the stronger EFE, we see almost exclusively negative PDM zones on this capture (oriented towards Virgo, located at $(x, y, z) = (0.38, 2.26, 17.60)$ Mpc).
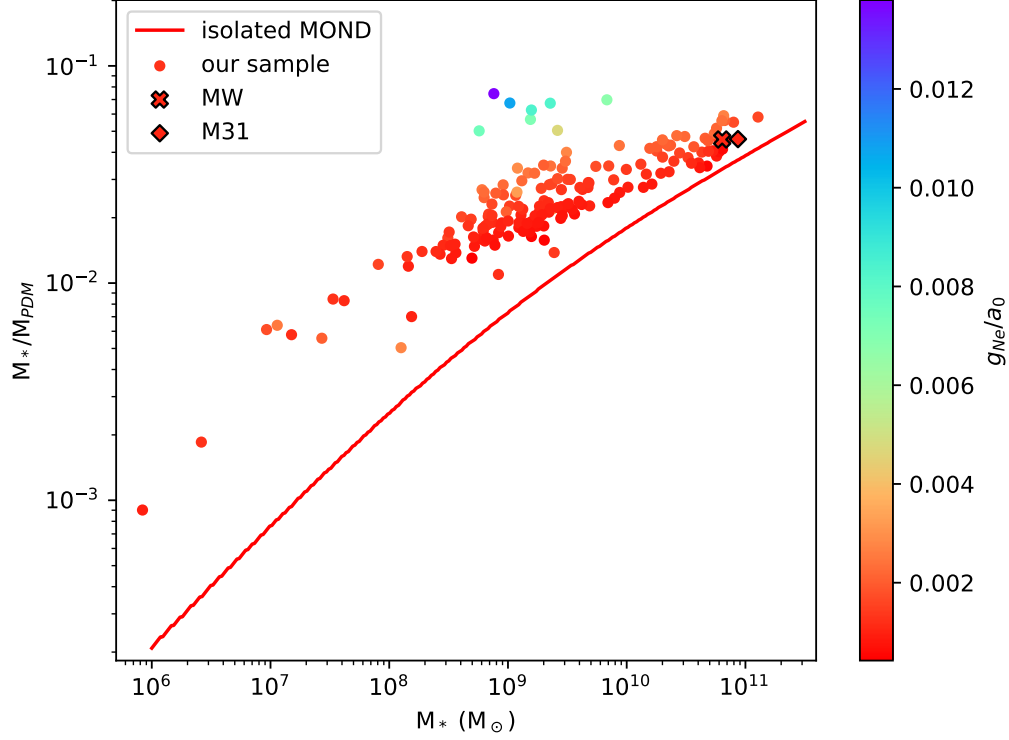
Figure 3.7: Stellar mass over PDM mass (at a computed r_{200}) as a function of stellar mass. Each coloured dot is a galaxy from Table 11.1. The color bar indicates the Newtonian external gravitational acceleration g_{Ne} at the location of each galaxy in units of a_0. The MW is represented by a cross and M31 by a diamond. The red curve is the analytically computed PDM mass at r_{200} for the isolated MOND case. We notice as expected because of the EFE a vertical gradient in terms of g_{Ne}, explaining the scatter at a given stellar mass.
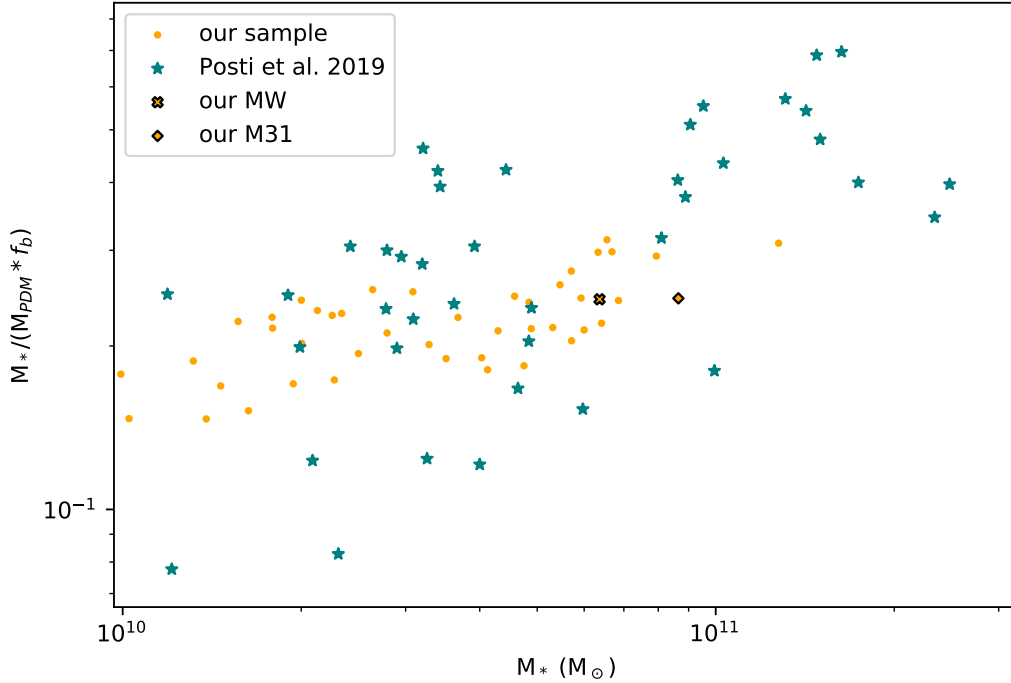
Figure 3.8: Stellar mass over PDM mass (at a computed r_{200}) divided by the cosmological baryon fraction $f_b = 0.188$ as a function of stellar mass. Zoom on the most massive galaxies. Each orange dot is a galaxy from Table 11.1. The MW and M31 from our computation are respectively the cross and the diamond. Star symbols represent fits of Posti et al. (2019a), in which a halo mass is estimated in the ΛCDM context for SPARC galaxies (Lelli et al., 2016a).

only explanation in this case would be an environmental one, either through varying degrees of EFE, or with a higher mass discrepancy for early-type galaxies residing in groups and clusters. Concerning massive late-type galaxies, we show as an illustration in Figure 3.8 a zoom on our MONDian SHMR for galaxies with stellar mass greater than 10^{10} M$_\odot$, where a tension with abundance matching was found in the standard context, and we compare them with data from Figure 2 of Posti et al. (2019a). The global agreement is striking.

We also find that both the MW and M31 have a dynamical mass below what is expected from a ΛCDM stellar-to-halo mass relation, in agreement with McGaugh & van Dokkum (2021). Indeed, we find PDM halo masses at r_{200} of 1.39×10^{12} M$_\odot$ for the MW and 1.88×10^{12} M$_\odot$ for M31, while abundance matching instead predicts a halo mass of approximately 2.5×10^{12} M$_\odot$ for our stellar mass of the MW (6.37×10^{10} M$_\odot$) and approximately 6×10^{12} M$_\odot$ for our stellar mass of M31 (8.65×10^{10} M$_\odot$), as can be seen on Figure 1 of McGaugh & van Dokkum (2021).

Finally, we explore again the question of the gas-to-halo mass relation in the case of an EFE, which was found to be flat in the isolated MOND case. On Figure 3.9, we update this figure by using as a lower limit the isolated MOND computation of Subsection 3.2.2 combined with the lowest possible gas mass from Eq (3.9), and as an upper limit, the PDM mass at r_{200} of test galaxies of a range of stellar masses and the highest possible corresponding gas
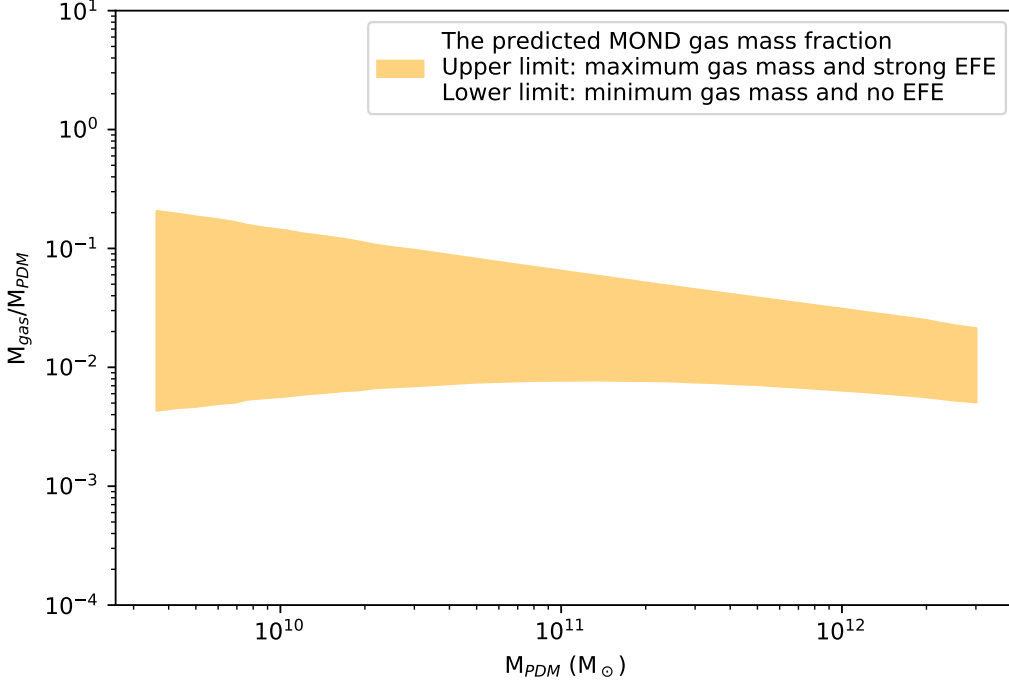
Figure 3.9: Gas mass over PDM mass (at a computed r_{200}) as a function of PDM mass. The shaded area represents the expected values, with the isolated MOND case combined with the lowest gas mass estimation from Eq (3.9) as a lower limit, and a strong EFE induced by a $g_{Ne} = 0.02\ a_0$ combined with the highest gas mass estimation from Eq (3.9) as the upper limit. The gas-to-halo mass relation predicted by MOND remains flat.

mass from Eq (3.9), under a $g_{Ne} = 0.02\ a_0$ EFE, which is the typical maximum EFE that can be reached in the volume occupied by the SPARC (Lelli et al., 2016a) galaxies, larger than the maximum EFE in the Local Volume. As can be seen on this figure, the inclusion of the EFE has strongly increased the scatter of the gas-to-halo mass relation predicted by MOND, but the overall shape remains very flat.

3.3.4 The average PDM density in the Local Volume

Karachentsev & Telikova (2018) find, in the context of ΛCDM, a total mass of 10^{14} M$_\odot$ for the volume enclosed in a sphere of radius 11 Mpc centred on the MW. For this, they simply add the halo masses expected from the SHMR around all galaxies of the UNGC catalog. On Figure 3.2, we add on the plot the mean PDM density as a function of distance to the MW for our sample of galaxies (orange curve). We then extrapolate this to the whole UNGC (black curve) by using a linear fit to the SHMR of Figure 3.7 to obtain the PDM mass at r_{200} as a function of stellar mass of the rest of the galaxies in the catalogue. Note that this indirectly includes a gas component since the PDM mass of the galaxies in our sample was computed with an added gas mass to the stellar mass. The difference in $\Omega_{\rm pdm}$ between our sample and the extrapolation to the whole UNGC is slim, showing that the galaxies we did not select do not contribute much mass to the Local Volume. For our 206 galaxies in MOND,

we find a total mass of 5.74×10^{13} M$_\odot$ for PDM and of 6×10^{13} M$_\odot$ when including baryons, corresponding to a mean PDM density (in galaxies only) $\Omega_{\mathrm{pdm}} = 0.07$. By extrapolating our SHMR of the previous subsection, knowing that it overestimates the PDM masses of galaxies which would reside in high external field environments for which no PDM mass was computed, we find an upper limit to the PDM mass enclosed in galaxies of the Local Volume, $\Omega_{\mathrm{pdm}} = 0.078$, hence much lower than the average CDM density in a ΛCDM Universe but close to the $\Omega_{DM} \approx 0.1$ corresponding to the mass of 10^{14} M$_\odot$ deduced by Karachentsev & Telikova (2018).

3.4 A fiducial MOND model for the Milky Way in its environment

This model of the Local Volume offers us a unique opportunity to produce a fiducial MOND model of the Milky Way when actually embedded in its gravitational environment.

Solving the QUMOND Poisson equation in (3.5) with appropriate boundary conditions gives us the MOND potential. We do it here for a cube of 1 Mpc side length centered on the MW, comprising 500 identical cells inc each dimension, for a resolution of 2 kpc. Our Poisson solver is based on a Gauss-Seidel iterative process with acceleration by over relaxation (which introduces a relaxation parameter, making the Gauss-Seidel iterative process converge faster). It operates on a grid with cells of identical size (no adaptive refinement) and gives a gravitational potential value for each vertex.

3.4.1 Computing the PDM density

The first step towards solving the QUMOND Poisson equation is to solve the baryonic Poisson equation $\Delta\Phi_b = 4\pi G\rho_b$ to obtain the baryonic potential Φ_b of the MW, since we do not use an analytical potential. For this computation, the MW is modeled as an exponential disk galaxy following Section 2.7 of Binney & Tremaine (2008), i.e. with density profiles for a bulge component, for a thin and a thick disk, and for a gas corona. We switch from the less realistic Miyamoto-Nagai profile of Subsection 3.3.1 since an analytical formula is not required anymore. The disks have a scale length of 2 kpc, and scale heights of 0.3 kpc and 1 kpc for the thin and thick disks respectively. The gas corona has a scale radius of 4 kpc, and a hole of 4 kpc radius at its center. The density parameters have been chosen to numerically give a total baryonic mass of 7.5×10^{10} M$_\odot$ for the MW, of which 6.8×10^{10} M$_\odot$ is in the disk (including 1.13×10^{10} M$_\odot$ in gas), and 7×10^9 M$_\odot$ is in the bulge. The boundary condition used for the baryonic Poisson equation is $-GM_b/r$ where G is the gravitational constant, M_b is the baryonic mass of the MW, and r is the distance from the MW.

The second step towards solving the QUMOND Poisson equation is to compute the PDM density ρ_{PDM}, which is done using Equation (3.7) as in Subsection 3.2.1. The Newtonian potential Φ_N used for this computation includes the baryonic potential of the MW obtained from the previous Poisson integration above, as well as the baryonic potential of all the sources used for the PDM density computation in Section 3.3, i.e. M31, plus all the Local Volume galaxies of Table 11.1, and all the external sources from Table 3.1. The result can be seen on Figure 3.10. The most notable features are the negative PDM areas. The large composite negative PDM area on the xy plane is the consequence of the EFE from M31 (at the position $(x, y, z) = (-383, 619, -286)$ kpc) and the EFE from the Virgo supercluster (at

the position $(x, y, z) = (0.38, 2.26, 17.60)$ Mpc); the one on the xz plane above the MW is the consequence of the EFE from the Virgo supercluster. We note that those negative PDM areas, which arise when the internal and external gravitational accelerations are comparable, are far from the center of the MW. It would be extremely interesting to be able to probe precisely those very outer regions of the stellar halo near the virial radius of the PDM halo, or to analyze the behaviour of what remains of the hot gas corona in these outer regions.
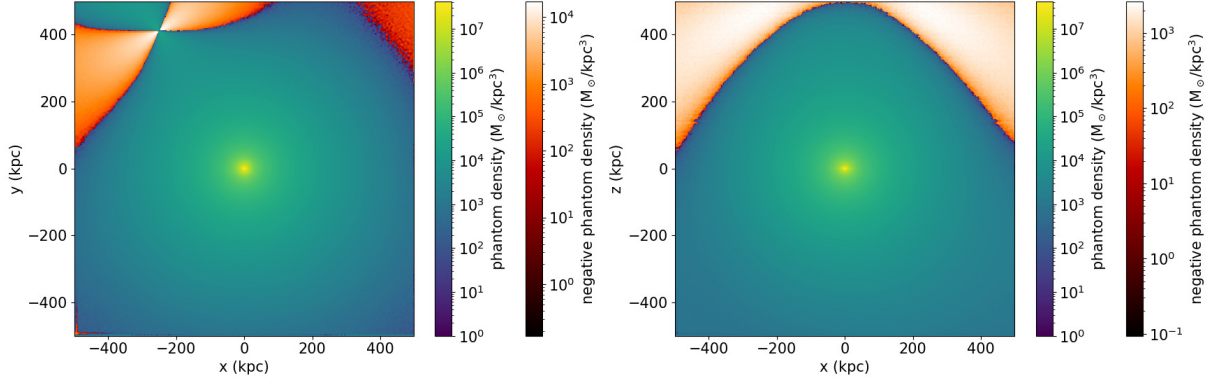
Figure 3.10: Phantom dark matter density map around the MW. Plane cuts. *Left panel:* galactic plane z=0. Zones of negative PDM density due to M31 at the position $(x, y, z) = (-383, 619, -286)$ kpc (top-left corner) and Virgo at the position $(x, y, z) = (0.38, 2.26, 17.60)$ Mpc (top-right corner). *Right panel:* edge-on view y=0. Zone of negative PDM density due to Virgo.

Before computing the MOND potential, we run a PDM density computation of the same volume without including the baryonic potentials of the MW and the LMC in order to obtain the background information. The PDM density from this background is subtracted from the full PDM density. This allows us to isolate the PDM from the MW and from the LMC while still taking into account the background field they are in. Note that this is not a perfect solution: negative PDM areas will be exacerbated by this process because we will take away from them some positive background PDM (since without the MW and the LMC, there is no negative PDM in the same area). We found however that it is a reasonable solution to a problem that is hard to solve because of its non-linearity.

This special treatment of the LMC is justified by its importance in the MW system. It would not make much sense to try to estimate its current PDM mass as it is now embedded in the halo of the MW and under a very strong EFE caused by its host. However, from its stellar mass of 1.78×10^9 M$_\odot$ (derived from the UNGC and our process of Subsection 3.3.1), we can estimate its PDM mass prior to its infall into the MW. In the isolated MOND case, we can use Eq (3.10), giving a PDM mass of 1.95×10^{11} M$_\odot$. More realistically, using an extrapolation of our SHMR of Subsection 3.3.3 and thus taking into account the EFE on the Local Universe, we find a PDM mass of 8.14×10^{10} M$_\odot$ prior to infall. Such a high PDM mass should have a noticeable effect in the response of the stellar halo of the MW to the LMC infall (Garavito-Camargo et al., 2019, see e.g.), in addition to creating interesting negative PDM density zones at infall. Studying the detailed response of the stellar halo of the MW to the LMC infall in MOND will be the topic of further work, using the fiducial model of the

MW presented here as a backbone.

3.4.2 Computing the MOND potential of the Milky Way

Equation (3.5) is solved with source terms ρ_b being the sum of all the baryonic density profiles for the MW described in Subsection 3.4.1, ρ_{PDM} being the PDM density for the MW obtained after the background substraction described in Subsection 3.4.1, and with boundary condition $-GM/r$ where M is the sum of the baryonic and PDM masses for the MW obtained by numerical integration of the density in our 1 Mpc side-length box. As expected from the PDM density plot of Figure 3.10, no strong asymmetry is noticeable in the derived QUMOND potential, a sign that the MW is not under a strong EFE.

The escape speed v_{esc} for the MW is computed from the MOND potential Φ via the following formula:

$$v_{esc} = \sqrt{2(\Phi_\infty - \Phi)} \tag{3.14}$$

where Φ_∞ is the weakest potential in our volume. The result of this computation can be seen in Figure 3.11. A zoom on the inner 20 kpc can be seen on the right panel, showing a reasonable agreement with the data from Monari et al. (2018). This is in line with our PDM halo mass of 1.39×10^{12} M$_\odot$, similar to the estimate of the total mass by Monari et al. (2018). Furthermore, we compute the rotation curves for the MW in the isolated MOND and EFE cases. The acceleration g is extracted by taking the norm of the gradient of the MOND gravitational potential. Then, the mean acceleration $g(r)$ at each radius r is computed. The circular velocity v_{rot} at a radius r is obtained via

$$v_{rot}(r) = \sqrt{g(r)r}. \tag{3.15}$$

The result can be seen on the left panel of Figure 3.11. The change in curvature induced by the EFE on the blue curve happens between 150 and 200 kpc and separates it from its asymptotically flat isolated MOND counterpart (red curve). As a comparison to observations, we add data points from Xue et al. (2008) and Huang et al. (2016). In Subsection 3.5.1, we take a look at this effect on the rotation curve in a more drastic case, with a less massive galaxy under a stronger EFE.

3.5 Dynamical and lensing signatures in galaxies under a strong EFE

3.5.1 NGC 5055: an archetypical galaxy under a strong EFE

In a recent study, Chae et al. (2020) have found that galaxy rotation curves in the SPARC database (Lelli et al., 2016a) were significantly better fitted in MOND when including a contribution from the EFE, which affects the few outermost observed datapoints. While a few extreme cases indicated that a stronger EFE was needed in gravitational environments that are effectively stronger, the global correlation was still weak. This might be because it is difficult to translate the large-scale gravitational accelerations expected in a ΛCDM Universe into those expected in a MOND Universe. Therefore, using the QUMOND formulation would
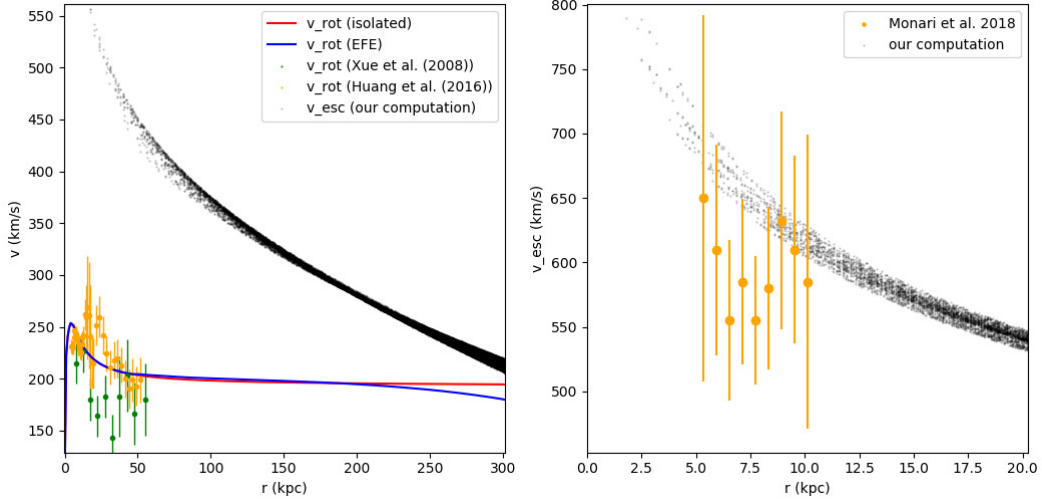
Figure 3.11: *Left panel:* Escape speed and circular velocity as a function of radius for the MW in QUMOND. Black dots are our escape speed computation. The vertical scatter, more pronounced after 200 kpc, is a consequence of the EFE. The red curve is the rotation curve in the case of isolated MOND, and the blue curve is the rotation curve with EFE. Green points are from Xue et al. (2008) and orange points are from Huang et al. (2016). *Right panel:* Zoom on the inner 20 kpc for the escape speed computation. The bigger orange dots are data points from Monari et al. (2018).

certainly allow to probe more clearly the possible correlation between the EFE needed to fit galaxy rotation curves and the true EFE in which galaxies reside.

In our sample, NGC5055 is a galaxy in the strong gravitational influence of the Virgo supercluster with $g_{Ne} = 2.7 \times 10^{-3} \, a_0$ at its location, and it is also present in the SPARC database. It therefore represents an interesting archetypical galaxy residing in a strong external field.

We compute and compare the rotation curve of NGC5055 both for the MOND isolated case, and for the case where all the Local Volume sources from Table 11.1 and external sources from Table 3.1 are included and cause an EFE. In our Local Volume cube, NGC5055 lies 8.99 Mpc away from the MW at the position $(-670, 2340, 8654)$ kpc. Among our selected galaxies, it is one of the closest to the Virgo supercluster, and thus one of the most affected by the EFE coming from it.

The galaxy is modeled using an exponential disk profile with an effective radius of 4.18 kpc, a disk scale length of 3.2 kpc, and a baryonic mass of 5.48×10^{10} M$_\odot$. Note that this is a mass close to that of the best fitting model of Chae et al. (2020) which we use here for the sake of comparison, although their mass is a bit lower than the mass we obtain via the process detailed in Subsection 3.3.1. This way, the model chosen here is in principle guaranteed to give a good representation of the data.

In order to recover the MOND potential in the case where all sources are included, a first integration of Equation (3.5) is done in a cube of 1 Mpc side length centred on NGC5055 with a resolution of 2 kpc. The boundary condition is $-GM/r$ where G is the gravitational constant, M is the sum of the baryonic and PDM masses for NGC5055, and r is the distance

to NGC5055. The computed PDM mass in this volume is 1.43×10^{12} M$_\odot$. Then a refined integration of Equation (3.5) is done in a smaller cube of 400 kpc side length with a resolution of 800 pc, with boundary condition extracted from the bigger cube. The computed PDM mass in this volume is 9.08×10^{11} M$_\odot$. The resulting potential can be seen in Figure 3.12. The asymmetry caused by the strong EFE can be seen on the xz plane cut. This potential in the shape of an egg oriented in the direction of the dominating EFE is typical, and already showcased in e.g. Thomas et al. (2017, 2018) for the case of a satellite under the EFE of its host. Similarly, lopsidedness of the potential has been investigated by Wu et al. (2017) in the case of galaxies in clusters. The effect is however mild, and it is therefore not clear that a direct dynamical detection of this asymmetric potential would ever be possible for such a disk galaxy residing in a strong EFE. Dynamically, the best we can probably hope to achieve is the Keplerian decline of the rotation curve associated to the EFE. With this in mind, we will now study in detail a new formula proposed in Freundlich et al. (2022) and compare it to our exact QUMOND calculations.

The rotation curves, computed as described in Subsection 3.4.2, are presented in Figure 3.13. The red and blue curves, respectively of the isolated and EFE cases, are extremely close up to a radius of approximately 55 kpc where a change of slope is noticeable, with the red curve of the isolated case staying more or less flat while the EFE kicks in and brings the blue curve down.

We note that the rotation curve with EFE is very well fit by the formula proposed by Freundlich et al. (2022), approximating the average radial acceleration $g_r(r)$ over a sphere at a given radius r in a constant external field :

$$
g_r(r) = \begin{cases} \nu\left(\dfrac{g_{Ni}(r) + \frac{g_{Ne}^2}{3g_{Ni}(r)}}{a_0}\right) g_{Ni}(r), & \text{if } g_{Ni}(r) \geq g_{Ne} \\[20pt] \nu\left(\dfrac{g_{Ne} + \frac{g_{Ni}(r)^2}{3g_{Ne}}}{a_0}\right) g_{Ni(r)}, & \text{if } g_{Ne} \geq g_{Ni}(r) \end{cases}
\tag{3.16}
$$

where ν is the transition function of Eq (3.4), $g_{Ni}(r)$ is the Newtonian internal acceleration at radius r from the baryonic profile of the system studied, and g_{Ne} is the (constant) Newtonian external acceleration. The rotation curve obtained from this formula when applied to NGC5055 with our parameters is the yellow dashed curve on Figure 3.13, with the difference relative to the EFE curve being shown in the inset panel. The description provided by this formula is impressive, and only starts noticeably departing from the numerically computed EFE curve at a radius of approximately 80 kpc, where it starts to underestimate the EFE. We thus advocate to use this formula in future studies of the EFE in a QUMOND context.

3.5.2 The concave-lens signature of the negative PDM zones

We have seen that the gravitational potential of a galaxy like NGC5055 under a strong EFE does display an egg-shaped asymmetry. It is however not clear that it would be easily detectable dynamically, and does not in itself represent a smoking gun of negative PDM zones. A perhaps better indicator could however be obtained via gravitational lensing from a large amount of such galaxies located in strong gravitational field environments.
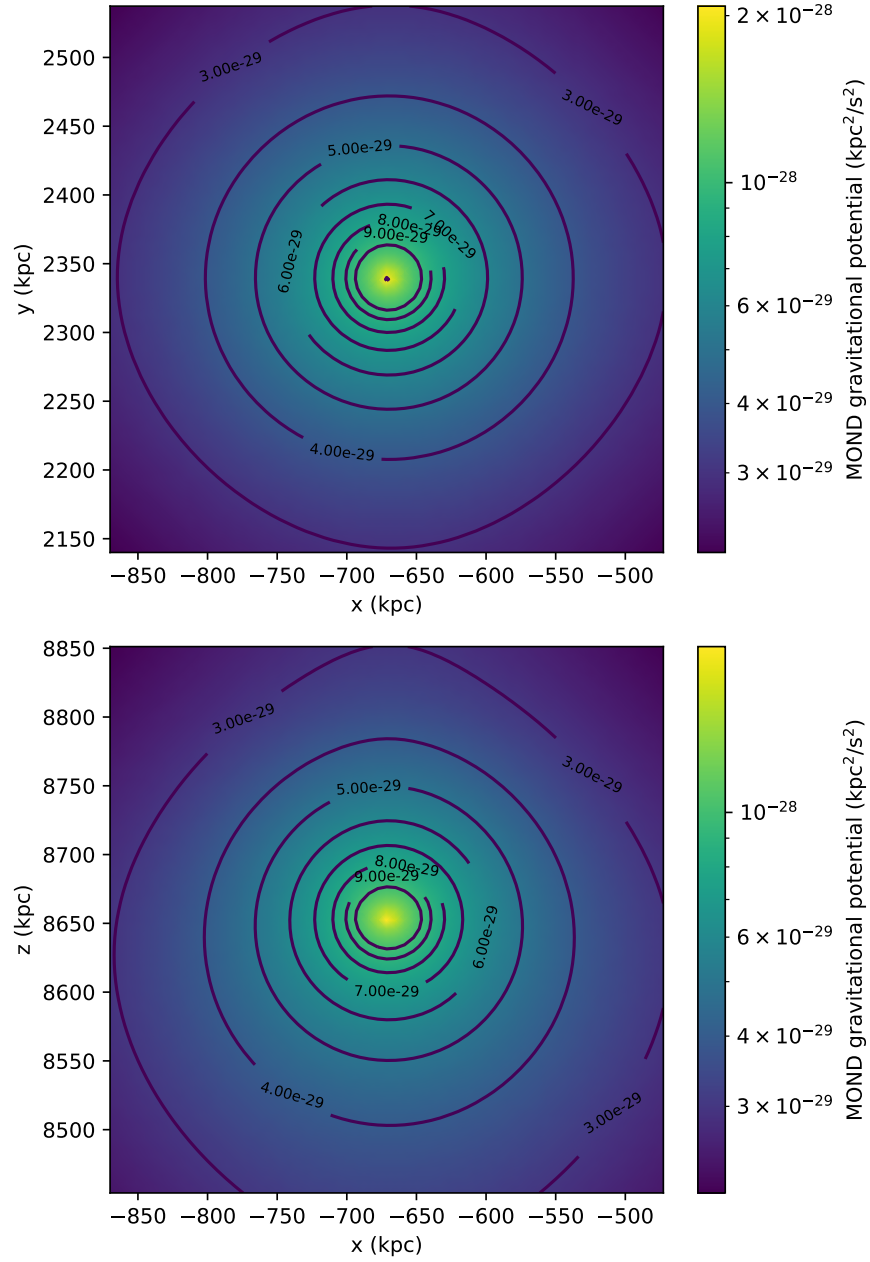
Figure 3.12: QUMOND gravitational potential of NGC5055 in the case of an EFE, with the egg-shaped contours visible. Plane cuts. *Top panel:* galactic plane z=0. *Bottom panel:* edge-on view y=0. The values on the axes are still centered on the MW position.
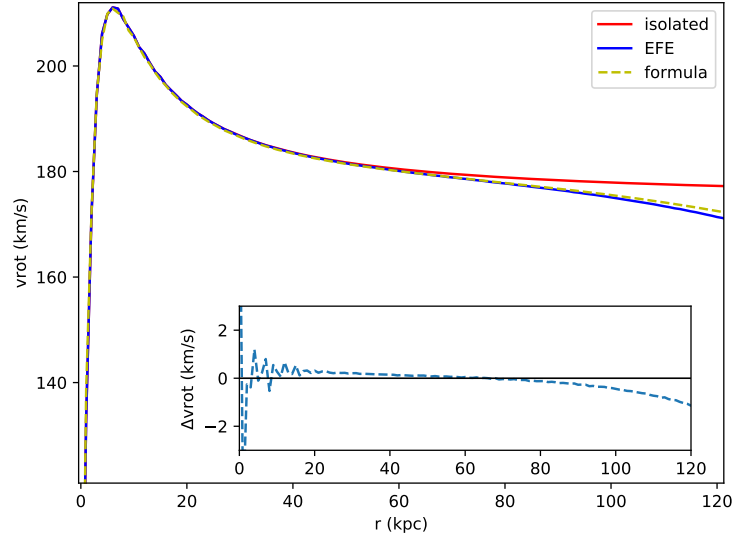
Figure 3.13: Computed rotation curves for NGC5055 with or without external field effect. The isolated MOND case is in red; the EFE case with all the sources from Table 11.1 and Table 3.1 is in blue; the yellow dashed curve is the one given by the analytical formula of Eq (3.16). *Inset panel:* difference between the blue curve of the EFE case and the yellow dashed curve of the analytical formula of Eq (3.16).

In order to investigate this, we computed the surface density of NGC5055 seen from various angles, which we show can be negative due to the EFE induced by the Virgo supercluster. This is possible if we look at the galaxy edge-on (i.e., observing it perpendicular the the EFE direction) but not face on (i.e., observing it along the EFE direction), in which case the PDM halo largely outweighs the negative PDM density. We then artificially place this system at a redshift $z = 0.3$ and see if it can act as a concave diverging lens for sources at $z = 5$. We compute the convergence parameter

$$\kappa = \frac{1}{2}\nabla^2\Upsilon \tag{3.17}$$

where Υ is the deflection potential, directly linked to the surface density and the distances of the lens and the source, as in Famaey & McGaugh (2012, equation 110). The result of this computation can be seen in Figure 3.14. The convergence parameter κ reaches negative values of the order of -10^{-3} in this case. This plot also highlights the double-bottleneck shape of PDM around the negative area which could already be noticed on the 3D plots (Figure 3.4, Figure 3.6).

Keeping the same distances for lens and source, we also considered a more extreme theoretical case of a galaxy of baryonic mass 5×10^{10} M$_\odot$ under an EFE of $g_{Ne} = 0.02\ a_0$, a high value that we already used in Subsection 3.3.3 as an upper limit. We find in this configuration that the convergence parameter κ can reach negative values of -3×10^{-3}. The phenomenon of lensing with negative convergence parameter has already been studied in e.g. Izumi et al. (2013) and Nakajima et al. (2014), where it was argued that it should produce radially distorted images.
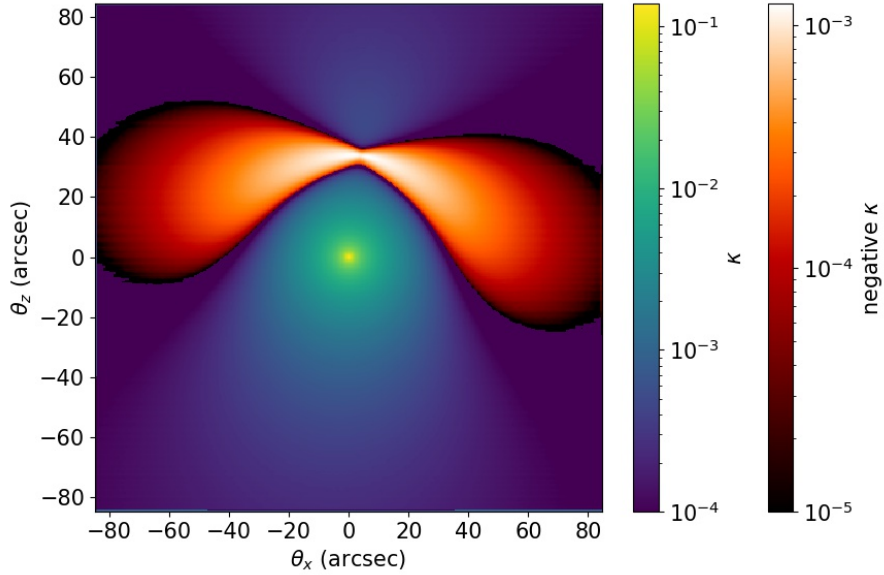
Figure 3.14: Convergence parameter κ for an NGC5055-like galaxy centred at $\theta_x = \theta_z = 0$ under the EFE of Virgo as in our study, seen edge-on, used as a gravitational lens placed at $z = 0.3$ for sources at $z = 5$.

Here, from the convergence parameter, we compute the shear $\gamma = \gamma_1 + i\gamma_2$ as in Hoekstra (2013, Eq. 13), and plot the resulting shear amplitude $|\gamma| = \sqrt{\gamma_1^2 + \gamma_2^2}$ and shear angle $\text{Arg}(\gamma)$ in Figure 3.15. We observe a strong asymmetry on the shear amplitude following the NGC5055-Virgo axis, with a feature around $(\theta_x = 0, \theta_z = 40)$ arcsec, the position (when placing the galaxy at $z = 0.3$) of the peak intensity of the negative PDM caused by the EFE. Perhaps more strikingly, the shear angle map is heavily distorted at this same position around $(\theta_x = 0, \theta_z = 40)$ arcsec. As a means of comparison, we plot in Figure 3.17 (Appendix) the shear map for the same configuration but in the isolated MOND case (i.e. no EFE).

Such a negative PDM zone signature cannot in principle be distinguished from the effect of a prominent underdensity in the standard context, but a statistical analysis correlating them with the direction of the expected EFE would be a smoking gun for MOND. This is something that could potentially be detected only statistically in weak galaxy-galaxy lensing. Stacking lenses that are in strong EFE environments near large scale structures or galaxy clusters could perhaps allow such a detection: the correlation of the location of the drop in κ with the large-scale environment would be the key. We leave it to further work to develop mock catalogues of negative convergence maps expected in MOND, their associated shear, and whether this could be observable with future space missions dedicated to weak-lensing studies.

3.6 Conclusion

In this contribution we developed a grid-based potential solver for the quasi-linear formulation of MOND, in order to explore how the potentials of galaxies in the Local Volume out to ~ 10 Mpc in Milgromian dynamics are affected by other mass concentrations in the
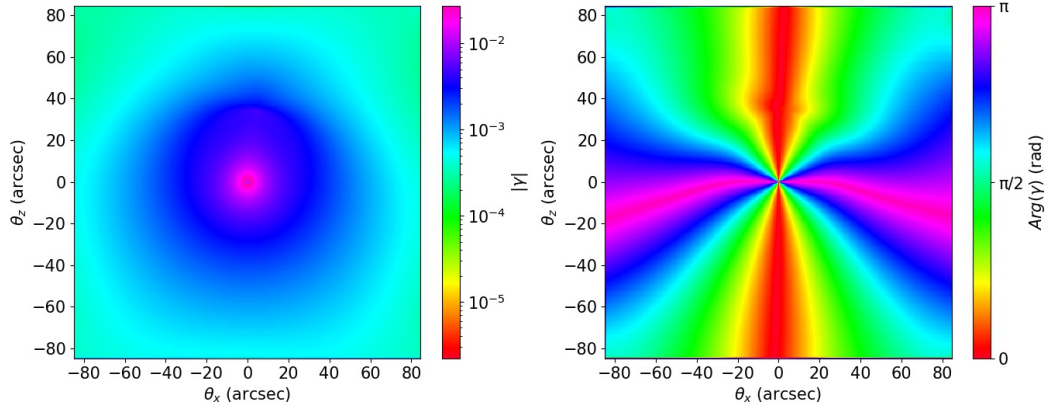
Figure 3.15: Shear vector γ corresponding to the convergence map of Fig. 3.14. *Left panel:* shear amplitude $|\gamma|$. *Right panel:* shear angle $\mathrm{Arg}(\gamma)$.

nearby Universe. We solve for the PDM halo in MOND, which in this theory is a convenient abstraction to allow one to readily derive accelerations by using the Newtonian formula. The corresponding 'phantom' density (PDM) distribution then appears similar to a ΛCDM dark matter halo, although with the striking difference that it may also display regions of negative density.

The concept of PDM is particularly useful as it allows to re-express some predictions of MOND in a Newtonian framework, in terms of relations between the baryonic components of the galaxy and the (phantom) halo mass. We show that MOND predicts a monotonically increasing power-law for the stellar-to-(phantom)halo mass relation (SHMR) and a flat gas-to-halo mass relation.

We show that the so-called External Field Effect (EFE) of MOND can give rise to PDM densities with surprisingly complex spatial distributions in some situations. However, we find that the dominance of the Virgo supercluster tends to wash out most of these complexities in the Local Volume, generally giving rise to donut-shaped regions of negative phantom density aligned with the direction towards that mass concentration. We also computed the average density of PDM residing around galaxies in the Local Volume $\Omega_{\mathrm{pdm}} \approx 0.1$, below the average cold dark matter (CDM) density in a ΛCDM Universe but comparable to estimates of the DM mass associated with galaxies in the standard context.

In the Milky-Way Andromeda binary system, we find that a region of negative PDM should be located between the two galaxies, presumably affecting the shape of the outskirts of their stellar halos or hot gas coronae. We also found that the LMC PDM mass prior to its current infall was of the order of $8 \times 10^{10} \mathrm{M}_{\odot}$, which should be sufficient to affect the relax motion of the MW and induce a signature in the stellar halo. However, the LMC is "losing" PDM when it penetrates in the MW halo, so that the signature would probably be weaker than in the standard context. We leave to further work a detailed modelling of the effect of the LMC on the MW dynamics in the MOND context.

Finally, we show that probably the most promising way to detect the negative PDM densities predicted by Milgromian gravity would be through weak-lensing. By placing a galaxy of baryonic mass $5 \times 10^{10} \mathrm{M}_{\odot}$ under an EFE of $g_{Ne} = 0.02\, a_0$, the gravitational lensing convergence parameter κ can reach negative values of the order of -3×10^{-3}.

We conclude that if the Local Universe is Milgromian, looking at it with Newtonian eyes can give a broad picture which is surprisingly similar to the standard one. There are nevertheless some noticeable differences. We for instance make for the first time the prediction that the gas-to-(phantom)halo mass relation expected in MOND should be roughly flat. This however, would not necessarily be impossible to explain in the standard context. We highlight that concave weak-lensing with negative convergence at specific locations correlated with the large-scale environment would on the other hand be a true smoking gun of MOND, which might be achievable with future weak-lensing surveys.

Appendix to the article

3.6.1 List of UNGC sources

A list of Local Universe sources and their MONDian characteristics (such as PDM mass, external field strength) is available in the Appendix to this thesis (Table 11.1).

3.6.2 List of galaxy clusters

Table 3.1: List of sources outside of the Local Volume. For galaxy clusters, the given galaxy is the one chosen for the cluster center. Columns are object name (cluster name), distance to MW, r_{200}, MOND mass, g_N/a_0 at the center of the MW, g_N/a_0 at the cluster's r_{200}.

| Object	d (kpc)	r_{200} (kpc)	M_{MOND} ($M_\odot$)	g_N/a_0 at MW	g_N/a_0 at r_{200}
NGC4884 (Coma)	9.45e+04	2.65e+03	8.19e+14	1.07e-04	1.35e-01
N4472 (Virgo)	1.78e+04	2.02e+03	1.71e+14	6.30e-04	4.89e-02
N4696 (Centaurus)	4.39e+04	2.33e+03	2.13e+14	1.29e-04	4.56e-02
NGC6166	9.72e+04	2.55e+03	8.58e+14	1.05e-04	1.54e-01
NGC3842 (Leo)	8.22e+04	1.85e+03	2.36e+14	4.06e-05	8.02e-02
NGC3311 (Hydra)	4.32e+04	1.73e+03	8.23e+13	5.13e-05	3.21e-02
PGC056962	1.69e+05	3.96e+03	2.53e+15	1.02e-04	1.87e-01
ESO444-046	2.05e+05	3.52e+03	9.12e+15	2.52e-04	8.57e-01
NGC1275 (Perseus)	8.92e+04	2.67e+03	5.15e+14	7.52e-05	8.39e-02
IC4765 (PavoII)	7.85e+04	1.50e+03	9.16e+13	1.73e-05	4.73e-02
NGC0708 (Pisces)	6.51e+04	2.01e+03	2.84e+14	7.79e-05	8.16e-02
PGC015524	1.42e+05	2.00e+03	5.67e+14	3.26e-05	1.64e-01

3.6.3 The local universe PDM map with exclusively baryonic galaxy clusters
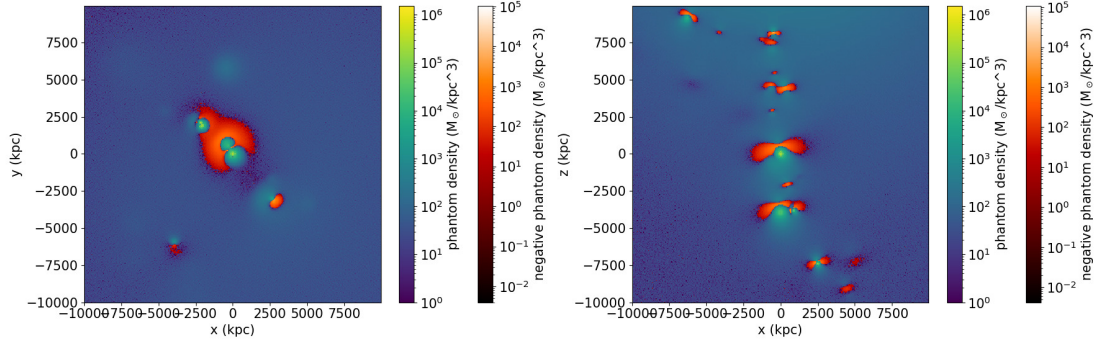
Figure 3.16: Phantom dark matter density map of the Local Volume centred on the MW (0,0,0). Plane cuts. *Left panel:* MW galactic plane z=0. *Right panel:* MW edge-on view y=0. In this case, clusters are taken into account with their baryonic mass only. This leads to an intermediate situation between those of Figure 3.3 and Figure 3.5, in which the most massive galaxies in the Local Universe regain importance compared to the case where the clusters have their MONDian mass, but the clusters still remain the most important sources of EFE.

3.6.4 Shear map in the isolated MOND case

As a comparison to Fig. 3.15, we provide the shear map corresponding to the same galaxy in the isolated MOND case in Fig. 3.17.
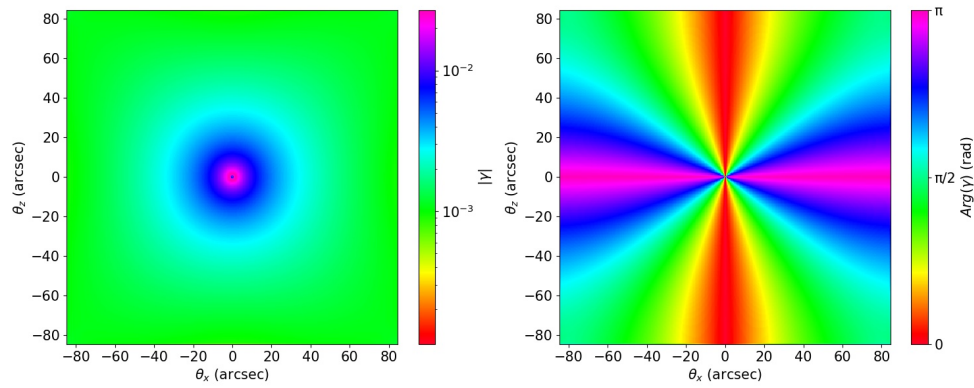
Figure 3.17: Shear vector γ for an NGC5055-like galaxy centred at $\theta_x = \theta_z = 0$ in the isolated MOND case (i.e. no EFE), used as a gravitational lens at $z = 0.3$ for sources at $z = 5$. *Left panel:* shear amplitude $|\gamma|$. *Right panel:* shear angle $\mathrm{Arg}(\gamma)$.

Chapter 4 Probing the radial acceleration relation and the strong equivalence principle with the Coma cluster ultra-diffuse galaxies

After exploring in the previous chapter the expected structure of the Local Volume in MOND under the influence of the external field, as well as unique weak lensing signatures that such a theory could leave, we now turn to testing the paradigm in a much denser environment, where the external field effect should be much more evident. We found this not to be the case, contrary to a priori expectations in MOND, but surprisingly, we also found the data to be in remarkable agreement with isolated MOND predictions, which did not have to be the case in a dark matter-based framework.

Foreword

This is intended to be a quick review of the main results from the work of Freundlich, J.; Famaey, B.; Oria, P.-A.; Bílek, M.; Müller, O.; Ibata, R.

For technical details and the complete work, please refer to Freundlich et al. (2022), published in Astronomy & Astrophysics, Volume 658, id.A26, 29 pp.

Abstract

The tight radial acceleration relation (RAR) obeyed by rotationally supported disk galaxies is one of the most successful a priori prediction of the modified Newtonian dynamics (MOND) paradigm on galaxy scales. Another important consequence of MOND as a classical modification of gravity is that the strong equivalence principle (SEP) – which requires the dynamics of a small free-falling self-gravitating system to not depend on the external gravitational field in which it is embedded – should be broken. Multiple tentative detections of this so-called external field effect (EFE) of MOND have been made in the past, but the systems that should be most sensitive to it are galaxies with low internal gravitational accelerations residing in galaxy clusters, within a strong external field. Here, we show that ultra-diffuse galaxies (UDGs) in the Coma cluster do lie on the RAR, and that their velocity dispersion profiles are in full agreement with isolated MOND predictions, especially when

including some degree of radial anisotropy. However, including a breaking of the SEP via the EFE seriously deteriorates this agreement. We discuss various possibilities to explain this within the context of MOND, including a combination of tidal heating and higher baryonic masses. We also speculate that our results could mean that the EFE is screened in cluster UDGs. The fact that this would happen precisely within galaxy clusters, where classical MOND fails, could be especially relevant for the nature of the residual MOND missing mass in clusters of galaxies.

4.1 Introduction

Galaxy clusters are an ideal test bed for a detection of the EFE (or a breaking of the strong equivalence principle) because of the high external gravitational field of their interior environment. Indeed, galaxy clusters are host to hundreds of galaxies and have dynamical masses reaching up to $10^{15} \sim 10^{16} \, \mathrm{M_\odot}$ for the most massive ones.

In particular, galaxies with low internal gravitation within clusters are prime candidates. Such a class of galaxies that gained popularity recently are Ultra-Diffuse Galaxies (UDGs), spatially extended dwarf galaxies with very low surface brightness.

We detail below some of the results we come up with in Freundlich et al. (2022), in which we take a closer look at the internal dynamics of a selection of eleven UDGs in the Coma cluster which have velocity dispersion measurements.

4.2 The UDGs and the RAR

A first interesting check was to see whether the sample of UDGs agreed with the Radial Acceleration Relation (Section 1.4.5). Using the formula from Wolf et al. (2010):

$$M_{1/2} \approx 4G^{-1}\sigma_{\mathrm{eff}}^2 R_e \qquad (4.1)$$

where σ_{eff} is the observed stellar velocity dispersion and R_e is the half-light radius in the sky allowed us to obtain the Newtonian dynamical mass at (the deprojected) half-light radius for each UDG, which in turn gave us the corresponding observed gravitational acceleration g_{obs}. Then from the observed stellar distribution, the baryonic inferred gravitational acceleration g_{bar} was also computed.

With those two quantities, we checked where the UDGs lied on the RAR; the result can be seen in Figure 4.1. We find a reasonable agreement with the relation meaning that the UDGs appear to have the same correlation between dynamical and baryonic masses as both spheroidal dwarf galaxies and bigger spirals. Furthermore, the best fit from McGaugh (2016) (black curve) virtually being a MOND isolated fit for a specific interpolation function, we find that UDGs agree with the isolated MOND prediction, an intriguing sign given the high external field they are embedded in. Indeed, in the regime of low g_{bar}, we expect the MOND prediction to result in slightly lower g_{obs} due to the EFE.
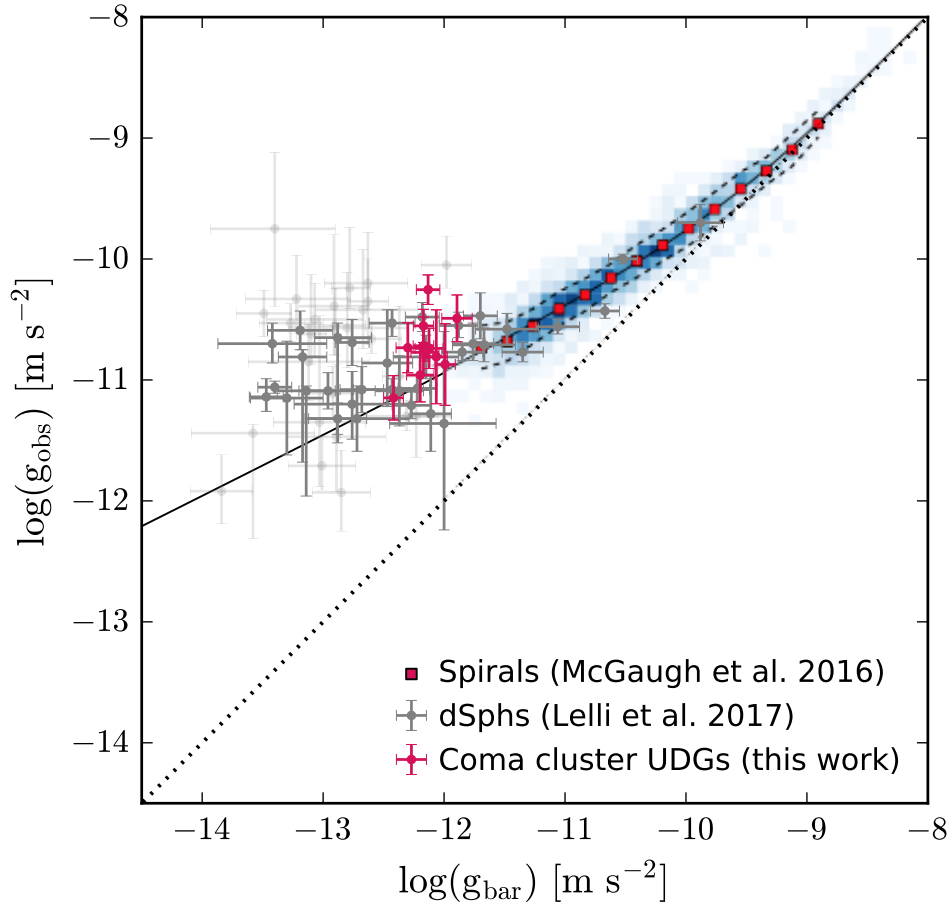
Figure 4.1: The Radial Acceleration Relation augmented with our sample of UDGs (magenta dots with error bars). The black curve is the best fit from McGaugh (2016), reproducing the isolated MOND phenomenology. Plot taken from Freundlich et al. (2022).

4.3 New formula for the gravitational field under a constant EFE

In Section 1.2.2, we gave an overview of the EFE and mentioned that the usually applied formula (Equation (1.22), Famaey & McGaugh (2012)) for computing the QUMONDian gravitational acceleration g under a constant external field, which stems from the one-dimensional case where the internal and external fields are aligned, did not compare well with our numerical results and systematically overestimated the strength of the EFE. In light of this, and since we needed to evaluate the gravitational acceleration taking into account the EFE for our sample of UDGs, we propose in Freundlich et al. (2022) another formula comparing better with our numerical results.

The driving idea was to place ourselves in the three-dimensional case, and in particular, for simplicity, a spherical approximation, which should already be significantly more realistic than the one-dimensional approximation. Let us consider such a spherical system with internal gravitational acceleration g_N under a constant external field g_{Ne}. Averaging the

gravitational field g_r over spherical shells gives, for a radius r (see Freundlich et al. (2022, Equations 20-29, Figure 7) for the detailed computation):

$$\langle g_r \rangle (r) = \begin{cases} \nu \left(\frac{g_N(r)}{a_0} + \frac{g_{Ne}^2}{3g_N(r)a_0} \right) g_N(r) & \text{if } g_N(r) \geq g_{Ne}, \\ \nu \left(\frac{g_{Ne}}{a_0} + \frac{g_N(r)^2}{3g_{Ne}a_0} \right) g_{N(r)} & \text{if } g_N(r) < g_{Ne}. \end{cases} \tag{4.2}$$

Note that from this formula, a particular case where the internal and external fields are perpendicular can be obtained:

$$g_\perp \approx \nu \left(\frac{\sqrt{g_N^2 + g_{Ne}^2}}{a_0} \right) g_N. \tag{4.3}$$

In order to test the accuracy of Equation (4.2), we compare the acceleration it yields to the QUMOND gravitational acceleration obtained by numerical computation on a given test case. We consider for this purpose a UDG modeled as a Plummer sphere of baryonic mass $M = 3.9 \times 10^8 \, \mathrm{M_\odot}$ and characteristic radius $a = 3.6 \, \mathrm{kpc}$ (and thus a half-mass radius of 4.7 kpc) located at distances $d = 0.5, 1, 2, 5, 10$, and $20 \, \mathrm{Mpc}$ from a point mass representing the center of the Coma cluster. The mass and radius of this UDG model are comparable to those of DF44, one of the UDGs from our Coma sample.

The MOND gravitational potential Φ is obtained by numerical integration of the QUMOND Poisson equation (Equation (1.18)) using the codes of Section 2.1 (PDM solver) and Section 2.2 (Poisson solver). Figure 4.2 compares the resulting average QUMOND acceleration profile $\langle g_r \rangle$ with the analytical expression from Equation (4.2) for different distances from the point mass modeling the Coma cluster. For comparison, we also consider $g_\parallel$ corresponding to the case where g and g_e are aligned (Equation (1.22)), and $g_\perp$ (Equation (4.3)).

The different plots confirm that $\langle g_r \rangle \approx g_\perp$ and show that $\langle g_r \rangle$ fits the numerically computed acceleration much better than $g_\parallel$, which systematically overestimates the EFE and thus underestimates the acceleration field. Another comparison, as a function of g_{Ne}, can be seen in Figure 4.3, which confirms the good agreement with QUMOND numerical computations.

Recently, Chae & Milgrom (2022) also compared different formulae for the MONDian gravitational acceleration g, for different formulations of MOND and different cases of EFE. Their results for QUMOND, in the specific case of a disk with a fiducial constant EFE coming from a tilt of 60° from the disk rotation axis can be seen in Figure 4.4. One can see that the one-dimensional approximation of Equation (1.22) seems indeed to be an upper limit for the EFE, which strays far from the numerical computations in the low g_N values especially.

Chae & Milgrom (2022, Fig. 7) then apply some of those formulae, including our new 3D average $\langle g_r \rangle$ (Equation (4.2)), to NGC 5055, an ideal galaxy under a strong external field modeled as well in Chae et al. (2020); Oria et al. (2021). They confirm our results of Section 3 that in the context of QUMOND, the departure from the isolated MOND case, i.e. the EFE, happens at fairly large radii. It is interesting to note that in the AQUAL formulation of MOND, the deviation from the isolated case due to the EFE is larger than in QUMOND.
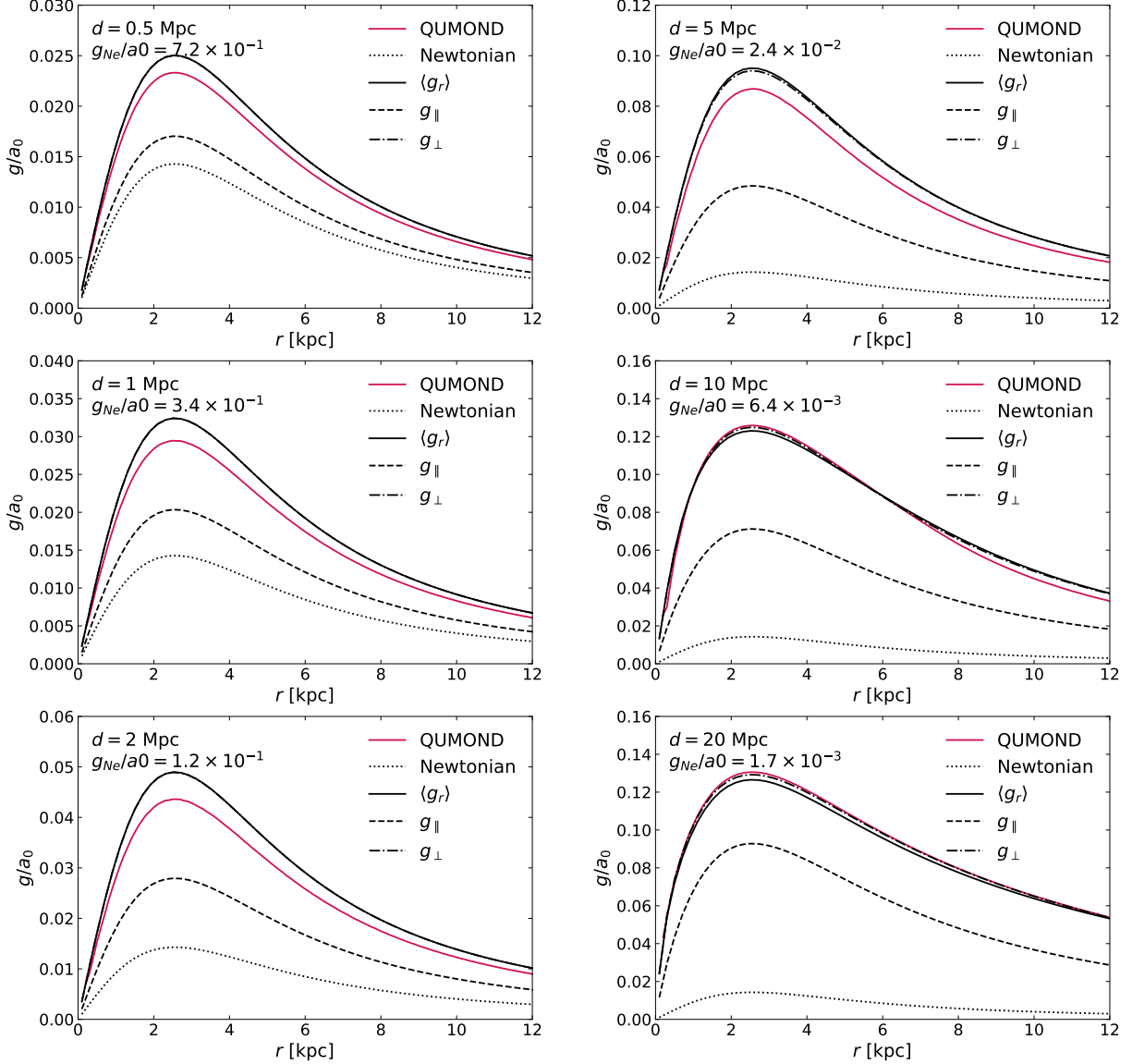
Figure 4.2: Comparison between the MOND acceleration with EFE resulting from a QUMOND numerical integration (red full curve) and the analytical expressions $\langle g_r \rangle$ from Equation (4.2) (black full curve), $g_\parallel$ from Equation (1.22) (black dashed curve), and $g_\perp$ from Equation (4.3) (black dotted curve), for a Plummer sphere ($M = 3.9 \times 10^8$ M$_\odot$, $a = 3.6$ kpc) at different distances d from a point mass equal to that of the Coma cluster at that distance. Plots taken from Freundlich et al. (2022).

4.4 The dynamics of UDGs with and without EFE

Using the new formula for $\langle g_r \rangle$ (Equations (4.2)) just introduced in Section 4.3, we were able to estimate the expected MONDian gravitational acceleration under a constant EFE. This EFE was obtained by the external gravitation applied to the location of each UDG (for a range of reasonable deprojected distances) based on a MONDian mass profile for the Coma cluster. On the other hand, the isolated MOND gravitational acceleration was more
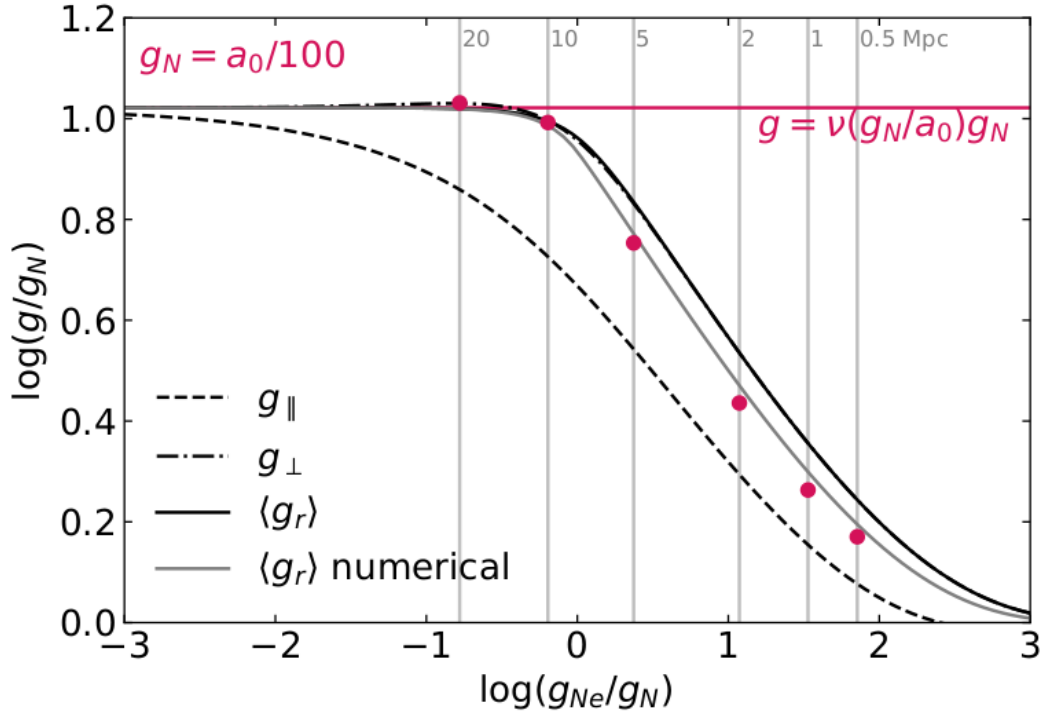
Figure 4.3: MONDian gravitational acceleration g as a function of the Newtonian external field g_{Ne} for different analytical formulae: $g_\parallel$ denotes the one-dimensional approximation (Equation (1.22), black dashed curve), $g_\perp$ denotes the formula for perpendicular internal and external fields (Equation (4.3), black dashed-dotted curve), and $\langle g_r \rangle$ is the new analytical expression from Equation (4.2) (black full curve). The red dots are results of the numerical QUMOND computations using the codes of Section 2.1 (PDM solver) and Section 2.2 (Poisson solver), for different distances of the UDG model (grey vertical lines). Plot taken from Freundlich et al. (2022).

straightforward to obtain directly from the baryonic g_{bar} and Milgrom's law (Equation (1.4).

Since we were interested in comparing both isolated and EFE cases to observations, we used the Jeans equations (using computation techniques from Mamon & Łokas (2005); see Freundlich et al. (2022, Section 3.2.1)) to obtain the velocity dispersion profiles from the gravitational accelerations.

We find that for each UDG, the agreement with observations is much better for the isolated MOND values than when including EFE. The inclusion of the strong EFE from the Coma cluster makes the dynamics of the UDGs almost Newtonian, which strays far from the observed profiles.

4.5 Discussion and conclusion

From this work we conclude that the observed dynamics of our sample of UDGs agree with the isolated MOND prediction, and thus that the same UDGs seem not to feel the EFE, leading to no violation of the strong equivalence principle. For low internal gravitational
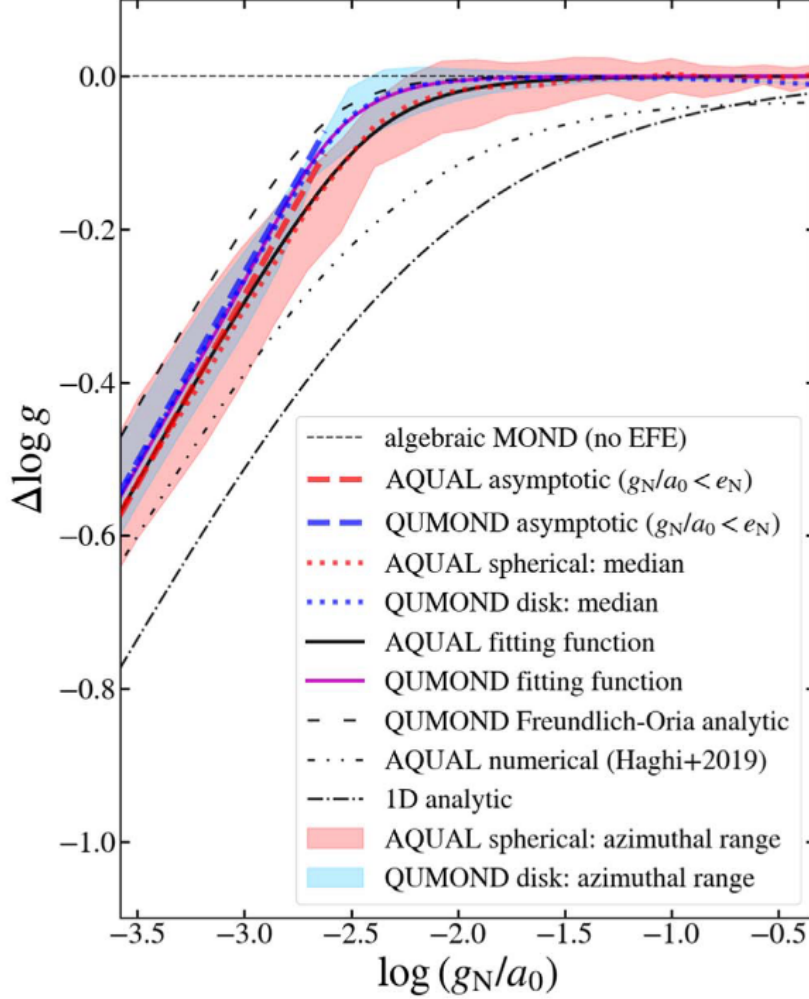
Figure 4.4: Comparison of gravitational accelerations for different formulations of MOND and different formulae or numerical computations. For QUMOND, this is for the case of a disk with a fiducial constant EFE coming at a 60° tilt from the disk's rotation axis. Our new $\langle g_r \rangle$ analytical formula (Equation (4.2)) corresponds to the black dashed curve. Plot taken from Chae & Milgrom (2022).

acceleration systems such as those we studied, and with a strong external field from the Coma cluster, the dynamics expected in MOND should however be almost Newtonian. Freundlich et al. (2022, Section 5) provide many interesting discussions regarding this situation and how to possibly make it work for MOND, which we summarize briefly here.

4.5.1 Survivor bias

There are several ways in which our sample of UDGs could be "survivor biased". Indeed, it could be that similar galaxies get disrupted rapidly in MONDian galaxy clusters, and thus we are left with detections of objects that only recently fell into the gravitational well of Coma and have yet to feel the EFE and tidal disruption. In this vein, our Jeans modeling provides better agreement with observations when considering radially biased anisotropy, which itself

could easily be explained in the context of UDGs that are themselves on radial orbits.

4.5.2 Missing mass

As we know (Section 1.4.2), MOND has a missing mass issue in galaxy clusters (discrepancy of a factor $2 \sim 3$) and this failure could highlight a fundamental misunderstanding of MONDian physics in this kind of environment. A simple solution would be dark mass, either in the form of yet undetected baryonic matter or from a dark sector (*e.g.* sterile neutrinos). However in this particular context, this matter would have to be concentrated in UDGs in order to make them match observations individually; this is very reminiscing of issues that dark matter theories face (see for example the BTFR in Section 1.4.4), and is thus both unlikely and unappealing.

4.5.3 Extended MOND

In the Extended MOND framework of Zhao & Famaey (2012), the MOND phenomenology is not the same at all scales, but instead the critical acceleration varies with the depth of the potential well of the systems considered. In this context, this critical acceleration would be comparable to the a_0 we know in individual galaxies, but would be much higher in the environment of galaxy clusters. This means a departure from Newtonian gravity in clusters at higher accelerations than a_0, and thus an overall higher velocity dispersion for our UDGs which would enjoy boosted gravity compared to the standard MOND phenomenology. In this context, we find that the predictions are in good agreement with the data.

4.5.4 EFE screening

Our sample of galaxies being seemingly immune to the EFE might mean that a mechanism is shielding them from the external field. A possibility is offered by Superfluid Dark Matter (Berezhiani & Khoury (2015), Section 1.3), in which the external field from a source is expected to be applied only to objects inside that source's superfluid core. This would provide a huge difference compared to standard MOND phenomenology in galaxy clusters, since the superfluid core of a cluster is expected to be fairly small (relatively to its large spatial extent). For the Coma cluster, this core would have a size of a few hundreds of kpc, not extending up to the UDGs from our sample.

Chapter 5 The Sagittarius stellar stream

After an excursion to the Coma cluster in the previous Chapter, we will now return to the Milky Way, and concentrate ourselves on the superb probes of the gravitational potential provided by stellar streams in the halo of the Galaxy. In particular, if one wants to probe the potential at large radii, the Sagittarius stream appears to be a true treasure trove. However, it is a very complex structure, and some of its features like its bifurcation are not understood in any model.

Indeed, the Sagittarius dwarf spheroidal (Sgr dSph) is a galaxy orbiting the Milky Way which was discovered by Ibata et al. (1994, 1995). It is the third most massive satellite of the Milky Way, after both of the Magellanic clouds, and also one of the closest. Sgr is particularly interesting as example of an ongoing merger, the latest big merger known to happen in the MW, with an infall $\sim 6\,\mathrm{Gyr}$ ago. Shortly after its discovery, Ibata et al. (1997) put forward many dynamical constraints for the Sgr, most of which are still very accurate by today's standards. In their work, we learn that the Sgr is prolate with axis ratios close to $3:1:1$, has already completed several orbits around the MW (period of $\sim 1\,\mathrm{Gyr}$) and should soon - by next pericentric passage - be completely disrupted.

5.1 Characteristics and models

Tidal disruption over the last few billion years has created the Sagittarius stellar stream, the longest and most spectacular in our galaxy's stellar halo, and which was first detected in Mateo et al. (1998). With an orbital plane almost orthogonal to the MW's disk plane, a pericenter at $\sim 20\,\mathrm{kpc}$ from the center of the MW, and an apocenter at $\sim 80\,\mathrm{kpc}$, the resulting kinematic structure is an invaluable tool to probe the DM-dominated region of the MW and thus its gravitational potential. The most recent view of the Sgr stellar stream comes from the *Gaia* EDR3 selection of Ramos et al. (2021) and is shown in Figure 5.1.

A lot of effort has been dedicated to providing a model explaining Sgr's orbit and all the peculiarities of its stellar stream in terms of *e.g.* angular positions, distances, velocities. As discussed before, such a model includes not only information on the Sgr itself but also on the MW, other MW satellites, and gravitation in general, making producing one a very difficult task.

A very popular model was put forward by Law & Majewski (2010) satisfying most observational constraints at the time, although not managing to address the bifurcation (see Section 5.2), which they think could be due to substructure or internal dynamics. The key to this model is the introduction of a non spherical component to the potential of the MW in the form of a triaxial DM halo, although they themselves deem their particular configuration

(a) colored by density

(b) colored by faint branch probability
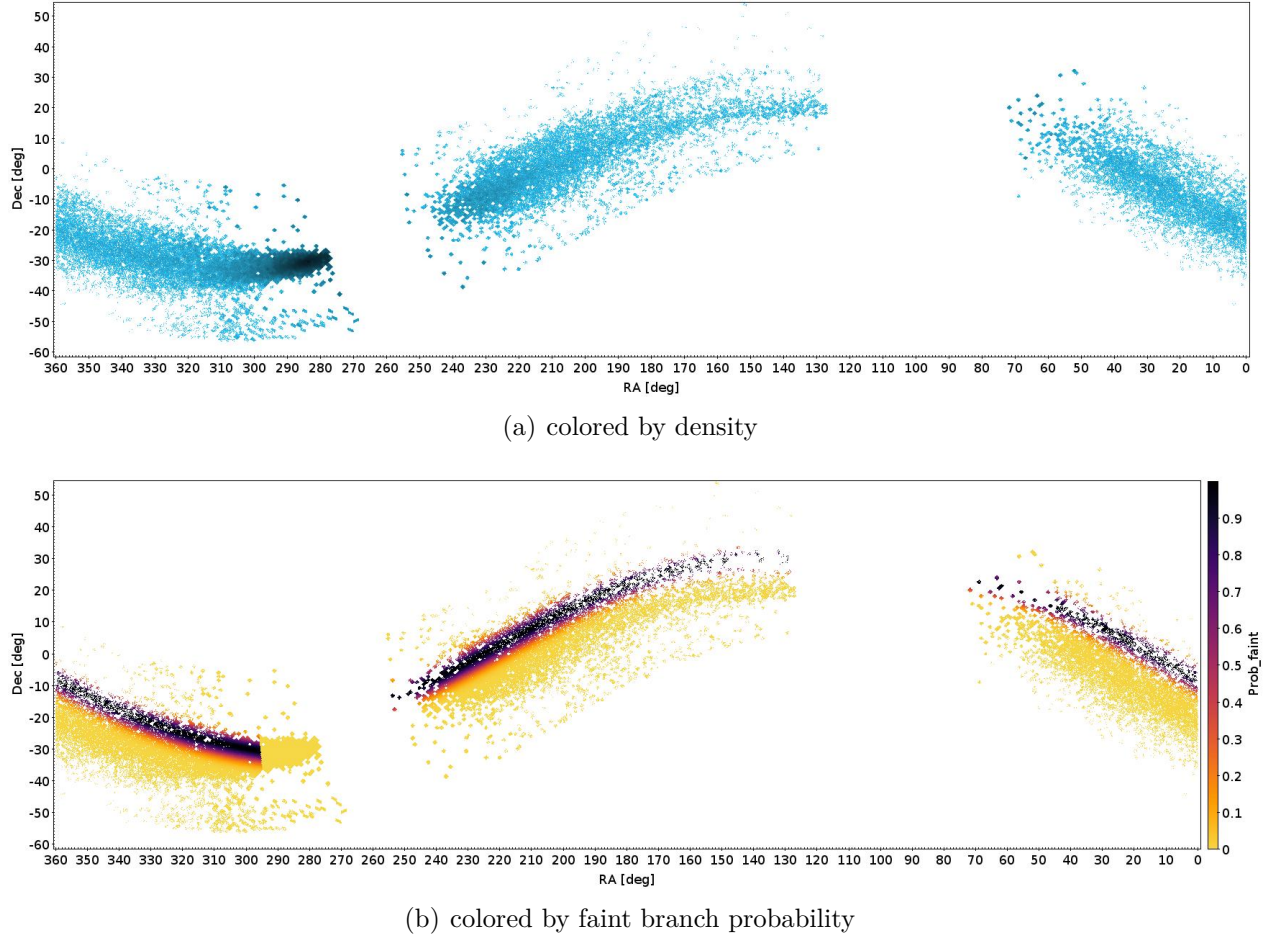
Figure 5.1: The Sgr stellar stream based on the *Gaia* EDR3 selection of Ramos et al. (2021). The remnant of the progenitor is located around RA = 280° and the bifurcation is visible, especially obvious in the leading arm (130° ≤ RA ≤ 200°). *Panel (a):* colored by density (darker is denser); *Panel (b):* colored by probability of belonging to the faint branch as derived in Ramos et al. (2021).

unstable and tricky to reconcile with observed galactic dynamics, as was shown a few years later by Debattista et al. (2013). They also use their good fit to wide-field surveys to discuss the probablity of being part of the Sgr stream for some groups in the stellar halo of the MW, and estimate a current remnant mass of $\sim 2.5 \times 10^8 \, \mathrm{M_\odot}$.

The most recent and arguably the best model comes from Vasiliev et al. (2021a) in which the authors let the Sgr fall into the joint evolving potential of the MW and the LMC, with the latter being on its first infall. Their Sagittarius galaxy is a spherical model for the stellar component, immersed in a cold dark matter halo. The background potential with the inclusion of the LMC allows for a very good agreement between the model and recent *Gaia* DR2 data (and an even more recent comparison with *Gaia* EDR3 data in Ramos et al. (2021)), in particular reproducing for the first time the observed line-of-sight velocities in the leading arm, a task that no model came close to accomplishing before.

However, no satisfying explanation has been found so far for a very peculiar feature of

the Sgr stream: its "bifurcation". We address this topic in the next section.

5.2 The bifurcation in the Sagittarius stream

In Belokurov et al. (2006), the authors use the Sloan Digital Sky Survey (SDSS) DR5 to look at the Sgr stream and find that two separate branches are clearly defined in the leading arm, in a region of the sky they dub the "Field of streams". Figure 5.2 is taken from their article, showing the area of interest. This is the first detection of what will become the bifurcation of the Sgr stream, *i.e.* a fainter branch running parallel to the main bright branch of the stream. In Koposov et al. (2012), a few years after the detection in the leading arm, the authors use a newer release of SDSS (DR8) and detect the bifurcation in the trailing arm as well. Today, the most recent view of the bifurcation comes from the *Gaia* EDR3 selection of Ramos et al. (2021) and is shown in Figure 5.1, with Panel (b) highlighting the faint branch selection.
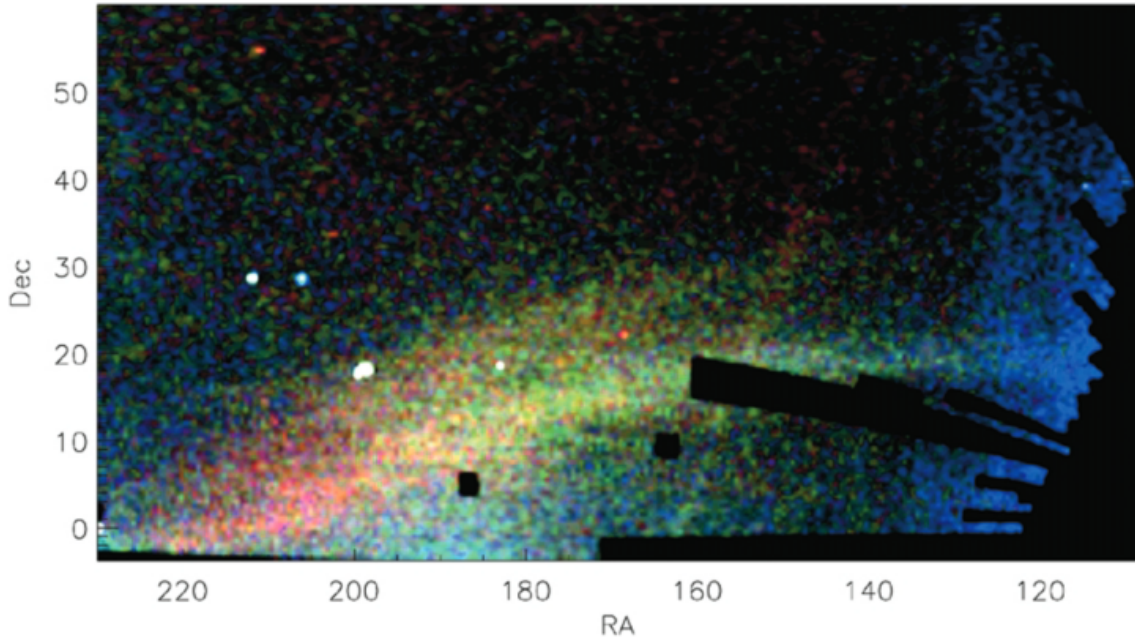
Figure 5.2: SDSS DR5 data of the "Field of streams" region of the sky, showcasing the leading arm of the Sgr stream in the foreground color coded by distance (red is furthest, blue is nearest). The bifurcation can be seen around $140° \leq RA \leq 180°$. Plot taken from Belokurov et al. (2006).

At the time, Belokurov et al. (2006) ventured the hypothesis that the two branches might be made of material stripped at different times. This was investigated in Fellhauer et al. (2006), in which the authors explain the bifurcation as the result of the young leading, old leading and trailing wraps overlapping and being slightly displaced due to the precession of the orbit. However this did not agree with later observations, one reason being that both branches have very similar metallicities, hinting towards a production of both branches at similar times.

### 5.2.1 Angular momentum and inclination angle

A particularly interesting work investigating the origin of the bifurcation came from Peñarrubia et al. (2010), in which the Sgr is modeled not as a spheroidal dwarf, but as a disky galaxy immersed in a cold dark matter halo. Their N-body simulations result in a good fit to the observations of Belokurov et al. (2006) for the same region, highlighting the role played by angular momentum in the creation of different branches. However, with subsequent observations, it was realised that the model is not as successful when it comes to fitting the rest of the stream. Moreover, the authors predict a rotation signal in the remnant of the progenitor which is much higher than the observed one (Peñarrubia et al., 2011).

One important element taught to us by Peñarrubia et al. (2010) is the role of the inclination angle θ between the orbital plane of the Sgr dwarf and its disk plane: varying this parameter greatly alters the geometry of the stellar stream. In Figure 5.3, the result of a few handpicked N-body simulations of a disky Sgr falling into the MW is shown for different values of the inclination angle θ. Those simulations - and all that follow in this section, unless explicitely stated otherwise - start 3 Gyr ago and are launched into the evolving joint potential of the MW and the LMC of Vasiliev et al. (2021a) using the N-body code GYRFALCON (Dehnen, 2000). The disks have a stellar mass of $2.325 \times 10^8 \, M_\odot$, scale radius of 0.9 kpc, scale height of 0.18 kpc, and are immersed in a NFW DM halo of mass $4.185 \times 10^9 \, M_\odot$. They are generated using AGAMA (Vasiliev, 2019) and initially rotate counter clockwise. Each disk is made of 10^5 particles, as is each halo. It is clear, looking at those results, that reproducing the entirety of the Sgr stream as seen in Figure 5.1 with a disky model alone seems very difficult, with all parts never getting populated by a single disk angle. However if we were interested in producing only the faint branch, Panel (c) in particular would look very relevant, with an inclination angle θ close to the best fit value of $-20°$ put forward by Peñarrubia et al. (2010).

This is in agreement with the results of Łokas et al. (2015), in which the authors find that disky satellites with a prograde rotation (*i.e.* having inner angular momentum in the same direction as their orbital rotation axis) tend to produce thin streams with more easily disrupted progenitors which form a bar, resulting in a prolate shape, while retrograde disks produce thicker streams, with progenitors conserving their initial shape longer and losing rotation slowly. The creation of a faint thin branch then seems more likely in the scenario of a prograde disk.

5.2.2 Double disk

Kazantzidis et al. (2011b) put forward the hypothesis that dwarf spheroidals could be the result of two disky dwarf galaxies merging. They ran N-body simulations to reproduce cosmological merger events and conclude that this is a valid mechanism for the formation of dwarf spheroidals, by comparing to the Local Group and other known environments. We investigate this idea in the context of the Sgr and the formation of the bifurcation. Going by the results of Łokas et al. (2015) on the importance of the inclination angle between internal disk plane and orbital plane, this is an interesting idea because a prograde disk could create the thin faint branch while a retrograde disk could create the thicker bright branch. Having two superposed disks rotating in opposite directions would also make the model consistent with observations of very low rotation in the remnant of the progenitor (Peñarrubia et al., 2011; del Pino et al., 2021), since the angular momentum signatures from

(a) $\theta = \pi/6$ rad

(b) $\theta = 0$ rad

(c) $\theta = -\pi/6$ rad

(d) $\theta = -\pi/2$ rad
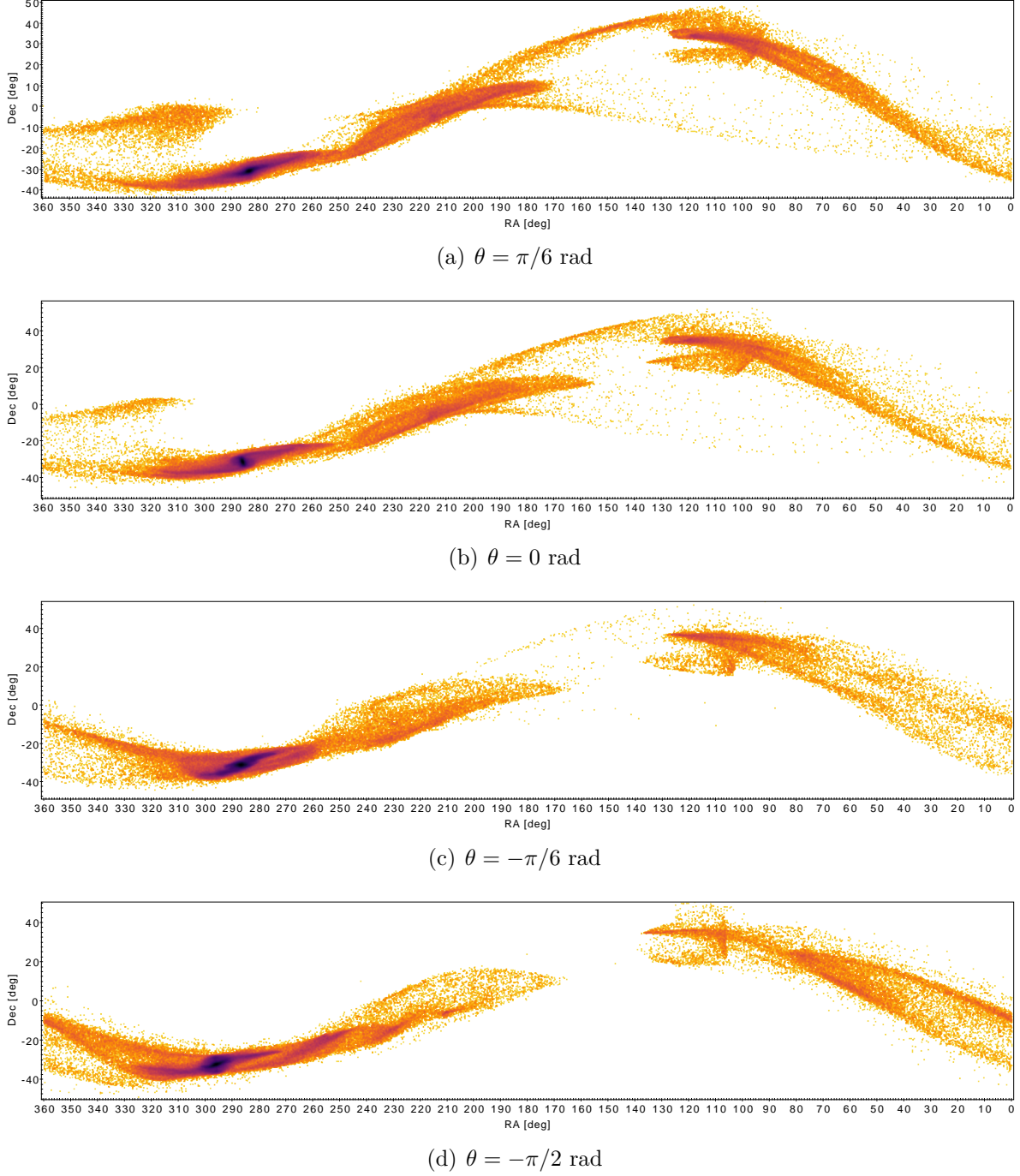
Figure 5.3: Final snapshots of N-body simulations of a disky Sagittarius dwarf galaxy falling inside the combined evolving potential from the MW and the LMC of Vasiliev et al. (2021a). Only stellar particles are plotted. In each simulation a different inclination angle θ between the orbital plane of the Sgr dwarf and its disk is chosen. Color indicates particle density, with darker being denser. The remnant of the progenitor is located around RA = 290°.

the two disk populations would mix up and we would only observe the difference via radial velocities.

(a) prograde disk   (b) retrograde disk
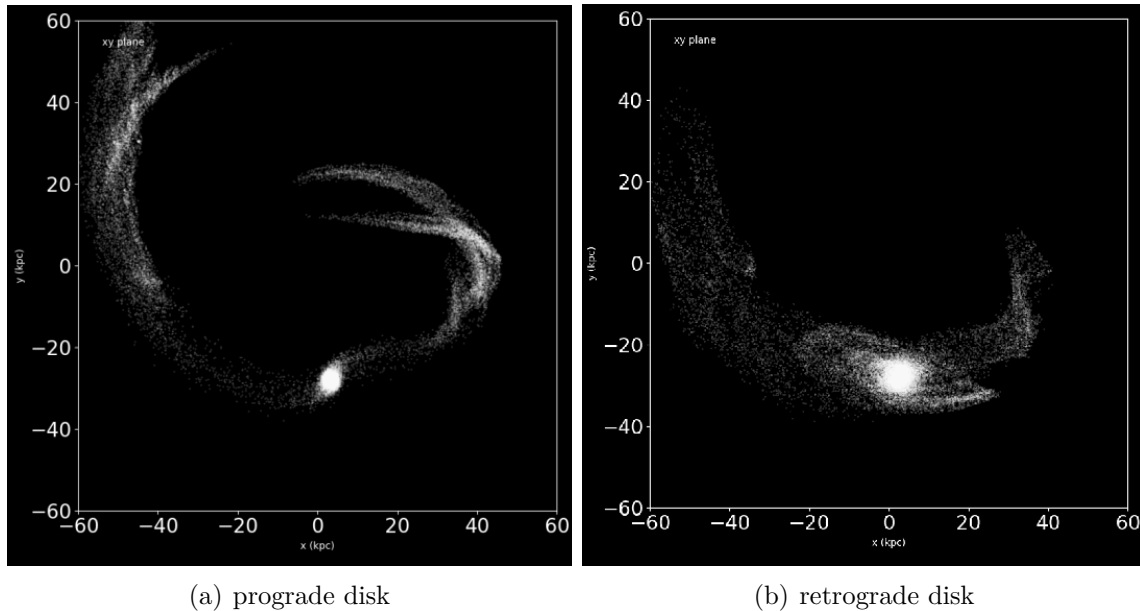
Figure 5.4: *N*-body simulation of two disky galaxies launched on circular orbits around the Milky Way in a toy-model logarithmic gravitational potential. Coordinates are galactic Cartesian with the MW center at $(x, y, z) = (0, 0, 0)$ kpc and the xy plane as both the MW disk plane and the disky galaxies' disk plane and orbital plane. The difference in stream geometry between the prograde and retrograde disks is glaring.

As a first step, we investigated a toy model to compare streams generated by prograde and retrograde disks. We examined *N*-body simulations of superposed disky galaxies started on circular orbits around a toy-model Milky Way and stop once tidal disruption is advanced enough to study the differences between both cases. The results can be seen in Figure 5.4. As in Łokas et al. (2015), we see that the retrograde disk is harder to disrupt and produces a thick stream, while the prograde disk has a longer, thinner stream, and a characteristic "s" shape around its flattened progenitor. What is more, the prograde disk already produces two distinct branches per arm, and at this point of evolution, noticeable underdensities appear in zones of the stream closest to the progenitor.

We then tried this situation in the context of the disruption of the Sagittarius with the background potential of Vasiliev et al. (2021a) and similar initial conditions in phase space and masses, except that our stellar component is made of two superposed disks of same mass that are counter-rotating. We show our best simulation in Figure 5.5. While this also shows interesting features, the model cannot be easily reconciled with *Gaia* data (Figure 5.1). The prograde disk almost exclusively populates the faint branch as we had hoped, although it does less accurately in the trailing arm part near the progenitor ($360° <= $ RA $ <= 290°$). However the retrograde disk does not populate the bright branch as well as a spherical model. Furthermore, there is a significant underdensity in the $200° <= $ RA $ <= 140°$ region that is not present in the data: both arms in this leading arm part of the simulation fail to extend as far as observed. It is nonetheless very encouraging to see that this two superposed disks configuration yields realistic results, with no abnormal behaviour due to autogravity.
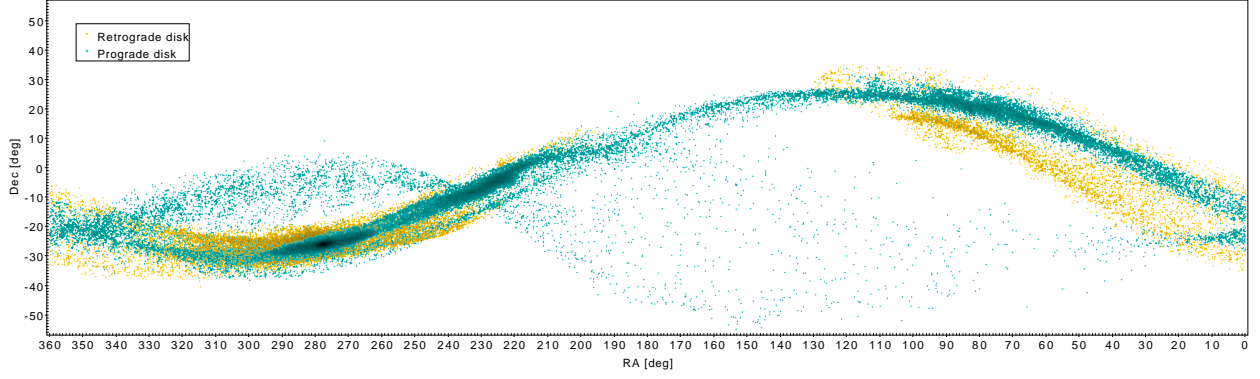
Figure 5.5: Two superposed counter-rotating disks as the stellar component of the Sgr dwarf galaxy, after being disrupted 3 Gyr in the evolving joint potential of the MW and the LMC from Vasiliev et al. (2021a).

5.2.3 Accreted stream

Another possibility entirely to bring angular momentum into play is the tidal disruption of a GC or dwarf galaxy inside the Sgr system. This disruption will create a stellar stream, and it is interesting to investigate what will become of those stream stars with high angular momentum from the orbital movement of their progenitor once accreted by the MW.
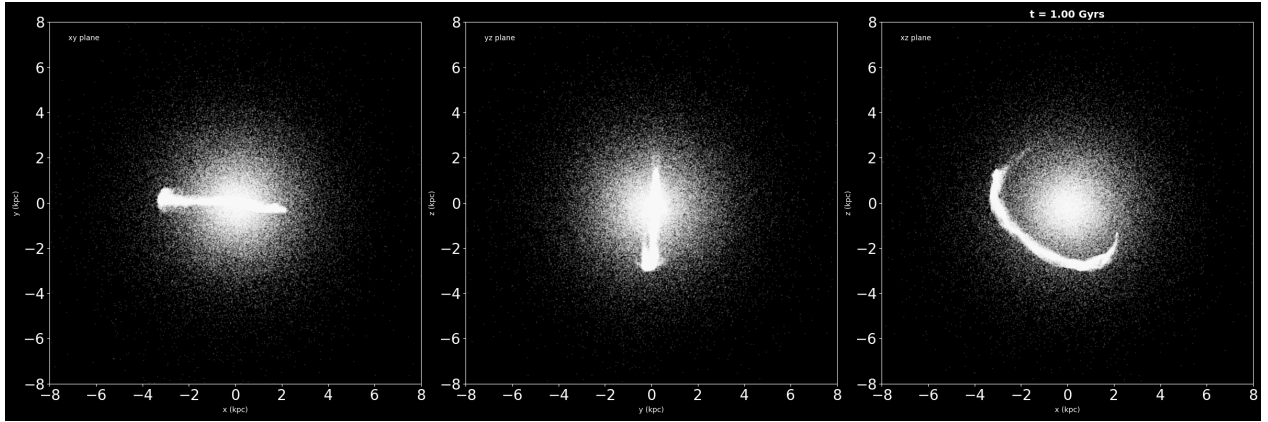
Figure 5.6: Tidal disruption of a spherical distribution of stars representing a globular cluster around a Sgr-like body. After 1 Gyr, a tidal stream has formed.

In Figure 5.6, we let a spherical distribution of stars representing a globular cluster get disrupted around a Sgr-like body for 1 Gyr. We generate the Sgr just as in Vasiliev et al. (2021a) (King model stellar distribution of 10^5 particles inside a spherical DM halo of 10^5 particles), and the GC as a 5×10^4 particles Plummer model of scale radius 20 pc. We initially put it 3 kpc from the Sgr's center of mass and make it orbit in what will later be the Sgr's orbital plane around the MW. By this time, the GC-like object has already formed a stream. We then let this system fall into the potential well of the MW, and see what becomes of the GC stream particles.

Figure 5.7 shows what the system looks like after evolving for 1.25 Gyr in the potential

93
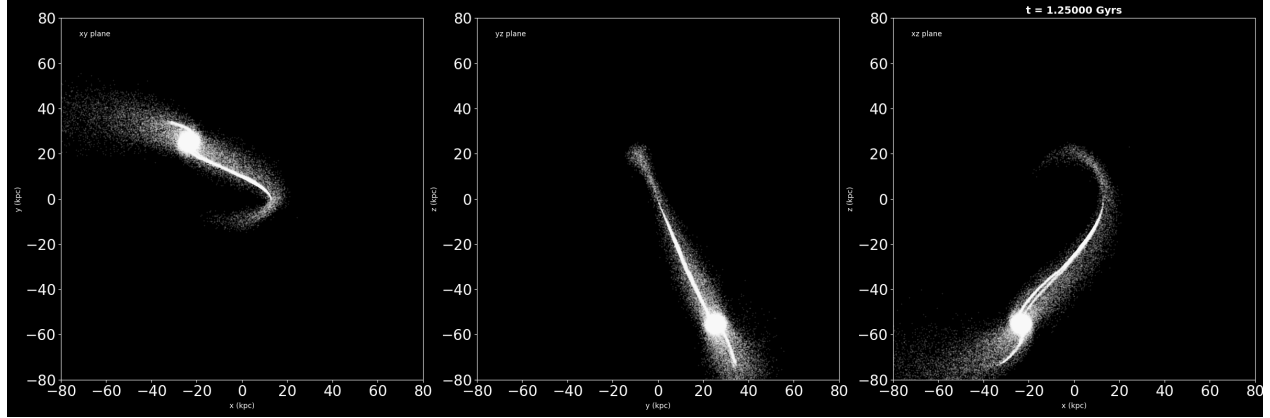
Figure 5.7: The Sgr plus GC stream system of Figure 5.6 after evolving for $1.25\,\mathrm{Gyr}$ in the potential of the MW. Coordinates are Galactic Cartesian with the MW center at $(x, y, z) = (0, 0, 0)\,\mathrm{kpc}$ and xy as the MW disk plane. In the xz plane ($\sim$ Sgr's orbital plane), we can see two parallel arms forming at the same time, caused by two different wraps of the GC stream being pulled out.

of the MW. A particularly interesting feature can be seen on the xz plane plot, in which two parallel arms are formed at the same time, caused by two different wraps of the GC stream being pulled. This is enticing since it has been shown (Ramos et al., 2021) that parallel arms are more likely than a cross or "X" shape for the bifurcation, and this would be one way to get them.
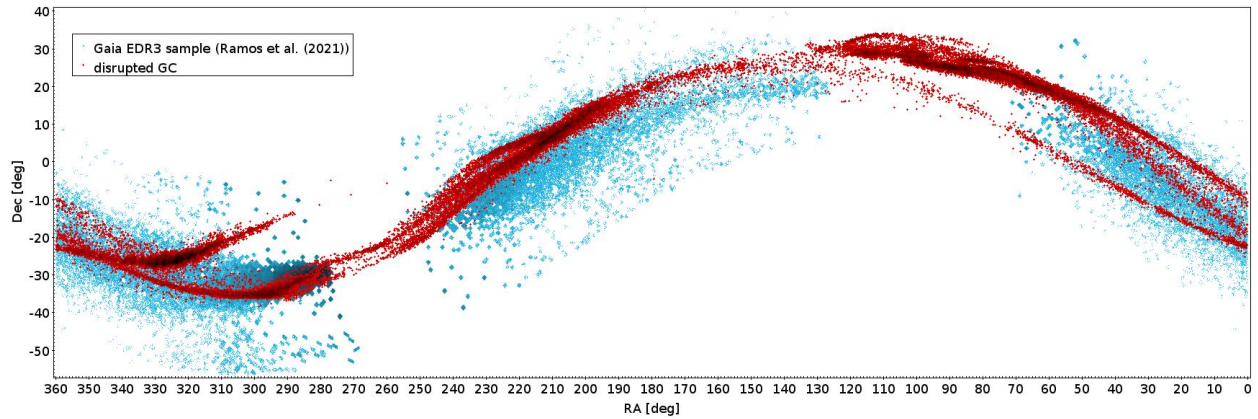
Figure 5.8: The Sgr plus GC stream system of Figure 5.6 after evolving for $3\,\mathrm{Gyr}$ in the potential of the MW, up to present time. We overplot GC stellar particles in red over the Sgr *Gaia* EDR3 sample of Ramos et al. (2021). An accreted stream can be a good way (dynamically) to create the faint branch of the Sgr stream.

Figure 5.8 shows the system fully evolved up to present time (after $3\,\mathrm{Gyr}$) with the GC particles in red, which we plot over *Gaia* EDR3 data from Ramos et al. (2021). Here again, we realize that much like the disk model, this is an interesting possibility for populating the faint branch. However, the question of the stellar population rises: do we expect the faint branch to be made of the same material as the bright branch? If yes, how likely is it that

a satellite has a similar enough population to that of the Sgr? In the case of a globular cluster, one would expect both populations to be strikingly different since GCs are made of a single stellar population and have a very low spread in metallicity. However a small satellite galaxy could maybe have a similar enough population. In any case, according to Ramos et al. (2021), the difference in metallicities between faint and bright branches is very small.

This last experiment gave us an idea: this scenario of a disrupting body inside the Sgr that later gets accreted is plausible, but what if we treated the disrupted globular cluster stream of Figure 5.6 simply as a tracer for an overdensity in the Sgr dwarf, and we tried with many more of such tracers? Indeed, this overdensity could represent *e.g.* a clump, a moving group, or spiral arms. In Chapter 6, we thus present a work detailing a way to create the faint branch of the Sgr stream which emerges naturally after a systematic probing of various dynamical parameters.

Chapter 6 Revisiting a disky origin for the faint branch of the Sagittarius stellar stream

Foreword

This is a slight modification, to fit this manuscript, of the work of Oria, P.-A.; Ibata, R.; Ramos, P.; Famaey, B.; Errani, R. which was published in The Astrophysical Journal Letters, Volume 932, Issue 2, id.L14, 7 pp. (Oria et al., 2022a).

Abstract

We investigate ways to produce the bifurcation observed in the stellar stream of the Sagittarius dwarf galaxy (Sgr). Our method consists in running N-body simulations of Sgr falling into the Milky Way for the last 3 Gyr, with added test particles on disk orbits that span a wide range of initial positions, energies, and angular momenta. We find that particles that end up in the faint branch are predominantly high angular momentum particles that can all originate from a single plane within the progenitor, nearly perpendicular both to the orbital plane of the progenitor and to the Milky Way stellar disk. Their original configuration at the start of the simulation corresponds to spiral features already present 3 Gyr ago, which could be, *e.g.*, the result of a disk-like component being tidally perturbed, or the tidal tails of a satellite being disrupted within Sgr. We then run a simulation including the self-gravity of this disky component. Despite the remaining ambiguity of its origin, this disk component of the Sgr dwarf with spiral over-densities provides a first step towards a working model to reproduce the observed faint branch of the bifurcated Sgr stream.

6.1 Introduction

Since its discovery (Ibata et al., 1994, 1995), the Sagittarius dwarf galaxy (Sgr) has been under intense scrutiny as the closest example of an on-going galactic merging event. The stellar stream generated by its tidal disruption (Ibata et al., 2001; Majewski et al., 2003) is an extended and complex kinematic structure in the stellar halo of the Milky Way (MW), and as such constitutes an invaluable source of information on the gravitational potential and history of *both* the MW and the progenitor dwarf galaxy itself.

Over the years, several models have been put forward in order to reproduce the shape of the stream and its kinematics (e.g. Ibata et al. 1997; Helmi 2004; Law et al. 2005). Among those, Law & Majewski (2010) reproduced most of the observational constraints at the time, involving however an unrealistic and unstable triaxial dark matter halo configuration for the MW. The latest up-to-date model by-passing this problem is that of Vasiliev et al. (2021b, hereafter V21), in which the Sgr dwarf is infalling in the joint evolving gravitational potential of the MW and the Large Magellanic Cloud (LMC), yielding a very good agreement with recent Gaia data.

One of the remaining mysteries about the Sgr stream is the presence of a bifurcation, in the form of a faint branch running parallel to the main brighter branch, observed first in the leading arm (Belokurov et al., 2006), then in the trailing arm (Koposov et al., 2012). More recently, this bifurcation has been outlined with great precision by Ramos et al. (2021) using the latest Gaia EDR3 data (Gaia Collaboration et al., 2021).

Fellhauer et al. (2006) proposed an early explanation for the bifurcation, as the result of the young leading, old leading and trailing wraps overlapping and being slightly displaced due to the precession of the orbit (Yanny et al., 2009; Niederste-Ostholt et al., 2010), but this model did not match later observations of the stream.

Peñarrubia et al. (2010) then proposed a model in which the Sgr dwarf originally consisted of a rotating stellar disk embedded in a cold dark matter halo. A disk slightly misaligned with respect to the orbital plane was shown to produce a bifurcation as observed in the Sgr stream. However, the model predicted some remnant rotation in the centre of Sgr today, which was not observed (Peñarrubia et al., 2011).

Although not in the context of the bifurcation, an originally disky Sgr was also studied by Łokas et al. (2010) in order to explain the elongated shape of the remnant. This model makes use of the tidal stirring mechanism (Mayer et al., 2001; Kazantzidis et al., 2011a) according to which dwarf spheroidal galaxies are the outcome of disky satellite galaxies being deformed due to galactic tides.

In this letter, we re-investigate the production of a bifurcation by selecting, within simulations of the Sgr stream, particles that end up in the observed faint branch, and then examine the properties of the initial conditions.

6.2 Methodology

6.2.1 Reference model

The underlying model that we use for the present work is the *N*-body simulation proposed by V21 of the Sgr dwarf falling into a joint, evolving MW and LMC gravitational potential.

This model constitutes an ideal basis for our investigations as it already reproduces many observational constraints (e.g. positions, proper motions, distances and line-of-sight velocities, with the inclusion of the LMC being key for the latter two, especially in the leading arm), leaving us free to focus our efforts on the production of the bifurcation. In this context, the simulation starts 3 Gyr ago, at which point Sgr is made of a spherical King distribution stellar component of mass 2×10^8 M$_\odot$, immersed in a spherical dark halo of mass 3.6×10^9 M$_\odot$. The stellar and dark matter components are made of 2×10^5 particles each. The MW and LMC models are described in detail in V21.

6.2.2   Sagittarius model and simulation

Using the N-body code GYRFALCON (Dehnen, 2000), we first reproduce the simulation provided by V21. Then, we add test particles to the initial conditions of the Sgr dwarf (self-gravity will be included in §6.3.2) to see which ones are more likely to end up in the faint branch of the Sgr stream by the end of the simulation.

Given the aforementioned works hinting strongly at the importance of rotation in Sgr to produce a bifurcation, we choose to populate our simulations with test particles with wide ranges of angular momenta. The sample of test particles is produced by generating stellar disks using AGAMA (Vasiliev, 2019) and giving them each a different inclination w.r.t. the orbital plane of Sgr. Each disk has a scale radius $R_{\mathrm{disk}} = 0.9$ kpc (V21's King model has a scale radius of 1 kpc), a scale height $H_{\mathrm{disk}} = 0.18$ kpc, central velocity dispersion $\sigma_{r,0} = 4$ kms^{-1}, and is generated through a QuasiIsothermal distribution function. The full AGAMA script for generating the disk is available in the shared data.

We use a right-handed Cartesian coordinate system centered on the MW with the xy plane being its disk plane, and the x-axis pointing along the Sun-Galactic center direction, with the sun at $(x, y, z) = (-8, 0, 0)$ kpc. Our disks are generated in this plane, then we rotate them before launch by probing inclination angles i every 20°, both around the x-axis and around the y-axis using the following matrices respectively:

$$R_x = \begin{pmatrix} 1 & 0 & 0 \\ 0 & \cos(i) & -\sin(i) \\ 0 & \sin(i) & \cos(i) \end{pmatrix}, \tag{6.1}$$

$$R_y = \begin{pmatrix} \cos(i) & 0 & -\sin(i) \\ 0 & 1 & 0 \\ \sin(i) & 0 & \cos(i) \end{pmatrix}. \tag{6.2}$$

For reference, for such a disk to be in the orbital plane of Sgr (at present), it would have to be rotated around the x-axis with the R_x matrix by an angle of $i \simeq 100°$. Before applying a rotation, our disk models have angular momentum aligned with the positive z-axis. Preliminary tests showed us that particles in the inner regions of the disk would not end up in the faint branch, but rather end up close to the remnant of the progenitor. This is understandable as those particles are deeper in the potential well of the King model and much harder to strip. We thus select from those disks the 2×10^4 outermost test particles out of the 5×10^4 particles generated, allowing us to better probe the regions of interest. This corresponds to a hole in the inner $\simeq 1.5$ kpc of the disks.

6.2.3 Stream selection
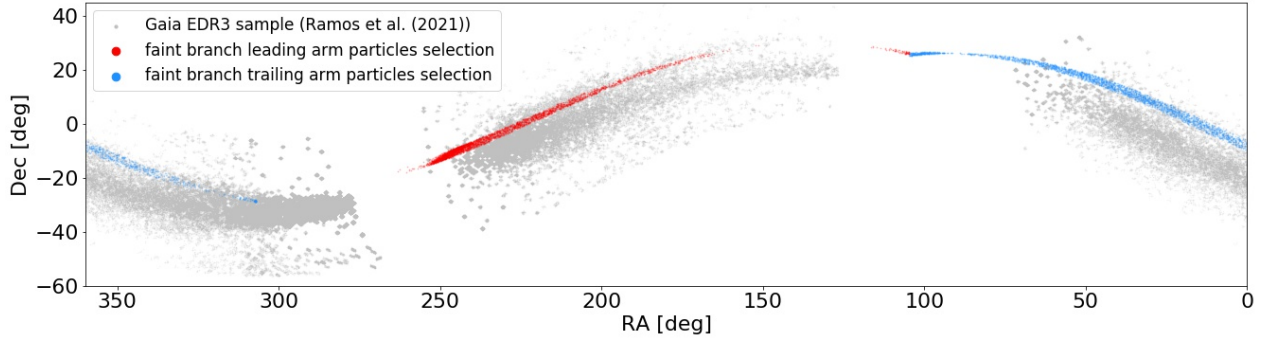
Figure 6.1: The Gaia EDR3 Sgr sample from Ramos et al. (2021) in the background (grey), with our selection of faint branch test particles from our simulations from Section 6.3.1 overplotted (red for leading arm, blue for trailing arm). The remnant of the progenitor lies in the $275 \leq \mathrm{RA} \leq 300$ region.

In order to pick the particles that best match the observations of the faint branch of the Sgr stream, we use the polynomial fits proposed by Ramos et al. (2021, Table 1) for the $(\tilde{\Lambda}_\odot, \tilde{\beta}_\odot)$ coordinate system centred on Sgr, introduced in Majewski et al. (2003) and representing the latitude and longitude along its stream. We use the slight sign modification of Belokurov et al. (2014) for this coordinate system, in which $\tilde{\Lambda}_\odot$ increases towards the leading arm. In the final snapshot of our simulations, we thus select the test particles with $\tilde{\beta}_\odot$ such that $|\tilde{\beta}_\odot / P(\tilde{\Lambda}_\odot) - 1| < 0.2$ where

$$P(\tilde{\Lambda}_\odot) = -0.0003819\tilde{\Lambda}_\odot^2 + 0.01904\tilde{\Lambda}_\odot + 6.084 \tag{6.3}$$

applies to the leading arm part of the faint branch, and

$$P(\tilde{\Lambda}_\odot) = -0.001563\tilde{\Lambda}_\odot^2 - 0.2805\tilde{\Lambda}_\odot - 3.040 \tag{6.4}$$

applies to the trailing arm part of the faint branch. We also require that $|\tilde{\Lambda}_\odot| \geq 20$ in order to exclude the progenitor. In Figure 6.1, we show the Gaia EDR3 Sgr sample from Ramos et al. (2021), and we over-plot what our faint branch selection of Section 6.3.1 based on Equations (6.3) and (6.4) from our simulations with test particles looks like.

6.3 Results

6.3.1 The faint branch as test particles

We trace our selection of disk particles in the faint stream (see Equations (6.3) and (6.4) and Figure 6.1) back to the initial conditions.

Figure 6.2 shows the fraction of test particles that end up in the faint branch based on initial disk inclination and rotation. We only show the exploitable results: disks rotated around the x-axis by an angle $0° \leq i \leq 180°$ (top-panels) and disks rotated around the y-axis by an angle $180° \leq i \leq 360°$ (bottom-panels). We find that other rotations and angles do not lead efficiently to the creation of a faint branch, with at best $\simeq 2 - 3\%$ of particles ending in the desired regions.
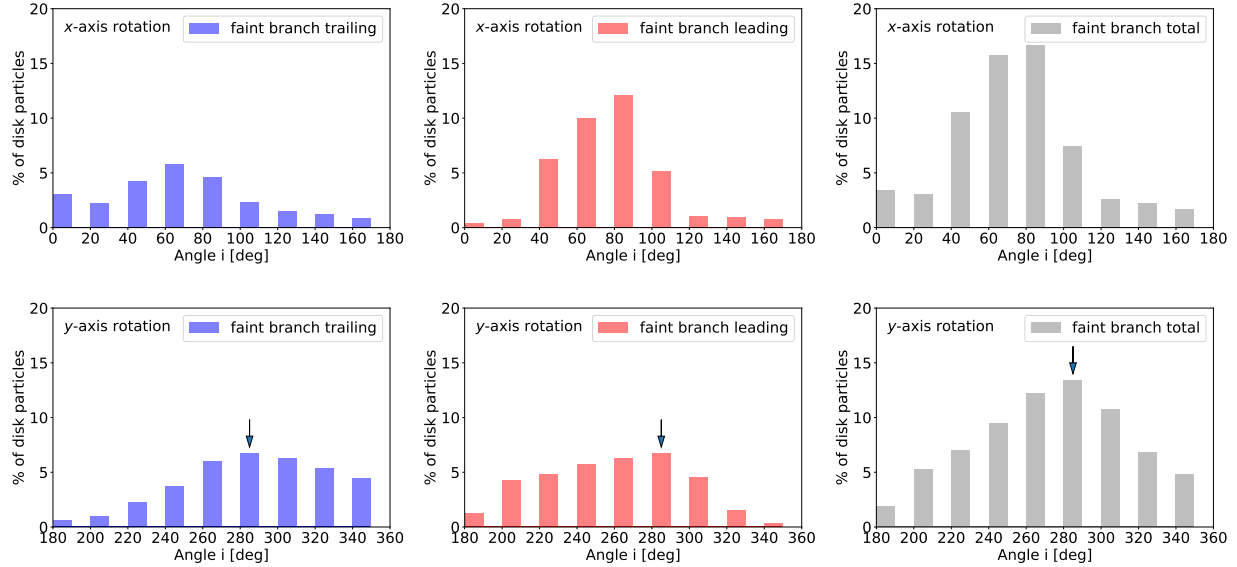
Figure 6.2: Fraction of disk particles that end up in the faint branch for a given disk inclination i. Each inclination angle is probed by a holed disk made of the 2×10^4 outermost test particles, with the holed disk rotated as explained in Section 6.2 around the x-axis (Sun-MW center axis) for the top panels, and around the y-axis for the bottom panels. The arrow points to our best model.

Best model: rotation around the y-axis

The most appealing model consists of a single disk rotated by an angle $i = 280°$ around the y-axis, which leads to a faint branch with roughly the same amount of stars in the leading and trailing parts, as can be seen in Figure 6.2. We pick this option as the preferred model in this work. In this case, the disk almost lies in the yz MW plane, making it nearly perpendicular both to the MW disk ($\sim xy$ MW plane) and to the Sgr orbital plane ($\sim xz$ MW plane).

We thus run another simulation with the single disk rotated by an angle $i = 280°$ around the y-axis added to the model of V21, still as test particles, but keeping this time the full disk, made of 10^5 particles. After this rotation, our disk has angular momentum nearly aligned with the positive x-axis, with a small positive z component. A majority of this initially full disk ends up in the bright branch or near the progenitor, and is not part of our selection. However, picking the disk test particles that end up in the faint branch once more, we are now interested in their distribution in the initial conditions. We find that our selection picks out high energy and angular momentum particles of the disk, and traces spiral arm-like features (Figure 6.3, top-left panel) in the outer disk, which would be sufficient to lead to the creation of the faint branch.

In order to highlight the importance of angular momentum, we note in passing that doing the same exercise (selecting the faint branch and looking back in initial conditions) with the stellar particles of the King model of V21 does not lead to any clear signature distribution in position, energy, or angular momentum.

100
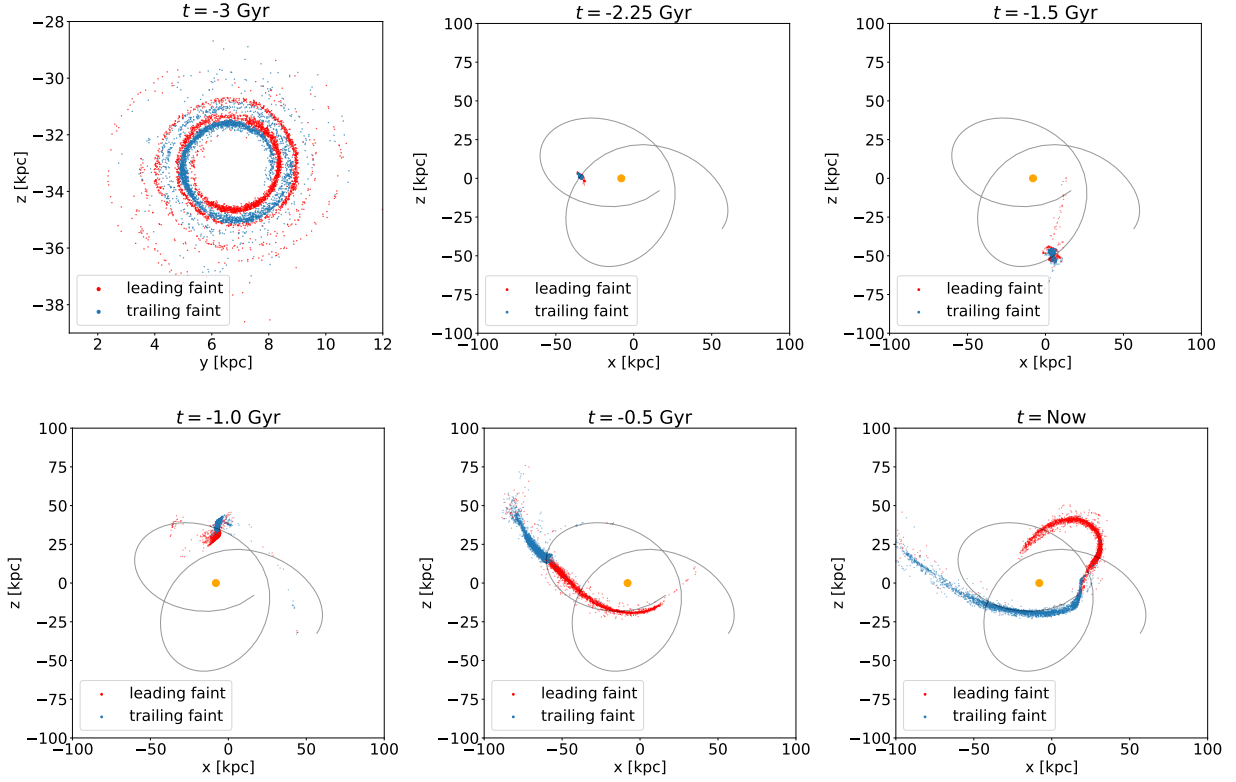
Figure 6.3: Evolution of the faint branch selection, from spirals at the start of the simulation 3 Gyr ago (top-left panel, in the initial disk plane, close to the yz MW plane) to present time (bottom-right panel). The evolution is seen in the xz MW plane, close to the Sgr orbital plane. Particles that will make up the final leading arm are shown in red, and the final trailing arm in blue. The black curve represents the progenitor's orbit, and the orange ball represents the Sun. Pericentric passages of the Sgr occur around $t \simeq -2.3$ Gyr and $t \simeq -1.1$ Gyr. Similar plots for every snapshot of the simulation and the corresponding video are available in the shared data.

Alternative model: rotation around the x-axis

Disks rotated around the x-axis with inclination angles $i = 60°$ and $i = 80°$ are also interesting, with $\simeq 16 - 17\%$ of the particles that end up in the faint branch (Figure 6.2). This is not too surprising: at such inclinations, the disk plane matches closely the Sgr orbital plane. In this configuration, stars in the Sgr disk are on prograde orbits with respect to the orbit of Sgr around the MW. This has been shown in Łokas et al. (2015) to lead to stars being stripped easily, producing thin streams.

The model with a disk rotated by an angle $i = 70°$ around the x-axis is not implausible, but produces slightly worse results than our best disk model rotated by 280 degrees around the y-axis: the trailing arm is harder to populate, and the agreement with Gaia kinematics is not as good. From the Sgr orbital plane, the plane of such a disk makes an angle $-30°$ around the x-axis. This value, which emerges naturally from our probing of the initial conditions when considering rotations around the x-axis, is very close to the value of $-20°$ originally

proposed by Peñarrubia et al. (2010). Data and plots for this model are provided in the repository.

6.3.2 Including self-gravity
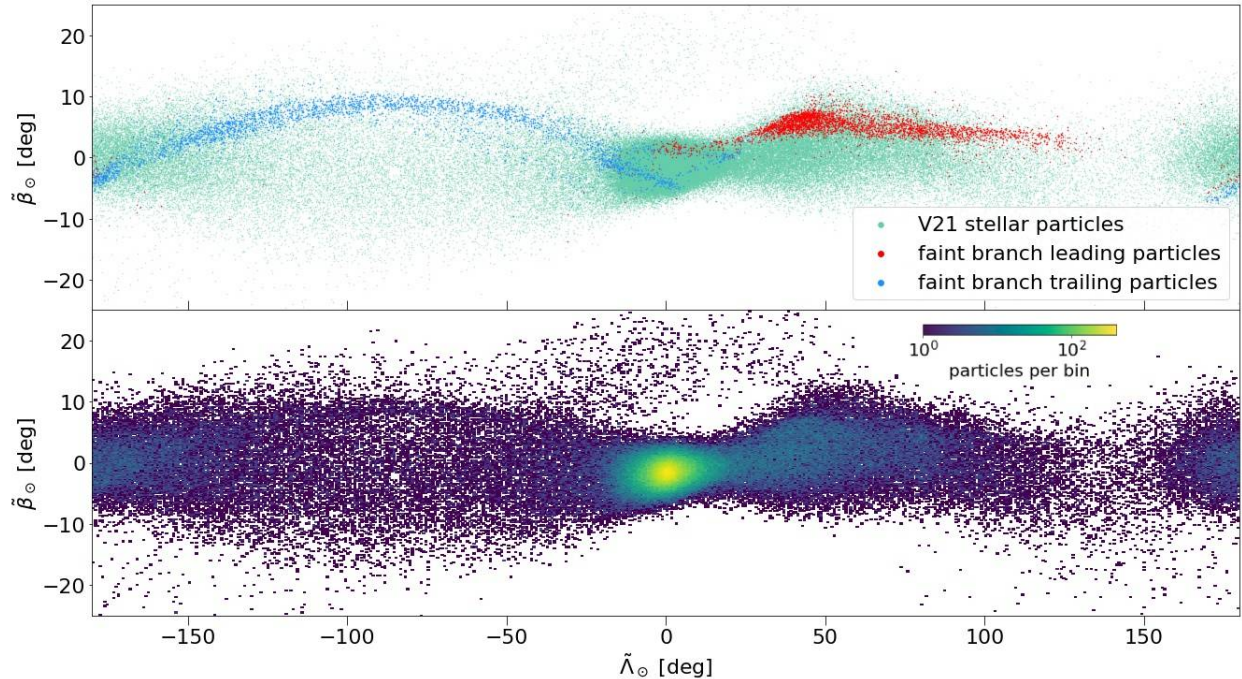
Figure 6.4: Final snapshot of the simulation (at present time) of our model with massive particles replacing some stellar particles of V21's initial model. *Top panel:* The faint branch (red for leading arm, blue for trailing arm) is well populated over-plotted on V21's particles (green). *Bottom panel:* Density plot of all stream stars (V21's stellar particles plus our faint branch particles).

We now study whether the results of the previous section, obtained assuming that disk stars are mass-less tracers of the underlying potential, also hold when taking into account the self-gravity between disk stars. This will allow us to put forward a model that creates a faint branch like the one observed in the Sgr stream, using the initial conditions and gravitational potential of V21 as a backbone. In the Gaia EDR3 sample of Sgr of Ramos et al. (2021), stars with probability $\geq 80\%$ of being part of the faint branch make up $\simeq 4\%$ of the total. We thus aim to be close to this ratio, and replace 6600 of the 2×10^5 stellar particles in the V21 model by new ones following our initial disky distribution. In order to include our particles into the reference model, we give them the same mass as the stellar particles of V21, and for each particle that we include, we remove one stellar particle from V21 sitting at the closest radius from that of our particle. Doing so ensures that we keep the same total mass, and does not alter the non-linear dynamics too much.

We follow the evolution of our faint branch selection along the simulation in Figure 6.3, from initial spirals to eventually forming the faint branch. Our selection remains largely bound with angular momentum still pointing towards the positive x direction until the second

pericentric passage (around $t \simeq -1.1$ Gyr), which strips the faint branch particles from the progenitor.

Figure 6.4 (top panel) shows the $\tilde{\Lambda}_\odot$-$\tilde{\beta}_\odot$ view of the simulation at present time. The faint branch can be seen to be well populated, although with self-gravity now playing a role, a few of our particles end up close to the progenitor.

An issue is that the thick stream of the V21 model extends to the faint branch region already, resulting in an overly dense faint branch in Figure 6.4 (bottom panel). In a complete bifurcation model, the bright branch should ideally be thinner, which could probably be achieved with *e.g.* a different initial density profile, or a non-equilibrium transitional situation. We leave this exploration to a future study.

We compute the mean line-of-sight velocity in the remnant of the progenitor to make sure that our faint branch particles did not perturb the spherical model of V21 by adding significant rotation. We find a gradient of ~ 10 km s^{-1}, similarly to the pressure-supported model of Peñarrubia et al. (2011, Fig. 2).

Interestingly, we note an over-density of our particles in the $-180° \leq \tilde{\Lambda}_\odot \leq -130°$ region ($70° \leq \mathrm{RA} \leq 120°$), for which we do not have Gaia data. This signature appeared in all our simulations with disks of inclination close to that of the chosen model. It would be interesting to see if such an over-density can be observed.

Finally, we compare in Figure 6.5 our faint branch particles to the faint branch selection (probability $\geq 80\%$) from the Gaia EDR3 sample of Ramos et al. (2021). The radial velocities follow the observed trend for the faint branch in the trailing and leading arms, and are different from those of the bright branch in agreement with the data. We remind that our initial selection has been made purely in configuration space, so that this phase-space agreement is impressive. For proper motions, the difference in trends between the bright and faint branches is small in the data, as can be seen in Ramos et al. (2021, Fig. 3). We note in passing that our faint branch simulation has smaller scatter than the observed data in proper motions, probably due to both intrinsic dispersion (both in velocity and distance) and observational uncertainties. However, transforming our model into star particles with magnitudes and hence Gaia astrometric uncertainties is far beyond the scope of this contribution.

6.4 Discussion

Despite the obvious similarities with a full disk model (Peñarrubia et al., 2010), there are a few differences. For one, this spiral disky distribution allows to populate only the faint branch and can be combined with a more massive spherical model to also populate the bright branch. It also alleviates the issue of requiring substantial rotation in the progenitor's remnant at present time (Peñarrubia et al., 2011). While out of the scope of the present work to produce a full Sgr model, we discuss possibilities that would lead to the presence of our faint branch selection and how the inner Sgr could be populated.

A possible scenario for the presence of this disky spiral distribution 3 Gyr ago could be a disky dwarf perturbed by tidal effects (Gajda et al., 2017), and/or having been affected by disk-shocking while crossing the MW-disk. In addition to the spirals, the rest of the disk could be transitioning to a pressure supported spheroidal galaxy as in the tidal stirring mechanism (Mayer et al., 2001). In this context, the inner galactic disk often goes through
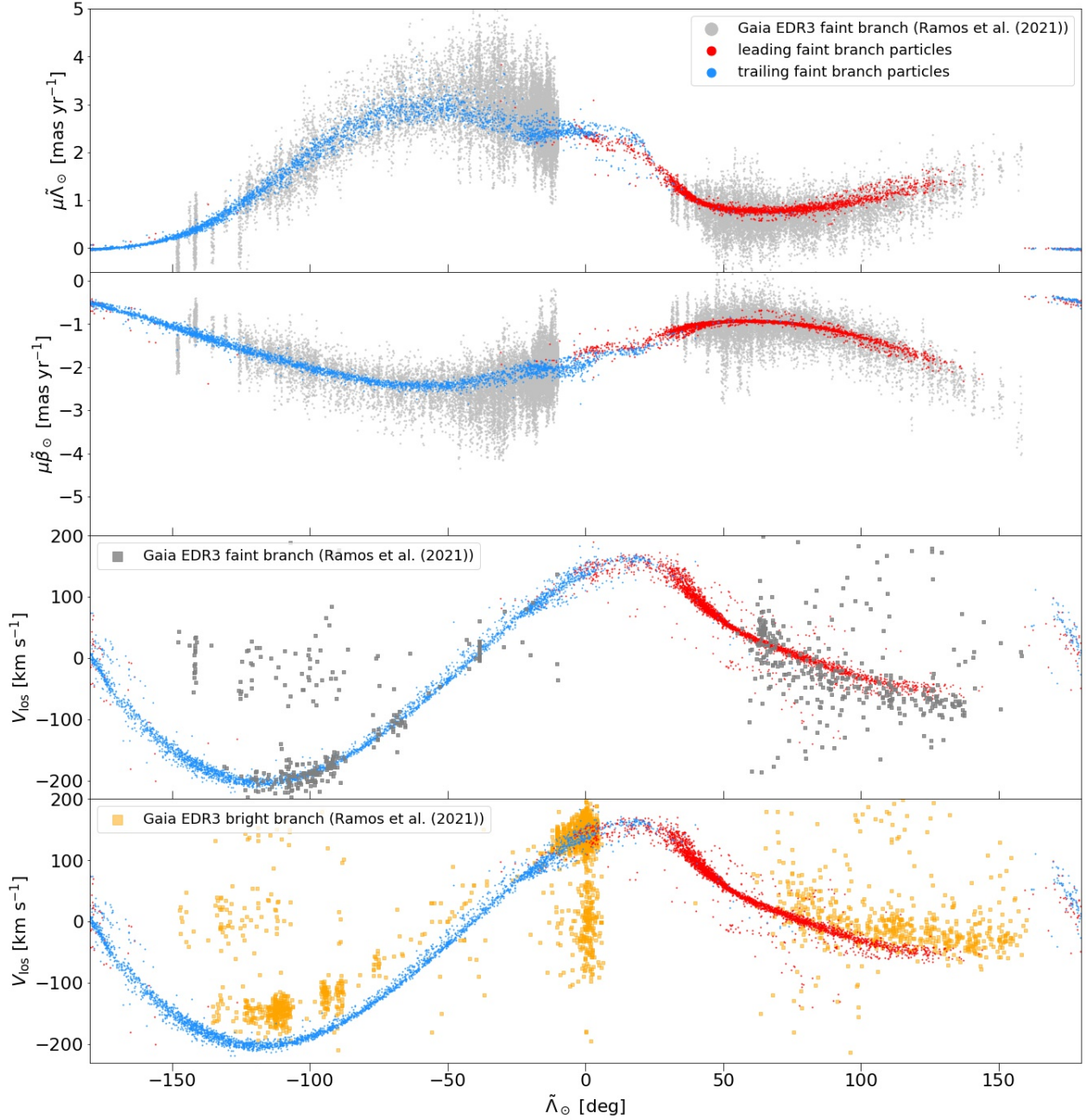
Figure 6.5: Comparison of the faint branch (probability $\geq 80\%$) from the Gaia EDR3 Sgr sample of Ramos et al. (2021, grey) with the faint branch selection in our N-body model including self-gravity (red for leading arm, blue for trailing arm). From top to bottom: proper motions in $\tilde{\Lambda}_\odot$, in $\tilde{\beta}_\odot$, and line-of-sight velocities (heliocentric reference frame). For comparison, the bottom panel shows bright branch members (probability $\geq 80\%$, yellow).

a bar perturbation (Kazantzidis et al., 2011a; Łokas et al., 2014). It is thus possible that a bar would be present in Sgr 3 Gyr ago. With tidal heating, the bar transforms into a diffuse spheroid, part of which would then end up in the bright branch of the stream, and the rest would form the elongated remnant of the progenitor that is now observed. This model

is attractive because both branches of the Sgr stream would come from the same stellar population, consistent with the small difference observed in metallicity between the faint and bright branches (Ramos et al., 2021).

Another possibility would be that Sgr was already having a substantial spheroidal component and that only a remaining rotating disk was affected. Indeed, fitting a full exponential density profile from the surface density profile of our spiral selection and extrapolating it to the inner disk, we find that a total disk mass of $2 \sim 3 \times 10^7$ M$_\odot$, or $10 \sim 15\%$ of the mass of the stellar component in V21's model would be sufficient (the mass range depending on the proportion of faint branch stars, $\simeq 4\%$ of stream stars in the data). Such a minor disk component would produce a very low rotation signal in the Sgr remnant at present time.

The spiral features could also be the tidal tails or stellar stream of an accreted globular cluster or dwarf galaxy inside the Sgr system. This is however less enticing as it would require the stellar populations of Sgr and the putative satellite to be fairly similar.

It is also interesting to compare the stripping history and geometry of this faint branch to full models (see *e.g.* Ramos et al. 2021, their Fig. 7). As shown in Figure 6.3 and in the shared material, our particles for the leading and trailing faint branch are both mostly stripped during the second pericenter of the simulation ($t \simeq -1.1$ Gyr). In addition, this stripping produces a single "upper" faint branch that can be paired with another Sgr component that would produce the parallel bright branch, as opposed to the undesired "X-shape" (Ramos et al., 2021) that is usually obtained when considering inner rotation and/or orbital precession.

6.5 Conclusion

We propose a model for the bifurcation of the Sgr stream in which the faint branch is populated by stars that were distributed in a disky spiral distribution within the progenitor 3 Gyr ago, in a plane nearly perpendicular to both the Sgr orbital plane and the MW disk plane. This pattern emerged here naturally by probing a large range of initial position, energy and angular momentum distributions for stellar test particles that end up in both the leading and trailing parts of the observed faint branch. Populating the faint branch this way opens the possibility of freely pairing this work with other Sgr components that would produce the parallel bright branch.

In the context of the tidal stirring mechanism studied in detail in Kazantzidis et al. (2011a) for the formation of dwarf spheroidals, Sgr could previously have been a disky galaxy which 3 Gyr ago already held a bar (Łokas et al., 2014) and started the transition from a disky galaxy to a more isotropic and diffuse one. Low rotational velocity would then be observed today in the remnant, in agreement with del Pino et al. (2021). The spiral features could be tidally-induced, bar-induced, or the result of disk shocking when crossing the MW. Although out of scope for the present study, it would be very interesting to see if this could be turned into a working model for the entire Sgr stream.

Another interesting albeit less likely possibility would be that this spiral distribution is the tidal tail or stellar stream caused by the disruption of a satellite of the Sgr system. Further observations of the stellar populations and their detailed chemistry in both the bright and faint branch will likely provide very useful information in deciding this matter.

Data Availability

We make available our addition to the model of V21 (DOI 10.5281/zenodo.4300977), including the particles leading to the creation of the faint branch as well as plots, a movie, and all related scripts, at DOI 10.5281/zenodo.6581185.

Chapter 7   Antaeus: retrograde tidal debris in the MW's disk plane

Still in the context of galactic archeology in the stellar halo of the Milky Way, we have been eager to take a look at the recent DR3 of *Gaia* and especially its new radial velocities, for which the sample of stars is ~ 4 times as large as in the previous data release. In this Chapter and the next, we present newly-discovered structures which are new pieces in the stellar halo conundrum, and whose origins, quite likely linked to major accretion events, might bring key elements for our understanding of our Galaxy's history.

Foreword

This is a slight modification, to fit this manuscript, of the work of Oria, P.-A.; Tenachi, W.; Ibata, R.; Famaey, B.; Yuan, Z.; Arentsen, A.; Martin, N.; Viswanathan, A. which has been accepted for publication in the Astrophysical Journal Letters (ApJL) (Oria et al., 2022b).

Abstract

We present the discovery of a wide retrograde moving group in the disk plane of the Milky Way using action-angle coordinates derived from the *Gaia* DR3 catalog. The structure is identified from a sample of its members that are currently almost at the pericenter of their orbit and are passing through the Solar neighborhood. The motions of the stars in this group are highly correlated, indicating that the system is probably not phase mixed. With a width of at least $1.5\,\mathrm{kpc}$ and with a probable intrinsic spread in metallicity, this structure is most likely the wide remnant of a tidal stream of a disrupted ancient dwarf galaxy (age $\sim 12\,\mathrm{Gyr}$, $\langle[\mathrm{Fe/H}]\rangle \sim -1.74$). The structure presents many similarities (e.g. in energy, angular momentum, metallicity, and eccentricity) with the Sequoia merging event. However, it possesses extremely low vertical action J_z which makes it unique even amongst Sequoia dynamical groups. As the low J_z may be attributable to dynamical friction, we speculate that the these stars may be the remnants of the dense core of the Sequoia progenitor.

7.1 Introduction

The complex formation and merging history of the Milky Way (MW) can perhaps be best understood by examining its stellar halo, host to many tidal debris of disrupted galaxies and globular clusters. Dynamical times in the halo are long, so the debris can persist there as coherent phase space structures for billions of years (see e.g. Helmi & de Zeeuw 2000), making them easier for us to detect.

With the advent of the *Gaia* mission (Gaia Collaboration et al., 2016) and its superb astrometric data, the task of digging into the stellar halo to uncover the past has been made more accessible. The stellar halo of the MW is now understood to be the product of several important accretion events making up most of its population (Di Matteo et al., 2019), the biggest of which being Gaia-Sausage/Enceladus (Belokurov et al., 2018; Helmi et al., 2018). Stream finding algorithms (Malhan et al., 2018; Ibata et al., 2021) have now detected dozens of kinematically coherent structures which will help chart the acceleration field of our Galaxy, providing a wealth of model-agnostic information.

The *Gaia* data also makes it possible to use action coordinates (J_r, J_ϕ, J_z) to detect stellar structures. Actions keep relevance over very long times if the potential evolves slowly and are thus especially useful to trace past mergers. Recently, Yuan et al. (2020), Naidu et al. (2020) and Malhan et al. (2022b) used these quantities to detect and construct maps of the MW's dynamical groups and link them to important merger events.

A similar technique was employed by Myeong et al. (2018) to find several retrograde structures in the stellar halo, which were then tentatively associated to the ω Centauri globular cluster, which Majewski et al. (2012) had already suspected of bringing in such material. Retrograde structures have been linked to accretion events for a long time (Carollo et al., 2007), and it has been confirmed by Helmi et al. (2017) that the less bound stars in the halo are typically on retrograde orbits. Sestito et al. (2021) also highlight the importance of the metal poor retrograde halo population for tracing the early building blocks of the galaxy.

Myeong et al. (2019) reexamined the structures from Myeong et al. (2018) and linked them to a substantial merger event they named Sequoia. The Sequoia progenitor galaxy could have brought those retrograde groups and possibly ω Centauri as well. The fact that its stellar population is distinct in metallicity and orbital parameters from the Gaia-Sausage makes the event another important piece of the stellar halo puzzle.

In this work we present the discovery of Antaeus[1], a retrograde high energy group of tidal debris in the MW's disk plane, made using action-angle coordinates derived from the *Gaia* DR3 catalogue (Gaia Collaboration, 2022) and the Stäckel fudge implemented in AGAMA (Vasiliev, 2019). The new structure has several properties which are similar to those of Sequoia stars, so we discuss its possible affiliation to this event, although both its position in the disk of the MW and its extraordinary low vertical action make it stand out.

---

[1]In Greek mythology, Antaeus is the child of Gaia and Poseidon, a giant whose name comes from "opponent".
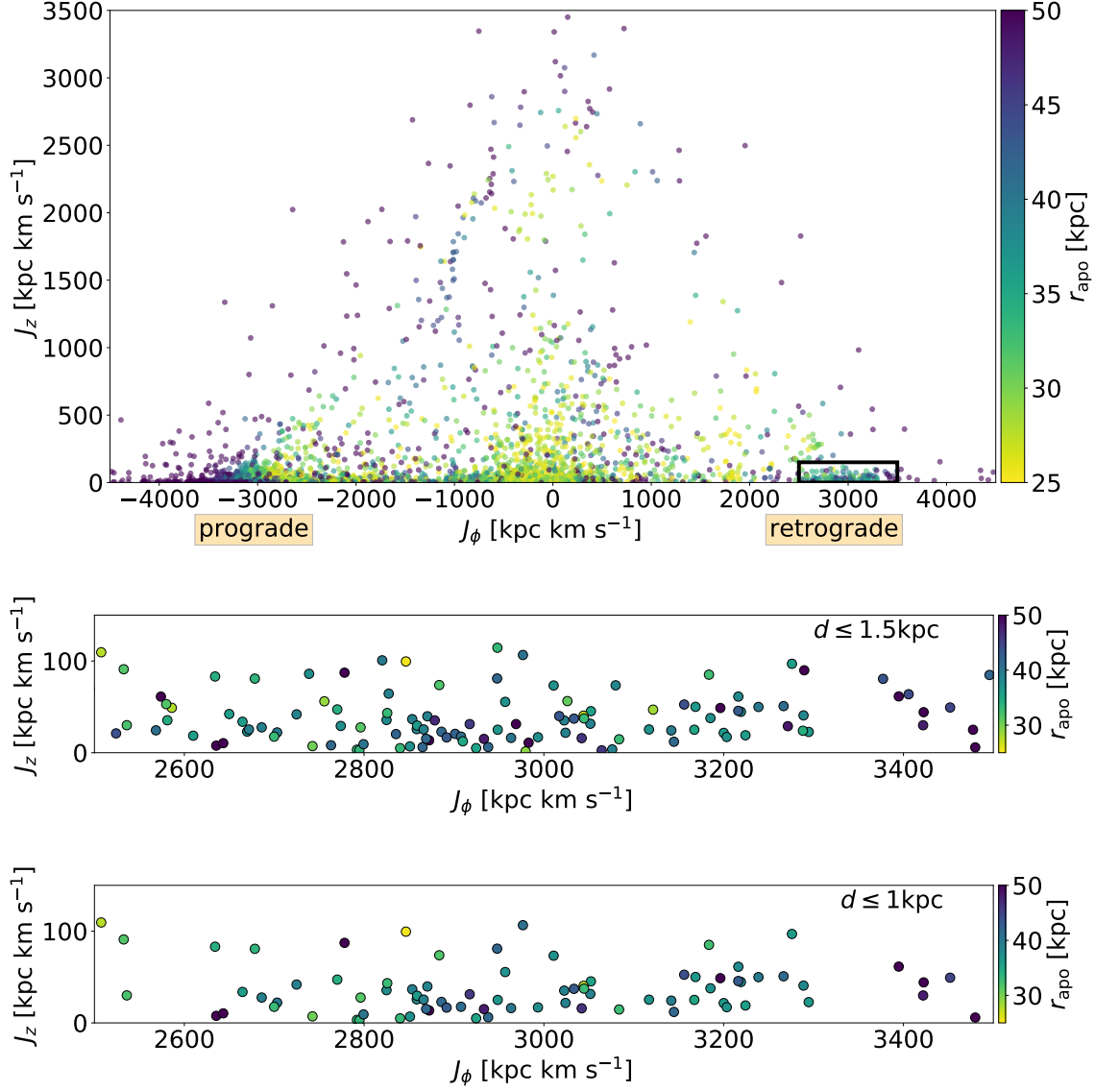
Figure 7.1: Selection procedure. Top panel: *Gaia* DR3 stars from the selection process described in Section 7.2 (i.e. $\varpi/\delta\varpi > 10$, $r_{apo} \geq 25\,\mathrm{kpc}$ and $d \leq 1.5\,\mathrm{kpc}$). Middle panel: zoom on the low J_z region delimited by the rectangle in the top panel ($2500 \leq J_\phi \leq 3500\,\mathrm{km\,s^{-1}\,kpc}$, $J_z \leq 150\,\mathrm{km\,s^{-1}\,kpc}$). Bottom panel: same region as the middle panel, but for our final cut using distances $d \leq 1\,\mathrm{kpc}$ from the Sun.

7.2 Selection process

Throughout this article, we use the right-hand side Galactic Cartesian coordinates for the MW with the Sun located at $(x, y, z)_\odot = (-8.2240, 0, 0.0028)\,\mathrm{kpc}$ (taking the Solar radius from Bovy 2020 and the height above the mid-plane from Widmark et al. 2021) having peculiar velocity $(v_x, v_y, v_z)_\odot = (11.10, 7.20, 7.25)\,\mathrm{km\,s^{-1}}$ (Schönrich et al. 2010, but with the velocity in the direction of Galactic rotation taken from Bovy 2020), and circular velocity
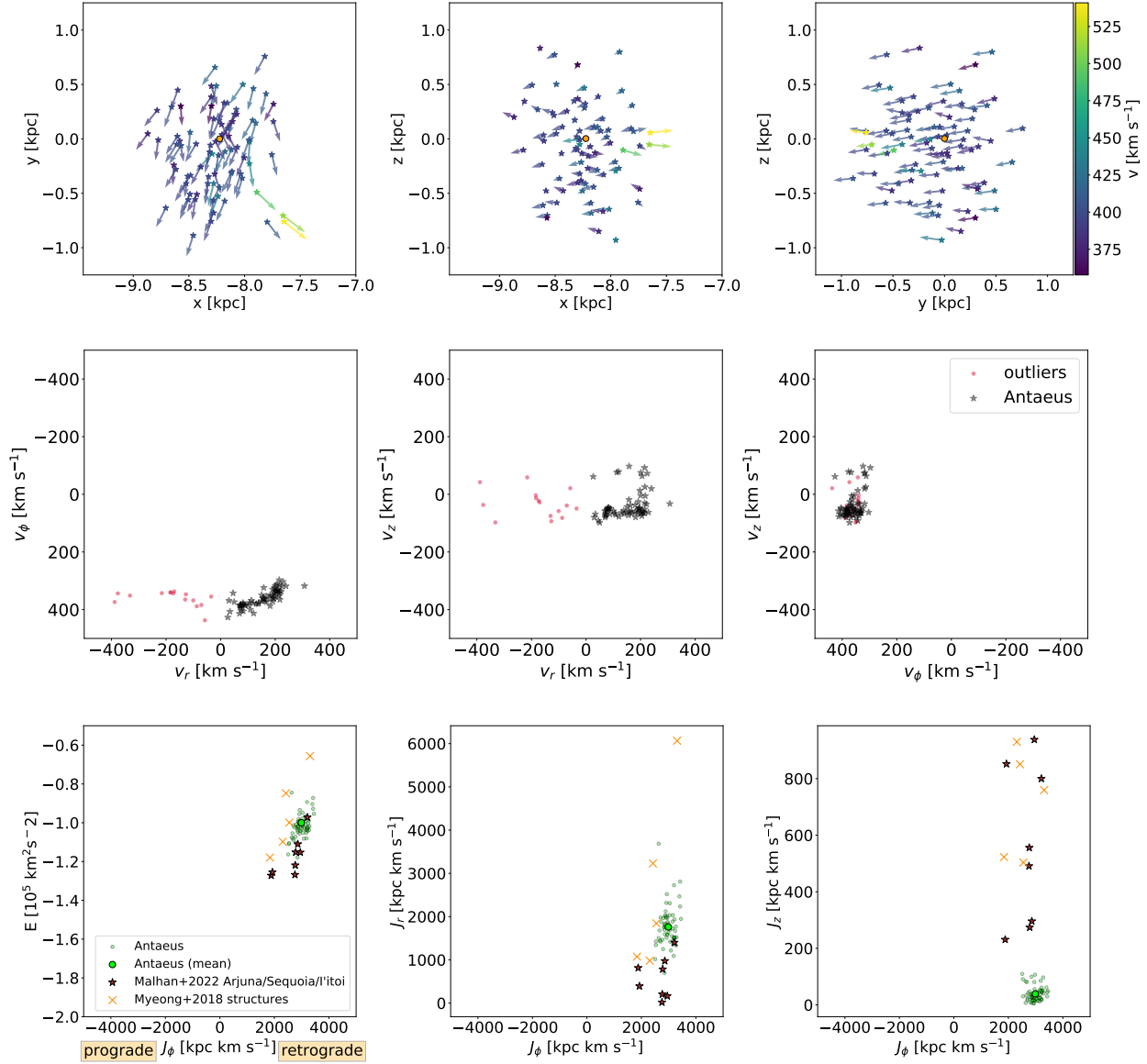
Figure 7.2: Top panel: position and velocity vectors of our selection of stars from Section 7.2 colored by total velocity; we plot bulk motion outliers with a slightly transparent line. The orange ball represents the Sun. Antaeus stars are currently passing through our Solar neighbourhood, going in a retrograde motion in the Milky Way's disk plane. Middle panel: velocity planes $v_r v_\phi$, $v_r v_z$, $v_\phi v_z$ with the outliers (red dots) from the top panel bulk motion separated from Antaeus' stars (black). Note that we inverted the v_ϕ axes to be coherent with usual velocity plots. Bottom panel: position of Antaeus (green dots) in energy E and actions J_r, J_ϕ, and J_z, compared to Sequoia-associated retrograde structures from Myeong et al. (2018) (orange crosses) and Arjuna/Sequoia/I'itoi-associated streams and globular clusters from Malhan et al. (2022b) (brown stars).

$v_c(r = r_\odot) = 243 \, \text{km s}^{-1}$ (Bovy, 2020). Our starting point is the Radial Velocity Spectrometer (RVS, Recio-Blanco et al. (2022)) sample of *Gaia* DR3, for which we derive action-angle

coordinates (J_r, J_ϕ, J_z) and orbital parameters using AGAMA (Vasiliev, 2019) in the MW gravitational potential of McMillan (2017). From this catalogue, we take the stars with good parallax measurements ($\varpi/\delta\varpi \geq 10$) and $d \leq 1.5\,\mathrm{kpc}$ so as to retain a good quality Solar neighborhood sample. Since our aim is to investigate the structures that are falling down onto the Milky Way, we choose to select stars with large apocenter distances, $r_{\mathrm{apo}} \geq 25\,\mathrm{kpc}$. These cuts leave us with 3624 stars; we plot the resulting selection in the $J_\phi J_z$ plane, coloured by r_{apo}, in Figure 7.1 (top panel).

Among the many interesting structures that stand out from this view, we focus our attention on the low J_z, retrograde moving group of stars delimited by the black rectangle ($2500 \leq J_\phi \leq 3500\,\mathrm{km\,s^{-1}\,kpc}$, $J_z \leq 150\,\mathrm{km\,s^{-1}\,kpc}$), into which we zoom in Figure 7.1 (middle panel). We notice a good agreement in apocenters for stars in this region, further suggesting the presence of a stellar structure with coherent motion.
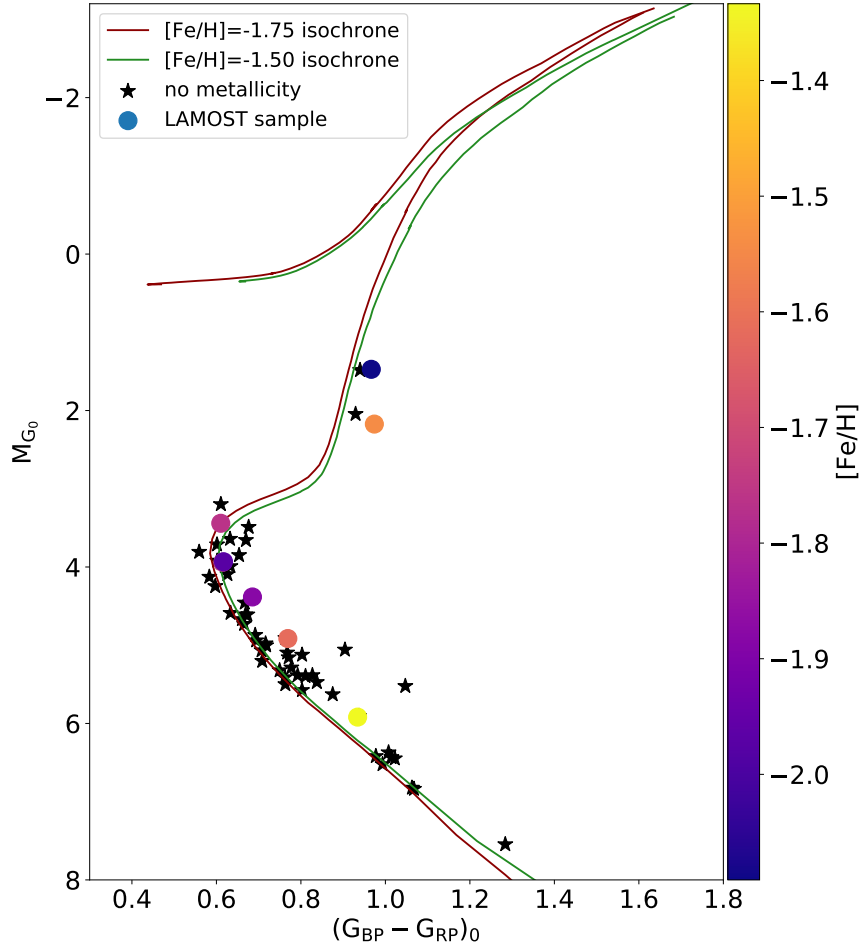
Figure 7.3: Colour magnitude diagram for our sample of Antaeus stars, compared to PARSEC model isochrones (Bressan et al., 2012) of age $12\,\mathrm{Gyr}$ and metallicities $\mathrm{[Fe/H]} = -1.75$ (red) and $\mathrm{[Fe/H]} = -1.50$ (green). The colorbar gives the $\mathrm{[Fe/H]}$ for the 8 LAMOST stars.

Finally, we experimented with the heliocentric distance cut to see how the selection changes. We noticed that by selecting stars within a distance of $d \leq 1\,\mathrm{kpc}$ from the Sun

(Figure 7.1, bottom panel) the agreement in apocenters is slightly better, removing in particular some extreme values from the previous cut. This leaves a sample of 80 stars.

In order to establish the statistical significance of this detection, we repeat the same selection on the *Gaia* Universe Model Snapshot (GUMS, Robin et al. (2012)) simulation updated for DR3. The initial $d \leq 1.5$ kpc cut on GUMS gives 3781 stars, very close to the number of stars in our DR3 selection. Normalizing for this small difference, we find that there is, in the final selection (black rectangle), more than 5 times the number of stars in DR3 than there is in GUMS. Furthermore, the distribution along the J_ϕ axis is bimodal in the GUMS data, with a main peak in the prograde region ($J_\phi \approx -3000$) and a small peak around $J_\phi = 0$, while the same distribution in our DR3 selection is trimodal with an additional peak in the retrograde region ($J_\phi \approx 3000$) corresponding to Antaeus, and the peak around $J_\phi = 0$ being more pronounced. Using the GUMS simulation as an estimate of the expected Galactic populations, the Antaeus feature corresponds to a $\approx 7\sigma$ detection.
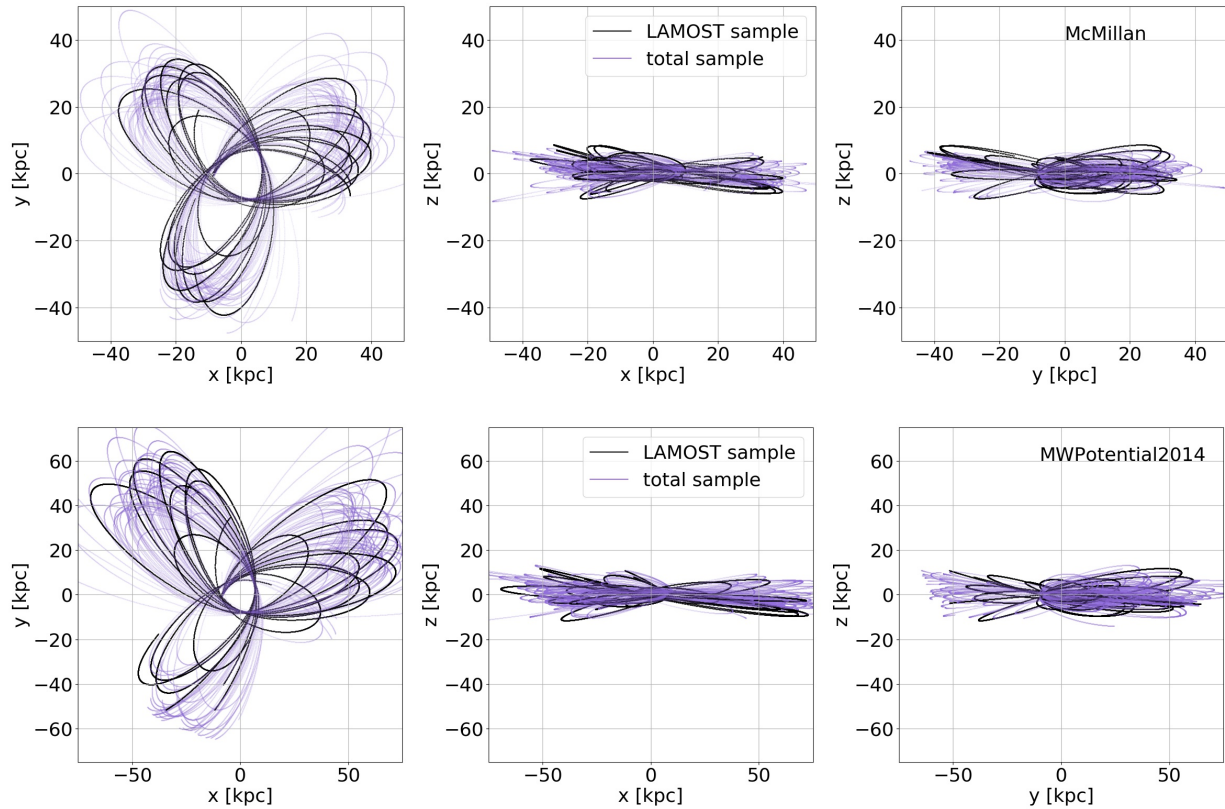
Figure 7.4: Orbits of Antaeus stars seen in Galactic Cartesian coordinates, integrated backwards in the McMillan (2017) MW potential for 1.5 Gyr (top panel), and in the MWPotential2014 model for 2.5 Gyr (bottom panel). Notice the change of scales, as stars go farther when integrated in the lighter MWPotential2014. Orbits of the LAMOST sample (8 stars) are in solid black, and orbits of the rest of our sample (57 stars) are in purple.

7.3 Sample characteristics

We show the positions and velocities of our selection of stars in Figure 7.2 (top panel). It appears clear that the stars belong to a coherent structure dynamically, moving in a retrograde motion in the disk plane of the MW. The structure is rather thick, with a width of at least 1.5 kpc. We identify some outliers from this bulk motion, which all have a distinctive positive velocity in the x direction ($v_x \geq 0$). For the remainder of this study, we will exclude those 15 outliers from our sample, leaving us with 65 stars of the Antaeus stream. In Figure 7.2 (middle panel), we plot velocity planes $v_r v_\phi$, $v_r v_z$, $v\phi, v_z$ with this separation taken into account, showing the compactness of Antaeus stars in those projections.

We crossmatch our selection with the LAMOST DR8 catalogue (Wang et al., 2022) and find 8 stars in common, for which we obtain metallicities from their "FEH_PASTEL" values. These LAMOST stars have a mean [Fe/H] $= -1.74^{+0.06}_{-0.07}$, with an intrinsic spread of $\sigma = 0.11^{+0.10}_{-0.04}$ (correcting for the LAMOST metallicity uncertainty estimates) and individual values ranging from [Fe/H] $= -1.33 \pm 0.23$ to [Fe/H] $= -2.09 \pm 0.30$. The colour magnitude diagram (CMD) of the sample is shown on Figure 7.3, compared to old metal poor isochrones (12 Gyr, [Fe/H] $= -1.75$ and [Fe/H] $= -1.50$) from the PARSEC library (Bressan et al., 2012). The photometry is corrected for interstellar extinction using the 3D extinction estimates calculated by Anders et al. (2022).

Finally, we integrate back in time the orbits of the Antaeus stars in the McMillan MW potential for 1.5 Gyr, and in the MWPotential2014 (Bovy, 2015); we show the results in Figure 7.4. Here also the structure appears very coherent dynamically. We find, for the McMillan MW potential ($M_{\rm vir} = 1.3 \times 10^{12}\,M_\odot$), a mean pericenter radius of $r_{\rm peri} = 7.3$ kpc, a mean apocenter radius of $r_{\rm apo} = 39.3$ kpc, a mean orbital eccentricity of $ecc = 0.69$, and a mean orbital time of $t_{\rm orbit} = 1.1$ Gyr. For the lighter MWPotential2014 however ($M_{\rm vir} = 8 \times 10^{11}\,M_\odot$), those values become mean $r_{\rm peri} = 7.3$ kpc, mean $r_{\rm apo} = 71.9$ kpc, mean $ecc = 0.81$, and mean $t_{\rm orbit} = 1.5$ Gyr. The 8 LAMOST stars, whose orbits are plotted in solid black, appear to be good representative members of the stream.

The mean actions of stars in the structure are ($J_r = 1761, J_\phi = 2990, J_z = 39$) kpc km s^{-1}, and their mean energy is $E = -10^5$ km^2 s^{-2} (in the McMillan 2017 potential model); we show this information for individual stars in Figure 7.2 (bottom panel).

7.4 Discussion and conclusions

Based on the characteristics derived in Section 7.3, in particular the thickness of the structure (width $\simeq 1.5$ kpc) and the range of metallicity of its constituent stars, it seems highly likely that this group of stars is the remnant of a tidal stream of a disrupted dwarf galaxy. The CMD (Figure 7.3) seems to indicate that the progenitor is likely to be very old, probably around ~ 12 Gyr in age. The agreement is better with a model metallicity of [Fe/H] $= -1.50$, although we derive a mean value of [Fe/H] $= -1.74^{+0.06}_{-0.07}$. It would thus be very helpful to extend our sample of metallicities to help decide the matter. Such metallicities give an estimated stellar mass of 10^6 to $10^7\,M_\odot$ according to the $z = 0$ mass-metallicity relation of Kirby et al. (2013). Taking into account the redshift evolution of such relations (for a given metallicity, higher mass at higher redshift is required), we can consider

that those constitute lower bounds and that the progenitor probably has a rather high stellar mass of $\geq 10^7 \, M_\odot$, making it likely that it is linked to an already known accretion event.

Indeed, when comparing with known halo structures, we find that the mean J_ϕ, energy, and eccentricities of our sample of Antaeus stars show many similarities with the Arjuna/I'itoi/Sequoia group of mergers (Naidu et al., 2020). However Antaeus seems more akin to the retrograde structures of Myeong et al. (2018) and to the retrograde tail of the Sequoia event (Myeong et al., 2019) (see the bottom row in Figure 7.2 for a comparison to the previously mentioned groups), especially when factoring in the metallicity of its population. The $\sim 12 \, \mathrm{Gyr}$ age derived from the CMD comparison is also consistent with estimates for Sequoia groups (Ruiz-Lara et al., 2022).

Nonetheless, Antaeus' extraordinarily low mean J_z and its position in the disk plane of the MW both make it unique, even when compared to the global atlas of halo structures from Malhan et al. (2022b). It may be the distinct, low J_z tail of the L-RL64 cluster discovered by Ruiz-Lara et al. (2022) and also detected by Dodd et al. (2022). If the structure is indeed related to Sequoia, this difference has to be explained.

The mere existence of such a streamy, retrograde structure in the disk of the MW is very puzzling. It is not clear how such kinematic coherence could be retained if this population came in with Sequoia $9 \sim 11 \, \mathrm{Gyr}$ ago (Myeong et al., 2019). Of course Antaeus' progenitor could have arrived initially with a small inclination, although this possibility appears somewhat contrived. See however the simulations from Amarante et al. (2022) in which nearly radial mergers could potentially produce such populations. It seems more natural to explain the very low quantity of vertical motion by dissipation due to dynamical friction, which might be consistent with an early arrival in the MW. This scenario would invite the possibility that Antaeus is the debris of the dense core of the Sequoia progenitor, which would have stabilized in the disk through dynamical friction before tidal disruption completely destroyed it.

The discovery of Antaeus opens many exciting possibilities for follow-up studies. A first step would be finding other members of the structure in *Gaia* with the information we now possess. Creating an N-body model for the infall of the progenitor dwarf galaxy in the potential well of the MW and exploring the possibilities for its survival in the disk would also be highly informative. Finally, it would be very helpful to measure the metallicity of more stars of our selection in order to facilitate discussions regarding the origin of the structure, and links to Sequoia in particular.

Data Availability

The sample of Antaeus stars is available at DOI 10.5281/zenodo.6912366.

Chapter 8 Typhon: a polar stream from the outer halo

Foreword

This is intended to be a quick review of the main results from the work of Tenachi, W.; Oria, P.-A.; Ibata, R.; Famaey, B.; Yuan, Z.; Arentsen, A.; Martin, N.; Viswanathan, A. For technical details and the complete work, please refer to (Oria et al., 2022b), which has been accepted for publication in the Astrophysical Journal Letters (ApJL).

Abstract

We report on the discovery in the Gaia DR3 astrometric and spectroscopic catalog of a new polar stream that is found as an over-density in action space. This structure is unique as it has an extremely large apocenter distance, reaching beyond 100 kpc, and yet is detected as a coherent moving structure in the Solar neighborhood with a width of $\sim 4\,\mathrm{kpc}$. A sub-sample of these stars that was fortuitously observed by LAMOST has a mean spectroscopic metallicity of $\langle[\mathrm{Fe/H}]\rangle = -1.60^{+0.15}_{-0.16}$ dex and possesses a resolved metallicity dispersion of $\sigma([\mathrm{Fe/H}]) = 0.32^{+0.17}_{-0.06}$ dex. The physical width of the stream, the metallicity dispersion and the vertical action spread indicate that the progenitor was a dwarf galaxy. The existence of such a coherent and highly radial structure at their pericenters in the vicinity of the Sun suggests that many other dwarf galaxy fragments may be lurking in the outer halo.

8.1 Introduction

In the same astrophysical context as in Chapter 7, *i.e.* the third data release of *Gaia* allowing us to probe the stellar halo of the MW, and using similar techniques, we report on the detection of another coherent structure. Typhon is a polar stream with apocenter at the edge of the galactic halo ($\geq 100\,\mathrm{kpc}$) currently passing through the Solar neighbourhood.

8.2 Selection and characteristics
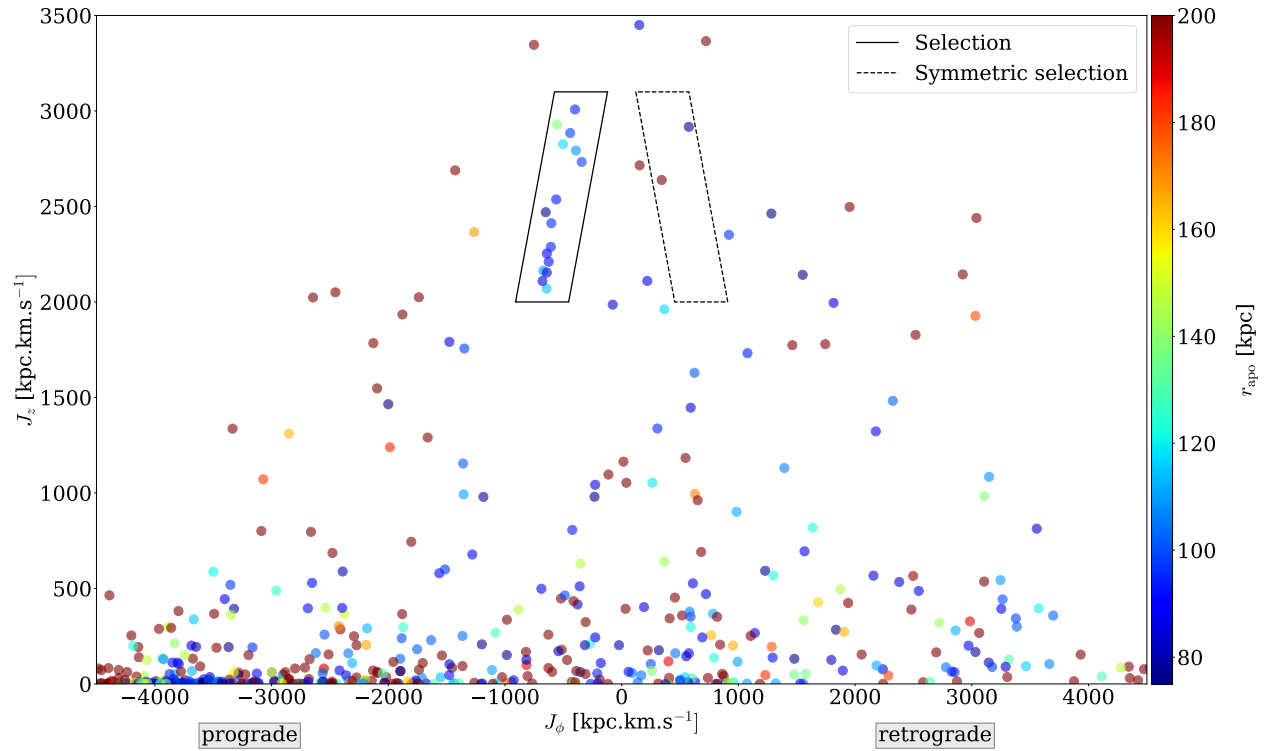
Figure 8.1: (J_ϕ, J_z) actions of the 573 stars having $\varpi/\delta\varpi > 10$, $r_{apo} > 75\,\mathrm{kpc}$ and $d_\odot < 4\,\mathrm{kpc}$, colored by their apocenter values in the potential model of McMillan (2017). The parallelogram selection of the structure depicted in a solid line encompasses 16 stars and is based on the following constraints: $J_z \in [2000, 3100]$ and $3.3J_\phi + 3500 < J_z < 3.3J_\phi + 5000$. The symmetric (retrograde) selection with respect to the $J_\phi = 0$ line is shown with a dashed line.

We use the same initial selection and transformation on the Radial Velocity Spectrometer sample of *Gaia* DR3 as for Antaeus in Section 7.2 (in fact, Typhon is visible in Figure 7.1 if one knows where to look).

The detailed selection for Typhon is visible in Figure 8.1. There, a polar structure can be spotted as a tight, almost vertical, linear grouping between $(J_\phi \sim -650\,\mathrm{kpc\,km\,s^{-1}}, J_z \sim 2100\,\mathrm{kpc\,km\,s^{-1}})$ and $(J_\phi \sim -400\,\mathrm{kpc\,km\,s^{-1}}, J_z \sim 3000\,\mathrm{kpc\,km\,s^{-1}})$. We find that this feature is most striking when the sample is limited to stars with heliocentric distances $d_\odot < 4\,\mathrm{kpc}$, approximately at the limit of useful 6-D phase-space data in the DR3 catalog. The 16 stars

possess similar apocenter distances ($r_{apo} \approx 100$ kpc), and are also highly correlated in the angle coordinates $(\theta_r, \theta_\phi, \theta_z)$ conjugate to the actions.

We then separate this structure from the bulk of the data by applying a simple parallelogram selection in the (J_ϕ, J_z) plane, as follows: $J_z \in [2000, 3100]$ and $3.3J_\phi + 3500 < J_z < 3.3J_\phi + 5000$, which results in a final sample of 16 stars for Typhon. This selection box is displayed as a solid black parallelogram in Figure 8.1.
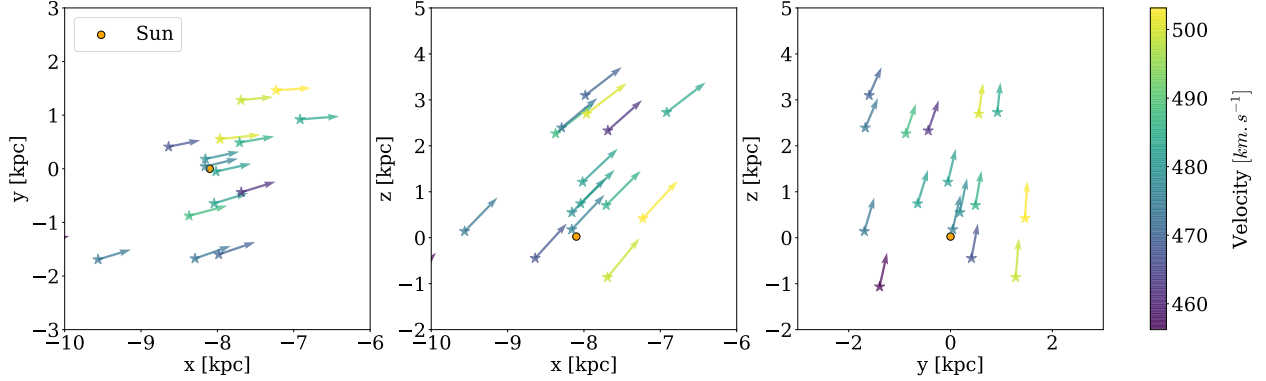
Figure 8.2: Positions and velocity vectors in Galactic Cartesian coordinates of Typhon sample members. The sample shows very clear streaming motion.

The positions and velocities of the sample members of the Typhon stream are shown in Figure 8.2. We find that member stars of this polar stream are spread out all around us, passing through the Solar neighborhood with a high vertical velocity.
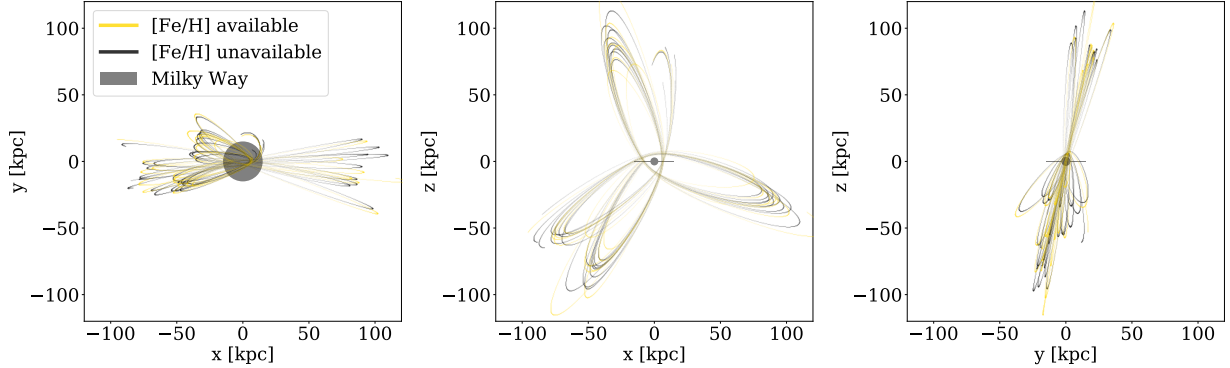
Figure 8.3: Trajectories of the sample members of Typhon during a 5 Gyr backward integration in the (McMillan, 2017) potential in galactic Cartesian coordinates. Trajectories of the 7 stars whose metallicity is available through LAMOST DR8 (Wang et al., 2022) are colored in yellow.

In Figure 8.3 we show the result of integrating Typhon members backwards in time for 5 Gyr in the McMillan Milky Way potential model. Although the stars were selected from a small region in the (J_ϕ, J_z) plane (but with no constraint on J_r), and so should therefore possess similar orbits, there was no a priori reason for the sample to be in phase, as is clearly the case. The sample is dynamically coherent, with very similar orbital parameters: $r_{\mathrm{peri}} =$

$6.0 \pm 0.5\,\mathrm{kpc}$, $r_{\mathrm{apo}} = 99 \pm 15\,\mathrm{kpc}$, $J_r = 6400 \pm 1000\,\mathrm{kpc\,km\,s^{-1}}$, $J_\phi = -560 \pm 110\,\mathrm{kpc\,km\,s^{-1}}$, $J_z = 2500 \pm 300\,\mathrm{kpc\,km\,s^{-1}}$ and eccentricity $e = 0.88 \pm 0.02$.
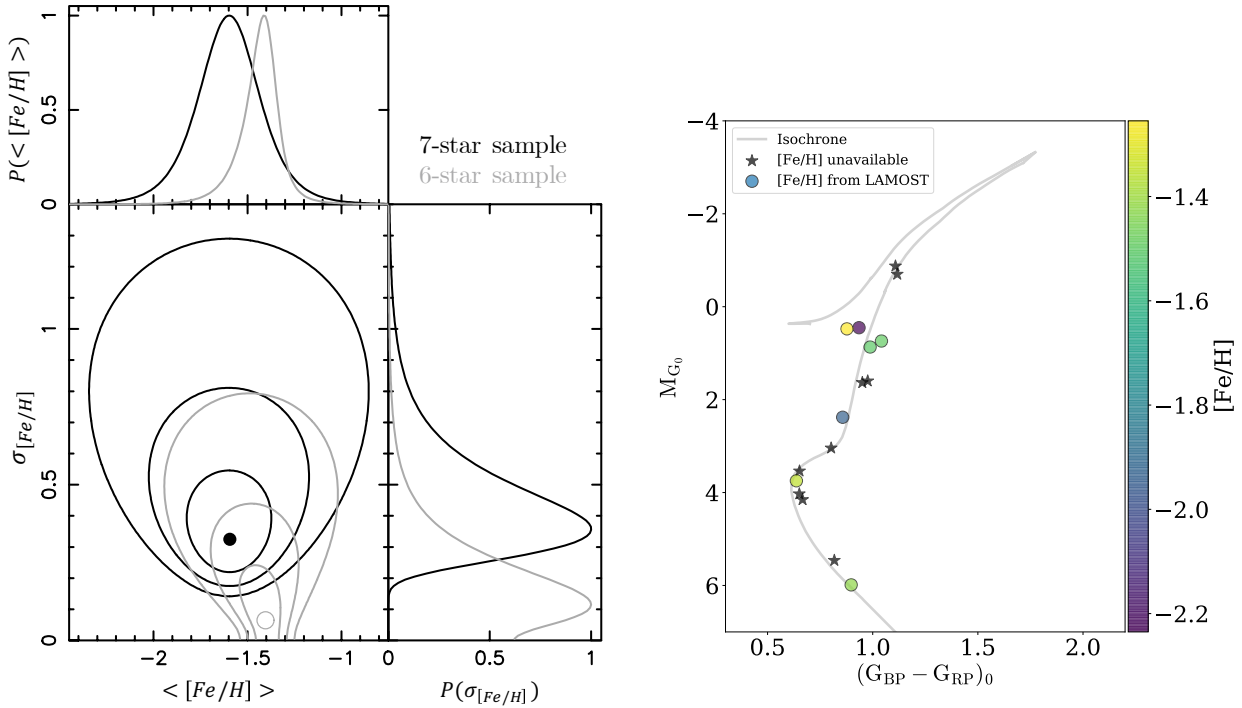
Figure 8.4: Left: Likelihood contours of the mean metallicity and metallicity dispersion of the spectroscopic sample, shown for the full 7 star sample (black lines), and removing the most metal poor star (grey lines). Right: Color magnitude diagram of the sample members of Typhon. For reference, the grey line shows a PARSEC isochrone model (Bressan et al., 2012) of age 12.5 Gyr and of metallicity [Fe/H] = −1.60. The reasonable correspondence of this model shows that the population is predominantly very old.

We further show on Figure 8.4 that metallicities of 7 Typhon stars obtained from LAM-OST DR8 (Wang et al., 2022) show a pronounced dispersion (spanning between [Fe/H] = -2.23 ± 0.06 and [Fe/H] = -1.25 ± 0.09 with mean $\langle[\mathrm{Fe/H}]\rangle = -1.60^{+0.15}_{-0.16}$ dex). This dispersion is much lower when not considering the most metal poor star of the sample, although we have no reason to believe that it is not part of the stream. The population seems to agree with a rather old and poor isochrone (age 12.5 Gyr, [Fe/H] = −1.60).

8.3 Discussion and conclusion

The characteristics of Typhon members lead us to believe that Typhon is likely the tidal remnant of a dwarf galaxy. In particular the metallicity spread, vertical action spread and structure width appear incompatible with a globular cluster progenitor. The mass-metallicity relation of dwarf galaxies (Kirby et al., 2013) suggests that the progenitor likely possessed a luminosity of $10^6 - 10^7\,\mathrm{L}_\odot$, perhaps similar to the Sculptor dSph.

We checked whether Typhon members could have had close encounters with the Large Magellanic Cloud (LMC) or the Sagittarius dwarf galaxy. Taking the trajectories of the two satellites from Vasiliev et al. (2021a), we find that the LMC remains always very distant ($\geq 40\,\mathrm{kpc}$). However, the Typhon stars probably did experience a relatively close flyby of Sagittarius ($\sim 20\,\mathrm{kpc}$, $0.10\,\mathrm{Gyr}$ ago). We note that Typhon and Sagittarius share very similar orbital planes, although they possess opposite angular momentum vectors (i.e. the direction of motion in the plane is opposite). The interaction between Typhon and Sagittarius will be interesting to analyse with N-body simulations.

A stellar stream with such a high apocenter certainly stands out and is incredibly informative when trying to understand the complexities of the stellar halo of the MW. Typhon could originate from a previously unknown dwarf galaxy progenitor, or could be a small part of a big accretion event. It would be very valuable to expand the sample with the detection of additional stream members and their chemical abundances to shed some light on these issues.

Typhon has since been re-detected by the clustering algorithm of Dodd et al. (2022). In addition, its member stars have been the subject of a detailed and high resolution chemical abundances study in Ji et al. (2022), with interesting discussions regarding Typhon's progenitor. These authors agree with our conclusion that the progenitor is most likely a dwarf galaxy although some puzzling facts remain, such as the apparent contradiction between its old age inferred by the chemical analysis in contrast with its large apocenter suggesting a recent accretion.

Data Availability

The sample of Typhon stars is available at DOI 10.5281/zenodo.6948668.

Chapter 9 On the Effect of the Large Magellanic Cloud on the Orbital Poles of Milky Way Satellite Galaxies

Finally, and still in the context of investigating the mysteries of the Milky Way halo, we investigate in this part the planes of satellites issue (presented in Section 1.4.11), in response to a recent work putting forward the Large Magellanic Cloud as a possible origin for its formation.

Foreword

This is intended to be a quick review of the main results from the work of Pawlowski, M.; Oria, P.-A; Taibi, S.; Famaey, B.; Ibata, R.

For technical details and the complete work, please refer to Pawlowski et al. (2022), published in The Astrophysical Journal, Volume 932, Issue 1, id.70, 10 pp.

Abstract

It has been demonstrated that the reflex motion and distortion of the Milky Way (MW) halo caused by the infall of a massive Large Magellanic Cloud (LMC) results in an excess of orbital poles of dark matter halo particles towards the LMC orbital pole. This was suggested to help explain the observed preference of MW satellite galaxies to co-orbit along the Vast Polar Structure (VPOS), the MW's satellite plane. We test this idea by correcting the positions and velocities of the MW satellites for the Galactocentric-distance-dependent shifts inferred from a LMC-infall simulation. While this should substantially reduce the observed clustering of orbital poles if it were mainly caused by the LMC, we instead find that the strong clustering remains preserved. We confirm the initial study's main result with our own simulation of an MW-LMC like interaction, and use it to identify two reasons why this scenario is unable to explain the VPOS: (1) the orbital pole density enhancement is very mild ($\sim 10\%$) compared to the substantial observed enhancement ($\sim 300\%$), and (2) it is very sensitive to the specific angular momenta of the simulation particles, with higher angular momentum particles being affected the least. Particles in simulated dark matter halos tend to follow more radial orbits (corresponding to lower angular momentum), so their orbital poles are more easily affected by small offsets in position and velocity caused by an LMC infall

than objects with more tangential velocity (higher angular momentum), such as the observed dwarf galaxies surrounding the MW. The origin of the VPOS thus remains unexplained.

9.1 Introduction

The Large Magellanic Cloud is the most massive satellite galaxy of the MW and as such a very important tool for studying the gravitational potential and history of the MW. In recent years, the LMC has been found to be both more massive than anticipated and supposed to be on its first infall into the MW (Kallivayalil et al., 2013). Those assumptions make the LMC an extremely important influence that one shouldn't neglect anymore when studying MW and satellite dynamics. For instance, arguably the best model so far for the Sgr stellar stream comes from Vasiliev et al. (2021a) who consider a joint evolving MW-LMC potential.

As already talked about in Subsection 1.4 and illustrated in Figure 1.6, the satellite galaxies of the MW are mostly found in a co-orbiting planar structure called the Vast Polar Structure (VPOS). Recently, it has been suggested in Garavito-Camargo et al. (2021) that here too the LMC could play an important part. Indeed, the LMC is itself part of the VPOS and has orbital poles aligned with it. In that work, the authors produce an N-body simulation of a LMC-like galaxy falling for the first time into a MW-like galaxy. This infall causes a reflex motion of the MW, a change in the center of mass of the MW, and a wake of DM particles following the LMC. In turn, this is linked in their work to an overdensity of DM particles from the halo of the MW-like galaxy having an orbital pole aligned with that of the LMC, which itself agrees well with the VPOS. We take a closer look at this possibility in Pawlowski et al. (2022), in which we started with a hunch that this effect would not be significant for DM particles with high angular momentum, and thus by proxy to satellite galaxies, which are on highly tangential orbits.

9.2 Simulation

To test our hypothesis, we run our own simulation of a MW-LMC-like interaction. The N-body simulation is run with GYRFALCON (Dehnen, 2000), and we use AGAMA (Vasiliev, 2019) to generate initial conditions. For the MW, we use the Model 1 of Binney & Tremaine (2008) as given in AGAMA, which includes a stellar bulge, a thin disk, a thick disk, and a DM halo. We make two changes: (i) we use the same halo mass of 1.2×10^{12} M$_\odot$ as Garavito-Camargo et al. (2021), and (ii) in order to have a spherical halo, we remove the z-axis flattening coefficient of its potential. We generate 2×10^5 particles for the stars and 8×10^5 for the dark matter halo. For the LMC, we generate 10^5 particles based on the spheroid potential of AGAMA for a total mass of 1.8×10^{11} M$_\odot$, following the fiducial model of Garavito-Camargo et al. (2021). The initial conditions of our simulated MW halo model deliberately adopt isotropic orbits, in order to facilitate our aim to examine the effect of the infall of the LMC model on the halo particles as a function of their specific angular momenta.

Initially we place the LMC with positions $(x, y, z) = (12, 215, 130)$ kpc and velocities $(v_x, v_y, v_z) = (12, 13, -77)$ km s^{-1} in the MW-centred reference frame, a slight alteration of the initial conditions of Garavito-Camargo et al. (2021). We run the simulation for 2 Gyr. For each snapshot, we use the *snapcenter* function of NEMO (Teuben, 1995) to obtain the positions

and velocities of the center of mass of the MW based on its stars, then we shift the positions and velocities of all particles by these values in order to make the MW the center of phase space. In this reference frame, the coordinates of the center of mass of the LMC after 2 Gyr are $(x, y, z) = (-1.87, -31.42, -17.07)$ kpc and $(v_x, v_y, v_z) = (-48.61, -207.98, 150.63)$ km s^{-1}. For comparison, the present day values retained by Vasiliev et al. (2021a) are $(x, y, z) = (-0.6, -41.3, -27.1)$ kpc and $(v_x, v_y, v_z) = (-63.9, -213.8, 206.6)$ km s^{-1}.

9.3 Results

We follow the evolution of dark matter particles in our MW model throughout the simulation, and divide them in three bins of initial angular momentum: low ($0 \leq h_{\mathrm{ini}} < 5000$ kpc km s^{-1}), intermediate ($5000 \leq h_{\mathrm{ini}} < 10000$ kpc km s^{-1}) and finally high ($10000 \leq h_{\mathrm{ini}}$ kpc km s^{-1}).

In Figure 9.1, we show the enhancement of the density of orbital pole directions for those particles. We confirm the result of Garavito-Camargo et al. (2021) that a LMC-like object falling into the halo of a MW-like host will result in more orbital poles of dark matter particles in the direction of the VPOS. However, even when taking into account all particles, the enhancement of 9% (top-left panel) found is far from sufficient to explain the observed orbital pole alignment with the VPOS of satellite galaxies.

When we look at the enhancement maps by our angular momentum bin separation, we confirm our suspicion that low angular momentum particles (on rather radial orbits, enhancement of 35%, top-right panel) will be much more affected by the arrival of the LMC compared to high angular momentum particles (enhancement of 3%, bottom-right panel). This makes it even less likely for the LMC to have a significant impact on the VPOS since satellite galaxies agree best with the angular momentum and orbital characteristics of the particles from our high angular momentum bin.

Next we look at the change in orbital pole direction between the initial conditions of the simulations and the final snapshot. This is shown in Figure 9.2. Here again we see that high angular momentum particles seldom undergo a significant change in orbital pole direction (right panel, blue line), with a mean change $\Delta\theta_{\mathrm{pole}}$ of 12.5°. Low angular momentum particles however are very affected, some even flipping their orbital pole direction entirely.

Furthermore, a change in orbital direction does not mean that this necessarily leads to an enhancement of poles towards the VPOS. To quantify this, Figure 9.3 uses the angle θ_{VPOS} between a particle's orbital pole and the normal vector to the VPOS. The left panel plots the initial $\theta_{\mathrm{VPOS}}^{\mathrm{ini}}$ against the final snapshot one $\theta_{\mathrm{VPOS}}^{\mathrm{obs}}$, superscripted "obs" since it is also used for observed satellites (colored dots). There is very little variation along the diagonal, hinting that the changes are small.

The right panel is even more telling. Only the low angular momentum bin (in dashed red) shows a clear enhancement of poles aligned with the VPOS ($\cos(\theta_{\mathrm{VPOS}}^{\mathrm{obs}}) = 1$), but even for those particles, the change is less than an order of magnitude lower than the observed MW satellites overdensity.
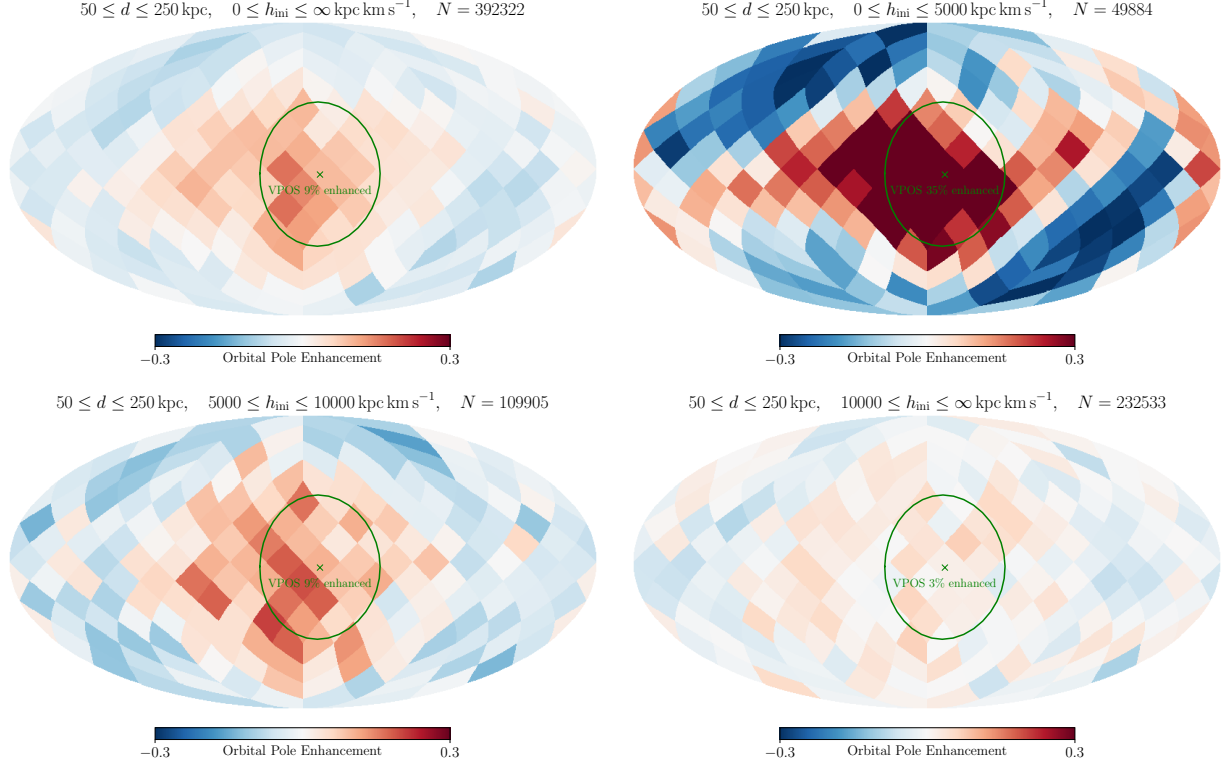
Figure 9.1: All-sky maps in Galactic Coordinates of the orbital pole enhancement for dark matter particles in our simulation. The top-left panel contains all particles within a distance range of 50 to 250 kpc ($N = 392322$ is the particle number for this criteria), while the other panels only show subsets based on the particles' initial specific angular momenta. The green cross marks the VPOS normal vector direction, and the green circle indicates the 10% area on the sphere where the relative VPOS enhancement is measured. While the top-left panel confirms the overall findings of Garavito-Camargo et al. (2021) that an LMC-like infall enhances the density of orbital poles towards the VPOS normal, low angular momentum particles (top-right panel) are most affected and show a pronounced overdensity, while high angular momentum particles (bottom-right panel) – which are comparable to the observed MW dwarfs – show only a very slight overdensity. Plots from Pawlowski et al. (2022).

9.4 Conclusion

While we generally agree with and confirm the results of Garavito-Camargo et al. (2021) with our own N-body simulation of the LMC falling into the MW, we disagree with their suggestion that this recent arrival of the LMC can have a significant impact on the formation of the VPOS.

Our simulation, simultaneously accounting for the reflex motion of the MW, the LMC-induced torque and dark matter wake, finds an overall orbital pole enhancement of 9% in the VPOS direction for a distance range of 50 to 250 kpc. This is compared, in the same region of the sky, to the observed fact that 12 out of 31 MW satellite orbital poles align with the VPOS, *i.e.* an enhancement of 300% over the expected isotropic share of three orbital poles.
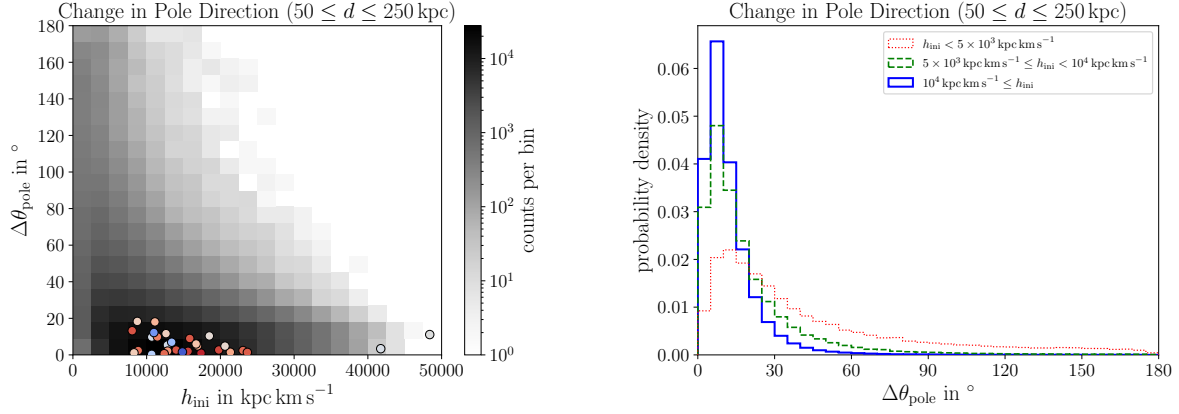
Figure 9.2: The change in orbital pole direction of particles in the simulation depends on the specific angular momentum they had initially. Left panel shows that particles with smaller initial specific angular momentum h_{ini} show larger changes in the direction of their orbital poles as measured by the angle $\Delta\theta_{pole}$ between their orbital pole in the initial and final simulation snapshot. Also shown are the observed MW dwarfs (colored dots). Right panel shows the distribution of $\Delta\theta_{pole}$ for three specific angular momentum bins. Low angular momentum particles (red dotted line) are affected most, while high angular momentum particles (blue solid line) show the least change in their orbital pole directions. Plots from Pawlowski et al. (2022).

The discrepancy gets even worse if we only account for high angular momentum particles in our simulation (which agree best with satellite galaxies), since the enhancement in that case only reaches 3%.

Note that independently, Correa Magnus & Vasiliev (2022) also reached the conclusion that the LMC can not be a major actor for the formation of the VPOS by "rewinding" the orbits of satellite galaxies of the MW, *i.e.* integrating them back in time in the joint MW and LMC potential, then integrating them forward again in the isolated static MW potential. They find the change too small to make the LMC a major influence, and that the distribution of satellite galaxies would be non-isotropic regardless.

The origin of the VPOS (and other similar observed phase space correlations around major galaxies, see Section 1.4.11) thus remains a mystery to be solved.

9.5 Data availability

The initial conditions and final snapshot of the simulation described in Section 9.2 can be obtained at DOI 10.5281/zenodo.6517799.
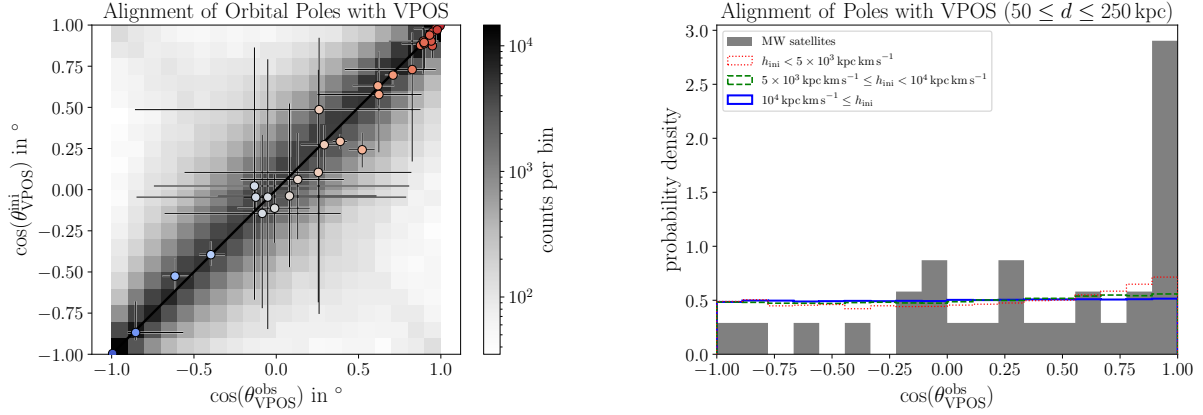
Figure 9.3: The enhancement in the alignment of orbital poles with the VPOS normal direction of particles in the simulation depends on the specific angular momentum they had initially. Left panel plots the Cosines of the angle between the VPOS normal vector and the particle orbital poles as measured in the initial ($\theta_{\mathrm{VPOS}}^{\mathrm{ini}}$) and final ($\theta_{\mathrm{VPOS}}^{\mathrm{obs}}$) simulation snapshot. The corresponding angles for the observed (and shifted) MW dwarf positions and velocities are also shown as colored symbols. Right panel compares histograms of $\theta_{\mathrm{VPOS}}^{\mathrm{obs}}$ for three different bins in specific angular momentum for the particles in the simulation, with the alignment of orbital poles of the observed set of MW dwarfs. Only the low angular momentum (red dotted line) particles show some enhancement towards the VPOS normal (at $\cos\left(\theta_{\mathrm{VPOS}}^{\mathrm{obs}}\right) = 1$). The high angular momentum particles (blue solid line) follow a flat distribution as expected for isotropically distributed orbital poles. The observed MW dwarfs have specific angular momenta that are comparable to the high angular momentum bin, but they display a very pronounced overdensity of orbital poles close to the VPOS normal, which is more than an order of magnitude higher than even the enhancement shown by the low angular momentum particles. Plots from Pawlowski et al. (2022).

125

Chapter 10 Conclusions

The missing mass problem reveals a lack of understanding about how gravitation works and/or an incomplete view of the standard model of particle physics, which might need a dark sector which interacts only gravitationally. To date, as we have seen in Chapter 1, no single model can reconcile observations of the universe at all scales, from the dynamics of stars and gas in galaxies to cosmological observations of the very young and very distant universe and large structures.

The ΛCDM (Section 1.1) paradigm, the standard model of cosmology, boasts remarkable predictions and impressive results concerning the first minutes of the universe (and the creation of matter), its expansion, the cosmological background, and the formation of large structures. However, as seen in detail in Section 1.4, this model faces many problems at "small" Galactic scales, the main one being the important role that baryons seem to play there, with relations of extraordinary regularity such as the BTFR and Renzo's rule pointing to a strong coupling between dark and baryonic matter that is not at all predicted by the theory.

Theories of modification of gravitation such as MOND explain and even predict very well these strong relationships and the central role of baryons in the dynamics of galaxies. However, beyond the dynamical problem, the introduction of non-baryonic matter seems to be necessary and motivated in particular by the power spectrum of the cosmic microwave background, primordial nucleosynthesis, the growth of large structures combined with the low baryonic content of the universe, and gravitational lensing. Without the addition of non-baryonic matter or a convincing relativistic extension, these theories are not able to explain the universe at cosmological scales.

It thus seems important to keep an eye on hybrid theories allowing to reconcile the good results of ΛCDM at large scales with those of MOND at galaxy scales, as proposed in particular by the superfluid dark matter model (Section 1.3), giving new relevance to baryons through a new force induced by phonons. Considering the possibility of dark matter particles with different characteristics than cold dark matter could also be a solution, with less massive particles radically changing the structure formation scenario. Also, relativistic and cosmological extensions of MOND (Section 1.2.3) could be interesting alternatives. During this thesis, we have been interested in our direct neighborhood, namely our own Milky Way galaxy (and the rich history of its stellar halo), the local group (including the Milky Way, its neighbor Andromeda, and all their satellites), and the local universe (extending to a distance of $\sim 10\,\mathrm{Mpc}$). High quality observational data make these environments ideal laboratories to

investigate the dynamics and evolution of the structures they contain, and to place constraints on gravitation, dark matter, and powerful postulates such as the strong equivalence principle of general relativity.

My first study (Chapters 2 and 3, Oria et al. (2021)) focused on the local universe in the framework of the QUMOND theory. I considered ~ 200 galaxies of the local universe (which represent $\geq 95\%$ of the mass of this volume) as well as several distant galaxy clusters, in order to draw up a realistic model of the Milky Way which takes into account its environment. Using the numerical codes detailed in this thesis, I computed phantom dark matter density profiles and MOND gravitational potentials. I showed that the external field due to the Virgo cluster is very important and must be taken into account when modeling the dynamics of a galaxy in the local universe. For the Milky Way, for example, it is comparable to that exerted by M31, its much closer neighbor. A large scale dark matter map is proposed as a result of this work, as well as the external field that applies on each galaxy of our sample of the local universe. I have also obtained the MOND gravitational potential for the Milky Way and compared the resulting rotation curve to the data, finding a reasonable agreement, and exhibiting the loss of circular velocity at large distances due to the external field effect. Finally, I studied in detail the external field effect on the phantom dark matter distribution and in particular the negative density regions predicted by the theory. This particular distribution can give rise to an asymmetric egg-shaped gravitational potential in the most extreme cases. In a specific configuration, I showed that this could also lead to a gravitational lensing effect with a negative convergence factor; if observed, this would constitute a strong detection of the external field effect, and thus disagree with the strong equivalence principle.

Still in order to study a possible detection of the external field effect, we then turned to the Coma cluster of galaxies and in particular to a sample of ultra-diffuse galaxies residing there (Chapter 4, Freundlich et al. (2022)). Via the numerically obtained QUMOND gravitational acceleration and a numerical integration of the Jeans equation, we obtained for each galaxy of our selection the radial velocity profile, and compared it to the observational data. To our surprise, the data are in agreement with the results obtained by MOND in the case where the galaxies would be isolated, while they are in fact in the strong external field produced by the dense environment of the cluster. If the observations are sufficiently precise and are confirmed in the future, this raises a new problem for MOND in the context of galaxy clusters: why are those galaxies shielded from the EFE? This study was also the occasion to propose a new analytical formula for the computation of the QUMOND gravitational acceleration of a system under a constant external field, more precise than the formula frequently used until now in the literature.

We then went back to the framework of ΛCDM and the Milky Way structures to focus on the tidal stream generated by the Sagittarius dwarf galaxy (Chapters 5 and 6, Oria et al. (2022a)). Since its discovery, many models have been proposed for this stream, getting better and better at reproducing the superb observational data available thanks to *Gaia*. However, this very particular structure still holds some mysteries, one of which is its "bifurcation": each arm of the stream is itself composed of two parallel arms, a bright branch (bigger and more populated) and a faint one. Our work proposes a model in which the Sagittarius dwarf galaxy had at least, 3 Gyr ago, a fairly minor disk component (whose mass would be of the order of $10 \sim 15\%$ of the total baryonic mass) whose outer parts produce the faint branch of the stellar stream. The plane of this disk is perpendicular to both the plane of the Milky

Way disk and the orbital plane of the progenitor. This possibility emerged naturally from a large and systematic survey of initial conditions in terms of energy and angular momentum. This model offers two big advantages: (i) the faint branch is created alone, allowing it to be coupled to another model for the parallel bright branch, a spherical model for example, and (ii) the disk being a low mass component, a very minor rotation would be expected in the progenitor remnants, in agreement with the observations. This is of course only one possibility to explain the bifurcation, but if it is in agreement with reality, the mystery is close to being solved. Moreover, our systematic probing of initial conditions has allowed us to exhibit the best models for the internal rotation scenario, and will in any case constitute a step forward on the way to an ideal model for Sagittarius.

The arrival of the third data release from the *Gaia* satellite has been the occasion for us to look for new structures in the stellar halo, which I detail in Chapters 7 and 8. These new data include many additional radial velocities compared to the previous release, which gave us the opportunity to search for kinematically coherent structures using angle-action coordinates. We also restricted ourselves to the solar neighborhood, which offers more precise data (less uncertainty on distances in particular), and looked at stars with very distant apocenters. This work has resulted in the detection of two new structures: Antaeus (Oria et al., 2022b), a group of stars - probably tidal debris - in retrograde motion in the Milky Way disk, and Typhon (Tenachi et al., 2022), parts of a stellar stream in a polar orbit. Antaeus is intriguing in particular for its position in the disk, but also for its very low amount of vertical motion, the lowest found among the stellar halo structures detected so far. This debris could be an important part of the Sequoia accretion event which is the origin of most of the high energy retrograde structures of the halo. Typhon is interesting for its orbit (its stars being currently close to the Sun but going up to 100 kpc distances) and its possible interaction with the Sagittarius stream with which it shares the orbital plane (but with an opposite angular momentum direction).

Finally, we investigated the plane of satellites, and in particular the influence that the Large Magellanic Cloud could have on its formation (Chapter 9, Pawlowski et al. (2022)). The Large Magellanic Cloud, now supposed to be very massive and in first infall into the potential well of the Milky Way, has an important influence on the orbit of some satellites, on the stellar streams, and on the structures of the stellar halo in general. We studied and quantified its impact on the formation of the Milky Way's plane of satellites using N-body simulations. By following the evolution of the orbital poles of the Milky Way dark matter particles through the simulation, and by binning them by initial angular momentum, we noticed that the impact of the infall of the Large Magellanic Cloud was particularly remarkable on the particles with low angular momentum, but very small on those with high angular momentum, to which we can assimilate the satellite galaxies by proxy which are, for the vast majority, on low eccentricity orbits. We conclude that the Large Magellanic Cloud is not the answer to the mystery of the Milky Way's plane of satellites.

During this thesis, we have thus brought new elements to various fields of research related to gravitation and dark matter by using our neighborhood, the Local Universe, as a laboratory. Many ways to use or continue these works are possible; we present some examples in the next chapter.

Le problème de la masse manquante révèle une incompréhension de notre part quant au fonctionnement de la gravitation et/ou une vision incomplète du modèle standard de la physique des particules, auquel il faudrait peut-être un secteur sombre n'intéragissant que de manière gravitationnelle. A ce jour, comme on a pu le voir dans le Chapitre 1, aucun modèle ne permet de concilier les observations de l'univers à toutes les échelles, de la dynamique des étoiles et du gaz dans les galaxies jusqu'aux observations cosmologiques de l'univers très jeune et très lointain et des grandes structures.

Le paradigme ΛCDM (Section 1.1), modèle standard de la cosmologie, a produit des prédictions remarquables et procure des résultats impressionnants concernant *e.g.* les premières minutes de l'univers (et la création de matière), son expansion, le fond diffus cosmologique, et la formation de grandes structures. Cependant, comme vu en détail dans la Section 1.4, ce modèle est confronté à de nombreux problèmes aux "petites" échelles galactiques, le principal étant le rôle important que les baryons semblent y jouer, avec des relations de régularité extraordinaires telles que la BTFR et la Renzo's rule pointant vers un couplage fort entre matières noire et baryonique qui n'est absolument pas prévu par la théorie.

Les modèles de modification de la gravitation telles que MOND expliquent et même prédisent très bien ces relations fortes et le rôle central des baryons dans la dynamique des galaxies. Cependant, au délà du problème dynamique, l'introduction de matière non baryonique semble nécessaire et motivée notamment par *e.g.* le spectre de puissance du fond diffus cosmologique, la nucléosynthèse primordiale, la croissance des grandes structures combinée au faible contenu baryonique de l'univers, et les lentilles gravitationnelles. Sans l'ajout d'une telle matière non baryonique ou une extension relativiste convaincante, ces théories semblent ne pas pouvoir expliquer l'univers aux échelles cosmologiques.

Il apparaît alors important de garder un oeil sur des théories hybrides permettant de concilier les bons résultats de ΛCDM aux grandes échelles à ceux de MOND à l'échelle des galaxies, comme le propose notamment le modèle de matière noire superfluide (Section 1.3), mettant en avant les baryons au travers d'une nouvelle force induite par des phonons. Considérer la possibilité de particules de matière noire ayant des caractéristiques différentes de celles de la matière noire froide pourrait également être une solution, des particules moins massives changeant radicalement le scénario de formation de structures. De même, des extensions relativistes et cosmologiques de MOND (Section 1.2.3) pourraient constituer des alternatives intéressantes.

Durant cette thèse, nous nous sommes intéressés à notre voisinage direct, à savoir notre propre galaxie la Voie Lactée (et la riche histoire de son halo stellaire), le groupe local (comprenant la Voie Lactée, sa voisine Andromède, et tous leurs satellites), et l'univers local (s'étendant jusqu'à une distance de $\sim 10\,\mathrm{Mpc}$). Des données observationnelles de qualité font de ces environnements des laboratoires idéaux pour enquêter sur la dynamique et l'évolution des structures qu'ils contiennent, et placer des contraintes sur la gravitation, la matière noire, et de puissantes hypothèses comme le principe d'équivalence fort de la relativité générale.

Ma première étude (Chapitres 2 et 3, Oria et al. (2021)) s'est portée sur l'univers local dans le cadre de la théorie QUMOND. J'ai considéré ~ 200 galaxies de l'univers local (qui représentent $\geq 95\%$ de la masse de ce volume) ainsi que plusieurs amas de galaxies lointains, afin notamment de dresser un modèle réaliste de la Voie Lactée tenant compte de son en-

vironnement. Via l'utilisation des codes de calcul numérique détaillés dans cette thèse, j'ai calculé des profils de densité fantômes et potentiels gravitationnels MOND. J'ai montré que le champ externe dû à l'amas de la Vierge est très important et doit être pris en compte lors de la modélisation dynamique d'une galaxie de l'univers local. Pour la Voie Lactée par exemple, il est comparable à celui exercé par M31, sa voisine bien plus proche. Une carte de la matière noire fantôme à grande échelle est proposée, ainsi que le champ externe qui s'applique sur chacune des galaxies de notre échantillon de l'univers local. J'ai également obtenu le potentiel gravitationnel MOND pour la Voie Lactée et comparé la courbe de rotation qui en est issue aux données, trouvant un accord raisonnable, et exhibant la perte de vitesse circulaire à grande distance due à l'effet de champ externe. Enfin, j'ai étudié en détail l'effet de champ externe sur la distibution de matière noire fantôme et en particulier les zones de densité négative prévues par la théorie. Cette distribution particulière peut donner lieu à un potentiel gravitationnel asymétrique en forme "d'oeuf" dans les cas les plus extrêmes. Dans une configuration bien précise, je montre que cela pourrait également mener à un effet de lentille gravitationnelle avec facteur de convergence négatif ; si observé, cela constituerait une détection forte de l'effet de champ externe, et donc de désaccord avec le principe d'équivalence fort.

Toujours dans le but d'étudier une possible détection de l'effet de champ externe, nous nous sommes ensuite tournés vers l'amas de galaxies de Coma et en particulier un échantillon de galaxies ultra-diffuses y résidant (Chapitre 4, Freundlich et al. (2022)). Via l'accélération gravitationnelle QUMOND obtenue numériquement ainsi qu'une intégration numérique de l'équation de Jeans, nous avons obtenu pour chacune des galaxies de notre sélection le profil de vitesse radiale, et l'avons comparé aux données observationnelles. A notre surprise, les données sont en accord avec les résultats obtenus par MOND dans le cas où les galaxies seraient isolées, alors qu'elles sont en réalité dans le champ externe fort produit par l'environnement dense de l'amas. Si les observations sont suffisamment précises et viennent à être confirmées dans le futur, cela soulève un nouveau problème pour MOND dans le contexte des amas de galaxies : pourquoi ces galaxies semblent-elles protégées de l'EFE ? Cette étude a également été l'occasion de proposer une nouvelle formule analytique pour le calcul de l'accélération gravitationnelle QUMOND d'un système sous un champ externe constant, plus précise que la formule fréquemment utilisée jusqu'alors dans la littérature.

Nous sommes ensuite revenus dans le cadre de ΛCDM et des structures de la Voie Lactée pour nous intéresser au courant de marée généré par la galaxie naine du Sagittaire (Chapitres 5 et 6, Oria et al. (2022a)). Depuis sa découverte, de nombreux modèles ont été proposés pour ce courant, reproduisant de mieux en mieux les superbes données observationnelles disponibles notamment grâce à *Gaia*. Cependant, cette structure très particulière comporte toujours quelques mystères, dont l'un est celui de la "bifurcation" : chacun des bras du courant est lui même composé de deux bras parallèles, l'un majeur (plus gros, plus peuplé, et plus brillant) et l'un mineur. Notre travail propose un modèle dans lequel la galaxie naine du Sagittaire comportait au moins, il y a 3 Gyr, un composant de disque assez mineur (dont la masse serait de l'ordre de $10 \sim 15\%$ de la masse baryonique totale) dont les parties externes produisent la branche mineure du courant stellaire. Le plan de ce disque est perpendiculaire à la fois au plan du disque de la Voie Lactée et au plan orbital du progéniteur. Cette possibilité a émergé naturellement d'un vaste sondage de conditions initiales en termes d'énergie et de moment angulaire. Ce modèle offre deux gros avantages : (i) la branche

mineure est créée seule, permettant de la coupler à un autre modèle pour la branche majeure parallèle, un modèle sphérique par exemple, et (ii) le disque étant un composant de faible masse, une rotation très mineure serait attendue dans les restes du progéniteur, en accord avec les observations. Ce n'est bien sûr qu'une possibilité pour expliquer la bifurcation, mais si elle est en accord avec la réalité, le mystère est proche d'être élucidé. Par ailleurs, notre sondage systématique des conditions initiales a permis d'exhiber les meilleurs modèles pour le scénario de rotation interne, et constituera quoi qu'il en soit un pas en avant sur le chemin d'un modèle idéal pour le Sagittaire.

L'arrivée de la troisième vague de données du satellite *Gaia* a été l'occasion pour nous de chercher de nouvelles structures dans le halo stellaire, ce que je détaille dans les Chapitres 7 et 8. Ces nouvelles données comportent notamment de nombreuses vitesses radiales additionnelles par rapport à la précédente, ce qui nous a permis de chercher des structures cohérentes cinématiquement en utilisant les coordonnées angle-action. Nous nous sommes de plus restreints au voisinage solaire, ce qui offre des données plus précises (moins d'incertitude sur les distances notamment), et avons regardé des étoiles avec un apocentre très lointain. Ce travail a donné lieu à la détection de deux nouvelles structures : Antaeus (Oria et al., 2022b), un groupe d'étoiles - sans doute un débris de marée - en mouvement rétrograde dans le disque de la Voie Lactée, et Typhon (Tenachi et al., 2022), un morceau de courant stellaire sur une orbite polaire. Antaeus est intrigant en particulier pour sa position dans le disque, mais également pour sa très faible quantité de mouvement vertical, la plus faible constatée parmi les structures du halo stellaire détectées jusqu'à présent. Ce débris pourrait notamment être une partie importante de l'évènement d'accrétion Sequoia qui est l'origine de la plupart des structures retrogrades à haute énergie du halo. Typhon, lui, est intéressant pour son orbite (ses étoiles étant actuellement proches du Soleil mais allant jusqu'à des distances de $100\,\mathrm{kpc}$) et sa possible interaction avec le courant du Sagittaire duquel il partage le plan orbital (mais avec un moment de direction opposée).

Enfin, nous nous sommes intéressés au problème du plan de satellites, et en particulier à l'influence que le Grand Nuage de Magellan pourrait avoir sur ce dernier (Chapitre 9, Pawlowski et al. (2022)). Le Grand Nuage de Magellan, supposé désormais très massif et en première chute dans le puits gravitationnel de la Voie Lactée, exerce une influence importante sur l'orbite de certains satellites, sur les courants stellaires, et sur les structures du halo stellaire en général. Nous avons étudié et quantifié son impact sur la formation du plan de satellites de la Voie Lactée à l'aide de simulations numériques de type N-corps. En suivant l'évolution des pôles orbitaux des particules de matière noire de la Voie Lactée au travers de la simulation, et en triant ces dernières par moment angulaire initial, nous avons remarqué que l'impact de la chute du Grand Nuage de Magellan était particulièrement remarquable sur les particules à faible moment angulaire, mais très léger sur celles à haut moment angulaire, auxquelles on peut assimiler les galaxies satellites qui sont en grande majorité sur des orbites peu excentriques. Nous concluons que le Grand Nuage de Magellan n'est pas la réponse au mystère du plan de satellites de la Voie Lactée.

Durant cette thèse, nous avons donc apporté des éléments nouveaux à divers domaines de recherche en lien avec la gravitation et la matière noire en utilisant notre voisinage l'univers local comme laboratoire. De nombreuses façons d'exploiter ou continuer nos travaux sont possibles ; nous en présentons quelques exemples dans le chapitre suivant.

Chapter 11 Future prospects

The observational phenomena reviewed in Section 1.4 reveal inconsistencies between our models that describe gravitation and cosmology, and the universe itself. It appears crucial to continue putting those models to the test, following up for example on some of the work done during this thesis.

11.0.1 Further probing of the external field effect and the strong equivalence principle

A very important point is investigating whether the strong equivalence principle holds by significantly detecting or not detecting the EFE, a crucial test for both ΛCDM, which relies on GR, and for MOND. This is probably the most immediate way, in the near future, to constrain different gravitation paradigms.

In Chapter 3, our work provides results that help understanding and quantifying the EFE especially in the context of the Local Universe. In Chapter 4, we investigated a possible break of the strong equivalence principle in the high external field environment of the Coma cluster, but found none. Yet, Chae et al. (2020, 2021) report a statistically significant detection of the EFE on rotation curves of spiral galaxies from the SPARC survey, by taking into account the EFE of large structures up to 300 Mpc away.

Those results seem to indicate that galaxy clusters, where the UDGs we worked on reside and where MOND faces a missing mass problem, are very much worth being investigated further. Why would the EFE not be detected in those environments, when it seems to be in individual galaxies out of clusters? Although many possibilities are provided in the discussion from Freundlich et al. (2022), a very helpful step would be to get more and better velocity dispersion data from UDGs in clusters and confirm or infirm the results we obtained (with, admittedly, high uncertainty data).

Some smaller efforts would also help understanding the EFE better. For example, it would be worthwhile to precisely quantify the impact of the orientation the EFE on a galaxy. While Chae & Milgrom (2022) already provide work on this topic, a systematic study would help picking the best analytical formula for the MONDian gravitational acceleration in every situation, and also perhaps reveal EFE-induced features for specific orientation cases, which could later be observed.

Finally, the RAR has recently been extended to low accelerations using weak-lensing in Brouwer et al. (2021). It would be interesting to see how the MOND expectation compares to the low acceleration data in the case of the EFE, using one of the new and more accurate analytical formulae (from Freundlich et al. (2022) or Chae & Milgrom (2022)).

11.0.2 A full model for the Sgr stream and its bifurcation

Our work in Chapter 6 calls for a followup study providing a full, self-consistent model for the Sagittarius stream and its bifurcation. Indeed, while we find a possible origin for the creation of the faint branch based on the outer stars of a low mass disk, we rely on the background Sgr model of Vasiliev et al. (2021a) for the bright branch. This has issues since this background model is very thick, when ideally we would want the faint branch populated by our model only.

The next step would thus be to couple our faint branch model to a thinner bright branch model, which could probably be a less extended spherical component than the one we currently use. It would be useful to also explore the tidal stirring mechanism scenario, and see if the spherical component (not perfectly spherical in this case) could be the result of a very perturbed disk after tidal effects, of which the low mass disk could be the remnant. In the same context, investigating the possibility and consequences of a bar being present in the Sgr disk 3 Gyr ago would also provide great insight on the dwarf galaxy's evolution. Indeed, in the tidal stirring scenario, perturbed dwarf galaxies often produce a bar (Kazantzidis et al., 2011a; Łokas et al., 2014).

It would also be highly interesting to compare the predictions of our model to the new Gaia DR3, for example the stars expected in the $-180° \leq \tilde{\Lambda}_\odot \leq -130°$ region ($70° \leq \mathrm{RA} \leq 120°$), stripped from our low-mass disk. The angular momentum of the disk component in the progenitor should also be looked at in detail, and compared to the results of e.g. del Pino et al. (2021). We have found that the infall of the LMC might induce a change in the angular momentum direction in the last tens of Myr of the orbit of the Sgr.

Finally, in the context of modified gravity, the inclusion of the LMC in a Sgr N-body model has yet to be done, and it would also be very interesting to see if our faint branch model stands there as well.

11.0.3 Investigating the formation of dwarf spheroidals

While the formation process of dwarf galaxies in ΛCDM is rather well understood, with baryonic processes quenching star formation early in the life of these low luminosity objects, the formation of dwarf spheroidals in particular, gas-poor structures supported by random motions, is still uncertain. In addition to this, those galaxies are heavily dark matter dominated and their inner dynamics is a problem for the standard cosmological model (see Section 1.4.7). It thus follows that explaining the formation of dwarf spheroidals would bring a lot of constraints to galaxy formation, dark matter, and gravitation models.

Several formation scenarios for these galaxies involve environmental, tidal effects in some way, be it resonances as in D'Onghia et al. (2009), or more complex processes also involving disk shocking and bar formation such as the tidal stirring mechanism (Mayer et al., 2001). Those often suggest that dwarf spheroidals were initially disky galaxies, which due to tidal effects transitioned to the spheroidal shape that we observe today.

The other major scenario is through mergers. Some of the dwarfs present features that cannot be explained through tidal effects alone such as shells, and some most likely did not have enough time to interact with their host in a way that would have altered them significantly. Lokas et al. (2014) explore this idea by modeling Andromeda II as the merger

between two disky galaxies. In Benítez-Llambay et al. (2016), the authors infer from cosmological simulations that dwarf spheroidals have a clear metallicity gradient, with a young metal-rich core population surrounded by an older metal-poor population which could be accreted through mergers (with other dwarf galaxies).

Our Sagittarius stream faint branch model of Chapter 6 discusses the possibility of the tidal stirring mechanism to produce a minor disk component by the time of the start of the simulation 3 Gyr ago. The rest of the disk might indeed be transitioning to, or already be a part of, a more isotropic pressure-supported component, or in a stellar bar. Confirming our model with observations (of *e.g.* stellar overdensities where we predict them, or detailed progenitor shape and kinematics hinting at the remnant of a minor disk component) would be a step forward for our understanding of dwarf spheroidal formation.

As more data will come from upcoming surveys for the kinematics of dwarfs, it will be crucial to have accurate models to test against. Further elaborating the merger and tidal stirring scenarios or proposing new ones via cosmological and N-body simulations to try and reproduce, as a first step, specific observed galaxies (as Lokas et al. (2014) did for Andromeda II), and then the global population of dwarf spheroidals, is a very exciting prospect.

11.0.4 Further digging in the stellar halo

As seen in Chapters 7 and 8 with the detection of new tidal debris, the stellar halo, even in the Solar neighbourhood, still holds many secrets that we are slowly unearthing with the superb *Gaia* data. Establishing a complete and precise history of structures, mergers and accretions for our MW is a crucial first step in order to understand galaxy formation as a whole.

Key elements for detecting structures in the halo is having access to the full kinematics profile of stars as well as their metallicity or even better global chemical contents. In this regard, while *Gaia* gives us incredible astrometric data such as proper motions, radial velocities are a crucial piece of information that is seldom provided, and can only be of good quality up to distances of ~ 10 kpc, due to limitations of its Radial Velocity Spectrometer (RVS). Indeed, for *Gaia* DR3, the radial velocity is provided for ~ 33 millions of stars while the complete sample is almost 2 billion stars! Similar limitations apply for the [Fe/H] measurements. Fortunately, upcoming surveys will help with that.

WEAVE (WHT Enhanced Area Velocity Explorer), a spectrograph based in the northern hemisphere in La Palma, will provide accurate radial velocities (for stars with V magnitude fainter than 15.5) and elemental abundances (for stars with V magnitude fainter than 12.0) for millions of objects that cannot be probed by Gaia's RVS.

Another survey similar in aims but based on the southern hemisphere is the upcoming 4MOST (4-metre Multi-Object Spectroscopic Telescope). 4MOST will obtain high-quality radial velocities out to ~ 100 kpc for the southern sky stars, as well as metallicities and α-elements abundance for stars out to ~ 50 kpc.

Combining all this information (by applying *e.g.* the techniques described in Section 1.5) is a very exciting prospect and will inevitably lead to detection of new structures in the stellar halo of the MW, and to a better understanding of already detected relics of the past, important accretion events such as the Gaia-Enceladus-Sausage (GES).

In particular Typhon (Chapter 8), whose star members recently underwent a detailed

chemical abundance analysis in Ji et al. (2022), will be a crucial piece of the stellar halo puzzle. With characteristics pointing towards a dwarf galaxy progenitor, it would be important to decide if it could be part of an already detected structure. While the orbital parameters and the high apocenters ($\geq 100\,\mathrm{kpc}$) are already a big constraint, detection of additional stream members and information on their chemical composition will be very helpful in deciding these matters.

11.0.5 Disentangling Sequoia

Sequoia (Myeong et al., 2019), a major accretion event responsible for bringing many high energy, retrograde stellar populations in the stellar halo of the MW, is particularly interesting since it presents similarities in kinematics and chemical composition with other large accretion events (*e.g.* Arjuna, I'itoi), and as a result the origin of some structures is hard to properly label. Naidu et al. (2021) even surmise that Sequoia could merely be the retrograde tail of Gaia-Enceladus-Sausage (GES), or even simply one of its satellite galaxies. Establishing a clear separation or relation between GES and Sequoia would thus be a great step forward.

I aim to shed light on the Sequoia conundrum, by establishing a clear connection to a progenitor galaxy (now most likely phase-mixed debris), and providing precise constraints, in terms of kinematic parameters and chemical composition, for Sequoia stars and structures. This will allow the community to know precisely where Sequoia stands in the merger history of the MW, and provide a quick way to determine whether newly discovered structures can be linked to Sequoia. The recent discovery of Antaeus (Chapter 7, Oria et al. (2022b)) will be of utmost importance since it is highly likely to be a part of Sequoia, and could possibly constitute the tidal debris of the core of its progenitor. I propose the following steps.

(i) I will extend the sample of known Antaeus stars, and determine the precise relation between Antaeus et Sequoia. Antaeus, as we have seen in Chapter 7, is a tidal debris made of stars in retrograde motion in the disk of the MW, and shares many similar characteristics with Sequoia-linked populations including total energy, amount of tangential motion, eccentricity of orbits, and metallicity. See Figure 7.2 in which the total energy and actions (J_r, J_ϕ, J_z, which encode the quantity of movement in cylindrical coordinates) are compared to Sequoia-associated objects. Antaeus has a distinctive characteristic: its extremely low amount of vertical motion J_z. This gives Antaeus great importance, firstly because a kinematically coherent structure with such a low amount of vertical motion had never been detected (when comparing, for example, to the global atlas of halo structures of Malhan et al. (2022b)), and secondly because it could mean that Antaeus constitutes the core of the progenitor of Sequoia. As a first step to this project, it thus seems crucial to determine what is exactly the relation between Antaeus and Sequoia, and to do so, it is of tremendous importance to expand our sample of stars to better constrain and understand the characteristics of Antaeus. We currently have 65 stars are labelled as Antaeus stars. Some more members could be provided by the L-RL64 population identified by Ruiz-Lara et al. (2022), although this group has a much higher quantity of vertical movement and it is not clear yet whether they belong to the same structure.

In order to extend the sample of Antaeus stars, I will use the information already at hand, the kinematics and derived orbital characteristics in particular, to search for similar

trajectories in the full *Gaia* DR3 catalog. Indeed, my current detection has been made using only the subset of *Gaia* stars with a radial velocity measurement, providing full 6D position and velocity information, and allowing actions to be derived. However with what we now know of Antaeus, it will be possible to extend the detection to stars without a radial velocity measurement (with only 5D information), since I will test a reasonable range of values of radial velocities for each star. I will also search for radial velocity measurements in public datasets from spectroscopic surveys (such as *e.g.* SEGUE, LAMOST).

Practically, the detection process will use an orbit integrator applied to stars sharing characteristics with Antaeus stars, and in their tubular neighbourhood in the sky. A metric will then be used provide a quantitative assessment of belonging to the same group as Antaeus.

Additionally, among the 65 Antaeus stars, only 8 have a metallicity measurement. It would be very useful to obtain additional spectroscopic measurements for other member stars to confirm the metallicity estimation for Antaeus, and also to carry out a detailed chemical abundance analysis of α-elements (such as magnesium and calcium) which will give information on properties such as star formation in the now disrupted population. A first step would be to crossmatch our catalog of stars, as for radial velocities, with existing surveys. But this chemical information could also be obtained with low to medium resolution spectra of the Antaeus candidate members, which many ground-based telescopes are able to provide.

(ii) I will examine and re-assess which known structures are currently tentatively associated with Sequoia. As investigated in Malhan et al. (2022b) and can be seen in Figure 7.2, the distinction between Sequoia and other mergers Arjuna and I'itoi (Naidu et al., 2020) is hard to make. While the three events have distinct metallicities, those are close enough that some populations cannot be associated with high certainty to either of the three accretion events. For instance, stellar streams GD-1 and Yglr are tentatively associated to the Arjuna/Sequoia/I'itoi group, but not precisely to one in particular. Using similar techniques as for the previous step, *i.e.* integrating orbits and trying to obtain radial velocities and metallicities for the structures with uncertain associations, I will establish a quantitative assessment on the likelihood of those structures being in fact associated to Sequoia.

This inventory of structures will be useful for the next step in which we will try to reproduce the Sequoia merger, but it could in fact go both ways: we could remark, when trying to model the merger, that certain structures are seldom reproduced and unlikely to be associated to Sequoia.

(iii) I will provide a complete model for the Sequoia merger using N-body simulations. Having come to a better understanding of Sequoia with the previous two steps, I will be able to provide a model for the merger based on N-body simulations. A recent example of such a work is provided by Naidu et al. (2021), who did it for another major merger event of the MW, the Gaia-Enceladus-Sausage. They were able to constrain the characteristics of stellar populations coming from GES, highlighting the importance of such a work when studying the stellar halo.

I intend to create a library of N-body simulations of the merger between Sequoia and the Milky Way for reasonable ranges of parameters such as inclination angle between the two galaxies and relative age. The simulations will also probe the satellites of Sequoia, which could host several globular clusters and dwarf galaxies before falling into the MW. Those could go on to reproduce the structures that we now associate with Sequoia in terms of tidal

debris or stellar streams.

Running many simulations will allow me to give a probability, based on statistics, of reproducing structures observed in the stellar halo at the present time, either rejecting or confirming associations with Sequoia. While Sequoia is known for bringing retrograde populations, we will be able to quantify whether we expect to find some minor stellar groups with low angular momentum as a result of this merger. We will also place an upper bound on the angular momentum and energy that stars from this accretion are expected to have.

Eventually, the best simulation in terms of probability to reproduce the Sequoia-associated structures will be proposed as a model for the Sequoia merger. This will provide predictions, as there will undoubtedly be in this model overdensities or specific features in the stellar halo. Looking for those in existing data or future surveys will provide clear tests of this model.

Appendix: MONDian characteristics of Local Universe objects

Table 11.1: List of sources extracted from Karachentsev et al. (2013) and processed as explained in Subsection 3.3.1. Columns are galaxy name, distance to MW, baryonic mass, PDM mass computed numerically up to r_{200} with EFE, associated r_{200}, Newtonian external gravitational acceleration g_{Ne} in units of a_0 at galaxy's location, and PDM mass computed numerically up to r_{200} without EFE. Bottom entries with N/A are galaxies too embedded in another galaxy's PDM halo for it to make sense to compute their PDM mass.

Galaxy	d (kpc)	M_b ($M_\odot$)	M_{PDM} ($M_\odot$) (with EFE)	r_{200} (kpc) (with EFE)	g_{Ne}/a_0	M_{PDM} ($M_\odot$) (no EFE)
MW	0	7.5e+10	1.39e+12	224.83	1.11e-03	1.88e+12
M31	770	1.03e+11	1.88e+12	248.63	1.08e-03	2.33e+12
WLM	970	1.87e+08	3.98e+09	31.93	1.28e-03	2.30e+10
NGC0024	9900	5.85e+09	1.75e+11	112.62	7.13e-04	2.97e+11
NGC0045	9200	4.69e+09	1.40e+11	104.65	7.22e-04	2.53e+11
NGC0055	2130	3.64e+09	9.34e+10	91.4	1.01e-03	2.10e+11
IC0010	660	5.20e+08	2.20e+10	56.45	1.01e-03	4.96e+10
NGC0185	610	4.52e+08	2.50e+10	58.87	2.78e-03	4.46e+10
MESSIER032	490	8.58e+08	1.93e+10	54.04	1.54e-03	7.21e+10
NGC0247	3650	3.61e+09	1.28e+11	101.6	4.85e-04	2.09e+11
NGC0253	3940	8.04e+10	1.50e+12	230.8	9.36e-04	1.98e+12
NGC0300	2150	3.35e+09	8.63e+10	89.01	1.00e-03	1.98e+11
IC1613	730	3.34e+08	6.63e+09	37.85	1.59e-03	3.55e+10
NGC0404	3050	2.51e+09	6.25e+10	79.96	1.05e-03	1.60e+11
MESSIER033	850	4.09e+09	1.08e+11	95.81	3.30e-03	2.29e+11
NGC0625	3890	1.38e+09	3.72e+10	67.24	9.30e-04	1.03e+11
NGC0628	7310	1.86e+10	5.01e+11	160.05	8.51e-04	6.85e+11
NGC0672	7200	4.86e+09	1.32e+11	102.64	8.78e-04	2.59e+11
Cas1	3300	8.03e+08	1.91e+10	53.82	1.13e-03	6.87e+10
NGC0855	9730	2.95e+09	8.22e+10	87.6	8.60e-04	1.80e+11
NGC0891	9770	6.78e+10	1.49e+12	229.9	8.77e-04	1.75e+12
NGC0925	9290	1.24e+10	3.34e+11	139.78	8.81e-04	5.11e+11
DDO024	9800	1.43e+09	3.56e+10	66.28	1.05e-03	1.05e+11
Maffei1	3010	1.12e+10	2.60e+11	128.56	1.37e-03	4.75e+11
ESO115-021	4990	9.61e+08	2.64e+10	59.99	8.82e-04	7.86e+10
ESO154-023	5550	1.26e+09	3.53e+10	66.11	8.48e-04	9.59e+10
NGC1156	7800	2.55e+09	7.00e+10	83.02	8.87e-04	1.62e+11
ESO300-014	9800	2.64e+09	7.68e+10	85.64	7.82e-04	1.66e+11

NGC1291	8800	7.09e+10	1.49e+12	230.12	7.34e-04	1.81e+12
NGC1313	4070	3.88e+09	1.04e+11	94.79	9.10e-04	2.20e+11
UGC02773	5400	1.24e+09	3.14e+10	63.59	1.03e-03	9.49e+10
NGC1400	24500	7.56e+10	1.55e+12	233.15	5.58e-04	1.89e+12
IC0342	3280	2.90e+10	6.99e+11	178.75	1.06e-03	9.46e+11
UGCA086	2960	1.52e+09	3.61e+10	66.58	1.19e-03	1.10e+11
IC2038	19200	1.79e+09	7.58e+10	85.27	1.23e-03	1.25e+11
NGC1533	19400	5.71e+10	1.37e+12	223.97	5.70e-04	1.54e+12
NGC1569	3060	2.58e+09	6.09e+10	79.26	1.18e-03	1.63e+11
NGC1560	3450	9.04e+08	2.58e+10	59.54	8.80e-04	7.50e+10
NGC1637	9290	1.13e+10	3.21e+11	137.89	8.04e-04	4.79e+11
NGC1744	10000	3.20e+09	9.54e+10	92.05	7.48e-04	1.91e+11
NGC1800	8000	1.65e+09	4.76e+10	73.0	7.90e-04	1.18e+11
UGCA105	3150	1.64e+09	3.89e+10	68.26	1.14e-03	1.17e+11
ESO364-029	7590	1.46e+09	4.09e+10	69.42	8.54e-04	1.07e+11
NGC2188	7400	2.43e+09	6.85e+10	82.43	8.37e-04	1.56e+11
UGCA127	8500	7.49e+09	2.15e+11	120.69	9.99e-04	3.55e+11
WHIB0619-07	8400	2.95e+09	9.62e+10	92.31	5.07e-04	1.80e+11
CGMW1-260	10800	3.08e+09	8.81e+10	89.65	8.04e-04	1.86e+11
IC2171	9900	1.50e+09	4.09e+10	69.43	8.29e-04	1.09e+11
NGC2283	10000	6.58e+09	1.82e+11	114.09	8.83e-04	3.23e+11
ESO558-011	8400	1.79e+09	4.89e+10	73.66	8.77e-04	1.25e+11
NGC2337	7870	1.47e+09	3.52e+10	66.02	1.14e-03	1.08e+11
HIZSS008	7430	5.16e+09	1.37e+11	103.75	9.34e-04	2.71e+11
NGC2366	3190	8.74e+08	1.86e+10	53.39	1.33e-03	7.32e+10
HIZSS012	7200	3.36e+09	9.16e+10	90.82	9.02e-04	1.98e+11
NGC2403	3180	7.41e+09	1.66e+11	110.77	1.29e-03	3.52e+11
NGC2500	12400	6.67e+09	1.57e+11	108.74	1.17e-03	3.26e+11
NGC2537	12200	7.29e+09	1.71e+11	111.87	1.21e-03	3.48e+11
NGC2541	12400	3.60e+09	8.41e+10	88.26	1.23e-03	2.08e+11
HolmII	3390	2.11e+09	4.56e+10	71.97	1.51e-03	1.41e+11
NGC2552	12400	3.85e+09	9.32e+10	91.35	1.15e-03	2.19e+11
ESO495-021	7960	3.96e+09	1.03e+11	94.4	9.79e-04	2.23e+11
NGC2683	7730	3.16e+10	6.86e+11	177.67	1.35e-03	1.01e+12
UGC04787	20300	2.43e+09	6.53e+10	81.13	9.46e-04	1.56e+11
NGC2784	9820	4.90e+10	1.13e+12	209.65	1.02e-03	1.38e+12
UGCA153	21900	1.70e+09	5.19e+10	75.16	7.28e-04	1.20e+11
NGC2835	10300	1.43e+10	3.71e+11	144.76	9.46e-04	5.65e+11
NGC2787	7480	1.39e+10	2.98e+11	134.49	1.40e-03	5.54e+11
DDO062	18600	2.08e+09	6.13e+10	79.45	7.88e-04	1.39e+11
NGC2915	3780	7.69e+08	1.97e+10	54.44	1.00e-03	6.65e+10
NGC2903	8870	5.20e+10	1.07e+12	206.13	1.44e-03	1.44e+12
SexB	1360	2.15e+08	5.03e+09	34.51	1.12e-03	2.55e+10
NGC3109	1320	7.27e+08	1.77e+10	52.54	1.12e-03	6.38e+10
NGC3077	3820	4.22e+09	1.77e+11	113.16	1.38e-03	2.34e+11
NGC3104	16000	2.32e+09	4.58e+10	72.09	1.69e-03	1.51e+11
NGC3115	9680	7.02e+10	1.29e+12	219.12	1.27e-03	1.79e+12
LeoI	250	1.12e+08	2.60e+09	27.69	1.16e-03	1.57e+10
NGC3184	11120	2.88e+10	5.27e+11	162.73	1.95e-03	9.41e+11
NGC3239	7900	3.91e+09	7.86e+10	86.29	1.62e-03	2.21e+11
IC2574	4019	2.87e+09	8.84e+10	89.73	7.31e-04	1.76e+11

NGC3299	10400	1.45e+09	2.55e+10	59.26	2.11e-03	1.06e+11
NGC3344	6850	1.03e+10	2.04e+11	118.54	1.67e-03	4.47e+11
NGC3351	10050	3.84e+10	6.52e+11	174.73	2.24e-03	1.16e+12
NGC3368	10420	5.52e+10	9.86e+11	200.54	2.00e-03	1.51e+12
NGC3377	10910	2.34e+10	4.41e+11	153.37	1.76e-03	8.09e+11
NGC3379	11120	6.50e+10	1.12e+12	209.25	2.26e-03	1.70e+12
NGC3384	11380	4.50e+10	8.66e+11	192.06	1.93e-03	1.30e+12
UGC05923	22300	3.35e+09	8.16e+10	87.39	1.11e-03	1.98e+11
NGC3412	10400	1.78e+10	3.73e+11	145.01	1.43e-03	6.63e+11
NGC3413	12020	2.80e+09	4.59e+10	72.12	2.47e-03	1.73e+11
NGC3432	9200	4.80e+09	8.47e+10	88.45	2.07e-03	2.57e+11
NGC3489	12080	2.98e+10	5.42e+11	164.27	2.00e-03	9.64e+11
NGC3521	10700	9.23e+10	1.44e+12	227.63	1.71e-03	2.19e+12
NGC3556	9900	2.74e+10	4.87e+11	158.55	2.05e-03	9.06e+11
LeoII	210	3.84e+07	1.41e+09	22.6	1.31e-03	7.24e+09
NGC3593	10800	2.34e+10	4.21e+11	150.94	2.01e-03	8.08e+11
NGC3621	6700	1.95e+10	4.61e+11	155.62	1.17e-03	7.10e+11
NGC3627	10280	7.85e+10	1.19e+12	213.64	2.11e-03	1.95e+12
NGC3738	4900	1.20e+09	2.48e+10	58.79	1.48e-03	9.25e+10
KDG082	16600	1.34e+09	1.14e+10	45.32	7.49e-03	1.01e+11
NGC3990	10300	3.99e+09	6.60e+10	81.43	2.37e-03	2.24e+11
NGC4080	15000	2.91e+09	2.73e+10	60.64	7.15e-03	1.78e+11
NGC4136	7900	3.10e+09	5.23e+10	75.33	2.29e-03	1.87e+11
NGC4144	7240	2.55e+09	4.42e+10	71.24	2.20e-03	1.62e+11
NGC4150	13740	9.98e+09	9.76e+10	92.74	6.78e-03	4.37e+11
NGC4204	8000	1.92e+09	3.21e+10	64.05	2.28e-03	1.31e+11
NGC4214	2940	1.54e+09	3.36e+10	65.01	1.35e-03	1.11e+11
NGC4236	4450	4.73e+09	1.05e+11	94.92	1.33e-03	2.54e+11
NGC4244	4490	4.07e+09	8.18e+10	87.45	1.61e-03	2.28e+11
NGC4242	7900	3.57e+09	5.72e+10	77.61	2.05e-03	2.07e+11
UGC7321	17200	3.97e+09	3.37e+10	65.08	8.34e-03	2.24e+11
IC3104	2270	4.98e+08	1.21e+10	46.28	1.05e-03	4.80e+10
NGC4258	7830	6.77e+10	1.11e+12	208.3	2.18e-03	1.75e+12
IC779	16670	1.67e+09	1.02e+10	43.7	1.38e-02	1.18e+11
NGC4308	14000	2.95e+09	2.51e+10	59.02	8.40e-03	1.80e+11
IC3247	24400	2.38e+09	3.55e+10	66.23	2.90e-03	1.54e+11
NGC4395	4610	3.44e+09	6.99e+10	82.97	1.60e-03	2.02e+11
NGC4449	4210	5.23e+09	1.06e+11	95.25	1.59e-03	2.73e+11
NGC4455	8400	1.40e+09	2.25e+10	56.86	2.48e-03	1.04e+11
NGC4460	9590	5.14e+09	7.77e+10	85.98	2.82e-03	2.70e+11
NGC4490	5800	8.30e+09	1.59e+11	109.24	1.77e-03	3.82e+11
NGC4517	9700	2.07e+10	3.75e+11	145.3	2.03e-03	7.42e+11
UGC07699	14500	2.12e+09	1.54e+10	50.09	1.08e-02	1.41e+11
NGC4559	8100	1.23e+10	2.02e+11	118.15	2.45e-03	5.09e+11
UGC07774	22600	4.45e+09	5.18e+10	75.09	4.72e-03	2.43e+11
NGC4594	9300	1.45e+11	2.20e+12	261.85	1.65e-03	3.05e+12
NGC4605	5470	5.47e+09	1.12e+11	97.02	1.55e-03	2.82e+11
NGC4600	7350	1.93e+09	3.59e+10	66.48	1.83e-03	1.32e+11
NGC4618	7900	5.06e+09	8.38e+10	88.14	2.33e-03	2.67e+11
NGC4631	7380	2.59e+10	4.38e+11	153.03	2.25e-03	8.70e+11
NGC4656	5400	4.46e+09	8.65e+10	89.1	1.74e-03	2.43e+11

NGC4736	4660	3.50e+10	7.03e+11	179.09	1.57e-03	1.08e+12
NGC4765	9700	1.44e+09	2.40e+10	58.08	2.30e-03	1.06e+11
NGC4826	4370	2.59e+10	5.27e+11	162.76	1.56e-03	8.71e+11
NGC4945	3800	4.06e+10	8.69e+11	192.24	1.42e-03	1.21e+12
IC4182	4700	1.04e+09	2.01e+10	54.81	1.63e-03	8.35e+10
ESO269-058	3800	1.21e+09	3.82e+10	67.84	4.23e-04	9.33e+10
NGC5023	6610	1.72e+09	3.04e+10	62.9	2.03e-03	1.21e+11
NGC5055	8990	7.71e+10	1.11e+12	208.69	2.70e-03	1.92e+12
NGC5068	5450	6.39e+09	1.46e+11	106.17	1.26e-03	3.16e+11
NGC5102	3400	4.72e+09	1.25e+11	100.68	9.29e-04	2.54e+11
NGC5128	3750	6.33e+10	1.31e+12	220.22	9.64e-04	1.67e+12
CVnI	220	1.95e+07	9.27e+08	19.64	9.64e-04	4.57e+09
NGC5204	4660	1.19e+09	2.48e+10	58.73	1.50e-03	9.20e+10
NGC5194	8400	7.46e+10	1.13e+12	209.97	2.37e-03	1.88e+12
NGC5195	7660	3.33e+10	5.53e+11	165.35	2.33e-03	1.04e+12
NGC5206	3470	1.55e+09	3.31e+10	64.7	1.46e-03	1.12e+11
ESO270-017	3600	2.01e+09	4.55e+10	71.89	2.05e-03	1.36e+11
NGC5236	4920	5.86e+10	1.21e+12	214.54	1.21e-03	1.57e+12
NGC5237	3400	5.99e+08	1.35e+10	47.98	1.21e-03	5.51e+10
NGC5253	3560	1.85e+09	4.77e+10	73.07	1.01e-03	1.28e+11
NGC5264	4530	1.15e+09	2.52e+10	59.06	1.29e-03	8.96e+10
ESO383-087	3450	1.88e+09	4.69e+10	72.67	1.05e-03	1.29e+11
NGC5398	8100	1.54e+09	3.64e+10	66.75	1.20e-03	1.11e+11
MESSIER101	7380	5.81e+10	1.07e+12	206.09	1.96e-03	1.56e+12
NGC5474	7200	2.36e+09	4.54e+10	71.86	3.28e-03	1.53e+11
CIRCINUS	4200	2.51e+10	6.05e+11	170.42	1.10e-03	8.52e+11
NGC5585	5700	1.62e+09	3.17e+10	63.76	1.66e-03	1.16e+11
ESO273-014	9900	3.13e+09	8.29e+10	87.83	9.59e-04	1.88e+11
ESO223-009	6490	2.07e+09	5.20e+10	75.17	1.06e-03	1.39e+11
ESO274-001	3090	1.42e+09	3.44e+10	65.5	1.11e-03	1.05e+11
ESO137-018	6400	4.45e+09	1.17e+11	98.66	9.50e-04	2.43e+11
IC4662	2440	8.91e+08	2.20e+10	56.48	1.04e-03	7.42e+10
NGC6503	5270	7.33e+09	1.64e+11	110.18	1.31e-03	3.50e+11
IC4710	7940	2.60e+09	7.78e+10	85.98	7.61e-04	1.64e+11
NGC6684	8700	2.15e+10	5.71e+11	167.09	8.91e-04	7.61e+11
NGC6744	8300	5.01e+10	1.21e+12	214.85	7.92e-04	1.40e+12
NGC6822	500	4.90e+08	1.07e+10	44.38	1.33e-03	4.74e+10
NGC6946	5890	4.32e+10	9.85e+11	200.45	1.15e-03	1.26e+12
Cepheus1	6000	2.42e+09	5.44e+10	76.34	1.38e-03	1.56e+11
IC5052	6030	2.76e+09	7.71e+10	85.74	8.56e-04	1.72e+11
KKR59	5890	1.62e+09	3.58e+10	66.39	1.35e-03	1.16e+11
NGC7090	6700	5.64e+09	1.59e+11	109.16	8.28e-04	2.89e+11
IC5152	1970	9.50e+08	2.37e+10	57.87	1.04e-03	7.78e+10
IC5201	8800	1.02e+10	2.96e+11	134.29	7.54e-04	4.43e+11
NGC7462	10100	3.58e+09	1.09e+11	96.33	7.01e-04	2.08e+11
NGC7640	7900	5.29e+09	1.39e+11	104.33	9.32e-04	2.76e+11
CasdSph	790	1.63e+08	4.86e+09	34.11	2.05e-03	2.07e+10
Pegasus	760	8.29e+07	1.52e+09	23.14	1.73e-03	1.26e+10
DDO217	9700	3.48e+09	9.38e+10	91.53	9.12e-04	2.03e+11
IC5332	7800	4.80e+09	1.40e+11	104.62	7.59e-04	2.57e+11
NGC7713	7800	3.30e+09	9.52e+10	91.97	7.93e-04	1.95e+11

PegdSph	820	9.43e+07	1.78e+09	24.43	2.53e-03	1.38e+10
NGC7793	3910	6.28e+09	1.66e+11	110.8	9.33e-04	3.13e+11
NGC0147	760	4.07e+08	N/A			
NGC0205	820	1.32e+09	N/A			
AndI	730	9.25e+07	N/A			
SMC	60	1.11e+09	N/A			
Sculptor	90	5.70e+07	N/A			
IC1727	7200	3.44e+09	N/A			
Fornax	140	1.54e+08	N/A			
Maffei2	2800	2.31e+10	N/A			
Dw1	2800	1.34e+10	N/A			
LMC	50	3.26e+09	N/A			
Carina	100	3.62e+07	N/A			
IC2233	12200	2.14e+09	N/A			
KK73	9800	1.69e+09	N/A			
NGC2976	3560	3.22e+09	N/A			
MESSIER081	3630	6.55e+10	N/A			
MESSIER082	3530	3.05e+10	N/A			
KKSG18	9700	2.50e+09	N/A			
SexDSph	90	3.08e+07	N/A			
NGC4625	7900	2.25e+09	N/A			
NGC4627	7300	3.85e+09	N/A			
BootesIII	50	7.28e+06	N/A			
BootesI	70	6.04e+06	N/A			
UMin	60	1.34e+07	N/A			
Draco	80	3.20e+07	N/A			
SagdSph	20	2.99e+08	N/A			

Bibliography

Alpher, R. A., Bethe, H., & Gamow, G. 1948, Physical Review, 73, 803, doi: 10.1103/PhysRev.73.803

Amarante, J. A. S., Debattista, V. P., Beraldo e Silva, L., Laporte, C. F. P., & Deg, N. 2022, arXiv e-prints, arXiv:2204.12187. https://arxiv.org/abs/2204.12187

Anders, F., Khalatyan, A., Queiroz, A. B. A., et al. 2022, A&A, 658, A91, doi: 10.1051/0004-6361/202142369

Angus, G. W. 2009, MNRAS, 394, 527, doi: 10.1111/j.1365-2966.2008.14341.x

Angus, G. W., Famaey, B., & Buote, D. A. 2008, MNRAS, 387, 1470, doi: 10.1111/j.1365-2966.2008.13353.x

Angus, G. W., Famaey, B., & Diaferio, A. 2010, MNRAS, 402, 395, doi: 10.1111/j.1365-2966.2009.15895.x

Angus, G. W., & McGaugh, S. S. 2008, MNRAS, 383, 417, doi: 10.1111/j.1365-2966.2007.12403.x

Angus, G. W., van der Heyden, K. J., Famaey, B., et al. 2012, MNRAS, 421, 2598, doi: 10.1111/j.1365-2966.2012.20532.x

Banik, I., Nagesh, S. T., Haghi, H., Kroupa, P., & Zhao, H. 2022a, MNRAS, doi: 10.1093/mnras/stac1073

Banik, I., Thies, I., Famaey, B., et al. 2020, ApJ, 905, 135, doi: 10.3847/1538-4357/abc623

Banik, I., Thies, I., Truelove, R., et al. 2022b, MNRAS, 513, 129, doi: 10.1093/mnras/stac722

Banik, I., & Zhao, H. 2018a, MNRAS, 473, 419, doi: 10.1093/mnras/stx2350

—. 2018b, MNRAS, 480, 2660, doi: 10.1093/mnras/sty2007

—. 2021, arXiv e-prints, arXiv:2110.06936. https://arxiv.org/abs/2110.06936

Behroozi, P. S., Wechsler, R. H., & Conroy, C. 2013, ApJ, 770, 57, doi: 10.1088/0004-637X/770/1/57

Bekenstein, J., & Milgrom, M. 1984, ApJ, 286, 7, doi: 10.1086/162570

Bekenstein, J. D. 2004, PhRvD, 70, 083509, doi: 10.1103/PhysRevD.70.083509

Belokurov, V., Erkal, D., Evans, N. W., Koposov, S. E., & Deason, A. J. 2018, MNRAS, 478, 611, doi: 10.1093/mnras/sty982

Belokurov, V., Zucker, D. B., Evans, N. W., et al. 2006, ApJL, 642, L137, doi: 10.1086/504797

Belokurov, V., Koposov, S. E., Evans, N. W., et al. 2014, MNRAS, 437, 116, doi: 10.1093/mnras/stt1862

Benítez-Llambay, A., Navarro, J. F., Abadi, M. G., et al. 2016, MNRAS, 456, 1185, doi: 10.1093/mnras/stv2722

Berezhiani, L., Famaey, B., & Khoury, J. 2018, JCAP, 2018, 021, doi: 10.1088/1475-7516/2018/09/021

Berezhiani, L., & Khoury, J. 2015, PhRvD, 92, 103510, doi: 10.1103/PhysRevD.92.103510

Bílek, M., Fensch, J., Ebrová, I., et al. 2022, A&A, 660, A28, doi: 10.1051/0004-6361/202141709

Bílek, M., Müller, O., & Famaey, B. 2019, A&A, 627, L1, doi: 10.1051/0004-6361/201935840

Bílek, M., Thies, I., Kroupa, P., & Famaey, B. 2021, Galaxies, 9, 100, doi: 10.3390/galaxies9040100

Binney, J., & Tremaine, S. 2008, Galactic Dynamics: Second Edition

Bonaca, A., Hogg, D. W., Price-Whelan, A. M., & Conroy, C. 2019, ApJ, 880, 38, doi: 10.3847/1538-4357/ab2873

Bovy, J. 2015, ApJS, 216, 29, doi: 10.1088/0067-0049/216/2/29

—. 2020, arXiv e-prints, arXiv:2012.02169. https://arxiv.org/abs/2012.02169

Bowman, J. D., Rogers, A. E. E., Monsalve, R. A., Mozdzen, T. J., & Mahesh, N. 2018, Nature, 555, 67, doi: 10.1038/nature25792

Boylan-Kolchin, M., Bullock, J. S., & Kaplinghat, M. 2011, MNRAS, 415, L40, doi: 10.1111/j.1745-3933.2011.01074.x

Boylan-Kolchin, M., Bullock, J. S., Sohn, S. T., Besla, G., & van der Marel, R. P. 2013, ApJ, 768, 140, doi: 10.1088/0004-637X/768/2/140

Brada, R., & Milgrom, M. 1999, ApJ, 519, 590, doi: 10.1086/307402

—. 2000, ApJL, 531, L21, doi: 10.1086/312510

Bressan, A., Marigo, P., Girardi, L., et al. 2012, MNRAS, 427, 127, doi: 10.1111/j.1365-2966.2012.21948.x

Brouwer, M. M., Oman, K. A., Valentijn, E. A., et al. 2021, A&A, 650, A113, doi: 10.1051/0004-6361/202040108

Bullock, J. S., & Boylan-Kolchin, M. 2017, ARA&A, 55, 343, doi: 10.1146/annurev-astro-091916-055313

Burkert, A. 1995, ApJL, 447, L25, doi: 10.1086/309560

Candlish, G. N., Smith, R., & Fellhauer, M. 2015, MNRAS, 446, 1060, doi: 10.1093/mnras/stu2158

Carollo, D., Beers, T. C., Lee, Y. S., et al. 2007, Nature, 450, 1020, doi: 10.1038/nature06460

Chae, K.-H., Desmond, H., Lelli, F., McGaugh, S. S., & Schombert, J. M. 2021, ApJ, 921, 104, doi: 10.3847/1538-4357/ac1bba

Chae, K.-H., Lelli, F., Desmond, H., et al. 2020, ApJ, 904, 51, doi: 10.3847/1538-4357/abbb96

Chae, K.-H., & Milgrom, M. 2022, ApJ, 928, 24, doi: 10.3847/1538-4357/ac5405

Collins, M. L. M., Chapman, S. C., Rich, R. M., et al. 2014, ApJ, 783, 7, doi: 10.1088/0004-637X/783/1/7

Combes, F. 2014, A&A, 571, A82, doi: 10.1051/0004-6361/201424990

Combes, F. 2016, in Astrophysics and Space Science Library, Vol. 418, Galactic Bulges, ed. E. Laurikainen, R. Peletier, & D. Gadotti, 413, doi: 10.1007/978-3-319-19378-6_15

Conroy, C., Bonaca, A., Cargile, P., et al. 2019, ApJ, 883, 107, doi: 10.3847/1538-4357/ab38b8

Copi, C. J., Schramm, D. N., & Turner, M. S. 1995, Science, 267, 192, doi: `10.1126/science.7809624`

Correa Magnus, L., & Vasiliev, E. 2022, MNRAS, 511, 2610, doi: `10.1093/mnras/stab3726`

Creasey, P., Sameie, O., Sales, L. V., et al. 2017, MNRAS, 468, 2283, doi: `10.1093/mnras/stx522`

Cyburt, R. H., Fields, B. D., Olive, K. A., & Yeh, T.-H. 2016, Reviews of Modern Physics, 88, 015004, doi: `10.1103/RevModPhys.88.015004`

Debattista, V. P., Roškar, R., Valluri, M., et al. 2013, MNRAS, 434, 2971, doi: `10.1093/mnras/stt1217`

Dehnen, W. 2000, ApJL, 536, L39, doi: `10.1086/312724`

Dekel, A., Ishai, G., Dutton, A. A., & Maccio, A. V. 2017, MNRAS, 468, 1005, doi: `10.1093/mnras/stx486`

del Pino, A., Fardal, M. A., van der Marel, R. P., et al. 2021, ApJ, 908, 244, doi: `10.3847/1538-4357/abd5bf`

Desmond, H. 2017a, MNRAS, 472, L35, doi: `10.1093/mnrasl/slx134`

—. 2017b, MNRAS, 464, 4160, doi: `10.1093/mnras/stw2571`

Desmond, H., Ferreira, P. G., Lavaux, G., & Jasche, J. 2018, MNRAS, 474, 3152, doi: `10.1093/mnras/stx3062`

Di Cintio, A., & Lelli, F. 2016, MNRAS, 456, L127, doi: `10.1093/mnrasl/slv185`

Di Matteo, P., Haywood, M., Lehnert, M. D., et al. 2019, A&A, 632, A4, doi: `10.1051/0004-6361/201834929`

Di Teodoro, E. M., Posti, L., Fall, S. M., et al. 2022, arXiv e-prints, arXiv:2207.02906. `https://arxiv.org/abs/2207.02906`

Dodd, E., Callingham, T. M., Helmi, A., et al. 2022, arXiv e-prints, arXiv:2206.11248. `https://arxiv.org/abs/2206.11248`

Doke, Y., & Hattori, K. 2022, arXiv e-prints, arXiv:2203.15481. `https://arxiv.org/abs/2203.15481`

Doliva-Dolinsky, A., Martin, N. F., Thomas, G. F., et al. 2022, arXiv e-prints, arXiv:2205.02831. `https://arxiv.org/abs/2205.02831`

D'Onghia, E., Besla, G., Cox, T. J., & Hernquist, L. 2009, Nature, 460, 605, doi: `10.1038/nature08215`

Duc, P.-A., Cuillandre, J.-C., Karabal, E., et al. 2015, MNRAS, 446, 120, doi: `10.1093/mnras/stu2019`

Dutton, A. A., & Macciò, A. V. 2014, MNRAS, 441, 3359, doi: `10.1093/mnras/stu742`

Ebrova, I. 2013, arXiv e-prints, arXiv:1312.1643. `https://arxiv.org/abs/1312.1643`

Einasto, J. 1965, Trudy Astrofizicheskogo Instituta Alma-Ata, 5, 87

Einstein, A. 1916, Annalen der Physik, 354, 769, doi: `10.1002/andp.19163540702`

Errani, R., Navarro, J. F., Ibata, R., et al. 2022, MNRAS, doi: `10.1093/mnras/stac1516`

Famaey, B., & Binney, J. 2005, MNRAS, 363, 603, doi: `10.1111/j.1365-2966.2005.09474.x`

Famaey, B., Bruneton, J.-P., & Zhao, H. 2007, MNRAS, 377, L79, doi: `10.1111/j.1745-3933.2007.00308.x`

Famaey, B., McGaugh, S., & Milgrom, M. 2018, MNRAS, 480, 473, doi: `10.1093/mnras/sty1884`

Famaey, B., & McGaugh, S. S. 2012, Living Reviews in Relativity, 15, 10, doi: 10.12942/lrr-2012-10

Fellhauer, M., Belokurov, V., Evans, N. W., et al. 2006, ApJ, 651, 167, doi: 10.1086/507128

Freundlich, J., Famaey, B., Oria, P.-A., et al. 2022, A&A, 658, A26, doi: 10.1051/0004-6361/202142060

Freundlich, J., Jiang, F., Dekel, A., et al. 2020, MNRAS, 499, 2912, doi: 10.1093/mnras/staa2790

Fukugita, M., & Peebles, P. J. E. 2004, ApJ, 616, 643, doi: 10.1086/425155

Gaia Collaboration. 2022, Astronomy & Astrophysics, doi: 10.1051/0004-6361/202243940

Gaia Collaboration, Prusti, T., de Bruijne, J. H. J., et al. 2016, A&A, 595, A1, doi: 10.1051/0004-6361/201629272

Gaia Collaboration, Brown, A. G. A., Vallenari, A., et al. 2021, A&A, 649, A1, doi: 10.1051/0004-6361/202039657

Gajda, G., Łokas, E. L., & Athanassoula, E. 2017, ApJ, 842, 56, doi: 10.3847/1538-4357/aa74b4

Garavito-Camargo, N., Besla, G., Laporte, C. F. P., et al. 2019, ApJ, 884, 51, doi: 10.3847/1538-4357/ab32eb

Garavito-Camargo, N., Patel, E., Besla, G., et al. 2021, ApJ, 923, 140, doi: 10.3847/1538-4357/ac2c05

Gentile, G., Famaey, B., & de Blok, W. J. G. 2011, A&A, 527, A76, doi: 10.1051/0004-6361/201015283

Ghari, A., Famaey, B., Laporte, C., & Haghi, H. 2019, A&A, 623, A123, doi: 10.1051/0004-6361/201834661

Haslbauer, M., Banik, I., & Kroupa, P. 2020, MNRAS, 499, 2845, doi: 10.1093/mnras/staa2348

Haslbauer, M., Banik, I., Kroupa, P., Wittenburg, N., & Javanmardi, B. 2022, ApJ, 925, 183, doi: 10.3847/1538-4357/ac46ac

Hees, A., Famaey, B., Angus, G. W., & Gentile, G. 2016, MNRAS, 455, 449, doi: 10.1093/mnras/stv2330

Helmi, A. 2004, ApJL, 610, L97, doi: 10.1086/423340

Helmi, A., Babusiaux, C., Koppelman, H. H., et al. 2018, Nature, 563, 85, doi: 10.1038/s41586-018-0625-x

Helmi, A., & de Zeeuw, P. T. 2000, MNRAS, 319, 657, doi: 10.1046/j.1365-8711.2000.03895.x

Helmi, A., Veljanoski, J., Breddels, M. A., Tian, H., & Sales, L. V. 2017, A&A, 598, A58, doi: 10.1051/0004-6361/201629990

Hodson, A. O., & Zhao, H. 2017, A&A, 598, A127, doi: 10.1051/0004-6361/201629358

Hoekstra, H. 2013, arXiv e-prints, arXiv:1312.5981. https://arxiv.org/abs/1312.5981

Huang, Y., Liu, X. W., Yuan, H. B., et al. 2016, MNRAS, 463, 2623, doi: 10.1093/mnras/stw2096

Ibata, R., Irwin, M., Lewis, G. F., & Stolte, A. 2001, ApJL, 547, L133, doi: 10.1086/318894

Ibata, R., Malhan, K., Martin, N., et al. 2021, ApJ, 914, 123, doi: 10.3847/1538-4357/abfcc2

Ibata, R. A., Gilmore, G., & Irwin, M. J. 1994, Nature, 370, 194, doi: 10.1038/370194a0

—. 1995, MNRAS, 277, 781, doi: 10.1093/mnras/277.3.781

Ibata, R. A., Wyse, R. F. G., Gilmore, G., Irwin, M. J., & Suntzeff, N. B. 1997, AJ, 113, 634, doi: 10.1086/118283

Ibata, R. A., Lewis, G. F., Conn, A. R., et al. 2013, Nature, 493, 62, doi: 10.1038/nature11717

Irrgang, A., Wilcox, B., Tucker, E., & Schiefelbein, L. 2013, A&A, 549, A137, doi: 10.1051/0004-6361/201220540

Iršič, V., Viel, M., Haehnelt, M. G., et al. 2017, PhRvD, 96, 023522, doi: 10.1103/PhysRevD.96.023522

Izumi, K., Hagiwara, C., Nakajima, K., Kitamura, T., & Asada, H. 2013, PhRvD, 88, 024049, doi: 10.1103/PhysRevD.88.024049

Jean-Baptiste, I., Di Matteo, P., Haywood, M., et al. 2017, A&A, 604, A106, doi: 10.1051/0004-6361/201629691

Ji, A. P., Naidu, R. P., Brauer, K., Ting, Y.-S., & Simon, J. D. 2022, arXiv e-prints, arXiv:2207.04016. https://arxiv.org/abs/2207.04016

Kallivayalil, N., van der Marel, R. P., Besla, G., Anderson, J., & Alcock, C. 2013, ApJ, 764, 161, doi: 10.1088/0004-637X/764/2/161

Karachentsev, I. D., Makarov, D. I., & Kaisina, E. I. 2013, AJ, 145, 101, doi: 10.1088/0004-6256/145/4/101

Karachentsev, I. D., & Telikova, K. N. 2018, Astronomische Nachrichten, 339, 615, doi: 10.1002/asna.201813520

Kazantzidis, S., Łokas, E. L., Callegari, S., Mayer, L., & Moustakas, L. A. 2011a, ApJ, 726, 98, doi: 10.1088/0004-637X/726/2/98

Kazantzidis, S., Łokas, E. L., Mayer, L., Knebe, A., & Klimentowski, J. 2011b, ApJL, 740, L24, doi: 10.1088/2041-8205/740/1/L24

Keller, B. W., & Wadsley, J. W. 2017, ApJL, 835, L17, doi: 10.3847/2041-8213/835/1/L17

Kirby, E. N., Cohen, J. G., Guhathakurta, P., et al. 2013, ApJ, 779, 102, doi: 10.1088/0004-637X/779/2/102

Koposov, S. E., Belokurov, V., Evans, N. W., et al. 2012, ApJ, 750, 80, doi: 10.1088/0004-637X/750/1/80

Kormendy, J., Drory, N., Bender, R., & Cornell, M. E. 2010, ApJ, 723, 54, doi: 10.1088/0004-637X/723/1/54

Kravtsov, A. V., Gnedin, O. Y., & Klypin, A. A. 2004, ApJ, 609, 482, doi: 10.1086/421322

Kroupa, P., Theis, C., & Boily, C. M. 2005, A&A, 431, 517, doi: 10.1051/0004-6361:20041122

Lage, C., & Farrar, G. 2014, ApJ, 787, 144, doi: 10.1088/0004-637X/787/2/144

Law, D. R., Johnston, K. V., & Majewski, S. R. 2005, ApJ, 619, 807, doi: 10.1086/426779

Law, D. R., & Majewski, S. R. 2010, ApJ, 714, 229, doi: 10.1088/0004-637X/714/1/229

Lelli, F., McGaugh, S. S., & Schombert, J. M. 2016a, AJ, 152, 157, doi: 10.3847/0004-6256/152/6/157

—. 2016b, ApJL, 816, L14, doi: 10.3847/2041-8205/816/1/L14

Lelli, F., McGaugh, S. S., Schombert, J. M., Desmond, H., & Katz, H. 2019, MNRAS, 484, 3267, doi: 10.1093/mnras/stz205

Lelli, F., McGaugh, S. S., Schombert, J. M., & Pawlowski, M. S. 2016c, ApJL, 827, L19, doi: 10.3847/2041-8205/827/1/L19

—. 2017, ApJ, 836, 152, doi: 10.3847/1538-4357/836/2/152

Li, P., Lelli, F., McGaugh, S., & Schombert, J. 2018, A&A, 615, A3, doi: `10.1051/0004-6361/201732547`

Li, Z., Dekel, A., Mandelker, N., Freundlich, J., & François, T. 2022, arXiv e-prints, arXiv:2206.07069. `https://arxiv.org/abs/2206.07069`

Llinares, C., Knebe, A., & Zhao, H. 2008, MNRAS, 391, 1778, doi: `10.1111/j.1365-2966.2008.13961.x`

Łokas, E. L., Athanassoula, E., Debattista, V. P., et al. 2014, MNRAS, 445, 1339, doi: `10.1093/mnras/stu1846`

Lokas, E. L., Ebrova, I., Del Pino, A., & Semczuk, M. 2014, MNRAS, 445, L6, doi: `10.1093/mnrasl/slu128`

Łokas, E. L., Kazantzidis, S., Majewski, S. R., et al. 2010, ApJ, 725, 1516, doi: `10.1088/0004-637X/725/2/1516`

Łokas, E. L., Semczuk, M., Gajda, G., & D'Onghia, E. 2015, ApJ, 810, 100, doi: `10.1088/0004-637X/810/2/100`

Londrillo, P., & Nipoti, C. 2009, Memorie della Societa Astronomica Italiana Supplementi, 13, 89. `https://arxiv.org/abs/0803.4456`

Ludlow, A. D., Benítez-Llambay, A., Schaller, M., et al. 2017, PhRvL, 118, 161103, doi: `10.1103/PhysRevLett.118.161103`

Lüghausen, F., Famaey, B., & Kroupa, P. 2015, Canadian Journal of Physics, 93, 232, doi: `10.1139/cjp-2014-0168`

Lynden-Bell, D. 1976, MNRAS, 174, 695, doi: `10.1093/mnras/174.3.695`

Majewski, S. R., Nidever, D. L., Smith, V. V., et al. 2012, ApJL, 747, L37, doi: `10.1088/2041-8205/747/2/L37`

Majewski, S. R., Skrutskie, M. F., Weinberg, M. D., & Ostheimer, J. C. 2003, ApJ, 599, 1082, doi: `10.1086/379504`

Malhan, K., & Ibata, R. A. 2018, MNRAS, 477, 4063, doi: `10.1093/mnras/sty912`

Malhan, K., Ibata, R. A., & Martin, N. F. 2018, MNRAS, 481, 3442, doi: `10.1093/mnras/sty2474`

Malhan, K., Valluri, M., & Freese, K. 2021, MNRAS, 501, 179, doi: `10.1093/mnras/staa3597`

Malhan, K., Valluri, M., Freese, K., & Ibata, R. A. 2022a, arXiv e-prints, arXiv:2201.03571. `https://arxiv.org/abs/2201.03571`

Malhan, K., Ibata, R. A., Sharma, S., et al. 2022b, ApJ, 926, 107, doi: `10.3847/1538-4357/ac4d2a`

Mamon, G. A., & Łokas, E. L. 2005, MNRAS, 363, 705, doi: `10.1111/j.1365-2966.2005.09400.x`

Mancera Piña, P. E., Fraternali, F., Oosterloo, T., et al. 2021, MNRAS, doi: `10.1093/mnras/stab3491`

Mancera Piña, P. E., Fraternali, F., Adams, E. A. K., et al. 2019, ApJL, 883, L33, doi: `10.3847/2041-8213/ab40c7`

Marasco, A., Posti, L., Oman, K., et al. 2020, A&A, 640, A70, doi: `10.1051/0004-6361/202038326`

Martin, N. F., Ibata, R. A., McConnachie, A. W., et al. 2013, ApJ, 776, 80, doi: `10.1088/0004-637X/776/2/80`

Martin, N. F., Venn, K. A., Aguado, D. S., et al. 2022, Nature, 601, 45, doi: `10.1038/s41586-021-04162-2`

Mateo, M., Olszewski, E. W., & Morrison, H. L. 1998, ApJL, 508, L55, doi: `10.1086/311720`

Mayer, L., Governato, F., Colpi, M., et al. 2001, ApJL, 547, L123, doi: `10.1086/318898`

McGaugh, S., & Milgrom, M. 2013a, ApJ, 766, 22, doi: `10.1088/0004-637X/766/1/22`

—. 2013b, ApJ, 775, 139, doi: `10.1088/0004-637X/775/2/139`

McGaugh, S. S. 2016, ApJL, 832, L8, doi: `10.3847/2041-8205/832/1/L8`

McGaugh, S. S., Lelli, F., & Schombert, J. M. 2016, PhRvL, 117, 201101, doi: `10.1103/PhysRevLett.117.201101`

McGaugh, S. S., Schombert, J. M., Bothun, G. D., & de Blok, W. J. G. 2000, ApJL, 533, L99, doi: `10.1086/312628`

McGaugh, S. S., & van Dokkum, P. 2021, Research Notes of the American Astronomical Society, 5, 23, doi: `10.3847/2515-5172/abe1ba`

McMillan, P. J. 2017, MNRAS, 465, 76, doi: `10.1093/mnras/stw2759`

Milgrom, M. 1983, ApJ, 270, 365, doi: `10.1086/161130`

—. 1986, ApJ, 306, 9, doi: `10.1086/164314`

—. 2001, MNRAS, 326, 1261, doi: `10.1111/j.1365-2966.2001.04653.x`

—. 2008, NewAR, 51, 906, doi: `10.1016/j.newar.2008.03.023`

—. 2010, MNRAS, 403, 886, doi: `10.1111/j.1365-2966.2009.16184.x`

—. 2016, PhRvL, 117, 141101, doi: `10.1103/PhysRevLett.117.141101`

Miyamoto, M., & Nagai, R. 1975, PASJ, 27, 533

Monari, G., Famaey, B., Carrillo, I., et al. 2018, A&A, 616, L9, doi: `10.1051/0004-6361/201833748`

Moreno, J., Danieli, S., Bullock, J. S., et al. 2022, Nature Astronomy, doi: `10.1038/s41550-021-01598-4`

Moster, B. P., Naab, T., & White, S. D. M. 2013, MNRAS, 428, 3121, doi: `10.1093/mnras/sts261`

Müller, O., Pawlowski, M. S., Jerjen, H., & Lelli, F. 2018, Science, 359, 534, doi: `10.1126/science.aao1858`

Myeong, G. C., Evans, N. W., Belokurov, V., Sanders, J. L., & Koposov, S. E. 2018, MNRAS, 478, 5449, doi: `10.1093/mnras/sty1403`

Myeong, G. C., Vasiliev, E., Iorio, G., Evans, N. W., & Belokurov, V. 2019, MNRAS, 488, 1235, doi: `10.1093/mnras/stz1770`

Naidu, R. P., Conroy, C., Bonaca, A., et al. 2020, ApJ, 901, 48, doi: `10.3847/1538-4357/abaef4`

—. 2021, ApJ, 923, 92, doi: `10.3847/1538-4357/ac2d2d`

Nakajima, K., Izumi, K., & Asada, H. 2014, PhRvD, 90, 084026, doi: `10.1103/PhysRevD.90.084026`

Navarro, J. F., Benítez-Llambay, A., Fattahi, A., et al. 2017, MNRAS, 471, 1841, doi: `10.1093/mnras/stx1705`

Navarro, J. F., Frenk, C. S., & White, S. D. M. 1997, ApJ, 490, 493, doi: `10.1086/304888`

Niederste-Ostholt, M., Belokurov, V., Evans, N. W., & Peñarrubia, J. 2010, ApJ, 712, 516, doi: `10.1088/0004-637X/712/1/516`

Ocvirk, P., Gillet, N., Shapiro, P. R., et al. 2016, MNRAS, 463, 1462, doi: `10.1093/mnras/stw2036`

Ocvirk, P., Aubert, D., Sorce, J. G., et al. 2020, MNRAS, 496, 4087, doi: `10.1093/mnras/staa1266`

Oman, K. A., Navarro, J. F., Fattahi, A., et al. 2015, MNRAS, 452, 3650, doi: `10.1093/mnras/stv1504`

Oort, J. H. 1932, BAN, 6, 249

Oria, P.-A., Ibata, R., Ramos, P., Famaey, B., & Errani, R. 2022a, ApJL, 932, L14, doi: `10.3847/2041-8213/ac738c`

Oria, P.-A., Tenachi, W., Ibata, R., et al. 2022b, arXiv e-prints, arXiv:2206.10404. `https://arxiv.org/abs/2206.10404`

Oria, P. A., Famaey, B., Thomas, G. F., et al. 2021, ApJ, 923, 68, doi: `10.3847/1538-4357/ac273d`

Ostriker, J. P., & Peebles, P. J. E. 1973, ApJ, 186, 467, doi: `10.1086/152513`

Ostriker, J. P., & Steinhardt, P. J. 1995, Nature, 377, 600, doi: `10.1038/377600a0`

Papastergis, E., Cattaneo, A., Huang, S., Giovanelli, R., & Haynes, M. P. 2012, ApJ, 759, 138, doi: `10.1088/0004-637X/759/2/138`

Pawlowski, M. S. 2018, Modern Physics Letters A, 33, 1830004, doi: `10.1142/S0217732318300045`

—. 2021, Nature Astronomy, 5, 1185, doi: `10.1038/s41550-021-01452-7`

Pawlowski, M. S., Oria, P.-A., Taibi, S., Famaey, B., & Ibata, R. 2022, ApJ, 932, 70, doi: `10.3847/1538-4357/ac6ce0`

Peñarrubia, J., Belokurov, V., Evans, N. W., et al. 2010, MNRAS, 408, L26, doi: `10.1111/j.1745-3933.2010.00921.x`

Peñarrubia, J., Zucker, D. B., Irwin, M. J., et al. 2011, ApJL, 727, L2, doi: `10.1088/2041-8205/727/1/L2`

Peebles, P. J. E. 2020, MNRAS, 498, 4386, doi: `10.1093/mnras/staa2649`

Piffaretti, R., Arnaud, M., Pratt, G. W., Pointecouteau, E., & Melin, J. B. 2011, A&A, 534, A109, doi: `10.1051/0004-6361/201015377`

Planck Collaboration, Ade, P. A. R., Aghanim, N., et al. 2016, A&A, 594, A13, doi: `10.1051/0004-6361/201525830`

Pontzen, A., & Governato, F. 2012, MNRAS, 421, 3464, doi: `10.1111/j.1365-2966.2012.20571.x`

Posti, L., & Fall, S. M. 2021, A&A, 649, A119, doi: `10.1051/0004-6361/202040256`

Posti, L., Fraternali, F., & Marasco, A. 2019a, A&A, 626, A56, doi: `10.1051/0004-6361/201935553`

Posti, L., Marasco, A., Fraternali, F., & Famaey, B. 2019b, A&A, 629, A59, doi: `10.1051/0004-6361/201935982`

Qian, Y., Arshad, Y., & Bovy, J. 2022, MNRAS, doi: `10.1093/mnras/stac238`

Ramachandran, P., & Varoquaux, G. 2011, Computing in Science and Engineering, 13, 40, doi: `10.1109/MCSE.2011.35`

Ramos, P., Antoja, T., Yuan, Z., et al. 2021, arXiv e-prints, arXiv:2112.02105. `https://arxiv.org/abs/2112.02105`

Recio-Blanco, A., de Laverny, P., Palicio, P. A., et al. 2022, arXiv e-prints, arXiv:2206.05541. `https://arxiv.org/abs/2206.05541`

Reddish, J., Kraljic, K., Petersen, M. S., et al. 2022, MNRAS, 512, 160, doi: `10.1093/mnras/stac494`

Reid, B., Ho, S., Padmanabhan, N., et al. 2016, MNRAS, 455, 1553, doi: `10.1093/mnras/stv2382`

Riess, A. G., Casertano, S., Yuan, W., Macri, L. M., & Scolnic, D. 2019, ApJ, 876, 85, doi: `10.3847/1538-4357/ab1422`

Riess, A. G., Yuan, W., Macri, L. M., et al. 2021, arXiv e-prints, arXiv:2112.04510. `https://arxiv.org/abs/2112.04510`

Robin, A. C., Luri, X., Reylé, C., et al. 2012, A&A, 543, A100, doi: `10.1051/0004-6361/201118646`

Roshan, M., Ghafourian, N., Kashfi, T., et al. 2021, MNRAS, 508, 926, doi: `10.1093/mnras/stab2553`

Rubin, V. C., Ford, W. K., J., & Thonnard, N. 1980, ApJ, 238, 471, doi: `10.1086/158003`

Ruiz-Lara, T., Matsuno, T., Sofie Lövdal, S., et al. 2022, arXiv e-prints, arXiv:2201.02405. `https://arxiv.org/abs/2201.02405`

Sales, L. V., Wetzel, A., & Fattahi, A. 2022, Nature Astronomy, doi: `10.1038/s41550-022-01689-w`

Sancisi, R. 2004, in Dark Matter in Galaxies, ed. S. Ryder, D. Pisano, M. Walker, & K. Freeman, Vol. 220, 233. `https://arxiv.org/abs/astro-ph/0311348`

Sanders, R. H. 1999, ApJL, 512, L23, doi: `10.1086/311865`

—. 2003, MNRAS, 342, 901, doi: `10.1046/j.1365-8711.2003.06596.x`

Schönrich, R., Binney, J., & Dehnen, W. 2010, MNRAS, 403, 1829, doi: `10.1111/j.1365-2966.2010.16253.x`

Sellwood, J. A., & Sanders, R. H. 2022, arXiv e-prints, arXiv:2202.08678. `https://arxiv.org/abs/2202.08678`

Sestito, F., Buck, T., Starkenburg, E., et al. 2021, MNRAS, 500, 3750, doi: `10.1093/mnras/staa3479`

Skordis, C., & Złośnik, T. 2019, PhRvD, 100, 104013, doi: `10.1103/PhysRevD.100.104013`

Skordis, C., & Zlosnik, T. 2020, arXiv e-prints, arXiv:2007.00082. `https://arxiv.org/abs/2007.00082`

Skordis, C., & Złośnik, T. 2021, PhRvL, 127, 161302, doi: `10.1103/PhysRevLett.127.161302`

Sola, E., Duc, P.-A., Richards, F., et al. 2022, arXiv e-prints, arXiv:2203.03973. `https://arxiv.org/abs/2203.03973`

Steinmetz, M., & Navarro, J. F. 1999, ApJ, 513, 555, doi: `10.1086/306904`

Tenachi, W., Oria, P.-A., Ibata, R., et al. 2022, arXiv e-prints, arXiv:2206.10405. `https://arxiv.org/abs/2206.10405`

Teuben, P. 1995, in Astronomical Society of the Pacific Conference Series, Vol. 77, Astronomical Data Analysis Software and Systems IV, ed. R. A. Shaw, H. E. Payne, & J. J. E. Hayes, 398

Thomas, G. F., Famaey, B., Ibata, R., Lüghausen, F., & Kroupa, P. 2017, A&A, 603, A65, doi: `10.1051/0004-6361/201730531`

Thomas, G. F., Famaey, B., Ibata, R., et al. 2018, A&A, 609, A44, doi: `10.1051/0004-6361/201731609`

Tiret, O., & Combes, F. 2007, A&A, 464, 517, doi: `10.1051/0004-6361:20066446`

Tollerud, E. J., Boylan-Kolchin, M., & Bullock, J. S. 2014, MNRAS, 440, 3511, doi: `10.1093/mnras/stu474`

Tully, R. B., Courtois, H. M., & Sorce, J. G. 2016, AJ, 152, 50, doi: `10.3847/0004-6256/152/2/50`

Tully, R. B., & Fisher, J. R. 1977, A&A, 54, 661

Vale, A., & Ostriker, J. P. 2004, MNRAS, 353, 189, doi: `10.1111/j.1365-2966.2004.08059.x`

van Albada, T. S., & Sancisi, R. 1986, Philosophical Transactions of the Royal Society of London Series A, 320, 447, doi: `10.1098/rsta.1986.0128`

van Dokkum, P., Shen, Z., Keim, M. A., et al. 2022, Nature, 605, 435, doi: `10.1038/s41586-022-04665-6`

Vasiliev, E. 2019, MNRAS, 482, 1525, doi: `10.1093/mnras/sty2672`

Vasiliev, E., Belokurov, V., & Erkal, D. 2021a, MNRAS, 501, 2279, doi: `10.1093/mnras/staa3673`

—. 2021b, MNRAS, 501, 2279, doi: `10.1093/mnras/staa3673`

Verlinde, E. 2017, SciPost Physics, 2, 016, doi: `10.21468/SciPostPhys.2.3.016`

Wang, C., Huang, Y., Yuan, H., et al. 2022, ApJS, 259, 51, doi: `10.3847/1538-4365/ac4df7`

Widmark, A., de Salas, P. F., & Monari, G. 2021, A&A, 646, A67, doi: `10.1051/0004-6361/202039852`

Willmer, C. N. A. 2018, ApJS, 236, 47, doi: `10.3847/1538-4365/aabfdf`

Wolf, J., Martinez, G. D., Bullock, J. S., et al. 2010, MNRAS, 406, 1220, doi: `10.1111/j.1365-2966.2010.16753.x`

Woudenberg, H. C., Koop, O., Balbinot, E., & Helmi, A. 2022, arXiv e-prints, arXiv:2202.02132. `https://arxiv.org/abs/2202.02132`

Wu, X., Famaey, B., Gentile, G., Perets, H., & Zhao, H. 2008, MNRAS, 386, 2199, doi: `10.1111/j.1365-2966.2008.13198.x`

Wu, X., & Kroupa, P. 2015, MNRAS, 446, 330, doi: `10.1093/mnras/stu2099`

Wu, X., Wang, Y., Feix, M., & Zhao, H. 2017, ApJ, 844, 130, doi: `10.3847/1538-4357/aa7b8a`

Xue, X. X., Rix, H. W., Zhao, G., et al. 2008, ApJ, 684, 1143, doi: `10.1086/589500`

Yadav, J. K., Bagla, J. S., & Khandai, N. 2010, MNRAS, 405, 2009, doi: `10.1111/j.1365-2966.2010.16612.x`

Yanny, B., Newberg, H. J., Johnson, J. A., et al. 2009, ApJ, 700, 1282, doi: `10.1088/0004-637X/700/2/1282`

Yuan, Z., Myeong, G. C., Beers, T. C., et al. 2020, ApJ, 891, 39, doi: `10.3847/1538-4357/ab6ef7`

Yuan, Z., Martin, N. F., Ibata, R. A., et al. 2022, MNRAS, 514, 1664, doi: `10.1093/mnras/stac1399`

Zhao, H., & Famaey, B. 2010, PhRvD, 81, 087304, doi: `10.1103/PhysRevD.81.087304`

—. 2012, PhRvD, 86, 067301, doi: `10.1103/PhysRevD.86.067301`

Zwicky, F. 1933, Helvetica Physica Acta, 6, 110

Pierre-Antoine ORIA

Exploration des théories de matière noire et de gravitation modifiée dans l'Univers Local et la Voie Lactée

UNIVERSITÉ DE STRASBOURG

Observatoire astronomique de Strasbourg

Alors que les expériences de détection de particules de matière noire froide demeurent inconcluantes et que des relations de régularité très fortes sont observées à l'échelle des galaxies - suggérant un rôle important pour la matière baryonique voire un couplage avec la masse manquante - il est crucial de s'intéresser à des modifications du modèle LCDM ou à des alternatives. Notre galaxie la Voie Lactée et son environnement l'Univers Local offrent un laboratoire idéal pour ce type d'étude, avec des données d'observation de qualité notamment pour les structures du halo stellaire.

Le travail mené pendant cette thèse a d'abord porté sur la modification de gravité MOND et en particulier sur l'effet de champ externe et des tests du principe d'équivalence fort. Nous avons quantifié l'effet de champ externe des grandes structures distantes sur la Voie Lactée et les galaxies de l'univers local. Puis, nous avons proposé une nouvelle formule analytique pour obtenir l'accélération MOND sous un champ externe constant, et établi que des galaxies naines de l'amas de Coma semblaient ne pas subir l'effet de champ externe, exhibant un nouveau problème potentiel pour MOND dans l'environnement des amas de galaxies.

Enfin, nous nous sommes penchés sur divers phénomènes posant problème au modèle LCDM. D'abord, nous avons établi que la chute du Grand Nuage de Magellan dans la Voie Lactée n'était pas une cause suffisante pour mener à la création du plan de satellites observé. Puis, nous avons proposé un modèle pour la bifurcation présente dans le courant stellaire du Sagittaire, basé sur un disque peu massif qui termine sa course dans la branche peu lumineuse du courant. Ce mystère observé il y a plus de quinze ans pourrait maintenant être proche d'être élucidé.

Mots-clés : astrophysique, dynamique galactique, matière noire, gravitation, courants stellaires

As cold dark matter particles remain elusive in detection experiments, and while extraordinary regularity is observed at the scale of galaxies - suggesting an important role for baryons and perhaps a coupling with the missing mass - it is of utmost importance to consider modifications to the LCDM model and alternatives. Our galaxy and the local universe constitute an ideal laboratory, with exquisite observational data for stellar halo structures in particular.

The work done in this thesis focused first on the MOND modification of gravity and on the external field effect and departure from the strong equivalence principle in particular. We quantified the external field from distant large structures on the Milky Way and the Local Universe. We then proposed a new formula for the MOND acceleration under a constant external field, and showed that some dwarf galaxies in the Coma cluster seemed to not suffer the external field effect, highlighting a potential new problem for MOND in the galaxy cluster environment.

Finally, we investigated various issues with the LCDM model. We showed that the infall of the Large Magellanic Cloud can not be a sufficient cause for the formation of the observed plane of satellites. Then we proposed a model for the bifurcation in the Sagittarius stellar stream, based on a low mass disk component which ends up populating the faint branch. This mystery first observed more than fifteen years ago could now be close to being solved.

Keywords: astrophysics, galactic dynamics, dark matter, gravitation, stellar streams